Charge Transport in Molecular Junctions Beyond Tunneling

by

Akhtar Bayat

A thesis submitted in partial fulfillment of the requirements for the degree of

Doctor of Philosophy

Department of Chemistry
University of Alberta

Abstract

Electrical behavior of thin layers of molecules sandwiched vertically between two carbon contacts is the subject of this thesis. The main focus was put on the effect of molecular structural variations on charge transport through the molecular layers. The charge transport mechanism was deduced by analyzing the dependence of current on voltage, thickness of the molecular layer and temperature. The effect of compositional asymmetry was investigated in bilayers made from two different molecules. Multilayers made from only one type of molecule by reduction of diazonium ions are compositionally symmetric and were found to exhibit symmetric current-voltage characteristics. Bilayers made from two different molecules also showed symmetric current-voltage behavior when the second layer of the bilayer was only a monolayer, attached via azide-alkyne click chemistry to a multilayer of ethynylbenzene, and the total thickness of the bilayer was less than 5 nm. The charge transport properties of thin bilayers were found to be consistent with tunneling charge transport mechanism. Bilayers consisting of multilayers of two different molecules were rectifiers, given the total thickness of the bilayer was more than 10 nm and the bilayer was composed of a multilayer of an electron acceptor molecule such as naphthalene diimide together with a multilayer of an electron donor molecule such as fluorene in a vertical stack. Reversing the order of the two multilayers in the bilayer resulted in reverse rectification direction, confirming the molecular origin of this rectification behavior. The rectification persisted even at low temperatures of liquid helium. Charge transport in thick molecular junctions was studies further in a series of phenylthiophene derivative molecular junctions with thickness of 2-16 nm. A multistep tunneling charge transport was suggested to be operative in these thick carbon-based molecular junctions.

Preface

Part of Chapter 2 of this thesis has been published as : S. Y. Sayed, A. Bayat, M. Kondratenko, Y. Leroux, P. Hapiot, and R. L. McCreery; "Bilayer Molecular Electronics: All-Carbon Electronic Junctions Containing Molecular Bilayers Made with "Click" Chemistry" Journal of the American Chemical Society 2013, 135, 12972-12975. This is an equally contributed first author paper in which I was responsible for synthesis of methyl and hexyl ferrocene azides, click chemistry reaction optimization, data collection and analysis. Dr. Sayed Y. Sayed contributed to click chemistry reaction optimization, data collection and analysis and manuscript preparation. Dr. Mykola Kondratenko synthesized the alkyl azides. Dr. Yan Leroux and Dr. Philippe Hapiot provided the TIPS molecule. Dr. Richard L. McCreery was responsible for the concept and assisted in data analysis and manuscript preparation.

Chapter 3 was designed by myself. I was also responsible for data collection and analysis with help from Dr. Adam J. Bergren for liquid helium temperature and Kelvin probe measurements. Dr. Mykola Kondratenko synthesized the NDI molecule and Dr. Richard L. McCreery assisted in data analysis and interpretation. Part of Chapter 3 of this thesis has been published as: A. Bayat, J. C. Lacroix and R. L. McCreery; "Control of Electronic Symmetry and Rectification through Energy Level Variations in Bilayer Molecular Junctions" Journal of the American Chemical Society 2016, 138, 12287-12296.

The molecules used in Chapter 4 were provided by Dr. Jean Christophe Lacroix at the University of Paris, Diderot. Dr. Richard L. McCreery planned the project. Raman spectra were collected by assistance from Dr. Oleksii Ivashenko and I was responsible for data collection, analysis and interpretation.

To the memory of my father, NiazAli Bayat

And for my mother, Masoumeh Yengi-Qaleh

Who made this possible.

Acknowledgements

First I wish to express my deep gratitude to my advisor, Dr. Richard McCreery for his continuous guidance and support. Without his patience and understanding I definitely couldn't finish this work. I am thankful for generously providing all the resources and always being available for discussions. I appreciate the opportunities given to me in his group and his valuable contributions to this work. Thanks!

I would also like to thank my thesis committee members Dr. Arthur Mar and Dr. Michael Serpe and my exam committee members Dr. Julianne Gibbs-Davis, Dr Jonathan Veinot and Dr. Bernhard Kraatz for their helpful input toward improving this work.

Parts of this work are the result of collaboration between RLM group and other groups. I like to thank Dr. Jean Christophe Lacroix at Paris Diderot University for providing materials needed for chapter 4 and useful discussions and Dr. Philippe Hapiot and Dr. Yann Leroux at Institut des Sciences Chimiques de Rennes for proving the TIPS molecule for click chemistry.

Special thanks go to Dr. Sayed Nagy for incredible help and encouragement during my second and third years. He taught me the precision needed is surface science and helped me in surface modification and characterization. Many thanks to Dr. Mykola Kondratenko for synthesizing some of the molecules used in this work. His contribution helped massively in successful execution of some of my thought experiments. Also I am thankful to Dr. Adam Bergren for teaching me the Kelvin probe method and trouble shooting in the lab and being accessible and willing to discuss my work.

I like to thank Dr. Haijun Yan and Dr. Jerry Fereiro for getting me started in the lab and teaching my how to make PPF and modify the surface. I also would like to thank Bryan Szeto for training me on various instruments and technical support. Also thanks to Dr. David James for training me on EIS and Dr. Oleksii Ivashenko for Raman measurements. I cannot forget to thank Amin Morteza Najjarian for his helps and useful discussions in which he played the devil's advocate that enabled me to see the weaknesses of my work and hone my arguments.

I also like to thank Sanaz Nikjah for the good moments we shared in the city of Edmonton as friends and Dr. Vineetha Mukundan for her support especially leading up to my defense. I want to also thank all my past and present labmates in Dr. McCreery's group, Ushula, Parkash, Mustafa, Nikola, Matt, Xiangyu, Rajesh, Bikas, Angela, Scott, Lian and Yueqin for friendly discussions and enjoyable lab experience.

Finally I cannot thank my family enough for tremendous encouragement, support and love. Very special thanks to my parents, sisters and brothers for everything.

Table of Contents

List of Tables

List of Figures

List of Abbreviations

CMOS	Complementary Metal Oxide Semiconductor
HOMO	Highest Occupied Molecular Level
LUMO	Lowest Unoccupied Molecular Level
LB	Langmuir Blodgett
SPM	Scanning Probe Microscopy
STM	Scanning Tunneling Microscopy
MCBJ	Mechanically Controlled Break Junction
EBJ	Electromigration Break Junction
AFM	Atomic Force Microscopy
PDMS	Polydimethylsiloxane
SCLC	Space Charge Limited Current
Fc	Ferrocene
PEDOT:PSS	Poly(3,4-Ethylenedioxythiophene) Polystyrene Sulfonate
DMF	Dimethylformamide
DCM	Dichloromethane
ACN	Acetonitrile
IPA	Isopropyl Alcohol
TEA	Triehtylamine
THF	Tetrahydrofuran
MeFc	Methylferrocene
HxFc	Hexylferrocene
EB	Ethynylbenzene
TMS	Trimethylsilyl
TIPS	Triisopropylsilyl
PPF	Pyrolyzed Photoresist Film
GC	Glassy Carbon
TBAF	Tetrabutylammonium Fluoride
eC	Electron-Beam Evaporated Carbon
PVD	Physical Vapor Deposition
XPS	X-ray Photoelectron Spectroscopy
UPS	Ultraviolet Photoelectron Spectroscopy

OLED	Organic Light Emitting Diode
ITO	Indium Tin Oxide
NAB	Nitroazobenzene
AQ	Anthraquinone
FL	Fluorene
LC-MS	Liquid Chromatography- Mass Spectrometry
BTB	Bisthienylbenzene
BTAB	Bisthienylaminobenzene
$TBABF_4$	Tetrabutylammonium Tetrafluoroborate
NDI	Naphthalene Diimide
EIS	Electrochemical Impedance Spectroscopy
DS	Diazonium Salt
KP	Kelvin Probe
EDOT	Ethylene Dioxy Thiophene
TAB	2-(4-Aminophenyl)thiophene
EAB	2-(4-Aminophenyl)-3,4-ethylenedioxy thiophene
ETAB	2-(4-Aminophenyl)-3’,4’-ethylenedioxy-5,2’-bithiophene
TEAB	2-(4-Aminophenyl)-3,4-ethylenedioxy-5,2’-bithiophene
TB	Thienyl Benzene
ETB	EDOT Thienyl Benzene
TEB	Thienyl EDOT benzene
AB	Azobenzene

Chapter 1

Overview and Introduction

1.1 Introduction

The field of molecular electronics strives to understand charge transport mechanisms at nanometric length scales to design functional electronic components with molecular size[1]. Interest in electronic behavior of molecules was originally fueled by the ever decreasing size of the electronic components and the challenges and fundamental limitations faced by complementary metal oxide semiconductor (CMOS) technology upon downscaling to molecular sizes[2]. Molecules may also offer other functions not attainable by conventional silicon based technology[3] owing to rich optical, electrochemical, magnetic, thermoelectric and selective recognition properties of the molecules[1], [4]. Additionally, the vast diversity of molecules available that can be synthesized in large quantities adds to the appeal of molecular electronic research. The difference between molecular and organic electronics is one of size. Organic electronics deals with devices with active device thicknesses of more than 100 nm and often involves charge transport via series of redox steps that is temperature dependent and therefore thermally activated[5]. Molecular scale devices typically have smaller sizes and are often ruled by quantum mechanical tunneling which depends mainly on the electrochemical potential of the wires attached to the molecule or Fermi levels of the contacts, and the energy levels of the molecules. The energy levels of the molecule define the barrier that the charge faces during transport. In the simplest case, the hole tunneling barrier is the offset between the highest occupied molecular orbital (HOMO) and the Fermi level of the contact while the electron barrier is the offset between the lowest unoccupied molecular level (LUMO) and Fermi level. Various charge transport mechanisms have variety of barrier heights which are explained later in this Chapter.

The aim of this thesis is to describe charge transport properties of carbon contact/molecule/carbon contact based junctions by keeping the contacts invariant and changing the molecules sandwiched inside the junction.

Chapter 1 is an overview of different charge transport mechanisms operative in organic molecular junctions.

Chapter 2 is an investigation of charge transport in carbon contact/molecule1/molecule2/carbon contact junctions in which the total molecular bilayer is less than 5 nm in thickness.

Chapter 3 is the study of charge transport in carbon contact/molecule1/molecule2/carbon contact junctions with molecular bilayer thickness in the range of 15-25 nm.

And finally Chapter 4 deals with transport properties of carbon contact/Molecule/carbon contact junctions with molecular layer thickness of 2-16 nm and using different molecules.

In all Chapters the dependence of current on voltage, thickness of the molecular layer, temperature and molecular energy levels was studied in detail to draw conclusions about charge transport mechanism.

1.2 Paradigms for studying charge transport in molecular junctions

To investigate charge transport through molecules, an individual molecule or a thin layer of many molecules are suspended between two conductor contacts to enable voltage application and current measurement. The molecule(s) are sometimes attached to one contact via Langmuir-Blodgett (LB) method, self-assembly or reaction and covalent bond formation with the surface of the contact (see Figure 1.1) and then the other contact is brought into proximity or formed on the opposite side.

In other experiments, molecule(s) bridge the two contacts in the solution as the nanoscale gap between the two contacts is formed. Sandwiching a molecular layer between two contacts is accomplished by various methods. The most common contact formation methods for molecular electronics are shown in Figure 1.2.

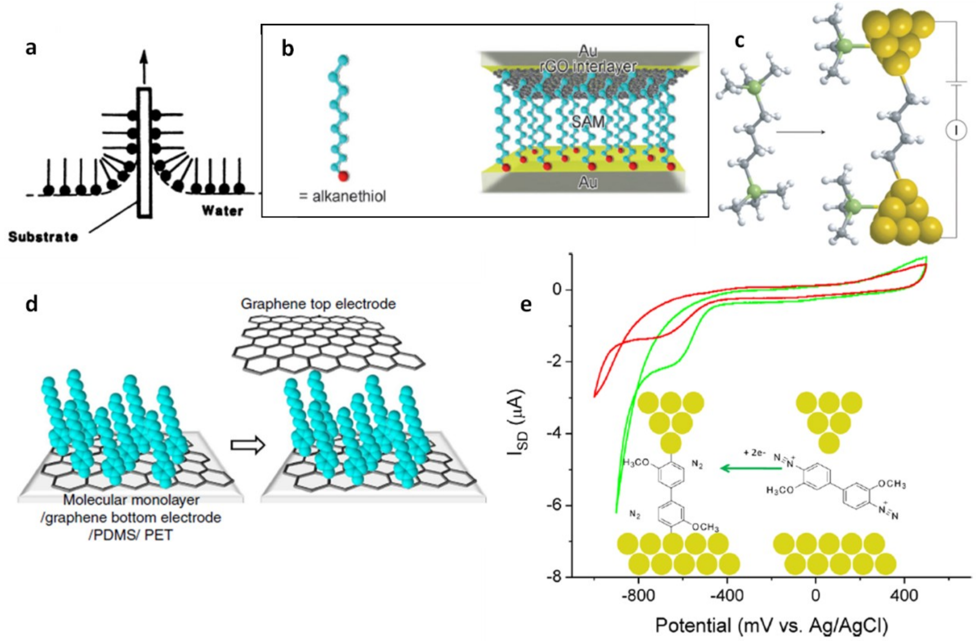

Figure 1.1: Common methods for molecular attachment to the contact in molecular electronics. a. LB method. Figure adapted with permission from ref[6]. b. self-assembly method in thiol self-assembly on gold. Figure adapted with permission from ref[7]. c. covalent bond formation between carbon and gold using 1,4-bis(trimethylstannyl)butane molecule. Figure adapted with permission from ref[8]. d. carbon-carbon covalent bond formation using diazonium molecules self-assembly on graphene. Figure adapted with permission from ref[9]. e. carbon-gold covalent bond formation via electroreduction of diazonium ions. Figure adapted with permission from ref[10].

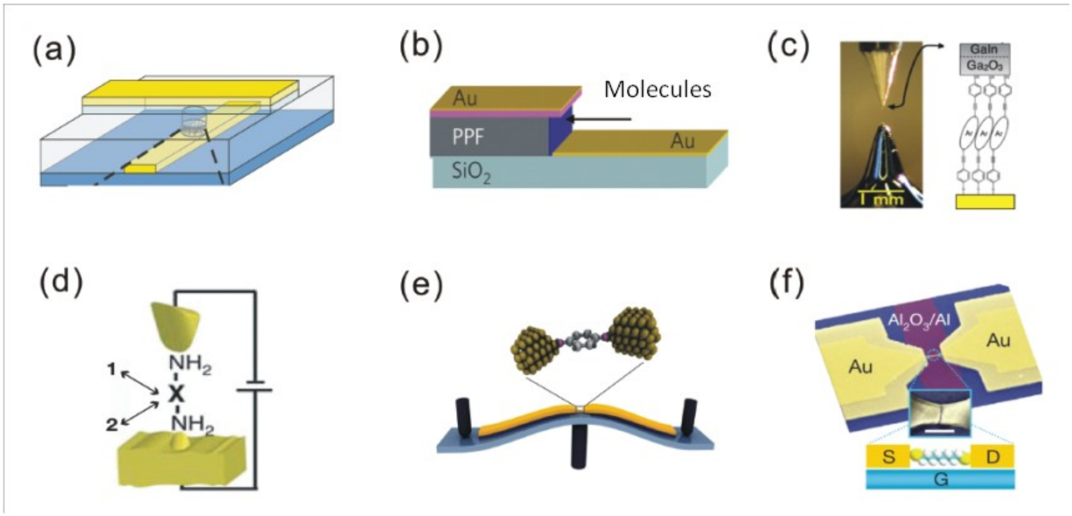

Figure 1.2: Common methods for molecular junction formation. a. conducting interlayer based junction using conducting polymer or graphene interlayers. b. evaporated top contact in direct deposition or surface diffusion mediated deposition. c. liquid top contact using gallium-indium alloy or Hg. d. SPM based methods including STM, conducting AFM and SECM. e. mechanically controllable break junction. f. electromigration break junction with gate. Figure adapted with permission from ref[11].

1.2.1 Single molecule junctions

A variety of methods have been used to form contact-single molecule-contact junctions including scanning probe microscopy (SPM) based techniques such as scanning tunneling microscopy (STM), mechanically controllable break junctions (MCBJs) and electromigration break junctions (EBJs). STM based junctions are formed either in a solution of molecules where molecules bridge the gap between the STM tip and the conducting substrate (Figure 1.3 a), or the STM tip is brought down on top of a conducting substrate that has been already modified by molecules. MCBJs are formed by stretching a metal wire that is glued on a bendable substrate by moving the piezo controlled pushing rods until the wire breaks and a nanogap is formed (Figure 1.3 b). A molecule with two anchoring groups can then bridge the gap. Formation of EBJs are very similar to MCBJs but instead of using mechanical force, an electric field is applied to a metallic nanowire formed by electron beam lithography to cause migration of metallic atoms and formation of the nanogap[12]. Other methods such as electrochemical deposition of top contact and electroburning of graphene electrode have also been reported for single molecule junction formation[13].

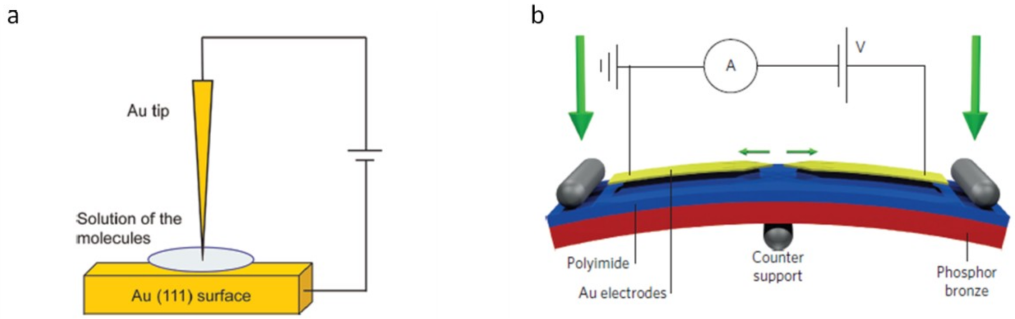

Figure 1.3: a. STM technique. Figure adapted with permission from ref[14]. b. MJBJ technique. Figure adapted with permission from ref[15].

Due to variations in the single molecule configuration and orientation relative to the contacts, electrical measurements on single molecule junctions are usually done many times to get an average of many possible configurations and orientations of the molecule[16]. Molecules with different structures or different substituents often show different electrical behavior[17] in single molecule junction paradigms as shown in Figure 1.4. However these differences between different molecules become clear only after many measurements to account for the effect of random orientations and contact geometry. The large variations in electronic behavior of single molecule junctions undermine their practical utility despite their promise for scientific studies.

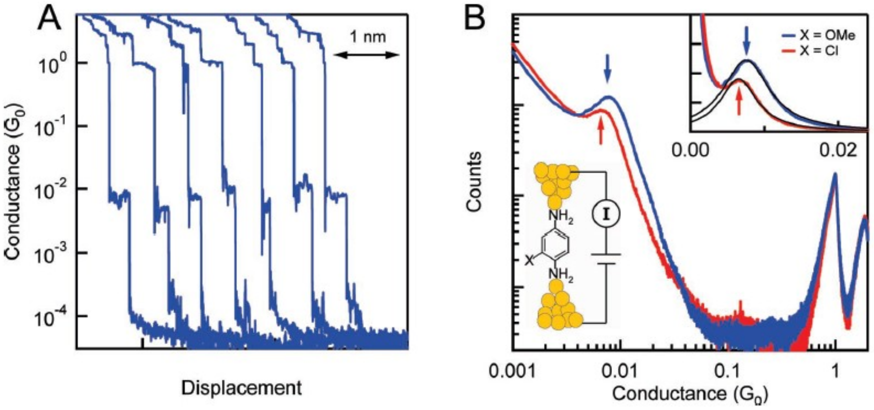

Figure 1.4: a. Sample conductance traces measured in the presence of a substituted benzene diamine molecule by breaking a gold point contact. With increasing the displacement, the gold point contact was broken and the conductance decreased to the single molecule conductance. The traces are offset along the x direction. b. Histograms of conductance for two benzene diamine molecules with OMe (blue) and Cl (red) substituents. The most probable conductance shows up as a peak in the histogram. The conductance is higher for the blue curve with electron donating molecule which is thought to decrease the hole tunneling barrier. Figure adapted with permission from ref[18].

1.2.2 Ensemble molecular junctions

In ensemble molecular junctions or “large area” molecular junctions, a thin layer of molecules is sandwiched between two conductors for electrical measurements. Techniques for fabrication of large area molecular junctions are more diverse than single molecule techniques and growing[13] with the most popular test beds shown in Figure 1.5. Large area conducting interlayer based junctions (Figure 1.2.a) are also common[19].

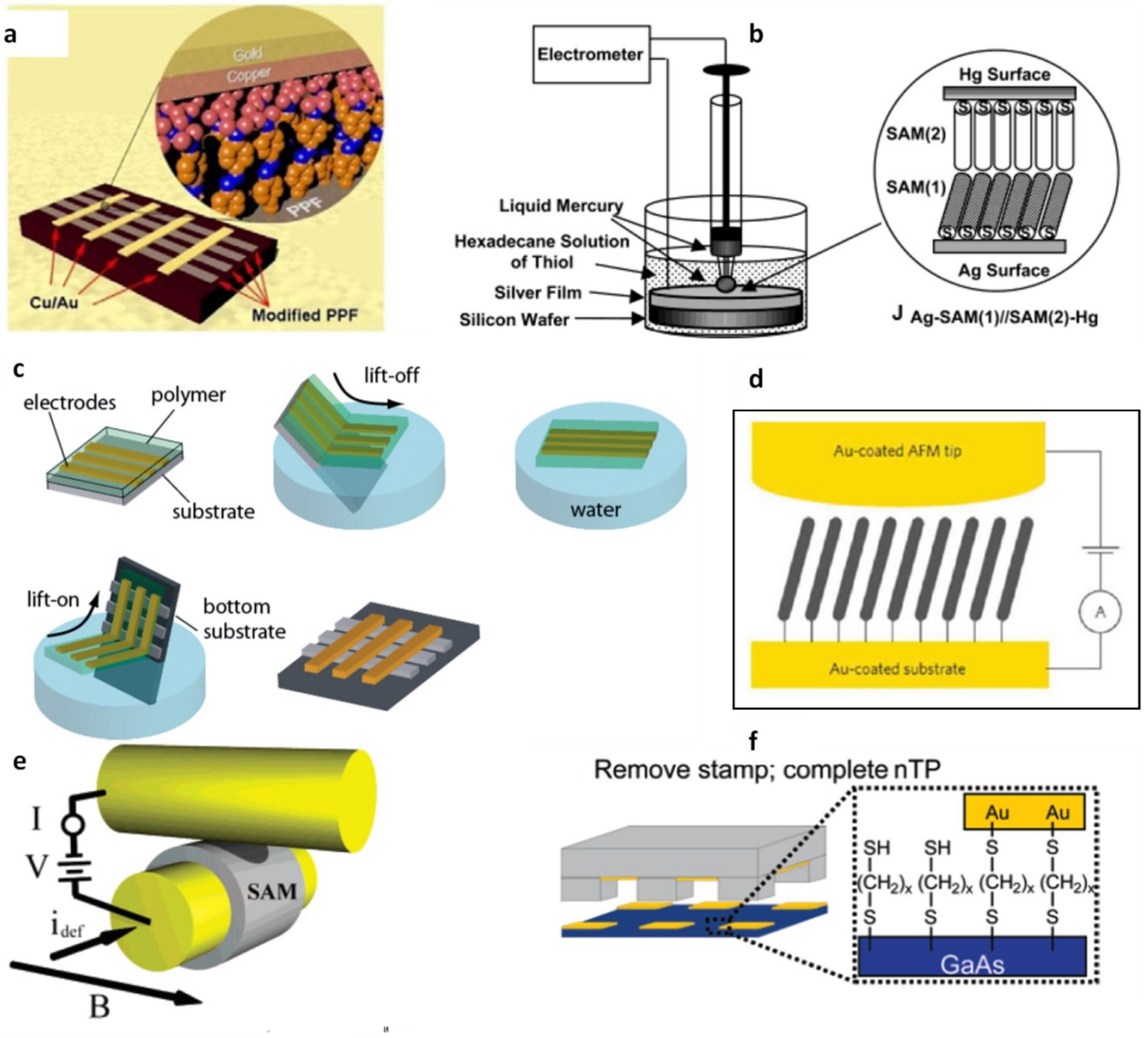

Figure 1.5: Common platforms for fabrication of ensemble molecular junctions. a. crossbar junction formation by evaporation of top contact. Figure adapted from ref[20]. b. using liquid top contacts. Figure adapted with permission from ref[21]. c. lift off float on method for top contact deposition. Figure adapted with permission from ref[22]. d. conducting AFM. Figure adapted with permission from ref[17]. e. crosswire junction. Figure adapted with permission from ref[23]. f. nanotransfer printing. Figure adapted with permission from ref[24].

The crossbar junction shown in Figure 1.5.a is formed by evaporation of a conducting contact on top of the covalently bonded molecular layer to form the molecular junctions at the crossing points between the bottom and top contacts. Liquid top contacts such as mercury or EGaIn are also widely used (shown in Figure 1.5.b)[21]. In the lift-off float-on method (Figure 1.5.c), a hydrophilic polymer is coated on the top contacts that are evaporated onto a sacrificial layer. The sacrificial layer is then dissolved or detached from the top contact and the polymer and leaves them on the surface of water. The bottom contact modified with molecules is then brought in contact with the top contact in the solution to form the complete junctions after drying[22]. Electrical measurement using conducting AFM (Figure 1.5.d) is another common method. The crosswire junction of Figure 1.5.e was formed by self-assembly of molecules on one gold nanowire. The two nanowires then were brought to close proximity by applying a DC voltage to one of the nanowires in an applied magnetic field which deflects the nanowire to bring it close to the other nanowire[23]. In nanotransfer printing (Figure 1.5.f), a gold coated PDMS stamp is brought into contact with the molecular layer. The removal of the stamp from the substrate leaves behind the gold layer and completes the junction[24].

Evaporation of top contact is the most straightforward method for formation of molecular junctions, but most molecular layers used in molecular electronics such as LB layers and thiol self assembled layers cannot tolerate the high energy impacts of the evaporated atoms of the top contact due to weak molecule-substrate bonds (Figure 1.6.a) which leads to formation of short circuits (Linear Current-voltage behavior with high conductivity) via penetration of top contact (Figure 1.6.b). The covalently bonded layers however don't easily desorb and can be successfully used for formation of molecular junctions by vapor deposition of top contact.

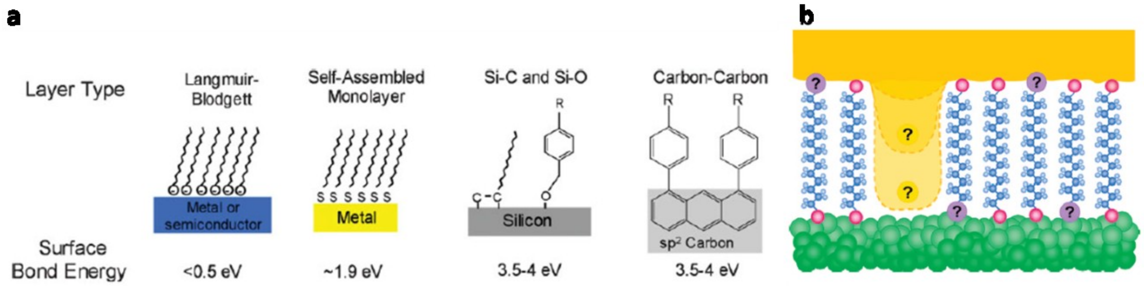

Figure 1.6: a. Surface-molecule bond energy for various surface attachment schemes. Figure adapted with permission from ref[1]. a. penetration of top contact due to desorption of the molecules or diffusion of molecules on the surface. Figure adapted with permission from ref[25].

Short circuits can also develop due to any imperfection or pinhole (unmodified spot) in the molecular layer which might cause a direct contact between the two contacts. Penetration of top contact through pinholes would generate an obviously large and linear JV response, and is easily detected. Electrochemical deposition of the molecular layer on a conducting substrate is an efficient way for formation of layers with very few pinholes and controlled thickness. Electrochemical deposition of the molecules ensures that the most conducting spots on the substrate (pinholes) get modified before other areas; therefore such layers are almost pinhole free. While short circuits occur occasionally (<10% of tested junctions), their rarity indicates a low density of pinholes. Fabrication of molecular junctions by electrochemical deposition of the molecular layer was first reported by McCreery and coworkers using electro reduction of diazonium salts on sp^2 carbon surface with mercury top contact[26]. Later, electro-oxidation of aliphatic amines was also reported for junction fabrication[27]. Evaporated copper top contact[20] and evaporated carbon top contact[28] were later successfully applied on these covalently bonded layers to form molecular junctions. Hence these molecular junctions shown in Figure 1.7, combine the advantages of electrochemical deposition of the molecular layer and top contact evaporation. Utilizing carbon as both contacts is particularly useful since carbon presumably evaporates as clusters and doesn't readily diffuse into the molecular layers, unlike metals that evaporate as atoms. Carbon also allows for application of high electric field to the junction because carbon is a covalent conductor and unlike metals it does not easily electromigrate.

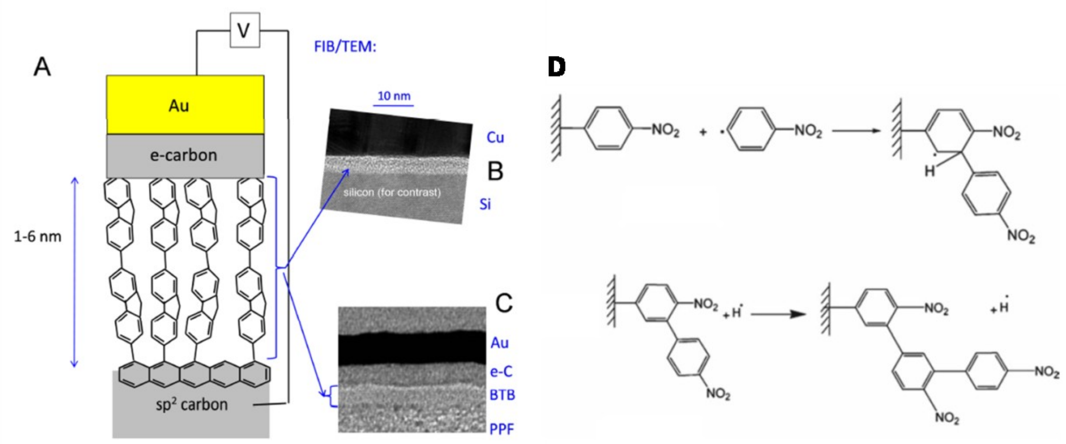

Figure 1.7: a. Schematic of two terminal molecular junction formed by electroreduction of aromatic diazonium salt on carbon or silicon substrate followed by e-beam evaporation of carbon and gold or copper top contacts. Focused ion beam/transmission electron microscopy cross section of b. silicon/molecules/copper junction and c. carbon/molecules/carbon-gold junction. Figures a,b,c adapted with permission from ref[29]. d. formation of multilayers by free radicals formed from electroreduction of diazonium ions. Figure d adapted with permission from ref[30].

The molecules in ensemble molecular junctions have a range of different orientations in the junctions and the electrical behavior of the ensemble is the average of all the molecules in the junction. This averaging reduces the need for repetitive measurements which increases the practical feasibility of these junctions for consumer applications. At the same time this averaging along with the interactions between the molecules and the contacts also may obscure the effects of molecular structure on electronic behavior. For instance minor differences were observed between ensemble molecular junctions with various aromatic molecules but the aromatics as a whole were more conducting than aliphatics[31]. Using a different ensemble junction structure, almost no difference was observed between a range of self assembled monolayers with different molecules as end groups in ensemble molecular junctions[32]. Additionally ensemble molecular junctions often have less conductance per molecule compared with single molecule junctions. This is thought to be due to smaller effective surface area between the molecular layer and the top contact compared with the geometrical area of ensemble molecular junctions which may be less than 1% for liquid top contacts[33].

1.3 Charge transport mechanisms in molecular junctions

A solid state molecular junction as described in the previous section, consists of a single molecule or a thin ensemble of molecules attached to at least two conducting leads (called contacts) as shown in Figure 1.8 for the case of a single molecule.

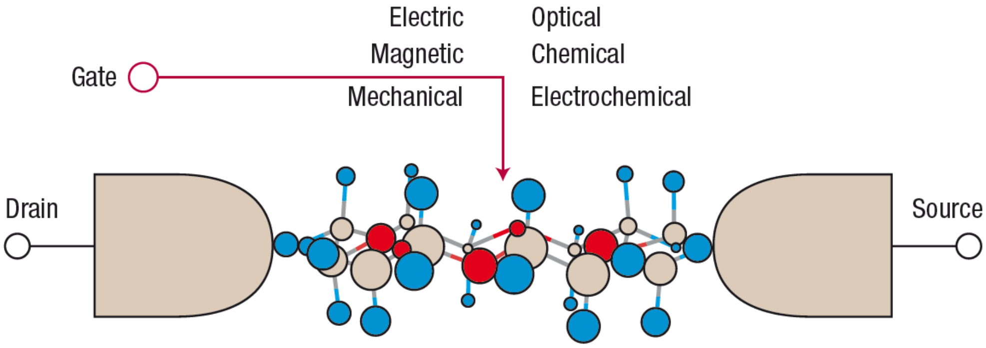

Figure 1.8: Schematic illustration of the basic component of the molecular junction. A molecule attached to two electrodes. Figure adapted with permission from ref[4].

The factors affecting the transport of charge through the molecular layer depend on the mechanism of charge transport, therefore by monitoring the effect of changing variables such as voltage and temperature on current, one can assign the charge transport mechanism in a molecular junction.

1.3.1 Tunneling

Tunneling has been reported to be the dominant mechanism of charge transport for molecular layers with thickness of less than ~5 nm [5], [34]. For a rectangular 1-D energy barrier with height φ and width d, the time independent Schrödinger Equation is written as:

$$\left[\frac{-\hbar^2}{2m}\nabla^2 + V(x)\right]\Psi = E\Psi \qquad (1.1)$$

In which m is the mass of the electron, E is the energy of the electron and V(x) describes the potential barrier shown in Figure 1.9 as a rectangle. An electron with energy less than the height of this rectangle (φ) can't classically overcome the barrier but considering the wave nature of the electron, the wave function of the electron outside of the barrier is written as superposition of the propagating and reflected waves:

$$\varphi_{I(x)=e^{ikx}+A.e^{-ikx}} \qquad (1.2)$$

In which A is a complex number and k=$\frac{\sqrt{2mE}}{\hbar}$. Φ_1 is a general solution to Schrödinger Equation for a free particle. Inside the barrier, the wave function decays exponentially:

$$\varphi_{II(x)=\alpha.e^{\kappa x}+\beta.e^{-\kappa x}} \qquad (1.3)$$

In which α and β are complex numbers and κ=$\frac{\sqrt{2m(\varphi-E)}}{\hbar}$. After passing the barrier, the wave function is a free particle again:

$$\varphi_{III(x)=B.e^{ikx}} \qquad (1.4)$$

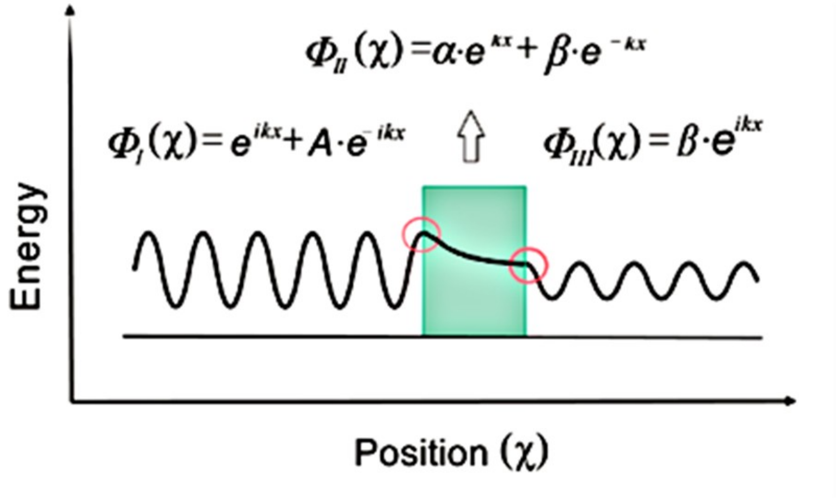

Figure 1.9: Schematic drawing of an electron tunneling through a rectangular barrier. Figure adapted with permission from ref[13].

The probability of an incident electron transmitting through the barrier is referred to as the transmission coefficient, with T=$|B|^2/|A|^2$. For a rectangular barrier T is given by[13]:

$$T = \left[1 + \left(\frac{k^2+\kappa^2}{2k\kappa}\right)^2 sinh^2(\kappa d)\right]^{-1} \tag{1.5}$$

For wide and thick potential barriers when φ>>E and κd>>1, T is simplified to:

$$T \approx \frac{16k^2\kappa^2}{(k^2+\kappa^2)^2}.e^{-2\kappa d} \tag{1.6}$$

The transmission coefficient is proportional to tunneling current, therefore the tunneling current decreases exponentially with the thickness of the molecular layer.

Coherent tunneling in molecular junction is described in Landauer formalism as[13], [35]:

$$I = \frac{2e}{h}\int T(E)[f_L(E) - f_R(E)]\,dE \tag{1.7}$$

Where e is charge of electron and L and R denote the left and right contacts. The Fermi function (f) is given by[13]:

$$f = \frac{1}{1+exp[(E-\mu)/kT]} \tag{1.8}$$

In which k is Boltzmann constant and μ is the Fermi level of the contact.

The discrete energy levels of the molecules become broadened due to interactions with contacts and the density of states of the broadened molecular levels in the contacts can be described as[13]:

$$D(E) = \frac{1}{2\pi}\frac{\Gamma}{(E-E_0)^2+(\frac{\Gamma}{2})^2} \tag{1.9}$$

In which E_0 is the discrete molecular orbital energy level and Γ describes the coupling strength of the molecule to the contact with the dimension of energy[36].

The transmission coefficient in the molecular junction in Equation 1.7 is then given by[13]:

$$T(E) = \frac{\Gamma_L\Gamma_R}{[E-E_0]^2+[\Gamma_L-\Gamma_R]^2} \tag{1.10}$$

Another common approach for describing tunneling in molecular junctions is using Simmons model[37]. In this approach, the shape of the potential barrier (Figure 1.10) is different from the rectangular shape due to image charge effects. The effect of the image charge is to reduce the width of the potential barrier to (S_2-S_1) shown in Figure 1.10 by rounding off the corners due to smaller barrier height close to a metallic surface as shown in Figure 1.11. The barrier height for electron tunneling is usually considered to be the LUMO to Fermi level energy offset if the LUMO level is more accessible and closer in energy to the Fermi level of the contact and the barrier for hole tunneling is considered to be HOMO to Fermi level energy offset when the molecular HOMO level is more accessible and closer in energy to the Fermi level of the contact. These barrier heights are smaller close to a metallic contact due to the stabilizing effect arising from the image charges, as shown in Figure 1.11.

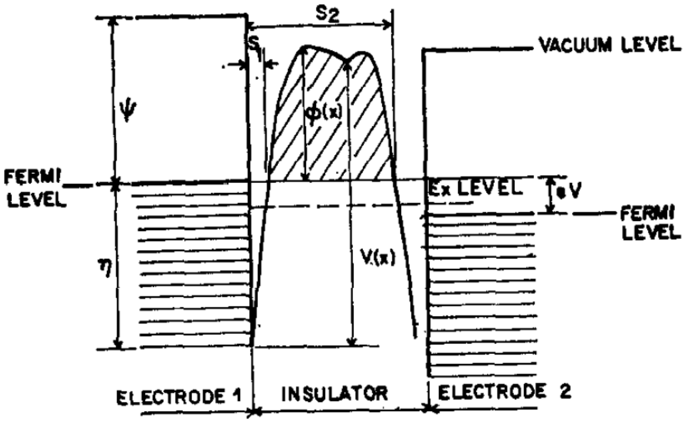

Figure 1.10: General shape of the tunneling barrier in Simmons model. Figure adapted with permission from ref[37].

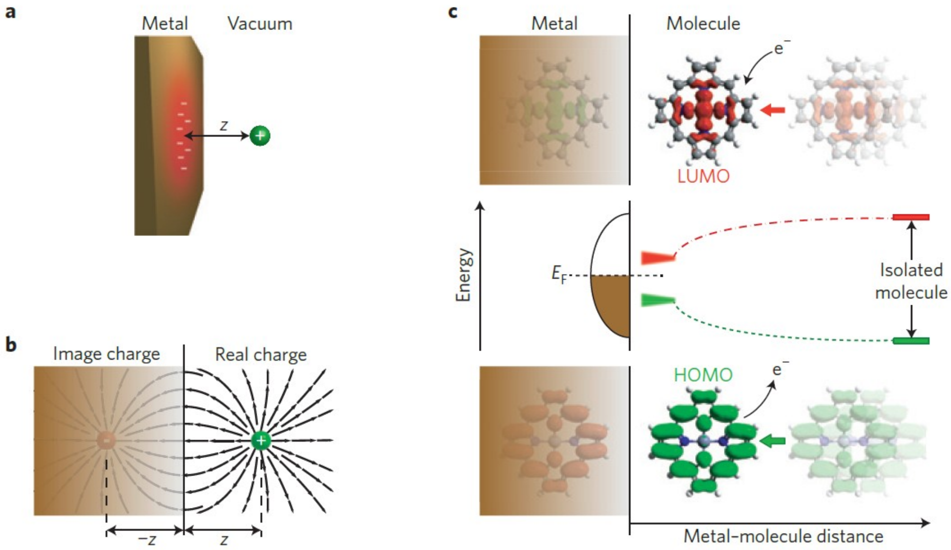

Figure 1.11: a. A positive charge inducing negative surface charges on the metallic contact. b. Electric field lines between the positive charge at distance z from the contact surface and its image charge at distance z inside the contact. c. An electron injected into LUMO is stabilized by the positive image charge inside the metal, thus lowering the LUMO level close to the contact. Likewise it is easier to take an electron out of the HOMO close to the contact because the resultant positive charge is stabilized by the negative image charge in the metal, shifting the HOMO upwards close to the contact. Figure adapted with permission from ref[38].

The average barrier height in Simmons model with the inclusion of image charge effect, is[39]:

$$\bar{\varphi} = \varphi_0 - qV\left(\frac{s_2+s_1}{2d}\right) - \left[1.15\lambda\frac{d}{s_2-s_1}\right] \times ln\left[\frac{s_2(d-s_1)}{s_1(d-s_2)}\right] \qquad (1.11)$$

In which $\bar{\varphi}$ is the average barrier height, φ_0 is the unmodified barrier height without consideration of the image charge, q is the charge of electron, V is voltage, d is the thickness of the molecular layer, s_2 and s_1 are distances between the contact and the barrier at the Fermi level as shown in Figure 1.3, and $\lambda = \frac{q^2 ln2}{8\pi\varepsilon_0\varepsilon d}$, with ϵ_0 being the permittivity of the free space and ϵ the relative dielectric constant of the molecular layer. The current density according to the Simmons model is then given by[39]:

$$J = c(\tilde{A} + \tilde{B} + \tilde{C}) \qquad (1.12)$$

Where $c = \frac{4\pi m_e q}{h^3}$ and

$$\tilde{A} = \frac{2qV}{A^2}\left\{\left(A\sqrt{\bar{\varphi}} + qV + 1\right)exp\left(-A\sqrt{\bar{\varphi} + qV}\right) - \left(A\sqrt{\eta + \bar{\varphi}} + 1\right)exp\left(-A\sqrt{\eta + \bar{\varphi}}\right)\right\} \qquad (1.13)$$

$$\tilde{B} = \bar{\varphi}\frac{2}{A^2}\left\{\left(A\sqrt{\bar{\varphi}} + 1\right)exp\left(-A\sqrt{\bar{\varphi}}\right) - \left(A\sqrt{\bar{\varphi} + qV} + 1\right)exp\left(-A\sqrt{\bar{\varphi} + qV}\right)\right\} \qquad (1.14)$$

$$\tilde{C} = \frac{2}{A}\left\{\left(\bar{\varphi}^{-\frac{3}{2}} + \frac{3}{A}\bar{\varphi} + \frac{6}{A^2}\sqrt{\bar{\varphi}} + \frac{6}{A^3}\right) exp\left(-A\sqrt{\bar{\varphi}}\right) - \left((\bar{\varphi} + qV)^{\frac{3}{2}} + \frac{3}{A}(\bar{\varphi} + qV) + \frac{6}{A^2}\sqrt{\bar{\varphi} + qV} + \frac{6}{A^3}\right) exp\left(-A\sqrt{\bar{\varphi} + qV}\right)\right\} \qquad (1.15)$$

In these three Equations, η is the Fermi level of the contact taken as a positive value (see Figure 1.10) and $A = \left(\frac{4\pi\Delta s}{h}\right)\sqrt{2m_e}$ in which Δs is the effective layer thickness (with image charge correction), h is Planck's constant and m_e is the effective mass of the charge carrier.

The simplified form of the tunneling current according to Simmons model is written as:

$$J = J_0 e^{-\beta d} \qquad (1.16)$$

Which shows that the tunneling current exponentially decreases with the thickness of the molecular layer and $\beta = 2\left(\frac{2m\varphi}{\hbar^2}\right)^{\frac{1}{2}}$, is defined as tunneling attenuation constant which depends mainly on the effective mass of the charge carrier and the barrier height. A plot of lnJ versus the thickness of the molecular layer is called a β plot and its slope yields the tunneling attenuation constant or β value which has been reported to be around 4.3-8.8 nm^{-1} for tunneling through alkane molecular layers and around 2.1-3.3 nm^{-1} for tunneling through aromatic molecular layers and less than 1 nm^{-1} for some redox active devices (like porphyrins)[40].

At high applied voltages when eV>φ, the barrier shape becomes triangular (see Figure 1.12) instead of the normal trapezoidal barrier shape of the Simmons model and the current is given by:

$$J_{FN} = BE^2 exp\left(-\frac{C}{E}\right) \tag{1.17}$$

This is the Fowler-Nordheim tunneling Equation in which E is the electric field (V/d), $B = q^3/16\pi^2\hbar m_e\varphi$ and $C = \left(4\sqrt{2m_e}/3q\hbar\right)\varphi^{3/2}$.

When the charge transport in a molecular layer is dominated by Fowler-Nordheim tunneling, a plot of ln(J/E^2) versus 1/E (called FN plot) is linear.

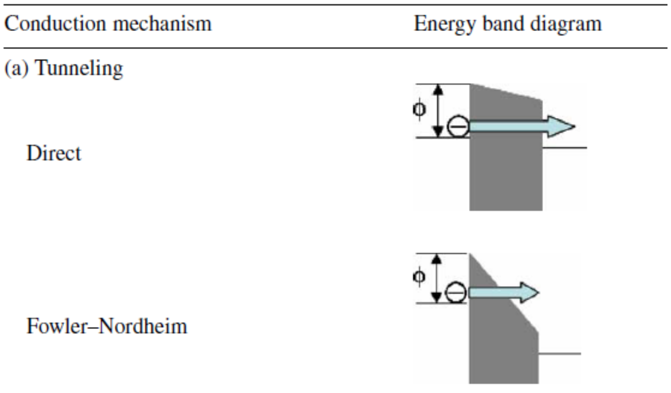

Conduction mechanism	Energy band diagram
(a) Tunneling	
Direct	
Fowler–Nordheim	

Figure 1.12: Comparison of the barrier shape of direct tunneling with Fowler-Nordheim tunneling for an electron. In FN tunneling, the carrier does not tunnel through the whole width of the layer but a portion of it. Figure adapted with permission from ref[41].

The conductance of a molecular layer is described by:

$$G = 2q^2/h\sum T_i \tag{1.18}$$

In which $2q^2/h$ is G_0 or the quantum of conductance and T_i is the transmission coefficient through each parallel molecule or conductance channel[17]. The Equation for G_0 is obtained from the Equation for current J=-qv(μ_1-μ_2)dn/dE in which v is the speed of electrons, μ_n the Fermi level of each contact and dn/dE is the density of states($cm^{-3}eV^{-1}$). The density of states in one dimension is 2/hv with 2 in the numerator indicating two states (spin up and down which are degenerate). By substituting dn/dE=2/hv and μ_1-μ_2=-qV in the Equation for J, we have J=$2q^2$V/h and $G_{(1D)}$ is J/V or $2q^2$/h. The conductance is generally obtained from:

$$G(V) = \frac{dI(V)}{dV} \tag{1.19}$$

Which has a roughly parabolic shape versus voltage[42].

Tunneling can also occur in several steps in a multi-step tunneling process as shown in Figure 1.13. The two step tunneling process shown in Figure 1.13 a follows the current conservation at the intermediate site, J_{01}=J_{12}. With the site half way through the barrier, the tunneling distance for each step is half of the thickness of the molecular layer which means the β value of the two step tunneling is half of the β value of direct tunneling[43] as shown in Figure 1.13 b.

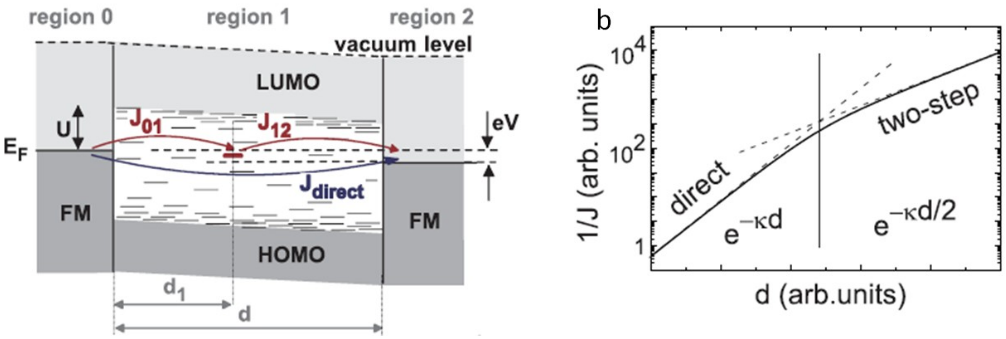

Figure 1.13: a. Multi-step tunneling process through an available molecular level. b. comparison of the β plot of direct and two-step tunneling. Figure adapted with permission from ref[43].

The tunneling process is in general elastic, meaning that the charge carrier does not lose energy during transport from one contact through the layer to the other contact. The excess energy of a carrier involved in an elastic tunneling process is entirely lost in the contact, but the multistep tunneling process can be elastic or inelastic[44], [45]. In inelastic multistep tunneling, the charge carrier loses some energy ($\hbar\omega$, with ω as the frequency of the vibrational mode localized in the barrier) inside the molecular layer, before tunneling out of the layer to the other contact[45].

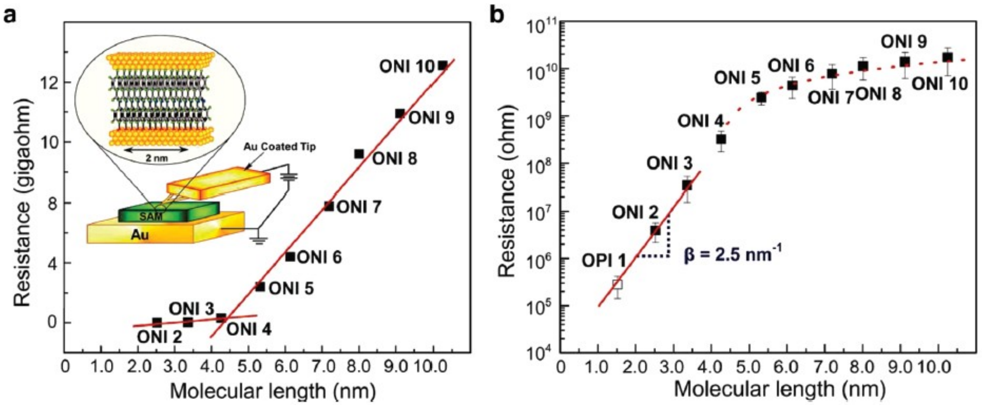

Figure 1.14: a. Plot of resistance versus the length of oligonaphthalenefluoreneimine (ONI) molecular layer for Au/molecules/Au junctions showing linearity of resistance with thickness for thicker layers. b. β plot for oligophenyleneimine (OPI) and ONI molecules, showing tunneling distance dependence for thinner layers. Figure adapted with permission from ref[46].

With increasing the thickness of the molecular layer beyond ~5 nm, a transition from tunneling charge transport to other charge transport mechanisms has been observed[46], [47]. An example of the transition from tunneling to hopping charge transport is shown in Figure 1.14 in which the exponential distance dependence of current for thinner layers gives way to linear dependence of inverse of current (resistance) on thickness for thicker layers[48].

1.3.2 Hopping

Charge hopping, also called "phonon assisted" tunneling is a process by which carriers move from one localized state to another by absorbing thermal energy (Figure 1.15). The general simplified expression for activated hopping is:

$$J = Ve^{-\frac{\Delta E_a}{kT}} \tag{1.20}$$

In which Ea is the activation energy (or the thermal energy) needed for the hopping process. According to Equation 1.20, lnJ is linear with 1/T for current in a device operating based on hopping. The slope of lnJ versus 1/T or Arrhenius plot can then be used to calculate the activation energy of the process.

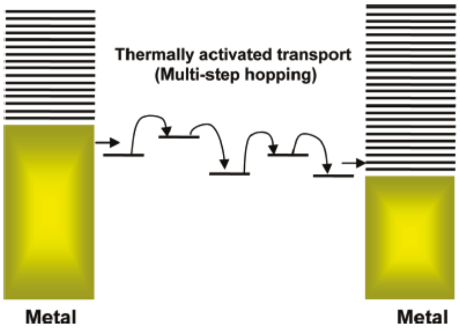

Figure 1.15: The schematic illustration of hopping process through a molecular wire. Figure adapted with permission from ref[49].

A charge carrier can hop from one site to another if the original site is occupied by a carrier but the destination site is empty and can accept the charge carrier. The hopping process is then described by a probability evolution master Equation[50]:

$$\frac{\partial}{\partial t} f_i(t) = -\sum_{j \neq i} W_{ij} f_i(t)\left[1 - f_j(t)\right] + \sum_{j \neq i} W_{ji} f_j(t)[1 - f_i(t)] - \lambda_i f_i(t) \tag{1.21}$$

In which $f_i(t)$ is occupational probability of site (i) with energy E_i and location R_i at time t. $[1-f_j(t)]$ is the probability that the site J is empty at time t. W_{ij} is the transition rate (or simply hopping rate) from site (i) to site (j) and λ_i is the decay rate of excitation at site (i).

There are two main expressions for W_{ij} transition rates[50]. One is given by Anderson and is knows as Miller-Abrahams expression[51], [52]:

$$W_{ij} = \upsilon \exp\left(-2\gamma R_{ij}\right)\begin{cases} \exp\left(-\frac{E_j-E_i}{k_B T}\right) & E_j > E_i \\ 1 & E_j < E_i \end{cases} \qquad (1.22)$$

υ is the jump-attempt frequency, γ is the overlap factor or inverse localization radius and R_{ij} is the distance between site (i) and (j). The first exponential is similar to Equation 1.16 and describes the exponential decay in overlap between the two sites with distance. The second exponential has the Arrhenius type temperature dependence for hopping upward in energy and is equal to 1 for jumping down in energy. Another expression for W_{ij} involves the coupling between molecular physical configuration and its electronic energy[53] and is given by Marcus[54]:

$$W_{ij} = \frac{t^2}{\hbar}\left[\frac{\pi}{k_B T \lambda_{reorg}}\right]^{1/2} exp\left[-\frac{\left(\lambda_{reorg}+E_j-E_i\right)^2}{4\lambda_{reorg} k_B T}\right] \qquad (1.23)$$

In which t (sometimes denoted as J or H, Figure 1.16) is electronic coupling between sites (i) and (j) and λ_{reorg} is the reorganization energy (see Figure 1.16) which is the energy for site (i) to take the configuration of the empty site (j).

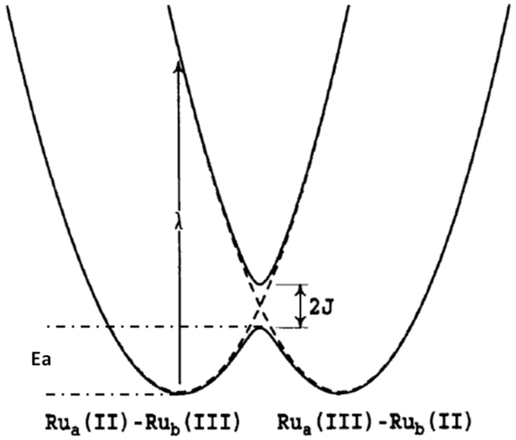

Figure 1.16: The Energy versus reaction coordinate for phonon assisted electron transfer between Ru^{++} and Ru^{+++} (Ru_a(II) means atom a being 2+ positive and Ru_a(III) means atom a being 3+ positive). Harmonic electron-phonon coupling leads to two Franck-Condon parabolic energy surfaces. The electronic coupling J (or t or H) determines the splitting at the intersection. The reorganization energy λ is the energy of vertical transition from the minimum to the other parabola. The activation energy for the electron transfer is also shown. Figure adapted with permission from ref[55].

Considering the Equation for the left hand side parabola in Figure 1.16 as $y=x^2$ with the minimum located on the origin, the minimum of the right side parabola is shifted to y+b and x+a, so the Equation for the right parabola is $(y+b) = (x+a)^2$ which gives y+b =

$x^2 + a^2 + 2ax$. At the point where two parabolas intersect, the y values are equal, therefore $x^2 + b = x^2 + a^2 + 2ax$ which gives $0 = a^2 + 2ax - b$ or $x=(a^2-b/2a)$ and from $y=x^2$ we have $y=(a^2-b)^2/4a^2$. The y value of the intersection between the two parabolas is the activation energy in Equation 1.23 and shown in Figure 1.16. b which is the displacement between two parabolas in the y direction is $(E_j – E_i)$ in Equation 1.23 and a was the displacement between the two parabolas in the x direction so from $y=x^2$, a^2 is the reorganization energy or λ in Equation 1.23 and shown in Figure 1.16.

The electronic coupling or t between the two sites in Equation 1.23 can be estimated from the splitting of the two HOMOs of the two sites or the two LUMOs of the sites. When two sites interact, the previous HOMOs of the individual sites split and form a common HOMO and HOMO-1 for both sites together and the same goes for LUMOs. Electronic coupling is estimated by[54] as shown in Figure 1.17:

$$t = \frac{E_{HOMO} - E_{HOMO-1}}{2} \quad \text{or} \quad t = \frac{E_{LUMO+1} - E_{LUMO}}{2} \tag{1.24}$$

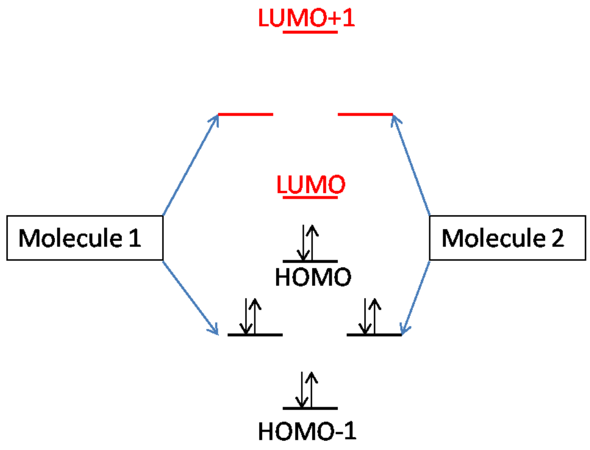

Figure 1.17: Splitting of energy levels due to electronics coupling between two molecules. The energy gap between HOMO and HOMO-1 or LUMO and LUMO+1 is approximately equal to 2t.

The variable range hopping (VRH) theory first introduced by Mott[56] is based on the idea that the hops don't have to be to closest neighbor sites if the activation energy for hops to the closest sites is large. Instead the hops might happen to sites farther away but closer in energy level to the original site with smaller activation energy. Hopping from a site is possible to the sites inside a sphere around the site, with the radius of the sphere changing with temperature. The charge transport through the organic layer then happens by charge carriers percolating through a net of these spheres that marginally touch. The rate of charge hopping through the layer is then limited by the smallest hopping rate in this percolation path. This is the basis of percolation theory of hopping describing hopping through the most optimal path or the path of least resistance formed by touching hopping spheres[57]. In percolation theory the hopping spheres are replaced by resistors in a network of resistors with the current between the two sites written as[50]:

$$I_{ij} = q[W_{ij} f_i (1 - f_j) - W_{ji} f_j (1 - f_i)] \tag{1.25}$$

To be able to distinguish the hopping process from other charge transport mechanisms, some form of temperature dependence study is needed as all hopping processes are thermally activated. If a hopping process was not activated, it turns to an elastic or inelastic tunneling process.

1.3.3 Poole-Frenkel emission from traps

The Poole- Frenkel effect, first described by Frenkel[58] in 1938 is the process of field enhanced thermal charge dissociation as shown in Figure 1.18.

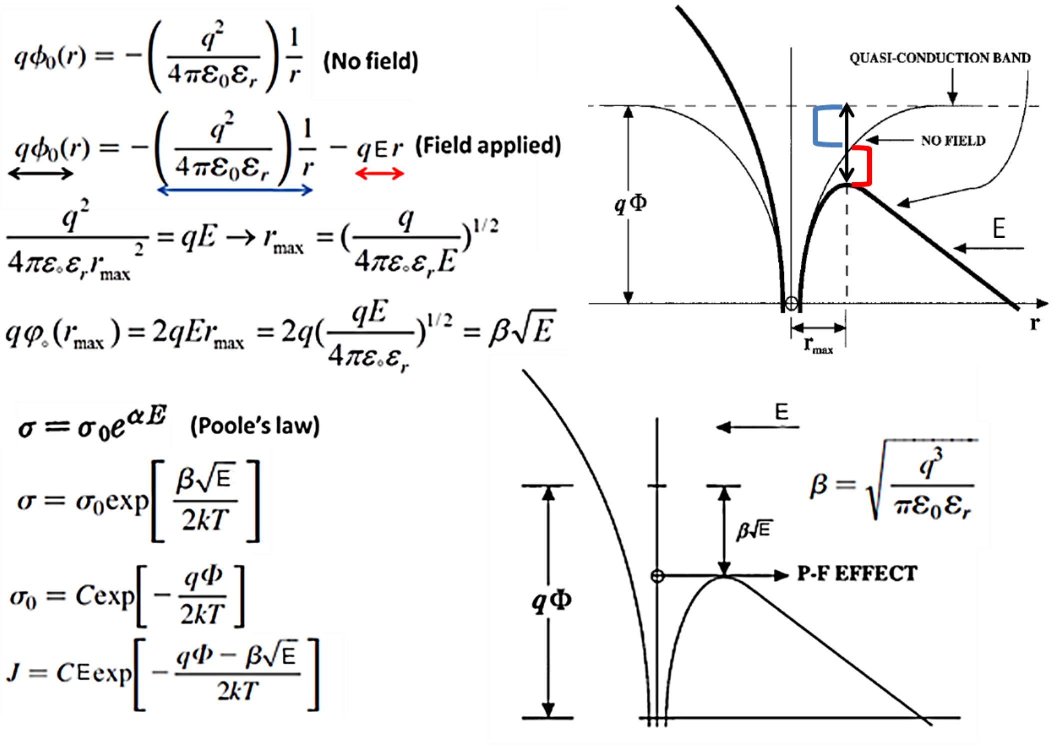

Figure 1.18: Description of the Poole-Frenkel barrier lowering for an electron escaping from a positively charged trap due to applied electric field. The barrier lowering (with the dimension of potential energy, qφ, eV) is calculated at the $r_{\max}$ point where the electric force (and potential energy) from the positively charged trap and the external electric field (E) are equal. The barrier lowering is then substituted in the Poole's law to give the Poole-Frenkel formula for thermal excitation out of coulomb traps with the Fermi level half way between the trap level and the conduction band. The conductivity (σ) is converted to current by multiplying by electric field (E).

The Poole-Frenkel (PF) process describes the thermal escape of a charge from a coulomb trap under an applied electric field, when the coulomb potential wall on one side of the trap is pushed down due to the external applied field (Figure 1.18). The PF effect happens for an electron dissociating from a neutral site which leaves behind a positive site. The electron is then escaping from the coulomb potential of the positively charged site it left behind. PF effect can also happen for a hole dissociating from a neutral site and leaving a negatively charged site behind[59].

Starting from Newton's second law and electric force, ma=qE and acceleration a=v/t, we obtain v=qEt/m, in which v is the speed of the carrier, E is the electric field and m is mass of the carrier. We can define μ=qt/m that gives v=Eμ. The drift current (Q/t) is then defined as the concentration of carriers multiplied by their speed:

$$J=qnv \text{ or } J=qn\mu \tag{1.26}$$

In which μ is called mobility. Mobility usually changes with the applied electric field in real devices and the general PF formula is given by[60]:

$$J = qn\mu_0 Eexp\left[-\frac{(q\varphi-\beta\sqrt{E})}{k_B T}\right] \tag{1.27}$$

In which μ_0 is mobility at zero electric field, E is electric field, $\beta=(q^3/\pi\epsilon_0\epsilon_r)^{1/2}$ determines the barrier lowering ($\beta E^{1/2}$ shown in Figure 1.18) and qφ is the ionization energy of the trap (shown in Figure 1.18).

From Equation 1.27, it is seen that PF charge transport mechanism has an Arrhenius temperature dependence with $E_a = q\varphi - \beta E^{1/2}$. Additionally, ln(J/E) is also linear with square root of the electric field for PF charge transport according to Equation 1.27. A PF like charge transport mechanism was observed[47] for carbon/bisthienylbenzene/carbon molecular junctions with the thicknesses of less than 16 nm which did not have a linear Arrhenius plot and was only weakly activated. The PF-like effect was attributed to field ionization of the molecular HOMOs in which the molecular HOMOs act as traps in the field driven PF process and are rapidly filled by tunneling from the contact.

If the number of traps increases such that the barrier lowering of different traps overlap, the PF conductions turns into Poole conduction in which ln(J/E) is linear with E instead of square root of E[61].

1.3.4 Schottky emission

The Schottky, or thermionic emission is the thermal injection of charge carriers from the contact into the organic layer due to injection barrier lowering under the applied electric field as shown in Figure 1.19. The thermionic emission process is an interface limited process (the interface between the contact and the organic layer) similar to tunneling process while PF and hopping processes are bulk limited. The thermionic emission process is also a charge dissociation process in which the carrier is escaping from the coulomb potential of its own image charge in the contact. The image charge is not fixed and has the same distance from the interface as the charge carrier, unlike the position of the trap in PF effect which is fixed, therefore the distance between the carrier and its image charge in Schottky effect is twice that in PF effect ($r_{max(Schottky)=}2r_{max(PF)}$ in Figure 1.18). The end result is that the Schottky barrier lowering is half of PF barrier lowering.

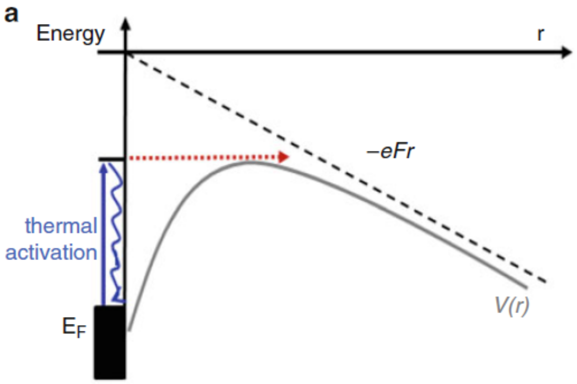

Figure 1.19: Schottky emission of an electron out of the Fermi level of the contact into the conduction band of the organic layer. Figure adapted with permission from ref[62].

The Schottky emission formula is[63]:

$$J_s = A^*T^2 exp\left[\frac{-q(\varphi_s - \sqrt{qE/4\pi\varepsilon_r\varepsilon_0})}{kT}\right] \qquad (1.28)$$

In which A^* is Richardson's constant, E is electric field and φ_s is the thermionic emission barrier at the interface. From Equation 1.28, the Schottky charge transport is recognizable from linearity of lnJ with square root of the electric field and the linearity of $\ln(J/T^2)$ with 1/T.

Schottky charge transport has been observed in both thick organic layers[64] and thin molecular junctions[65].

1.3.5 Space charge limited conduction

The accumulation of charges inside an insulator or semiconductor is generally modeled by a combination of continuity Equation ($\nabla.J = -\frac{\partial\rho}{\partial t}$) and Poisson Equation ($\nabla.E = \frac{\rho}{\varepsilon}$) with ρ= charge density, t= time, E= electric field and ϵ is the dielectric constant of the medium. The injection of charges into an insulator gives rise to space charge limited (SCLC) current when the density of injected charges exceeds the density of free thermal charges already present in the device. Since in organic semiconductors the electrons are bound in HOMO and do not easily create thermal free charges (like by jumping to conduction band in crystalline inorganic semiconductors), the density of free charges in organic semiconductors is low and SCLC current is observed routinely. The SCLC current I_{sclc}=Q/t_t can be obtained from Q=CV with C=$\chi_s/4\pi d$ and Q=$I_{sclc}t_t$ and t_t=$d^2/\mu V$ with d/t_t=μE and E=V/d. In this derivation t_t is the transit time for the charge carrier in the device, C is the capacitance, χ_s is the dielectric constant of the organic material, d is the thickness of the organic material, μ is the mobility of the charge carriers and E is the applied electric field. I_{sclc} is then given from above by[66]:

$$I_{SCLC} \sim \chi_s \mu \frac{V^2}{d^3} \tag{1.29}$$

This is the modified Child's law given by Mott and Gurney for SCLC current in a solid state device. Equation 1.29 or Mott-Gurney law describes the current in a device in which carriers are easily injected into the bulk of the device and are compensated for by opposite charges at the other electrode[67]. The injection of charges is then limited by the capacitance of the layer and its dielectric constant to shield the charges from each other.

The mobility of the carriers is considered to be independent of the electric field in 1.29 for a trap free layer. For a layer with traps and considering a Poole-Frenkel electric field dependence for the mobility, the SCLC current is approximated by[68]:

$$J = \frac{9}{8}\varepsilon\varepsilon_0\mu_0\frac{V^2}{d^3}exp\left(0.891\gamma\sqrt{E}\right) \tag{1.30}$$

In which μ_0 is the zero field mobility, E is electric field and γ is called the field enhancement factor[69]. The quadratic voltage dependence of Equation 1.29 for trap free case is replaced by more complex voltage dependence of Equation 1.30. In general the SCLC current in the presence of traps has the form:

$$I_{sclc}=V^m \tag{1.31}$$

With m as the slope of lnJ vs. lnV equal to 2 for trap free or trap filled regions of the J-V curve and m>2 for trap filling region of the J-V curve as shown in log-log plot of Figure 1.20. At low voltages in region A of Figure 1.20, the number of injected carriers has not yet exceeded the thermal free carrier and the current is ohmic J=qnμV/d with m=1 in Equation 1.31. With increasing the voltage the current first becomes quadratic in voltage in region T1 according to Equation 1.29 and then traps are activated at higher voltages to give rise to region B with m>2 in Equation 1.31. Finally at even higher voltages, all the traps are filled (more accurately all the traps are charged or in Figure 1.18 are empty or positively charged) and the SCLC current again has quadratic voltage dependence (Equation 1.29) in region C. For only one set of shallow traps with only one energy level, the region beyond T1 does not exist and the dependence of current on voltage at higher voltages remain quadratic. A shallow trap can be defined as a trap in which the residence time of the carrier is less than the transit time t_t. For only one set of deep traps with only one energy level, region B is almost vertical and quickly turns to quadratic dependence of the trap filled region. It is only for a distribution of traps that the region B is extended[66].

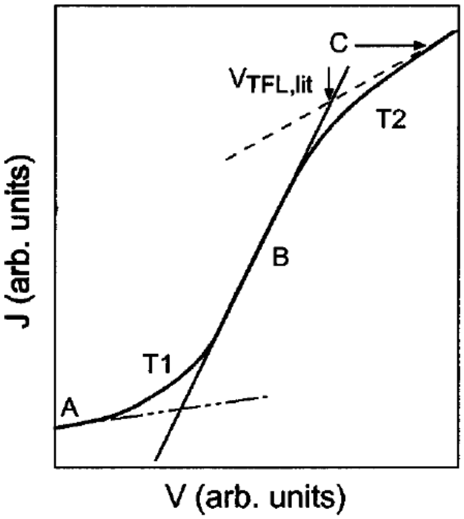

Figure 1.20: Log-log plot of J versus V for typical organic material. Region A is the ohmic region. Region T_1 is the transition region to trap filling region. Region B is the trap filling region with the slope of lnJ versus lnV bigger than 2. V_{TFL} is the trap filled limit voltage or the voltage that is required to charge all the traps. Region T_2 is transition to trap filled limit and region C is the trap filled region. Figure adapted with permission from ref[70].

In region B of Figure 1.20, the SCLC current is described by[70]:

$$J = q^{1-l}\mu N_{\vartheta}\left(\frac{2l+1}{l+1}\right)^{l+1}\left(\frac{l\varepsilon\varepsilon_0}{(l+1)H_b}\right)^{l}\frac{V^{l+1}}{d^{2l+1}} \qquad (1.32)$$

In which N_ϑ is the effective density of states and H_b is the density of traps. $l=T_c/T$ with T, temperature and T_c as the characteristic temperature of the trap distribution[71]. For a trap distribution wider in energy, T_c is larger and the slope of lnJ versus lnV ($l+1$ in Equation 1.32) is also larger.

1.4 Energy level shift at contact-molecule interface

The image charge effect (refer to Figure 1.11) is not the only force affecting the molecular energy levels close to the contact surface. As shown in Figure 1.21.a, the energy levels also become broadened. The electrons in the energy levels of the molecule have finite life time in the molecular state before transport into the contact. This finite lifetime results in uncertainty in energy and broadened energy levels. The electrostatic interactions between molecular dipoles and image charges in the contact (1.22.c) can broaden the energy levels further. Reaction of the molecule with the contact can also create hybrid molecule-contact states which broadens the isolated molecule's energy levels[72].

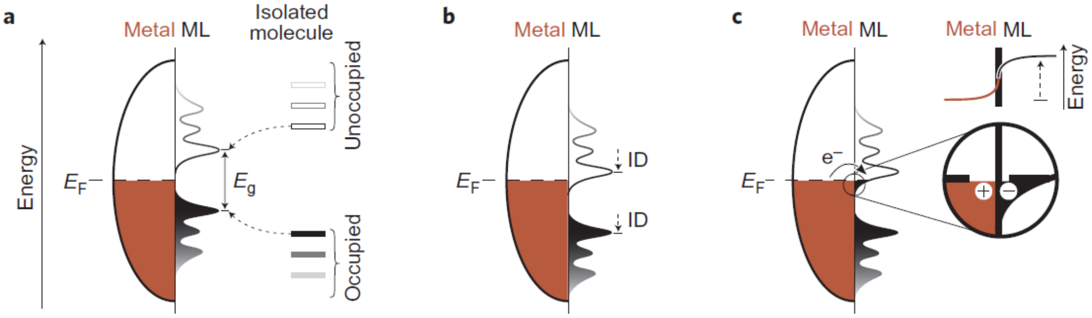

Figure 1.21: a. The isolated energy levels become broadened and the HOMO-LUMO gap decreases close to the contact. b. Interface dipole (ID) pushes the energy levels of molecule around relative to Fermi level of the contact. c. charge transfer between the broadened molecular states and contact. Figure adapted with permission from ref[73].

The development of interface dipole upon contact with the molecule can shift the molecule's energy levels (Figure 1.21.b) up or down depending on the direction of the dipole. If some of molecule's energy levels become equal in energy to the Fermi level of the contact, charge transfer between the contact and molecule can occur (Figure 1.21.c)[73]. The broadening of the energy levels is more pronounced when there is a reaction between the contact and the material. For example evaporation of a metal on a clean inorganic semiconductor in vacuum results in reaction between the dangling bonds of the semiconductor's surface and the metal and creation of hybrid metal-semiconductor states called gap states with energy levels inside the band gap of the semiconductor. Molecules normally have closed shells with no dangling bonds and do not easily react with the contact unless a bond is formed between the molecule and the contact. The bond formation process results in the formation of hybrid molecule-contact or gap states and broadening[74]. Regardless of whether a bond is formed between the molecule and the contact or not, upon close contact between the molecules and the contact, an interface dipole forms. The first component of interface dipole is the pillow effect which is the push back of the tail of electrons extending out from the surface of contact, due to repulsion from electrons in the molecules. This effect decreases the apparent work function of the contact metal. The permanent dipole of the molecule may also cause charge rearrangement within the contact and give rise to an interface dipole. If the molecule reacts with the contact, then electron withdrawing or donating nature of the molecule also contribute to the interface dipole.

Two extreme cases can be considered for the situation when molecule is brought in contact with a metal[75]. In one case, the energy levels of the molecules do not broaden or shift relative to contact as shown in Figure 1.22.a. In another case, gap states originated from reaction between molecules and contact, or broadened molecular states (called interface states) from electrostatic interactions between dipoles and the surface (Figure 1.22.c) fill the HOMO-LUMO gap and charge redistribution across the interface creates an interface dipole[76]. For partial or integer charge transfer from molecules to the contact (when an electron donating molecule is grafted to the surface), the energy required to take an electron out from the contact to vacuum level (where it is free) decreases, this is shown in 1.22.b by a downward step in vacuum level at the interface. Δ or vacuum level shift denotes the magnitude of the interface dipole. The gap states can be sufficiently numerous to bring the Fermi level of any contact to the same position relative to HOMO and LUMO level of the molecule at the interface[77].

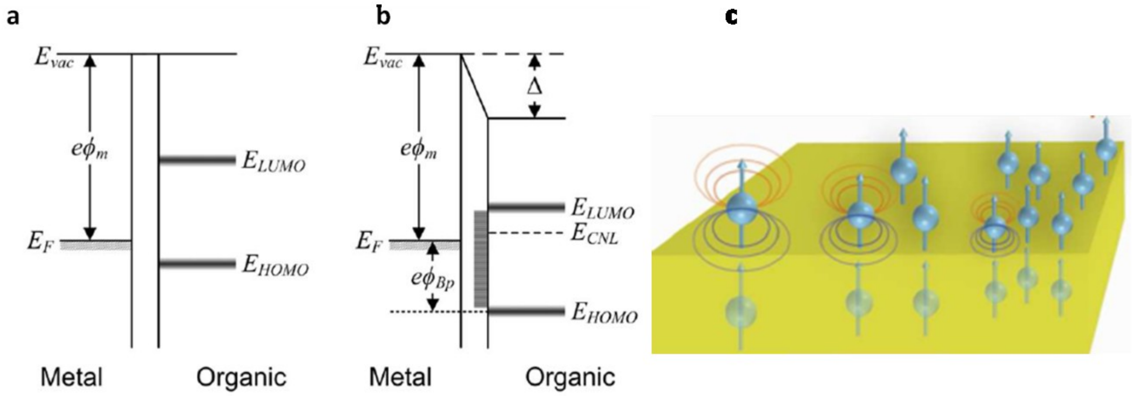

Figure 1.22: a. Metal-molecule interface with no surface dipole. b. Fermi level pinning at metal-molecule interface. Gap states shown as gray vertical column. E_{CNL} or charge neutrality level is an energy level in the gap states at which the molecular layer is neutral. Here the Fermi level of contact is under E_{CNL} showing that some charge transfer from molecular layer to contact has occurred. Figures a,b adapted with permission from ref[77]. c. electrostatic interactions between molecular dipoles and their image dipoles in the contact can broaden the molecular energy levels. Figure adapted with permission from ref[72].

This process of Fermi level pinning by charge transfer between gap states and the contact can frustrate attempts to control the hole or electron barriers by changing the molecule or the contact metal. It was observed that for eight aromatic molecules grafted covalently to the surface, the Fermi level of the contact was pinned at 1.2 eV above the HOMO levels of the molecules[31], making all hole tunneling barriers, β values and J-V curves statistically indistinguishable among the eight molecular layers.

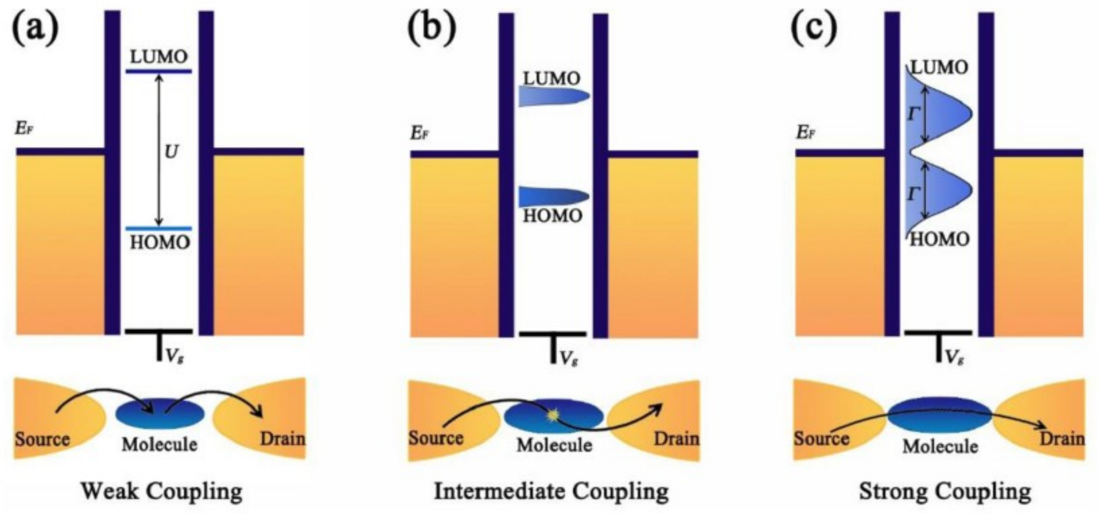

Figure 1.23: Coupling strengths in molecular junctions. a. weak coupling. b. intermediate coupling. c. strong coupling. Figure adapted with permission from ref[13].

The degree of interaction between the molecule and the contact in molecular junctions is described as coupling strength. Weak coupling (Figure 1.23.a) means very little interaction between the molecules and the contact. Strong coupling (Figure 1.23.c) on the other hand stands for strong interactions between molecule and contact that broadens the energy levels of the molecule so much that some energy levels may even come to resonance with the Fermi level of the contact. Such molecular junctions with strong coupling are therefore more conducting with smaller apparent tunneling barriers[13].

In general, the combination of energy levels of the molecule, Fermi level of the contact, molecule-contact interactions and molecule-environment interactions dictate the electronic behavior of the molecular junctions and its possible dynamic properties. By keeping the contacts and the bonding method to the surface unchanged, one can ask the question: How does the molecular structure affect the electronic behavior of the molecular junction?

The remaining Chapters consider examples of structural variation and its effect on current-voltage response of molecular junctions.

Chapter 2

Charge Transport Mechanism in “Click” bilayers

2.1 Introduction

Achieving and controlling a desired electronic function from a molecular junction by manipulating the structure and composition of the junction is one major motivation of the field of molecular electronics. The prerequisite for control over the properties of the molecular junction is the knowledge of the effect of different structural and compositional variations on the electronic properties of the device.

This Chapter describes an investigation of the rules governing charge transport in thin (<5nm) bilayer molecular junctions by introducing compositional asymmetry into the interior of the junction via click chemistry while keeping other aspects of junction structure constant. The compositional asymmetry is created as a result of the formation of a molecular bilayer which means the molecular layer is no longer composed of only one type of molecular subunit and is compositionally asymmetric. The first layer of the bilayer or primer layer was formed by the reduction of aromatic diazonium salts. The bilayer was then formed by the azide-alkyne click reaction which tolerates a wider range of molecular functional groups than diazonium chemistry, including alkanes, aromatics and redox active groups. Electronic measurements were then performed to determine charge transport properties of compositionally asymmetric thin junctions.

2.1.1 Transport through asymmetric two-step tunneling barriers

Tunneling through thin asymmetric inorganic barriers have been widely studied and demonstrated a range of attractive properties such as negative differential resistance (NDR)[78] and resonance tunneling[79]–[81] in resonant tunnel diodes based on inorganic bilayers.

Inorganic thin bilayers such as $CoFe_2O_4/MgAl_2O_4$[82] exhibit a slightly asymmetric current voltage behavior due to dependence of the highest barrier height on the applied bias as shown in Figure 2.1. The tunneling current is exponentially dependent on the square root of the barrier height, therefore the tunneling probability is largely determined by the highest barrier height rather than the average barrier height in bilayers with similar layer thicknesses[82]. The small asymmetry observed in inorganic bilayers due to bias dependent tunneling barriers and observation of NDR and resonant tunneling are strong motivators for investigation of the same tunneling barrier shapes in molecular electronics junctions.

The large variations in electronic conductivity and dielectric constant between different families of organic molecules such as alkanes and aromatics add to the complexity of the situation for organic bilayer barriers.

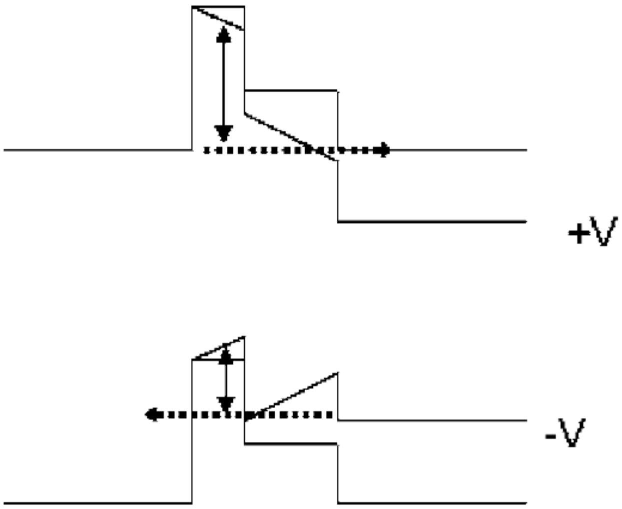

Figure 2.1: Schematic diagram of why tunneling current in asymmetric tunneling barriers is asymmetric in bias. The highest tunneling barrier in positive bias is higher than the negative bias, Therefore the current is larger at negative bias. Figure adapted with permission from ref[82].

Theoretical studies[83] suggested the possibility of constructing a rectifier from metal/molecule/ metal junctions using molecules with asymmetric tunneling barrier as shown in Figure 2.2. A rectifier is a device in which current is asymmetric in bias voltage. The suggested rectifier in Figure 2.2 is based on asymmetric voltage drop or in other words asymmetric coupling of the conductor (phenyl group) to the contacts. In Figure 2.2, the phenyl group is more strongly coupled to the left conductor and follows the Fermi level of the left contact while the right contact is decoupled from the phenyl group due to the presence of the long alkyl chain. The Fermi level of the right contact therefore can be easily moved relative to the molecular levels of the phenyl group which results in rectification. The experimental evidence for this rectification mechanism was observed in Si/alkylphenyl (or alkyl thiophen)/Al junctions with only one difference. Rectification was observed when the HOMO level of the phenyl or thiophene was brought into resonance with the contact instead of LUMO[84]. Later on it was theoretically suggested that using organometallics and specifically metallocenes can improve the rectification in alkyl-aromatic bilayers[85]. This is due to closeness of the HOMO level of metallocences to the Fermi level of the contact which should decrease the onset of rectification and result in more asymmetry in current-voltage characteristics.

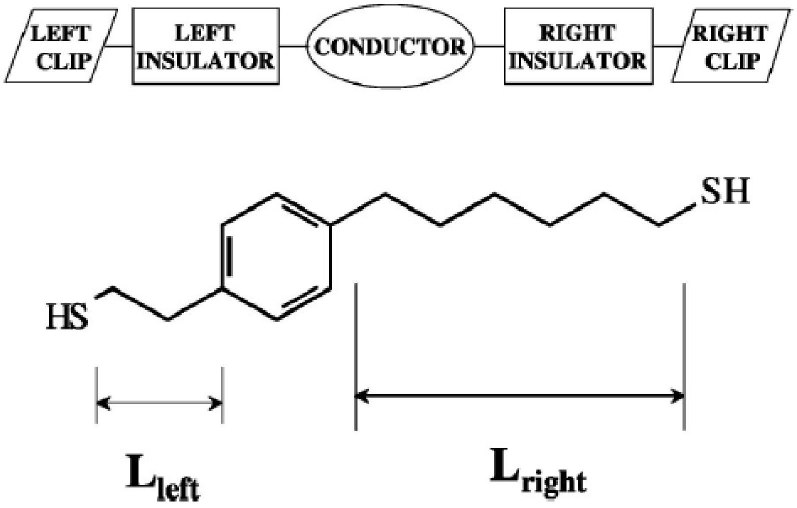

Figure 2.2: Schematic structure of asymmetric tunneling barrier expected to lead to rectification. Most of the voltage is expected to drop on the right hand side of the junction which makes bringing the right contact to resonance with the phenyl conductor easier. Thus the junction should show a higher current when the right contact is negatively biased to resonance with the LUMO level of the phenyl group or higher. Figure adapted with permission from ref[83].

The experimental realization of alkyl-metallocene rectifier was accomplished in a molecular junction with the structure Ag/alkylferrocene/Ga_2O_3-EGaIn (or template stripped Au top contact instead of eutectic gallium-indium liquid alloy)[86] with one difference. The experimentally observed rectification was temperature dependent[87] and almost completely vanished at 100 K which rules out tunneling as sole transport mechanism in alkylferrocene layers. The proposed temperature dependent mechanism for these bilayers is shown in Figure 2.3. Using other types of molecules such as quinones[88] or bipyridine[89] with available LUMO instead of HOMO, the opposite direction was observed for rectification in Ag/alkyl (quinine or bipyridine)/Ga_2O_3-EGaIn molecular junctions in which the LUMO of quinone or bipyridine falls between the Fermi levels of the contacts. The observation of opposite rectification using appropriate molecules suggested that the rectification arises mainly from the molecular layer and not the metal-oxide contact. Because the rectification depends on asymmetric voltage drop, the location of the molecule with accessible HOMO or LUMO (such as ferrocene) in the junction is also expected to be very important and experimental observation[90] confirmed that the rectifying behavior disappears when ferrocene (Fc) is located exactly in the middle of the alkyl chains which eliminates the asymmetric voltage drop. The direction of rectification was also reversed depending on whether Fc group was closer to EGaIn top contact or template stripped Ag bottom contact[90].

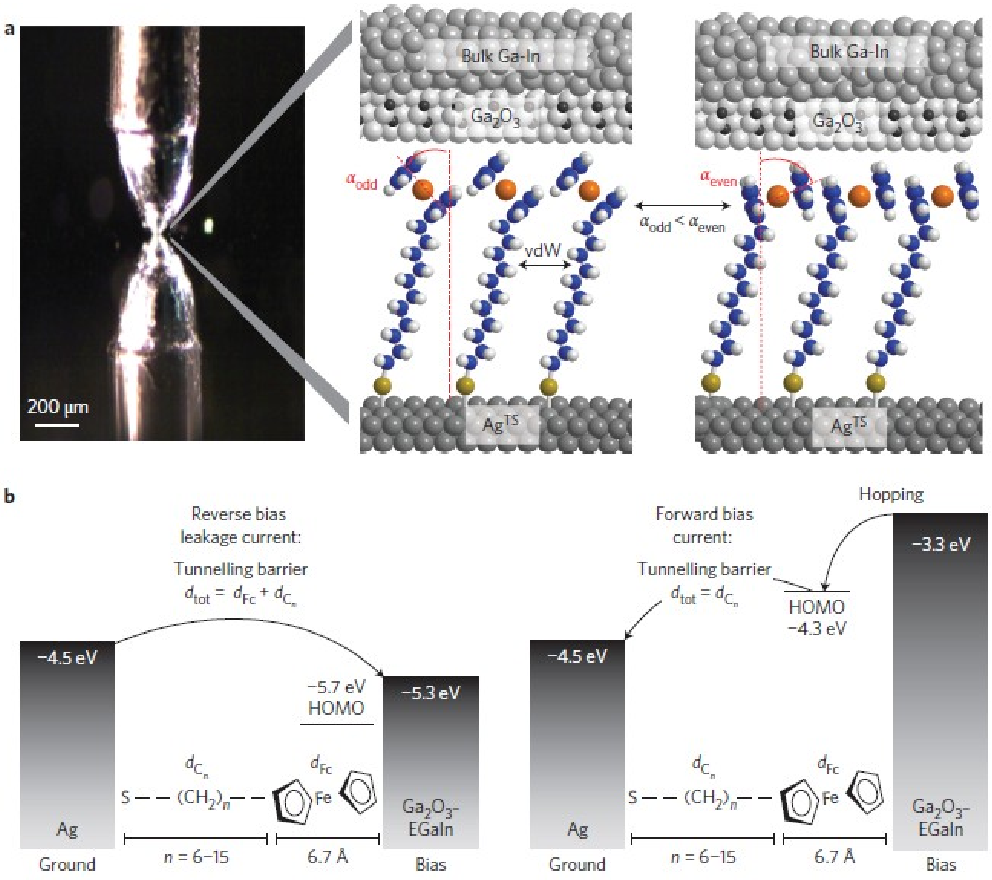

Figure 2.3: a. An image of Ag/alkylFc/Ga_2O_3/EGaIn molecular junction showing the cone shaped Ga_2O_3/EGaIn top contact suspended from a micro-needle on top of the alkylFc SAM on silver. The Ag surface is acting like a mirror. The layers with odd number of carbon atoms are more closely packed with more van der Waals interactions between the alkanes and therefore less disorder which led to more asymmetry and rectification. b. The mechanism of charge transport. In forward bias, the HOMO of Fc falls in between the Fermi levels of the contacts and charge transport happens by tunneling from the HOMO of Fc to Ag followed by temperature dependent hopping from EGaIn to HOMO of Fc. In the reverse bias, the HOMO of Fc is not accessible for charge transport and the whole width of the bilayer acts as tunneling barrier which results in small current. Figure adapted with permission from ref[91].

Although the interaction of the Fc group with top contact (the contact closer to it) might affect the rectification magnitude, the occurrence of rectification itself seems to be mainly due to asymmetric voltage drop due to small dielectric constant of the alkanes, because rectification in alkyl-Fc bilayers have been observed using various top contacts with different degrees of coupling to Fc group such as polymeric (PEDOT:PSS) top contact[92] or even STM tip with a vacuum gap as top contact[93].

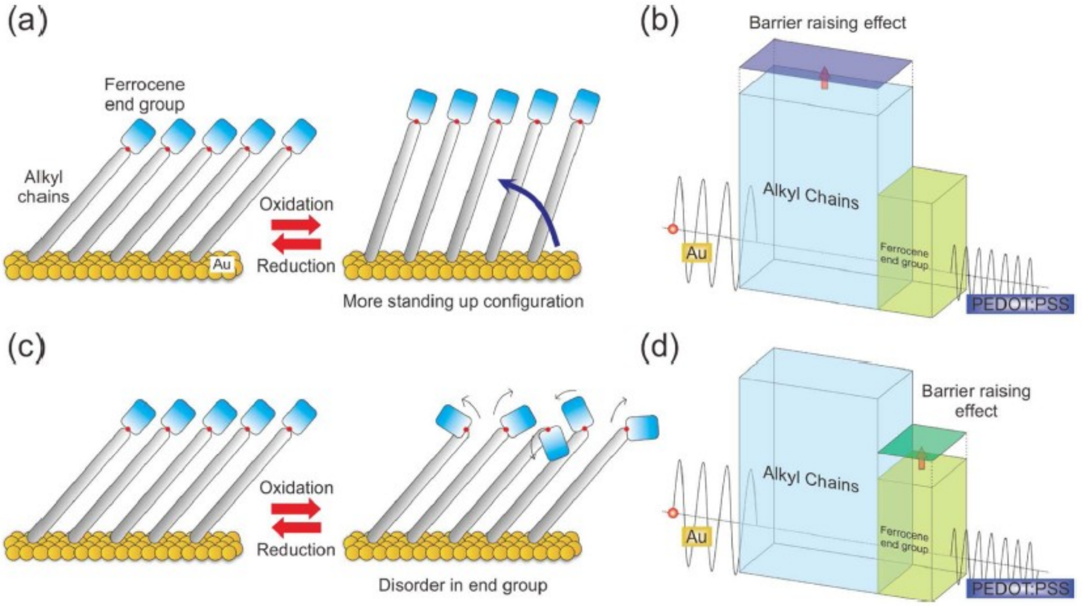

Figure 2.4: a. Schematic illustration of proposed redox induced conformational changes in alkylferrocene bilayers. a. forward bias leads to more standing up configuration and b. accompanied increase in the alkyl barrier height. c. reverse bias leads to more disordered Fc layer and d. corresponding increase in the barrier height of the Fc layer. Figure adapted with permission from ref[94].

Another suggestion for temperature dependence of rectification in alkyl-Fc devices is presented in Figure 2.4. In this mechanism at forward bias, the Au bottom contact is positively biased which repels Fc^+ and results in a more standing-up configuration for the alkyl chain which also decreases the repulsion between Fc^+ groups. This movement of the alkyl chain probably requires a movable soft top contact such as polymeric top contact or liquid top contacts. Higher temperature helps to overcome the alkyl barrier and current increases. At reverse bias the Au is negatively biased and the top contact is positive, The Fc^+ groups in this situation repel both the top contact and each other and become disordered although when using a liquid top contact, the layer can repel the top contact and create smaller surface area between Fc groups and top contact which might result in even smaller reverse currents. In this case higher temperatures just increase the disorder and decrease the reverse bias current[94].

2.1.2 Click chemistry

Click reactions are defined by Sharpless and co-workers[95] as reactions that require simple workup, mild reaction conditions (ideally insensitive to oxygen and water) and simple product purification procedure (no chromatography needed) but still can rapidly generate molecular diversity with high yield and high selectivity by using reactive modular building blocks with few or no byproducts. The Sharpless-type click reactions[96] are shown in Figure 2.5. These reactions used activated alkynes (electron deficient such as acyl-alkynes) to produce 1,2,3-triazoles (Figure 2.5a), tetrazoles (Figure 2.5b), 1,2-oxazoles (Figure 2.5c) or [4+2] cycloaddition products (Figure 2.5d).

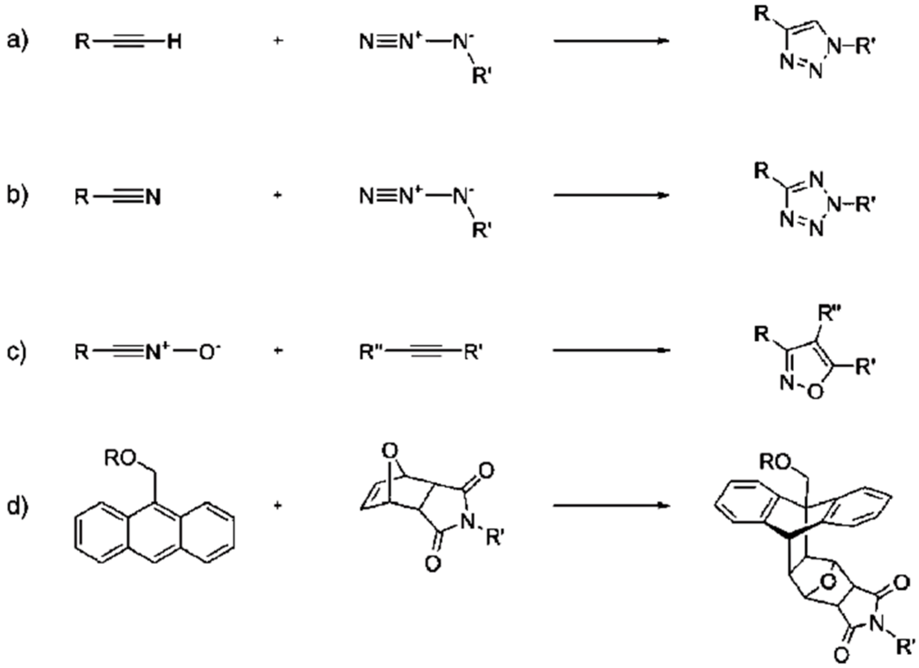

Figure 2.5: Sharpless-type click reactions. a. reaction between alkyne and azide. b. reaction between C-N triple bond with azide. c. reaction between C-NO triple bond and C-C triple bond and d. classical Diels-Alder reaction. Figure adapted with permission from ref[96].

In general, the metal-free click reactions as shown in Figure 2.6 include: strain promoted azide-alkyne [3+2] cycloaddition, thiol-alkene and thiol-alkyne radical addition reaction, oxime ligation, thiol-Michael addition reaction and Diels-Alder and retro Diels-Alder reactions[97].

The most famous click reaction is the 1,3-dipolar cycloaddition reaction between azides and terminal alkynes[98]–[101], which involves a reaction between a 1,3 dipole and dipolarophile. This reaction is known as the cream of the crop of click chemistry, also known as joint combinatorial chemistry. Both azides and alkynes are inert towards oxygen, water and most common reaction conditions in organic chemistry. Also the reaction proceeds in a wide range of solvents, pHs and temperatures and tolerates a variety of functional groups including unprotected alcohols, amines, carboxylic acids and steric factors[102], [103].

The basic 1,3-cycloaddition reaction (Figure 2.5a) between azides and alkynes to form 1,2,3-triazoles was first reported by Michael in 1893 and was studied in detail in 1960s by Rolf Huisgen[104].

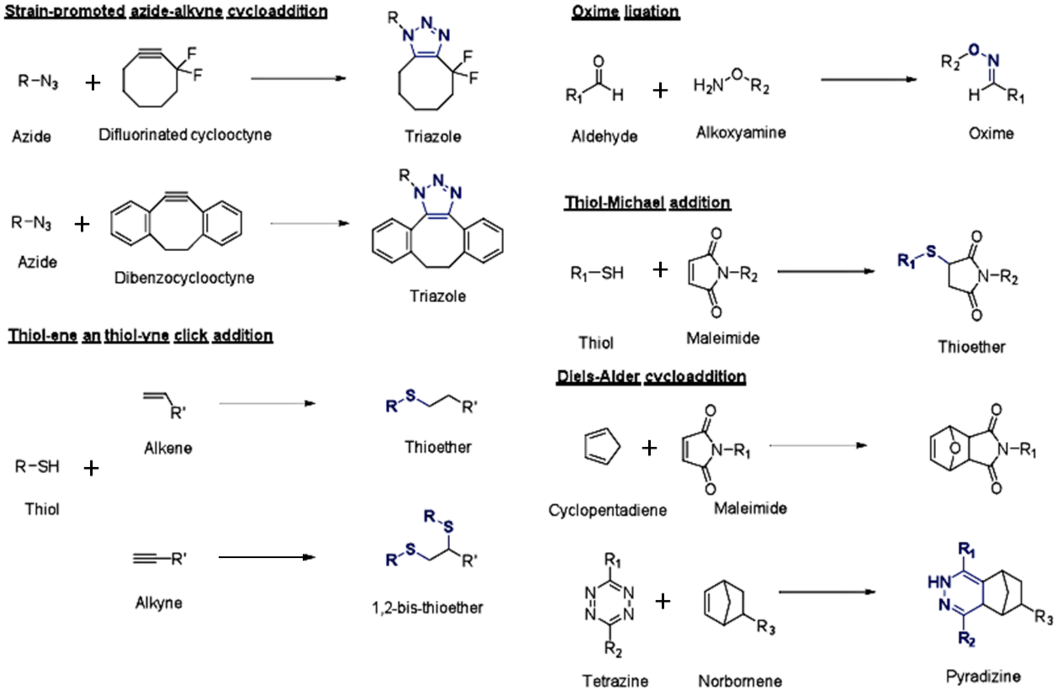

Figure 2.6: Most important metal-free click reactions resulting in functional groups in products shown in blue. Figure adapted with permission from ref[97].

The disadvantages of thermal 1,3-dipolar Huisgen cycloaddition reaction includes requiring high temperatures and long reaction times (due to stability of azides and alkynes) and complete lack of regioselectivity which leads to formation of a mixture of 1,4-disubstituted and 1,5-disubstituted regioisomers as shown in Figure 2.7.

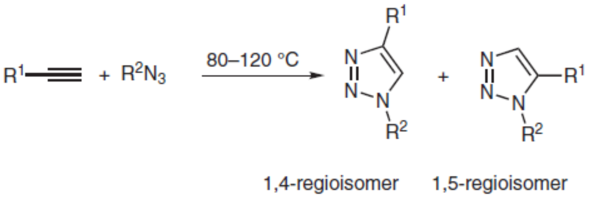

Figure 2.7: Huisgen thermal 1,3-dipolar cycloaddition reaction between azides and alkynes[105].

In 2002, Meldal and coworkers reported that 1,3-dipolar cycloaddition becomes regiospecific in the presence of Cu(I) salts as catalysts and produces only the 1,4-regioisomer at room temperature in solvents such as DMF, THF, DCM, toluene and ACN[106]. Shortly afterwards, Sharpless and coworkers independently reported the same reaction in protic polar solvents such as t-butyl alcohol, ethanol and water[95]. This Cu(I) catalyzed azide-alkyne coupling reaction is 10^7 times faster than the thermal Huisgen 1,3-dipolar cycloaddition and is an ideal click reaction as it produces 1,2,3-triazoles with minimal workup and purification[105]. The 1,4-disubstituted 1,2,3-triazole products are stable and have a strong dipole moment of ~5 D, hydrogen bond accepting capacity[107] and aromatic character which favors hole transfer over electron transfer[108]. The 1,3-dipolar cycloaddition process is mostly catalyzed by Cu(I) salts but Ru, Ni, Pd and Pt salts also have been used[96]. For instance it was reported that $Cp^*RuCl(PPh_3)_2$ catalyzed the Huisgen 1,3-dipolar cycloaddition reaction to produce 1,5-regioisomer triazoles with regioselectivity that was reverse to what is observed for Cu(I) catalyzed reactions[105].

The mechanism of Cu(I) catalyzed azide-alkyne reaction is depicted in Figure 2.8.

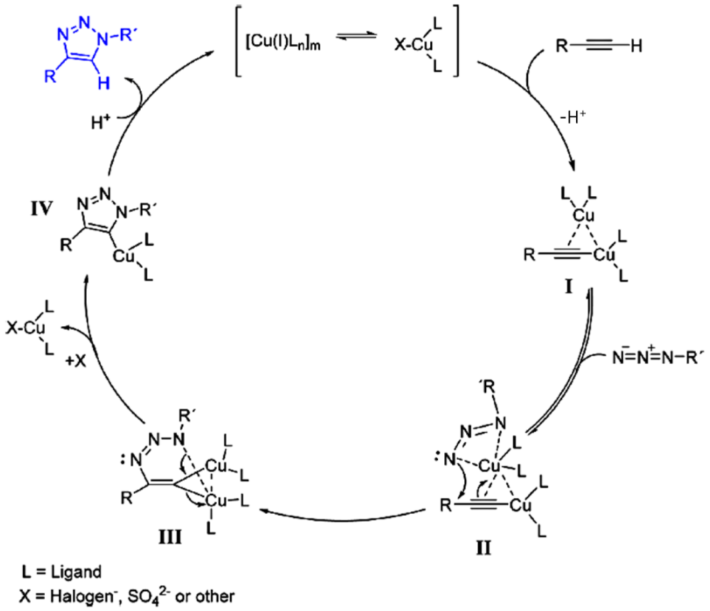

Figure 2.8: Cu(I) catalyzed azide-alkyne cycloaddition reaction mechanism. Figure adapted with permission from ref[107].

Although kinetic studies indicated that the rate of reaction was second order in copper concentration, the details of the mechanism are not yet known[102]. The reaction is done either using Cu(I) salts (such as CuBr or $[Cu(CH_3CN)_4]PF_6$) or Cu(II) salts such as $CuSO_4.5H_2O$ with the addition of a reducing agent like sodium ascorbate to reduce Cu(II) to Cu(I)[107]. The reaction is usually performed in a mixture of water and organic solvent for faster reaction time and preclusion of the need for an added base[102].

The azide-alkyne click reaction has been extensively used for modification of solid surfaces[109]–[112] and even in molecular electronics for fabrication of a compositionally symmetric molecular junction[113].

2.2 Experimental section

Acetonitrile (ACN), acetone, isopropanol (IPA), triethylamine (TEA), HBF_4 and $CuSO_4$ x $5H_2O$ were used as received from Fischer Scientific. $NaNO_2$ was bought from ACP chemicals inc. Tetrahydrofuran (THF) was acquired from Caledon. Ascorbic acid, benzene, and ammonium hydroxide were received from EMD. Anhydrous ethanol was purchased from Green Field Ethanol Inc. All other chemicals were purchased from Sigma-Aldrich and used without further purification.

2.2.1 Material synthesis

Azidomethylferrocene (MeFc)[114], azidohexylferrocene (HxFc)[115], 1-azidooctane (C_8 azide)[116], 1- azidododecane (C_{12} azide)[116], 1-azidohexadecane (C_{16} azide)[116], 4-Ethynylbenzene (EB) diazonium salt[117], and 4-((trimethylsilyl)ethynyl)benznene (TMS) diazonium salt[118] were prepared and purified according to published procedures, and 4-((triisopropylsilyl)ethynyl)aniline (TIPS) was received from our collaborators Dr. Yann R. Leroux and Dr. Philippe Hapiot.

The general procedure for synthesis of diazonium salts: 0.01 mole of the aromatic amine starting material was dissolved in ~20 mL of 48% HBF_4. The mixture was cooled to 0^oC. Then a solution of 2.07 g $NaNO_2$ in 12 mL cold water was slowly added to the reaction mixture such that the temperature never exceeded 4^oC. The reaction mixture was stirred for 30 min at 0^oC. The precipitate was vacuum filtered and dissolved in minimum amount of cold ACN. The impurities were separated out by gravity filtration and the pure diazonium salt was recovered by slowly adding cold anhydrous ether to the ACN solution to crystallize the diazonium salt. Finally the diazonium salt crystals were vacuum filtered.

The general procedure for synthesis of azides[116]***:*** The mixture of the corresponding bromine terminated precursor and sodium azide in dimethylformamide (DMF) was stirred at room temperature for 12 h. After all starting material was converted in to azide (confirmed by GC-MS) the reaction mixture was extracted with dichloromethane (DCM), washed with water and dried over $MgSO_4$. Purification was done by silica gel column chromatography with DCM. The desired products were obtained in almost quantitative yields.

Azidomethylferrocene[114]***:*** 0.6 g of (hydroxymethyl)ferrocene was reacted with 0.4 g of sodium azide in 10 mL glacial acetic acid under argon atmosphere at 50 ^{o}C for 3 hours. The crude reaction mixture was diluted with 50 mL of DCM and the organic phase was washed with saturated $NaHCO_3$ and water. The organic phase was then dried over $MgSO_4$, filtered and dried in vacuo to give the crude azide as an orange oil. The final product was separated as yellow/orange solid in 80% yield by silica gel column chromatography using ethylacetate/hexane (1:2) as solvent, ^{1}H NMR (600 MHz, $CDCl_3$) δ 4.24 (t, 2H, J=1.8 Hz), 4.20 (t, 2H, J=1.8 Hz), 4.17 (s, 5H), 4.12 (s, 2H).

1-Azidohexylferrocene[115]***:*** 1.25 g of 6-bromohexylferrocene was dissolved in 30 mL dry DMF. 0.26 g of sodium azide was added to the solution and reaction mixture was stirred at room temperature for 12 h. Reaction was quenched with 100 mL of H_2O and the product was extracted with ethyl acetate. The ethyl acetate layer was washed with brine and dried over anhydrous $MgSO_4$. The resulting solution was filtered and concentrated with rotary evaporator. Finally the product was obtained as reddish brown liquid in 98% yield. ^{1}H NMR (600 MHz, $CDCl_3$) δ 4.09 (s, 5H), 4.04 (m, 4H), 3.26 (t, 2H, J=6 Hz), 2.33 (t, 2H, J=6 Hz), 1.60 (t, 2H, J=6 Hz), 1.51 (t, 2H, J=6Hz), 1.32-1.42 (m, 4H).

1-Azidooctane: Prepared according literature procedure[116] from 1-bromooctane in quantitative yield, ^{1}H NMR (300 MHz, $CDCl_3$) δ 3.25 (t, 2H, J=6.9 Hz), 1.56-1.62 (m, 2H), 1.20-1.50 (m, 10H), 0.89 (t, 3H, J=6.9 Hz).

1-Azidododecane: Prepared according to literature procedure[116] from 1-bromododecane in quantitative yield. ^{1}H NMR (600 MHz, $CDCl_3$) δ 3.25 (t, 2H, J=7.2 Hz), 1.55-1.68 (m, 2H), 1.20- 1.42 (m, 20H), 0.88 (t, 3H, J=7.2 Hz).

1-Azidohexadecane: Prepared according to literature procedure[116] from 1-bromohexadecane in quantitative yield. ^{1}H NMR (600 MHz, $CDCl_3$) δ 3.25 (t, 2H, J=7.2 Hz), 1.55-1.68 (m, 2H), 1.20-1.42 (m, 26H), 0.88 (t, 3H, J=7.2 Hz).

The structures of all azides used in this Chapter are shown in Figure 2.9.

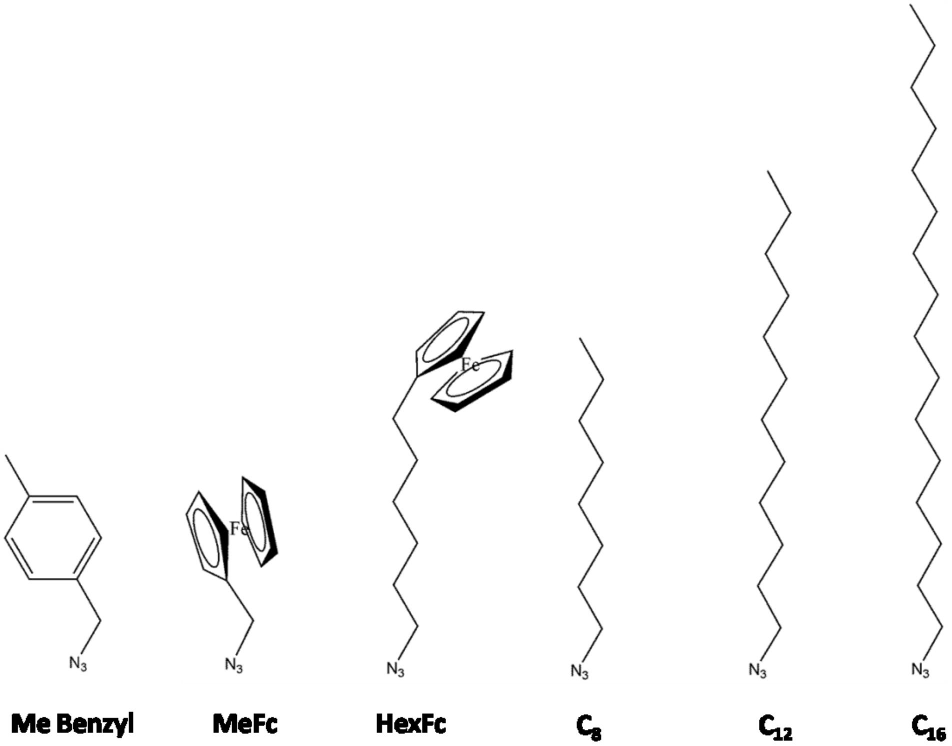

Figure 2.9: Structure of all azides used in this work.

2.2.2 Fabrication of crossbar junctions.

The general procedure for fabrication of PPF/Molecules/eC/Au crossbar junctions is schematically illustrated in Figure 2.10.

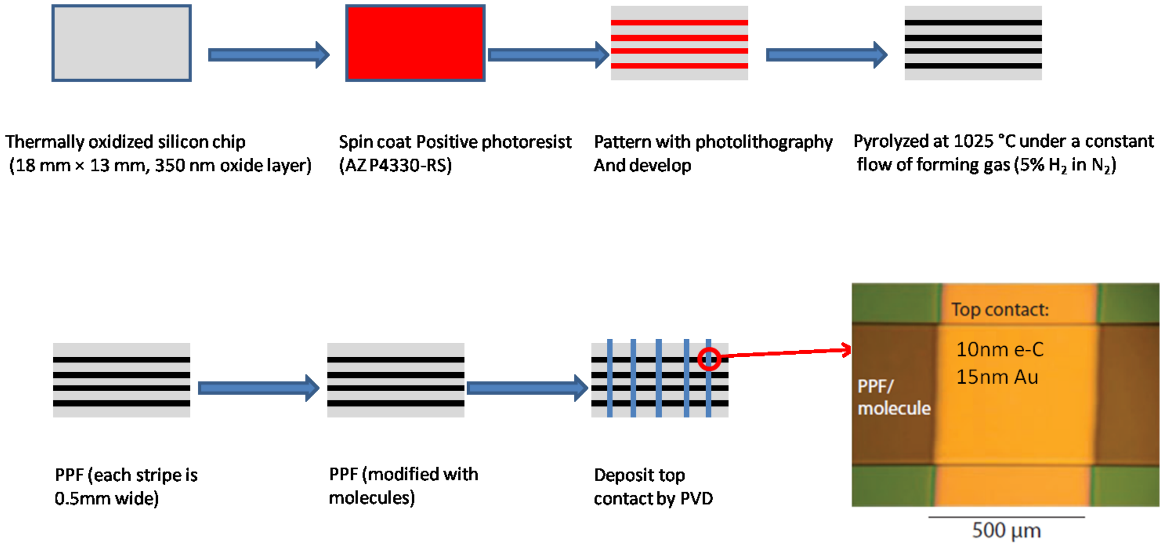

Figure 2.10: Fabrication procedure for PPF/Molecules/eC/Au junctions.

Each step in Figure 2.10 is explained in the following sections.

2.2.2.1 Fabrication of PPF bottom contact

Pyrolyzed photoresist films (PPF) were made on thermally oxidized silicon chips (18 mm length × 13 mm width× 1 mm thickness, with 350 nm surface oxide layer). The silicon/SiO_x chips were first cleaned with sequential immersion and sonication in acetone, IPA, and deionized Milli-Q water (TOC < 5 ppb) for 20 minutes each. The substrates were then dried in a nitrogen stream. Positive photoresist (AZ P4330-RS, AZ Electronic Materials) was spin-coated onto clean substrates at 500 rpm for 10 s followed by 6000 rpm for 50 s and soft baked at 95 °C for 10 min in air. For junction fabrication, photoresist was patterned photolithographically (using 500 W Hg arc lamp for 120 s) and developed in a (1:2 v/v) mixture of AZ400K developer and Milli-Q water to form four parallel 0.5 mm wide stripes. For XPS and UPS analyses, blanket sheets of PPF were used. The photoresist was finally pyrolyzed by heating the samples in a tube furnace to 1025 °C under a constant flow of forming gas (5% H_2 in N_2) to form PPF[119].

2.2.2.2 Modification of PPF by electro-reduction of diazonium salts

PPF films were modified by electrochemical reduction of diazonium ions[28] to form the desired molecular layers as primer layers for the second modification step via click chemistry as shown schematically in Figure 2.11.

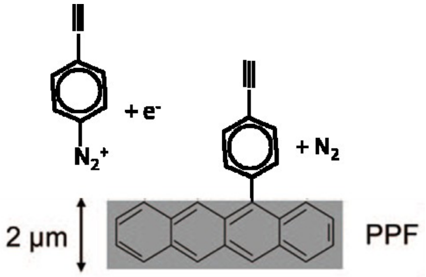

Figure 2.11: Deposition of the first molecular layer on PPF surface by reduction of diazonium ions.

The PPF was the working electrode in a conventional three electrode setup with a platinum wire as auxiliary electrode and Ag/Ag^+ (0.01M $AgNO_3$ in ACN) reference electrode. The Ag/Ag^+ reference electrode was calibrated against the redox potential of ferrocene. The redox potential of ferrocene is centered at ~87mV versus the Ag/Ag^+ reference electrode. The electroreduction step was performed in a 1 mM solution of the diazonium salt with 0.1 M tetrabutylammonium hexafluorophosphate as supporting electrolyte in ACN. Electroreduction was performed using a CHI-420A potentiostat (CH

Instrument Inc., USA) by sweeping the electrode potential in an argon-degassed solution from +0.3 V to -0.65 V versus Ag/Ag$^+$ for one cycle at a scan rate of 0.1 Vs^{-1} for EB diazonium ion and from +0.4 V to -1 V versus Ag/Ag$^+$ for 5 cycles at a sweep rate of 0.05 Vs^{-1} for TMS diazonium ion.

TIPS diazonium ions were generated in-situ according to previously reported procedure[120]: 30mg of sodium nitrite in 1mL water was added to a 1 mM solution of TIPS amine in 0.1 M tetrabutylammonium hexafluorophosphate in ACN and stirred for 20 min. The solution was cooled to 0 °C in an ice bath and degassed with argon for 20 min. Then 0.1 mL of concentrated H_2SO_4 was added and the mixture was stirred for another 5 min before scanning the potential from +0.4 V to -1 V versus Ag/Ag$^+$ for five cycles at a sweep rate of 0.05 Vs^{-1}. After surface modification, samples were rinsed thoroughly with benzene, THF and ACN and dried with nitrogen.

The same procedures were also conducted on glassy carbon (GC) electrodes for comparison. GC electrodes were polished[121] successively with 1.0, 0.3, and 0.05 µm alumina/MilliQ water slurries on microcloth pad. The GC electrodes were next rinsed with Milli-Q water and sonicated in activated carbon/ACN solution. Finally the GC electrodes were rinsed with IPA and ACN and dried with a nitrogen stream before modification.

The structures of all three diazonium ions used in this Chapter are shown in Figure 2.12.

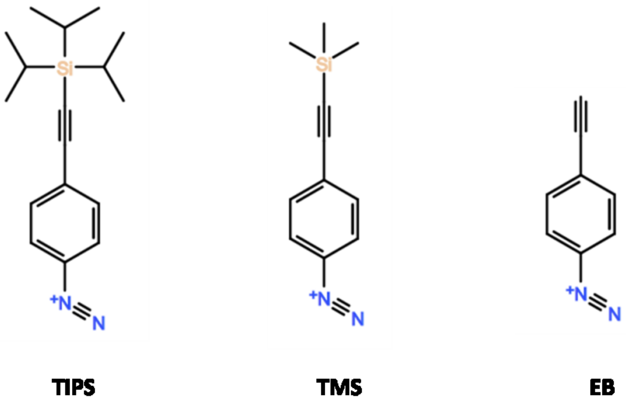

Figure 2.12: Structure of the diazonium ions used in this Chapter.

2.2.2.3 Post modification via click chemistry

To expose the terminal alkynes needed for the click reaction (Cu(I)-catalyzed Huisgen 1,3-dipolar cycloaddition) on TMS and TIPS modified surfaces, the silyl groups should be cleaved off to deprotect the terminal triple bonds. This deprotection step was done by immersing the TIPS or TMS modified chips in a 0.05 M solution of tetrabutylammonium fluoride (TBAF)[120] in THF at room temperature for about 1 hour. The resultant clickable surfaces were then thoroughly rinsed with THF, benzene and ACN and dried with nitrogen gas.

A teflon sample holder was used to hold the chips during the "click" reaction. The click reaction between deprotected acetylene moieties on the surfaces of EB, deprotected TMS or deprotected TIPS and various azides in solution was used for further modification as schematically shown in Figure 2.13.

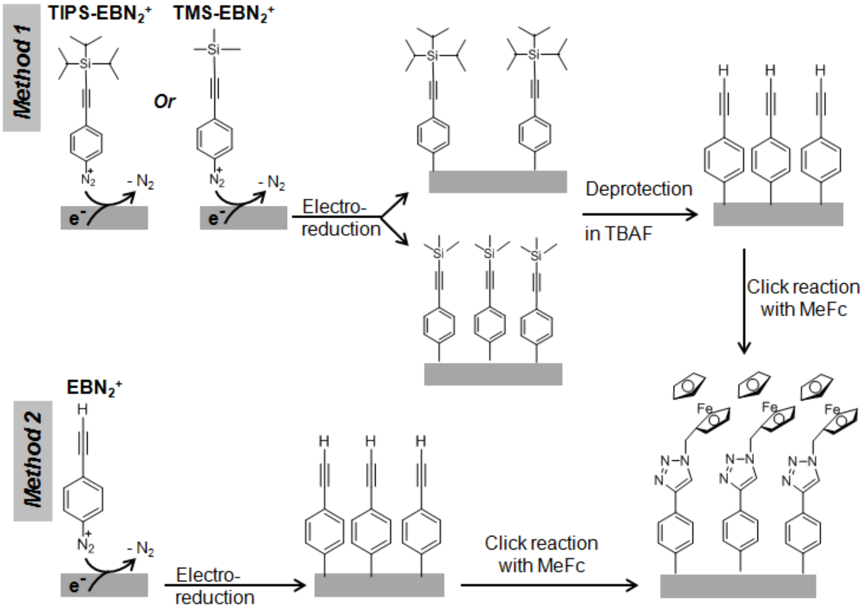

Figure 2.13: Click reaction between the azides in solution and alkyne modified surfaces (multilayers depicted as monolayers, except for TIPS) obtained by: method 1- deprotection of silyl groups of TMS and TIPS modified surfaces and method 2- EB modified surface.

Click reaction for MeFc azide, 1-(azidomethyl)-4-methylbenzene (Me benzyl), and HxFc azide*[120]*: 1:1 (v/v) water:ethanol solutions of $CuSO_4$ (0.5 mM) and dropwise added L(+)-ascorbic acid (2 mM) were stirred and bubbled with argon for 16 hours in the presence of 0.01 mM of the corresponding azide and EB (or deprotected TIPS or TMS) modified PPF substrates. Due to disproportionation reaction of Cu(I) ions, there were some copper particles on the chip surface after the reaction. The click modified samples were rinsed with THF and water and immersed in 10 mM EDTA for 1 min and 1 M ammonium hydroxide solution for 30 s to remove copper residues. Finally the modified chips were rinsed with water, acetone and ACN and dried with nitrogen gas.

Click reaction for or C_8 azide, C_{12} azide, and C_{16} azide[122]***:*** 4:1 (v/v) DCM:ACN solutions of tetrakis(acetonitrile)copper(I) tetrafluoroborate (0.2 mM) and TEA (2.5 mM) were stirred and bubbled with argon gas for 18 hours in the presence of 2.5 mM of the corresponding azide and EB modified PPF substrates. The samples were then rinsed with THF, acetone and ACN and dried with nitrogen gas.

The resulting click bilayers from above procedures are named as X-Y, in which X stands for the first layer and Y for the second layer. For example EB-C_{16} refers to a bilayer with EB as the first layer and C_{16} as second layer.

2.2.2.4 Deposition of top contact

Large area cross-bar junctions (area~0.0013 cm^2, see Figure 2.14) were fabricated by electron-beam deposition of carbon (10 nm) and gold (15 nm) successively[28] as top contacts through the openings in a shadow mask oriented perpendicular to the click modified PPF stripes in an electron-beam evaporator (Kurt J. Lesker PVD75) at a typical chamber pressure of <5×10^{-6} Torr. The deposition rates for the top contacts were 0.01 nm/s for evaporated-carbon (eC) and 0.05 nm/s for gold. E-beam deposited carbon has been described previously for electrochemistry[123] and molecular junctions[28], and exhibits metallic behavior and a resistivity of about 0.015 Ω.cm[28].

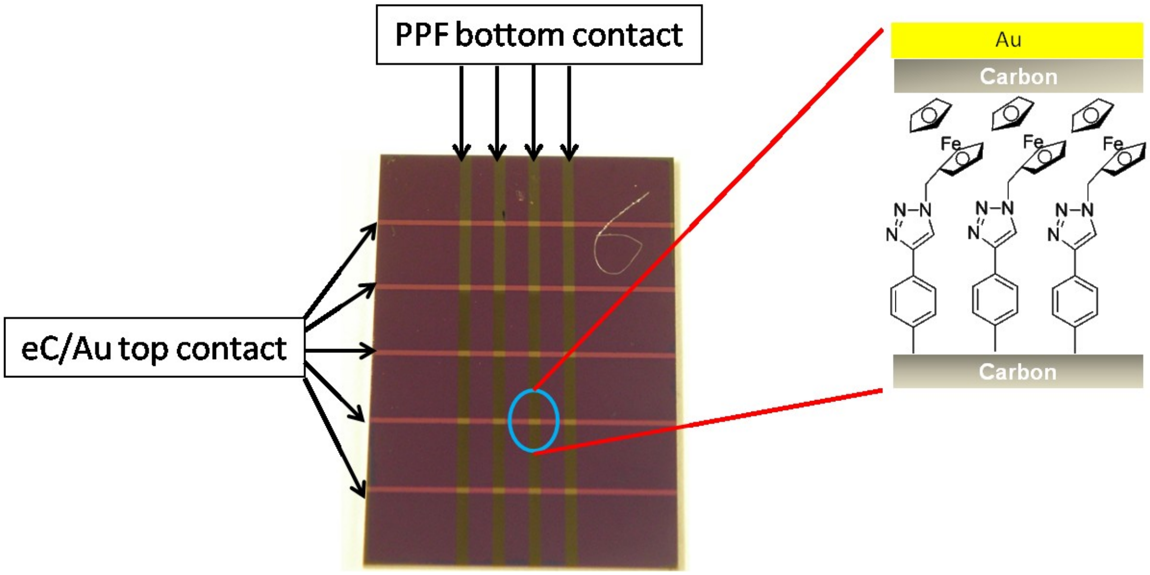

Figure 2.14: The complete large area molecular junction after top contact deposition.

2.2.3 Measurements

Molecular layer thicknesses were determined with AFM (Digital Instruments 3100 atomic force microscope) "scratching" as described previously[124]. In contact mode, an area of 1μm x 1μm was scanned under a set point of (0.25-0.8 V) using a silicon AFM probe (with Al backside) with a tip radius of 8nm purchased from MikroMasch. As a result of this scratching process, the molecular film was removed without scratching the PPF underneath, leaving a 1μm x 1μm trench in the molecular layer, which is used to determine the height of the molecular layer after scanning a larger area (5μm x 5μm) of the same spot in tapping mode (refer to Figure 2.15).

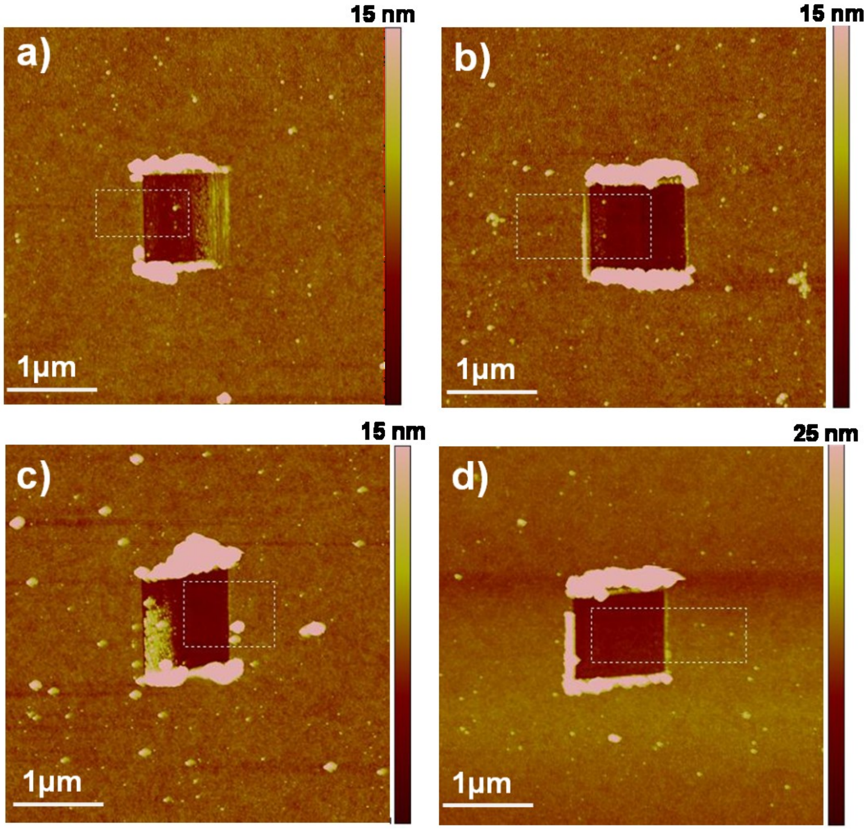

Figure 2.15: AFM image in tapping mode of the trench created in contact mode for a. EB layer, b. EB-MeFc layer, c. EB-Me benzyl and d. EB-HxFc. The high regions around the trenches are debris from the "scratching" action.

The molecular layer thickness was then determined as the difference in heights between the bottom of the trench and the top of the surrounding molecular layer. Two histograms, for the depth of the trench and the surrounding area were fit by two different Gaussian functions[31] (refer to Figure 2.16). The thickness of the molecular layer is the difference between the centers of the Gaussian distributions, with the uncertainty in thickness stated as the quadrature addition of the two best-fit σ values[31].

X-ray photoelectron spectroscopy (XPS) analyses were acquired with the AXIS 165 spectrometer equipped with a monochromatic Al K_α source (1486.6 eV). Ultraviolet photoelectron spectra (UPS) were acquired with a Kratos Ultra spectrometer with a He I source (21.21 eV).

Electrical characterization of molecular junctions was carried out using a Keithley 2602A or a LabVIEW-based voltage scanning unit in four-wire configuration. The four wire configuration was used to correct for ohmic losses in contacts and leads. All the voltages reported in this work are PPF relative to the Au top contact.

For temperature variation, a Janis ST-500-1 cryogenic probe station cooled with liquid nitrogen was utilized. The chamber was pumped to $< 10^{-4}$ torr before lowering the temperature and acquisition of J-V data. The temperature was varied between 100-400 K and J-V curves were collected every 10 K.

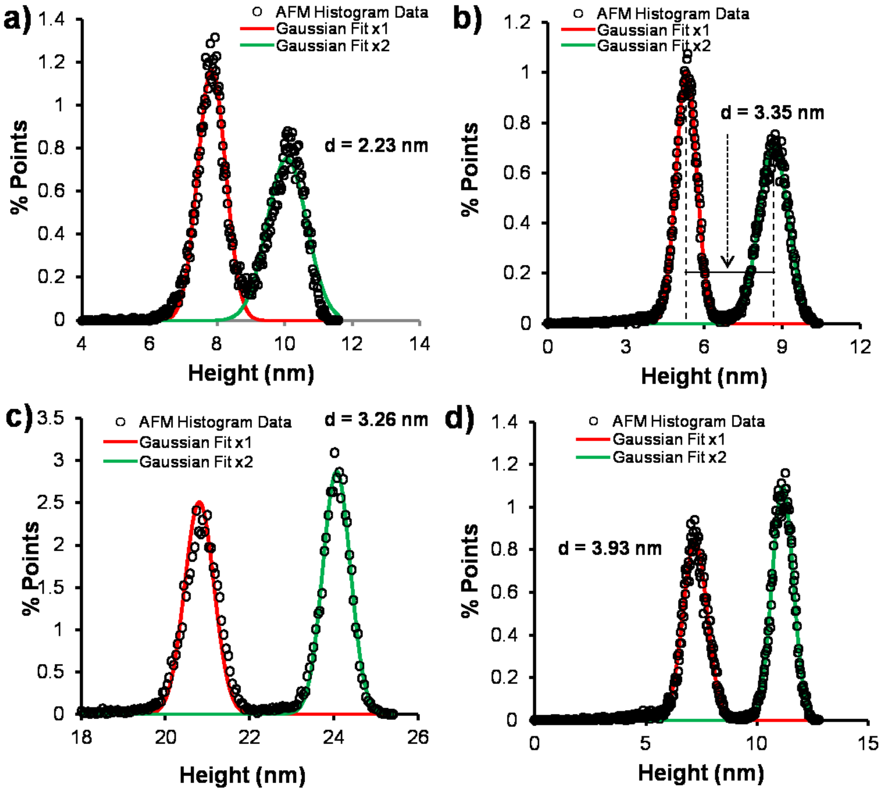

Figure 2.16: Fitting of the AFM depth data generated as a histograms[31] from images shown in Figure 2.15 for a. EB layer, b. EB-MeFc layer, c. EB-Me benzyl and d. EB-HxFc.

2.3 Results and discussion

The results for EB bilayers without the need for deprotection step are presented first, followed by results for TIPS and TMS based bilayers.

2.3.1 Click bilayer molecular junctions based on EB primer

The thickness of EB layer as measured by AFM was 2.2±0.5 nm (implying that it is a multilayer) which increased after click chemistry with Me-benzyl azide to 3.3±0.4 nm which is reasonable considering the added thickness of the triazole ring (~0.4 nm) and benzene ring (~0.5 nm). The thickness and roughness of all EB bilayers are listed in table 2.1. The thickness of the EB primer layer for alkane bilayer series was 2.6±0.5 nm and the increase in thickness with the addition of alkyl azides was less than what is expected for alkyl chains in upright configuration. The standing up configuration for alkanes is usually observed in SAMs with the ability of molecules to move around and form close packed alkane layers. In these covalently bonded layers, the alkanes once attached, cannot move on the surface and therefore they are not expected to be as orderly as SAMs.

Table 2.1: AFM thickness and roughness of EB bilayers.

Samples	Thickness, nm	Rms roughness, nm
EB	2.2±0.5	0.426
EB-Mebenzyl	3.3±0.4	0.513
EB-MeFc	3.4±0.6	0.437
EB-HxFc	3.9±0.7	0.508
Alkane Series		
EB	2.6±0.5	0.68
EB-C_8	3.0±0.6	0.49
EB-C_{12}	3.3±0.6	0.44
EB-C_{16}	3.8±0.5	0.46

The roughness of the PPF surface itself was less than 0.4 nm. The surfaces of the bilayers were all smooth with roughness less than 0.7 nm in all cases.

The redox activity of ferrocene as second layer on EB was studied in 0.1 M $LiClO_4$ solution in ethanol on both PPF and GC surfaces as shown in Figure 2.17. The hexyl ferrocene bilayers are more easily oxidized than methyl ferrocenes. This might be due to higher flexibility of hexylferrocene which may allow it to bend closer to the surface in solution[125] or due to less ordered Hex-Fc layer in which Fc groups don't experience the potential of other Fc groups as much as Me-Fc layers[126]. The higher background resistance in PPF CV voltammograms is due mainly to uncompensated resistance inside the thin PPF layer (~1μm thick) and the molecular layer before reaching the exposed area to the solution.

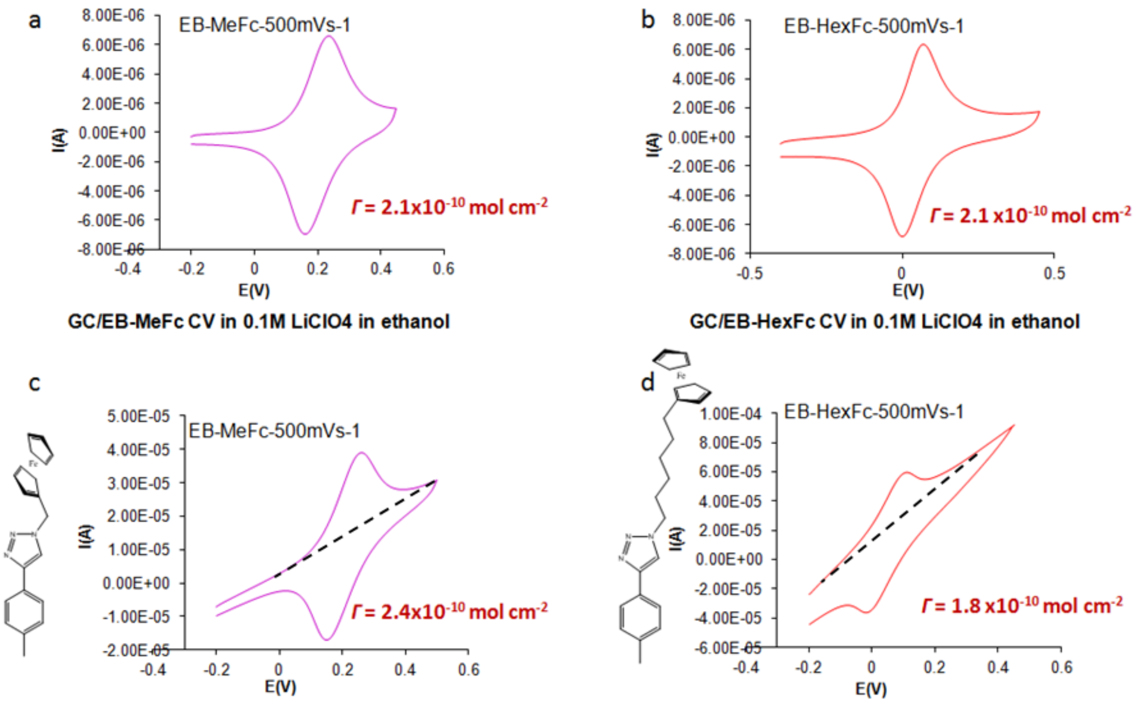

GC/EB-MeFc CV in 0.1M LiClO4 in ethanol **GC/EB-HexFc CV in 0.1M LiClO4 in ethanol**

PPF/EB-MeFc CV in 0.1M LiClO4 in ethanol **PPF/EB-HexFc CV in 0.1M LiClO4 in ethanol**

Figure 2.17: Cyclic voltammetry at 0.5 V/s of a,b. GC and c,d. PPF modified surfaces with a,c. EB-MeFc and b,d. EB-HexFc in ethanolic solution of 0.1 M $LiClO_4$ as supporting electrolyte. The coverage was determined from the area of the voltammogram above the dashed lines shown.

The surface coverage values were calculated using:

$$\Gamma = \frac{C}{F \times A} \tag{2.1}$$

In which C is charge from the area under current versus time. F is faraday constant and A is the area of the modified electrode. The ideal maximum coverage based on a cubic arrangement in 2D with Fc radius of 3.32 angstroms is 7.4×10^{-10} mole/cm^2. The high coverage of ~2×10^{-10} mole/cm^2 shows the near quantitative yield of alkyne-azide click chemistry in these covalently bonded layers.

The presence of iron in ferrocene was also observed in XPS spectra of EB-MeFc and EB-HexFc layers as shown in Figure 2.18. The Fe_{2p} peaks at 707 eV and 721 eV are representative of Fe^{2+} in ferrocene[125].

The current versus voltage curves of PPF/EB/aromatics/eC/Au molecular junction series are shown in Figure 2.19. The current was measured in 4-wire mode in ambient atmosphere. Each curve is the average curve of four junctions on a chip with standard deviations shown as error bars. The current-voltage behavior in the absence of any molecule on the surface of PPF is linear and very conducting, however with molecules on the surface, the J-V behavior becomes nonlinear.

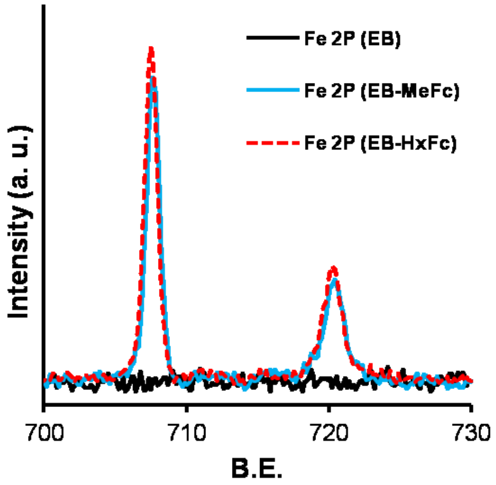

Figure 2.18: The Fe_{2p} region in XPS spectra of EB, EB-MeFc and EB-HexFc.

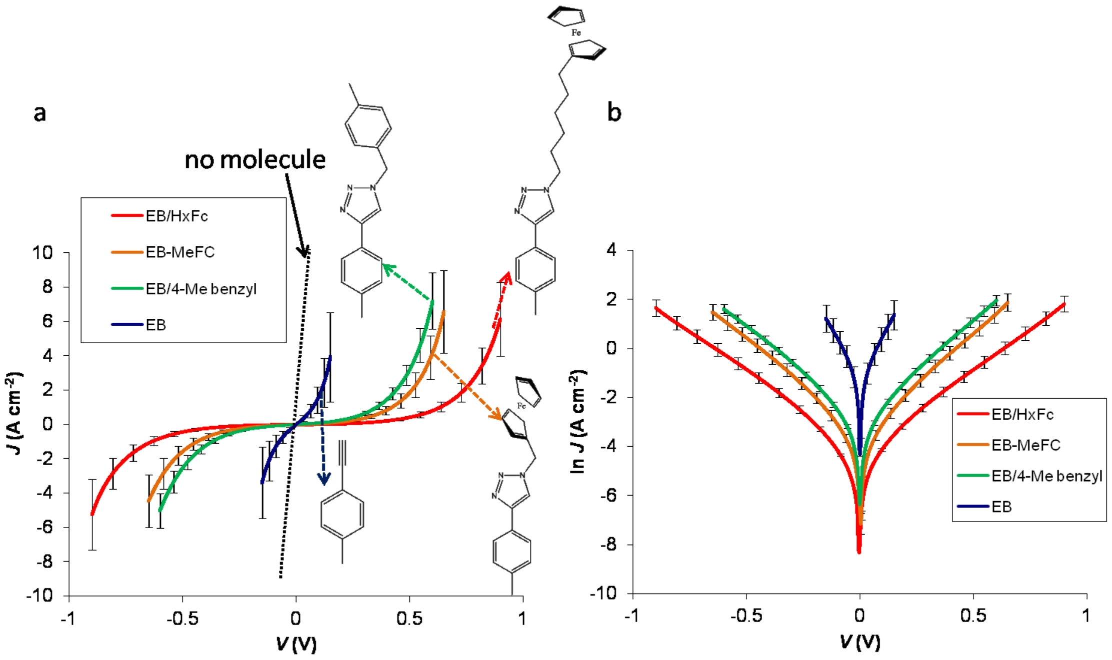

Figure 2.19: a.J-V and b. lnJ-V curves for EB, EB-Mebenzyl, EB-MeFc and EB-HxFc.

J-V curves for EB-alkane series are shown in Figure 2.20. Each curve in 2.20 is the average of 4 curves with standard deviations shown in error bars. The thickness and the yield of working junctions along with the standard deviation of J at 0.1 V for all EB based bilayers are listed in table 2.2. From table 2.2 and Figures 2.19 and 2.20, it is observed that the conductivity of the bilayers depend on their thicknesses. With increasing the thickness of the bilayers they become less conducting.

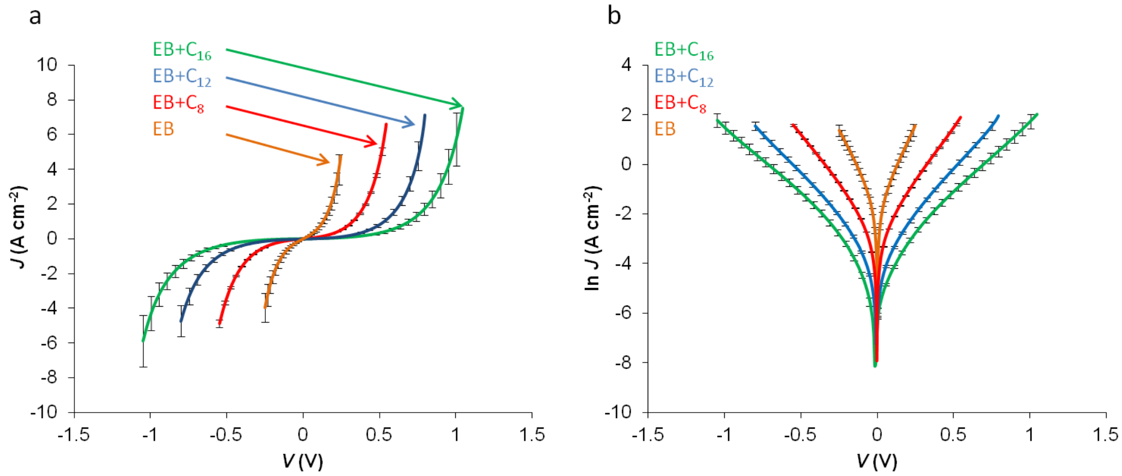

Figure 2.20: a.J-V and b. lnJ-V curves for EB, EB-C_8, EB-C_{12} and EB-C_{16}.

Table 2.2: Thickness, Yield and RSD of current at 0.1 V for all EB based bilayers.

Samples	Number of Junctions	d(nm)	Yield	$RSD_{0.1\ V}$
EB	16	2.2	14/16	25.8 %
EB-Mebenzyl	16	3.3	14/16	10.2%
EB-MeFc	16	3.4	16/16	21.3 %
EB-HxFc	16	3.9	15/16	6.70 %
Alkane series				
EB	8	2.6	8/8	13.6 %
EB-C_8	8	3.0	8/8	1.18 %
EB-C_{12}	8	3.3	8/8	4.80 %
EB-C_{16}	8	3.8	8/8	6.40%

The reproducibility of the J-V curves is shown in the overlay for 15 junctions of EB-HxFc on two chips in Figure 2.21. This good reproducibility argues against the random penetration of the evaporated top contact into the layer. The partial penetration of the top contact in the layer will likely result in smaller effective thickness and variations from one junction to another. The linear decrease of lnJ with thickness (shown in Figure 2.22) is additional evidence against penetration of top contact. The partial penetration of top contact leads to a smaller effective thickness than the measured thickness and smaller surface area for the thinnest part of the layer. Penetration of top contact into thicker layers results in the same thickness as the thinner layers but with smaller surface area, however lnJ versus surface area is not linear for any transport mechanism and the observed linearity of lnJ versus measured thickness, confirms that the top contact penetration is either absent or happens to the same degree in all bilayers.

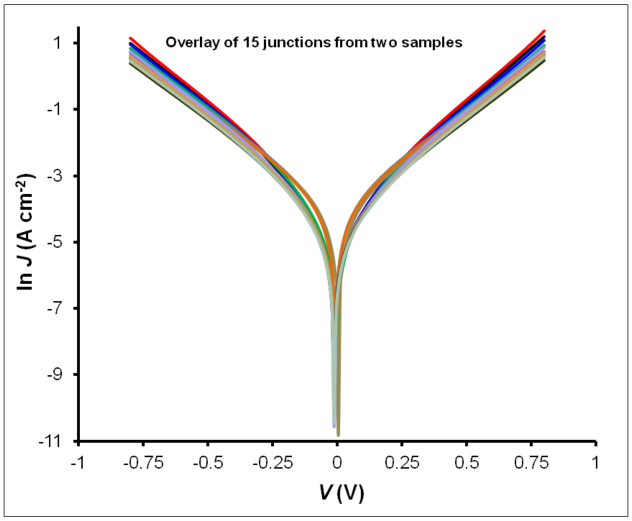

Figure 2.21: Overlay of lnJ vs. V curves for 15 EB-HexFc junctions on two chips.

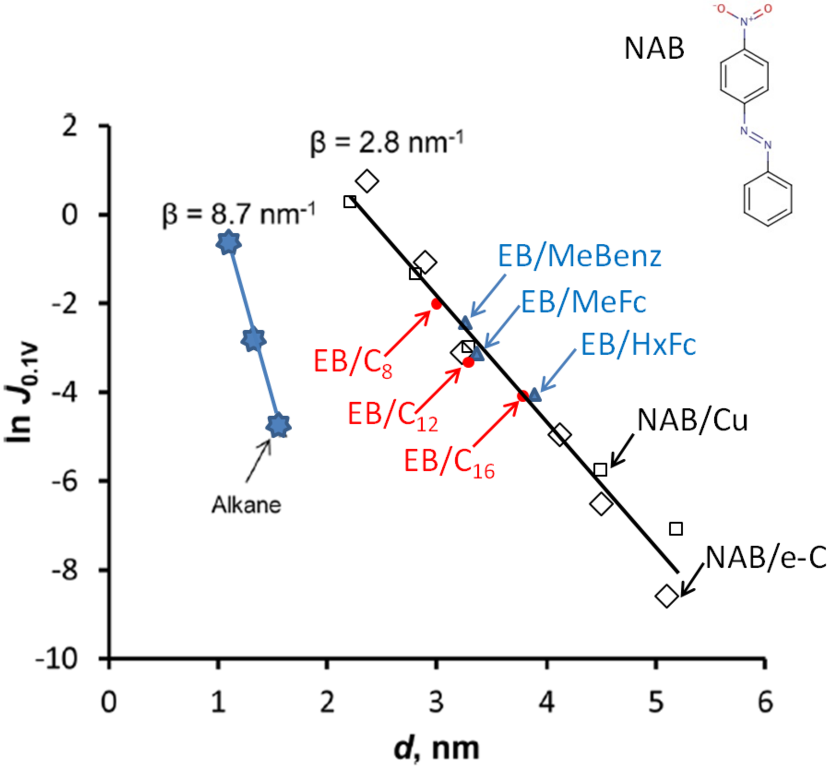

Figure 2.22: β plot of all EB based bilayers at 0.1 V compared with alkanes and NAB with eC[28] and Cu[28], [39] top contacts. The structure of NAB is shown at top right.

The plot of lnJ versus thickness, known as β plot or tunneling attenuation plot, is predicted to be linear for tunneling charge transport in accordance with the simple form of Simmons tunneling model:

$$J = Ae^{-\beta d} \tag{2.2}$$

In this Equation J is the current density and d is molecular layer thickness. β, the tunneling attenuation constant, is the slope of lnJ versus thickness and is given by:

$$\beta = B(m\varphi)^{\frac{1}{2}} \tag{2.3}$$

In which m is the effective mass of the carrier and φ is the barrier height. A and B are constants.

The β plot of Figure 2.22 for all EB based bilayers shows that the current depends only on the thickness of the bilayer and is insensitive to the structure of the second layer. EB-C_{16} and EB-HexFc have very close thicknesses and currents despite the difference in the structure of the clicked layer. This insensitivity of current to the structure of the end group has been also observed by others[31], [32], [127]. One reason in the EB bilayers may be that the small thickness of the second layer compared to the majority aromatic structure of EB, decreases the effect of the second layer on the overall barrier height. This majority aromatic structure of the bilayer is also probably the reason for symmetric J-V curves of Figures 2.19 and 2.20 instead of the rectifying alkyl-Fc layers reported in the literature. The aromatic EB layer does not drop the voltage as much as alkanes and is not expected to result in an asymmetric voltage drop and rectification, as proposed by Nijhuis, et. al[91]. The proximity of the second layer of the bilayer to the contact also increases its interaction with the contact and modifies its energy levels[31]. The overall effect is that the behavior of EB bilayers is no different than nitroazobenzene (NAB) layers[28] with copper or eC top contact as shown in Figure 2.22. It was reported that EB layers show the same conductivity and β value of ~3 nm^{-1} as NAB and a range of other aromatic molecules in PPF/molecule/Cu junctions[31]. The indifference of the β value to the structure of the aromatic layer was attributed to partial charge transfer between the molecular layer and the contacts. This partial charge transfer results in strong coupling between the contacts and the molecular layer and Fermi level pinning at ~1.2 eV above the HOMO level of the molecular layer. The Fermi level pinning then leads to a fixed value of ~1.2 eV as hole tunneling barrier in aromatic layers[31]. The same HOMO level of ~1.2 eV was found in EB bilayers using UPS spectroscopy as shown in Figure 2.23, with little effect of the structure of the second layer. This HOMO level belongs to the aromatic part of the bilayers and the overlay of β plots of bilayer/eC and NAB/Cu in Figure 2.22 suggests that the same strong coupling effect is in work in thin bilayers as it was in NAB layers.

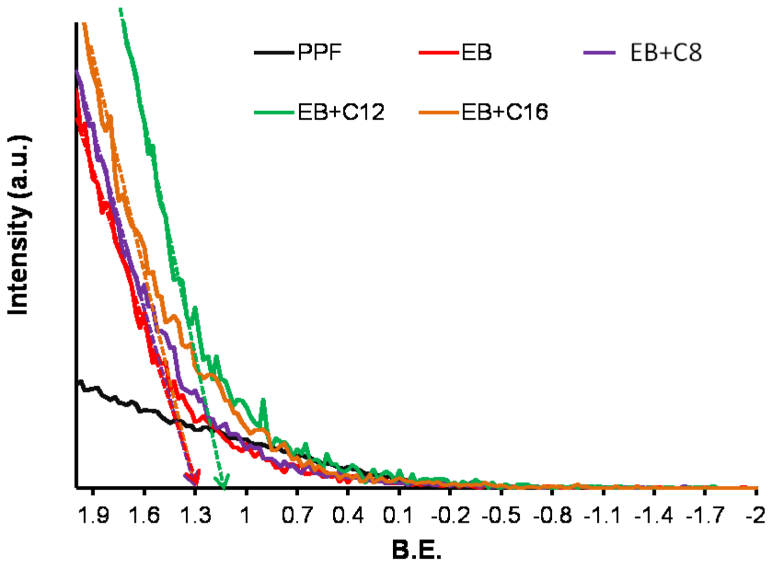

Figure 2.23: HOMO region in UPS spectra of PPF, PPF/EB, PPF/EB-C_8, PPF/EB-C_{12} and PPF/EB-C_{16}. HOMO level energy is considered the binding energy at which the intensity of the layer surpasses that of PPF electrode.

The exponential sensitivity of current to the thickness of bilayer manifested in Figure 2.22 and Equation 2.2 is consistent with tunneling as the charge transport mechanism in these bilayers.

These covalently bonded bilayers are also quite stable at ambient conditions as shown in Figure 2.24.

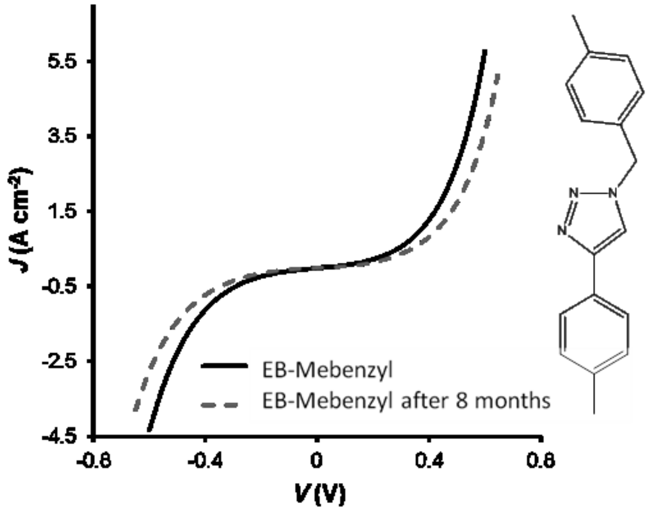

Figure 2.24: J-V curve for a EB-Me benzyl junction as-made compared with the same junction after 8 months.

2.3.1.1 Charge transport mechanism in click bilayers

The single step tunneling charge transport should be only weakly temperature dependent. The dependence of current on temperature for EB/aromatic series is shown in Figure 2.25.

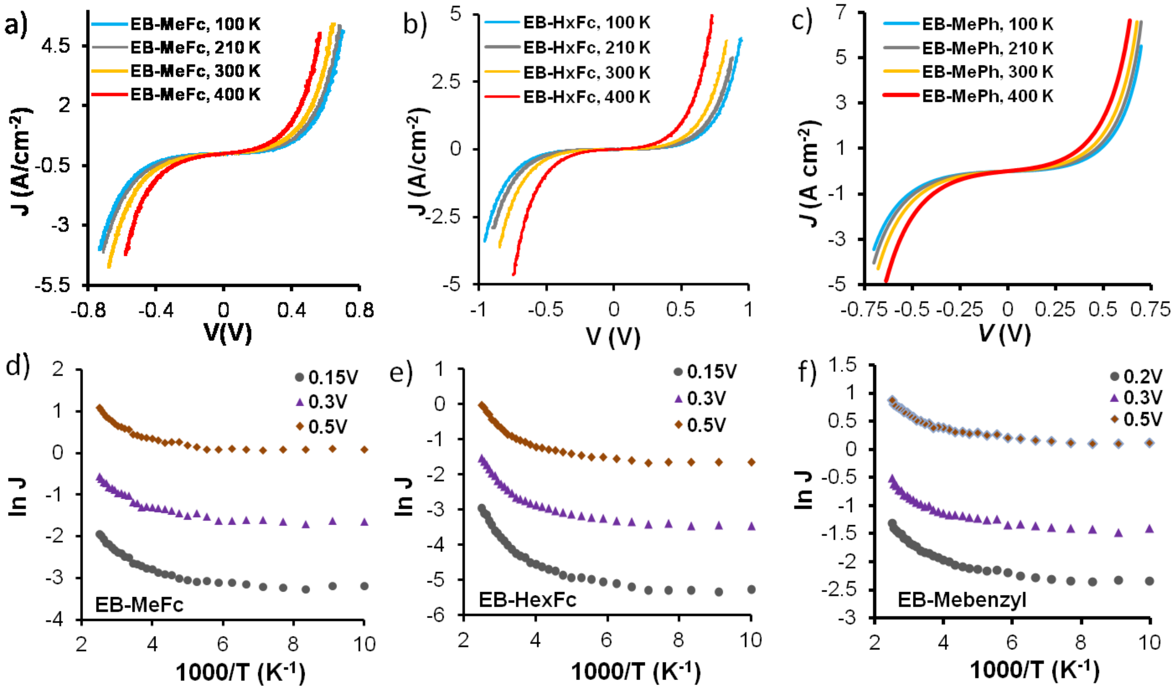

Figure 2.25: J-V curves at various temperatures for a. EB-MeFc. b. EB-HexFc and c. EB-Me benzyl bilayers. Arrhenius plots at various voltages for d. EB-MeFc. e. EB-HexFc and f. EB-Me benzyl bilayers.

The current is almost independent of temperature at temperatures below 200 K (1000/T = 5)and slightly increases at higher temperatures according to Arrhenius plots shown in Figure 2.25 d,e&f. The apparent activation energy for any temperature range is the slope of the Arrhenius plot in that temperature range. The activation energies at 0.2 V are shown on Arrhenius plots for EB-Aromatics in Figure 2.26. The activation energies at various voltages and temperature ranges are listed in table 2.3.

The temperature dependence and activation energies of EB-Alkane bilayer series are presented in table 2.4 and Figure 2.27. EB-alkanes exhibit similar temperature dependence to EB-aromatics and are temperature independent below 200 K and slightly temperature dependent at higher temperatures. This slight increase in current with temperature (Ea<0.1eV) and the exponential shape of the Arrhenius plots may be due to Fermi level broadening in the contacts which effectively decreases the barrier height with temperature[39].

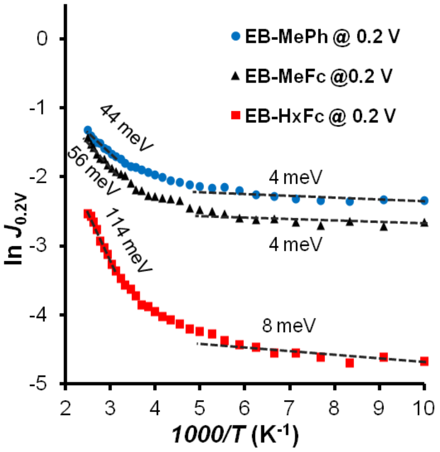

Figure 2.26: Slopes of the Arrhenius plots (Ea) at 0.2 V for EB-HexFc (red squares), EB-MeFc (black triangles) and EB-Mebenzyl (blue circles) at 100-210 K and 300-400 K temperature ranges.

Table 2.3: Activation energies for EB/Aromatics bilayer series.

	Ea, meV					
	EB-MeFc		EB-HxFc		EB-Mebenzyl	
Bias, V	100-210 K	300-400 K	100-210 K	300-400 K	100-210 K	300-400 K
0.1	6.4	63	9.6	128	6.0	53
0.15	3.5	60	8.0	121	5.3	50
0.2	3.7	56	7.9	114	4.2	44
0.3	3.4	48	6.2	104	3.9	40
0.5	1.6	54	4.8	95	3.4	35

Table 2.4: Activation energies for EB/Alkanes series.

	Ea, meV					
	EB-C_8		EB-C_{12}		EB-C_{16}	
Bias, V	100-210 K	300-400 K	100-210 K	300-400 K	100-210 K	300-400 K
0.1	5.3	54	9.4	78	1.9	61
0.2	3.9	47	6.5	68	1.6	46
0.3	2.5	43	5.3	61	0.9	51
0.4	1.9	40	4.5	57	1.3	36
0.5	1.2	36	4.2	53	0.8	32

The activation energies for all bilayers are generally larger at higher temperatures (300-400)K and lower voltages. The apparent higher Ea at higher temperatures is mainly due to Fermi level broadening in the contacts [39] and the voltage dependence of activation energy is probably due to some extent of parallel multistep tunneling happening at the same time with single step tunneling as explained further in Chapter 4.

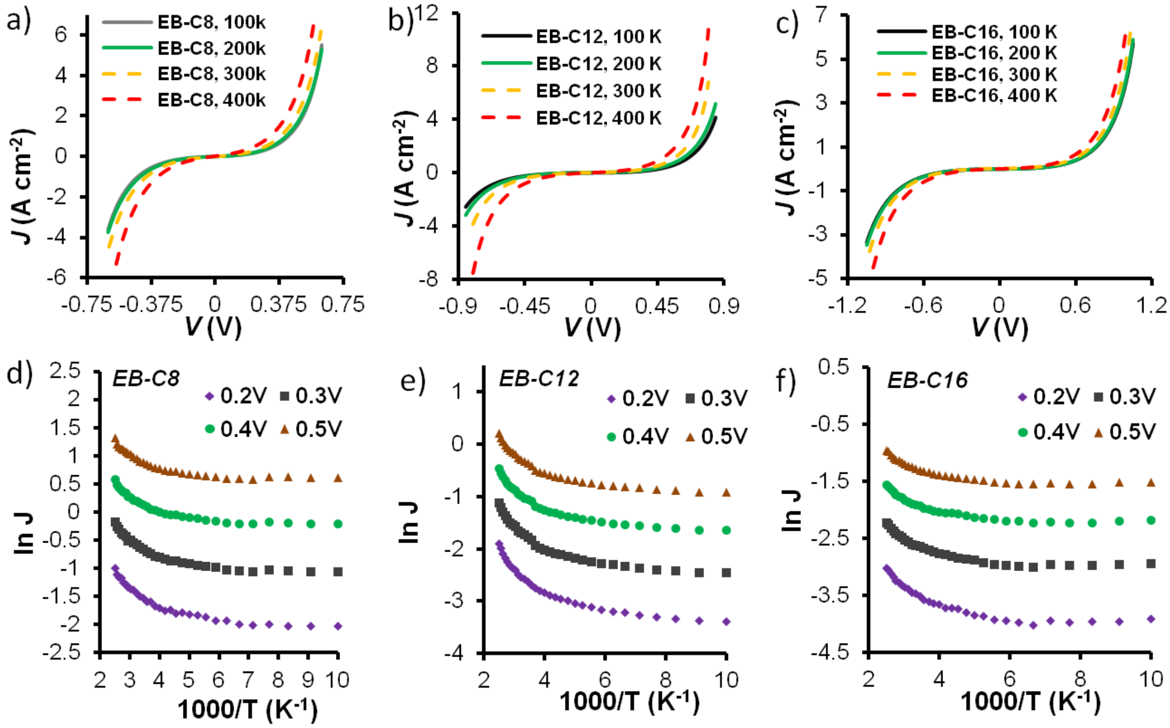

Figure 2.27: J-V curves at various temperatures for a. EB-C_8. b. EB-C_{12} and c. EB-C_{16} bilayers. Arrhenius plots at various voltages for d. EB-C_8. e. EB-C_{12} and f. EB-C_{16} bilayers.

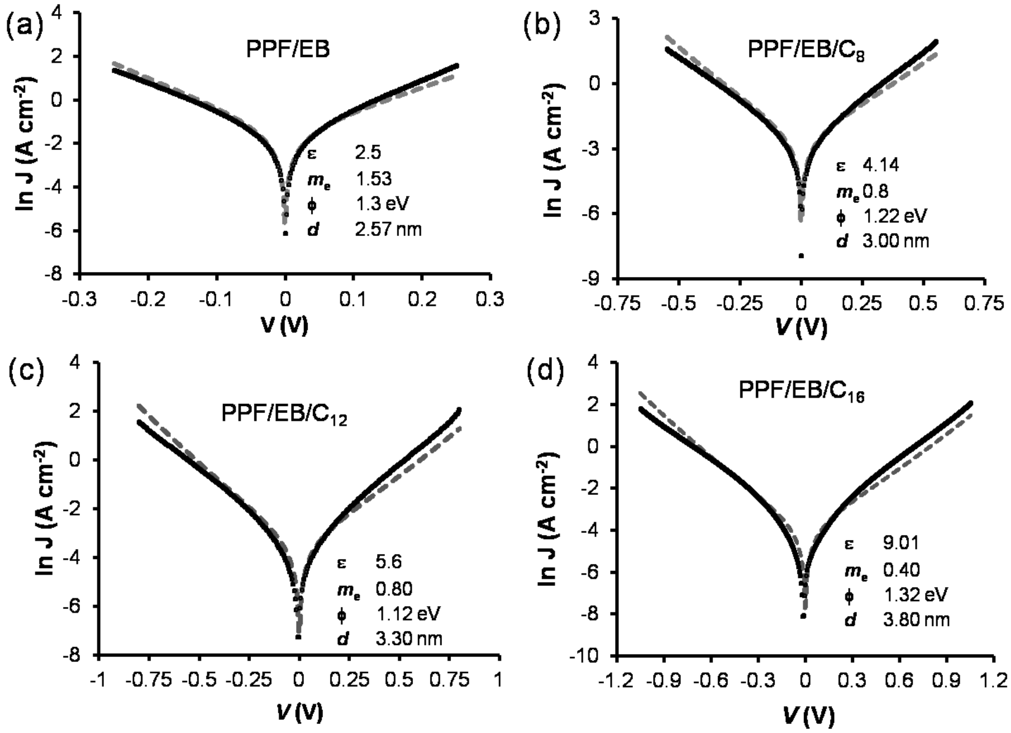

Figure 2.28: J-V curves for different EB based junctions fit to Simmons model as described previously[39]. a. EB. b. EB-C_8. c. EB-C_{12}. d. EB-C_{16}. The dashed gray lines are the results of modeling and black curves are the experimental data.

The small activation energies of less than ~0.1 eV and the nonlinear shape of the Arrhenius plots are not consistent with redox-hopping mechanisms.

The data are more consistent with tunneling mechanism. The full Simmons coherent tunneling model with the inclusion of image charge effects as reported previously[39] and explained in the introduction were fit to the bilayer data and the results are shown in Figure 2.28 along with the variables used for the fittings. The average barrier height of ~1.2 eV for all bilayers is consistent with the previous report for other aromatic molecules[31].

2.3.3.2 Thick EB-based molecular junctions

The EB multilayers were made thicker using higher negative voltages during electroreduction to give layers up to 8.7 nm in thickness by applying CV sweeps from +0.3 V to -1.5 V versus Ag/Ag$^+$ reference electrode at 0.2 V/s for 20 cycles.

The J-V curves for various thicknesses of EB multilayers and β plot at 1 V are shown in Figure 2.29. The current values below 1 V are below the detection limit of the instrument for the thick layers and thus the β plot is shown at 1V.

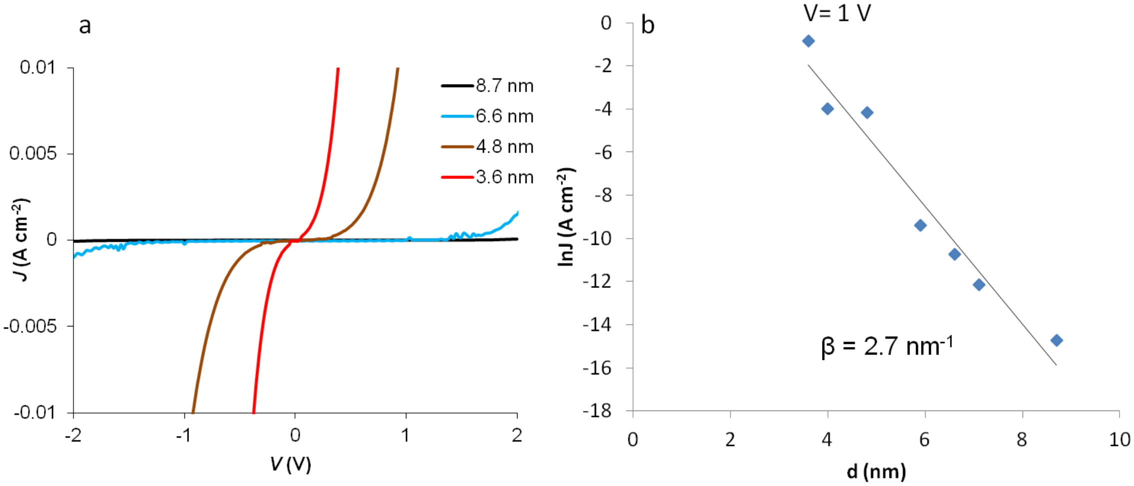

Figure 2.29: a. J-V curves for different thickness of EB. b. β plot at 1 V.

The β value of 2.7 nm^{-1} is similar to the β value for bilayers and other aromatics reported previously[31] for layers thinner than 5 nm. The continuation of tunneling transport to higher thicknesses is presumably due to wide HOMO-LUMO gap (~5.5eV) of the EB molecules which prevents the takeover of other transport mechanisms such as hopping and prevents the increase in the number of tunneling steps as explained in Chapter 4.

2.3.2 TIPS-based click bilayers

TIPS molecule was reported to produce monolayers by in-situ reduction of its diazonium ion[120]. The J-V curves and AFM thicknesses for TIPS layer before and after deprotection are shown in Figure 2.30 a.

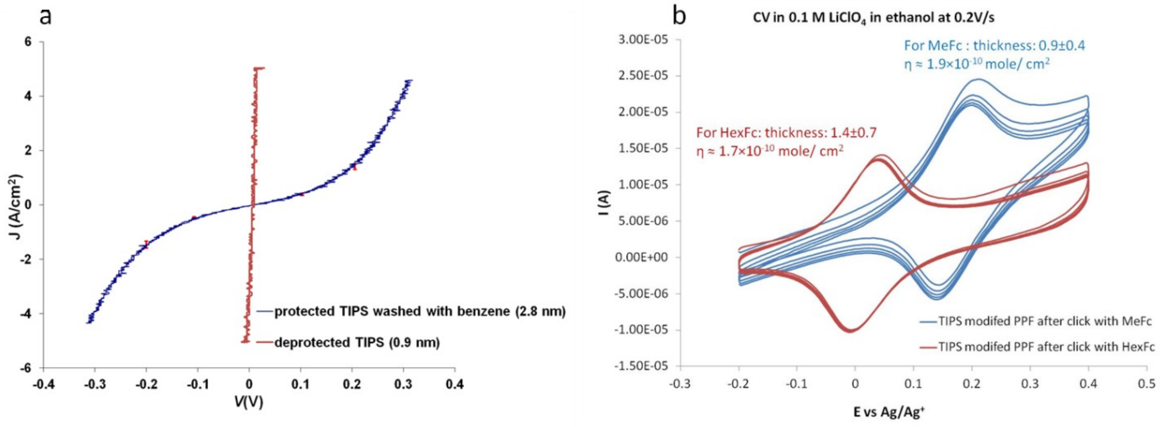

Figure 2.30: a. J-V curves of protected and deprotected TIPS on PPF. b. electroactivity of ferrocene grafted on deprotected TIPS layer as MeFc(blue) and HexFc(red) on PPF.

TIPS layer was 2.8 nm before deprotection with nonlinear J-V curve, however after deprotection, the thickness of the layer decreased to a monolayer with the thickness of 0.9 ± 0.5 nm and it exhibited direct PPF to eC contact (i.e. a short circuit). All bilayers made by click chemistry on the deprotected TIPS monolayer were shorts (linear and conductive). The success of click chemistry however was apparent from the redox activity of the clicked ferrocene on deprotected TIPS layer as shown in Figure 2.30 b.

The bulky TIPS head group prevents the further reaction of diazonium ions with the benzene rings of the TIPS monolayer on the surface and limits the layer growth, however the deprotection of the bulky silyl groups leaves behind large holes between deprotected TIPS molecules that top contact can penetrate through, causing short circuits.

2.3.2.1 Passivation by deposition of chromium oxide

To patch the holes existing on deprotected TIPS surface, deposition of chromium oxide was attempted[128]. The intent was to passivate the pinholes on the TIPS surface with non-conducting oxide such that the current mainly flows through the molecules. In this case the role of the oxide layer would be merely to inhibit top contact penetration and short circuits. The oxide is formed electrochemically and therefore probably favours forming on the bare electrode surface (pinholes) rather than on top of molecules.

The chromium oxide layer was deposited by applying a constant voltage of -0.3 V versus Ag/AgCl/Sat.KCl for 900 seconds in 5 mM solution of $K_2Cr_2O_7$ in 0.1 M NaCl using platinum electrode as counter electrode and (PPF) or (PPF/deprotected TIPS) as working electrode[128]. XPS analysis showed the chromium oxide layer to be a complex mixture of $Cr(OH)_3$ (mainly), Cr_2O_3 and CrO_3 (appendix-Figure A1).

The chromium oxide layer formed on both PPF and PPF/deprotected TIPS were smooth (see Figure 2.31) with roughness of 0.9 nm on PPF and 0.5 nm of PPF/deprotected TIPS.

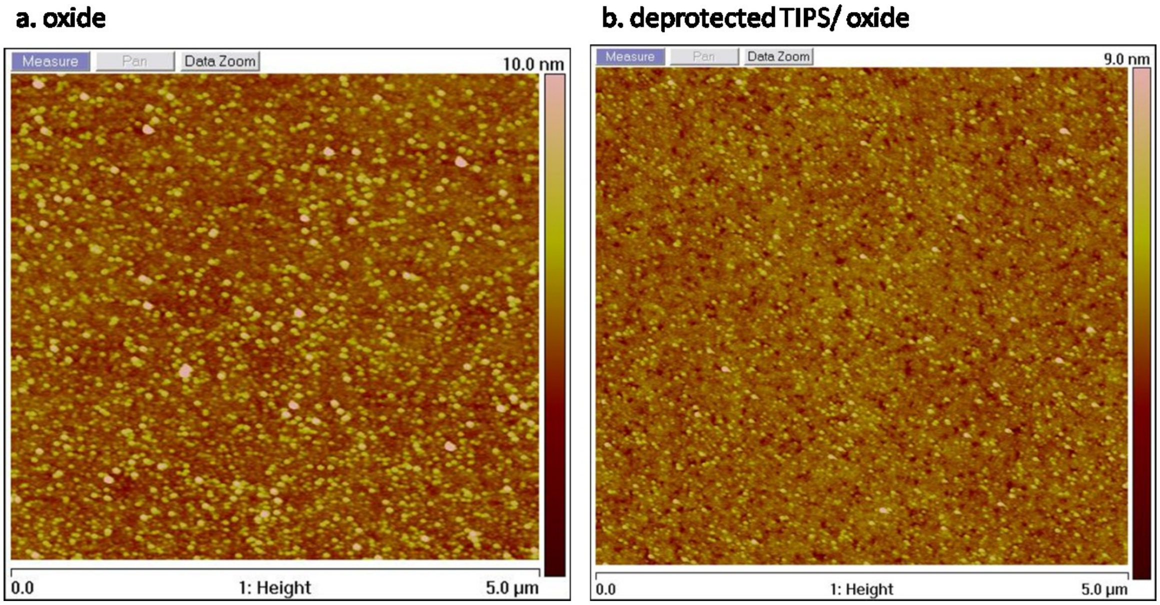
a. oxide

b. deprotected TIPS/ oxide

Figure 2.31: AFM images of a. chromium oxide on PPF. b. chromium oxide on deprotected TIPS on PPF.

The thickness of the chromium oxide layer on bare PPF electrode was 4.7 nm (from AFM) with J-V behavior shown in Figure 2.32. The J-V curve in Figure 2.32 is the average of 4 junctions with standard deviations shown in error bars.

The thickness of the chromium oxide layer on deprotected TIPS on PPF was 4.1 nm and its J-V curve is shown in Figure 2.33. From this thickness of 4.1 nm, it is obvious that the oxide layer is going much further than just filling the hole on the deprotected TIPS surface and is growing to more than 4 nm. The thickness of the deprotected TIPS layer itself is less than 1 nm from AFM.

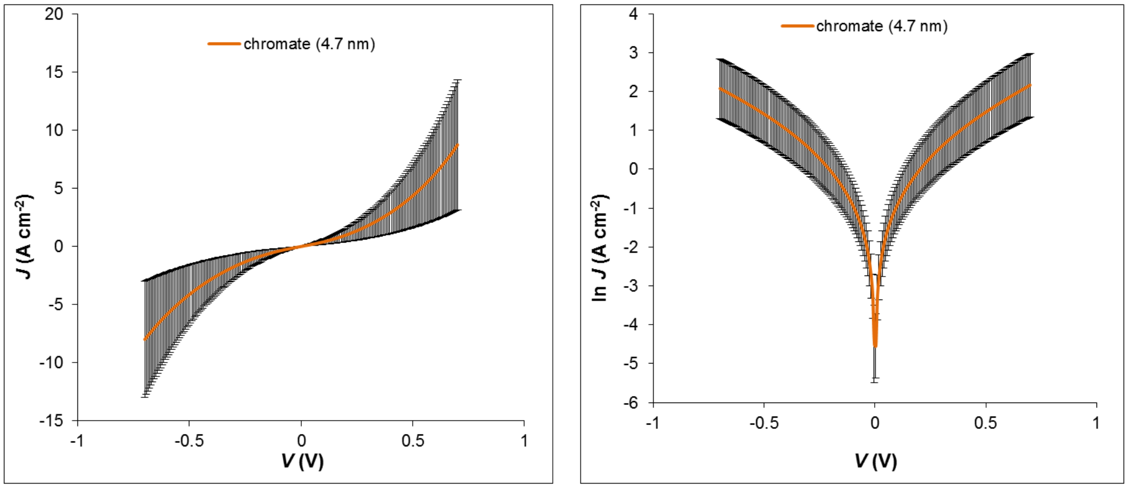

Figure 2.32: J-V and lnJ-V curves for chromium oxide layer on PPF with eC/Au top contact.

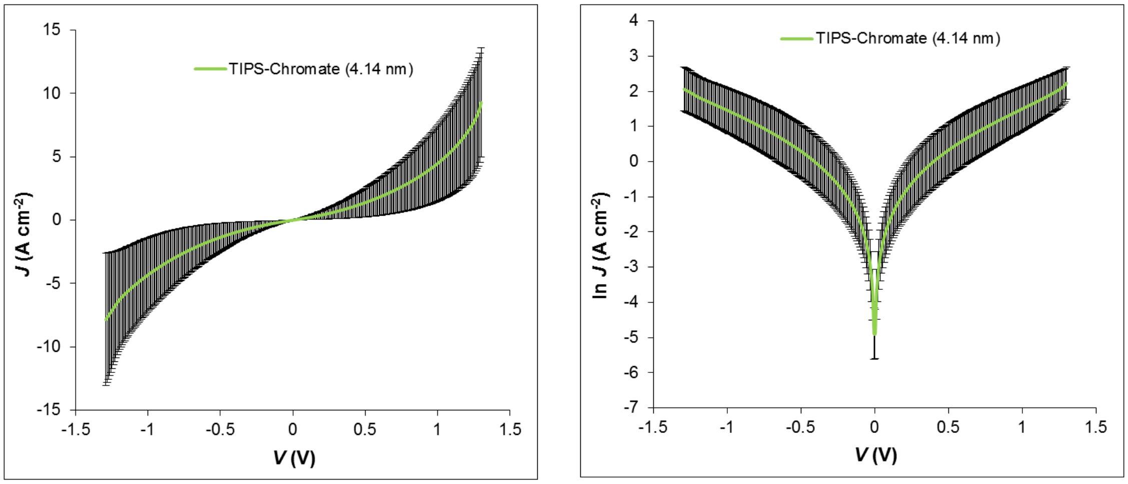

Figure 2.33: J-V and lnJ-V curves for chromium oxide layer on deprotected TIP on PPF with eC/Au top contact.

It was observed that the thickness of the chromium oxide layer on deprotected layer could be varied by changing the duration of applied voltage during the electroreduction process as shown in Figure 2.34.

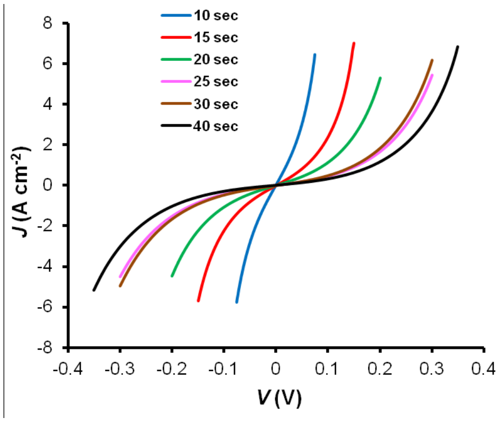

Figure 2.34: Varying the thickness of the chromium oxide layer by changing the modification time length.

Although the holes on deprotected TIPS can be successfully patched by deposition of the chromium oxide layer and give working nonlinear junctions, the lack of self-limitation in the deposition process of the chromium oxide layer leads to the growth of the oxide layer out of the pinholes and obscures the molecular transport information.

2.3.3 TMS-based click bilayer molecular junctions

To alleviate the problem caused by bulky TIPS groups, the smaller TMS molecule was tried for the formation of monolayers. The detachment of the silyl groups by TBAF (see Figure 2.35 a) and the attachment of the ferrocene azides by click reaction (see Figure 2.35 b) were probed by XPS.

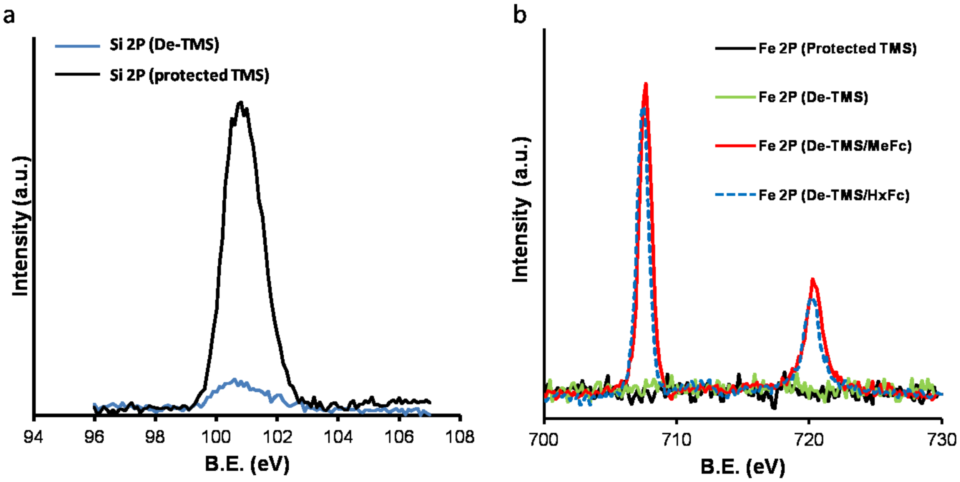

Figure 2.35: a. Si_{2p} region in XPS spectra of protected (black) and deprotected (blue) TMS layers. b. Fe_{2p} region in XPS spectra of protected TMS (black), deprotected TMS (green), deprotected TMS reacted with MeFc (red) and deprotected TMS reacted with HexFc (dashed blue) showing $Fe2P_{3/2}$ at lower and $Fe2P_{1/2}$ at higher binding energies.

The ferrocene electroacitivity (shown in Figure 2.36) was also observed on both PPF and GC surfaces modified with TMS after deprotection and reaction with methyl and hexyl ferrocene azides.

The thickness of the TMS layer before deprotection was measured at 4.3±0.5 nm which decreased to 2.9±0.5 nm upon deprotection. Since the TMS molecule itself is only ~0.5 nm long, this means that the TMS molecule does not form monolayers and its growth is not as limited as TIPS. The J-V curves for TMS molecular junctions before and after deprotection are presented in Figure 2.37 as the averages of 4 junctions on a chip. The deprotected TMS junctions were close to short circuit despite 2.9 nm of thickness. It is possible that the growth mode of TMS molecule is mushroom like[30] due to presence of the silyl group and the deprotection step and the removal of the silyl groups leaves a porous layer behind.

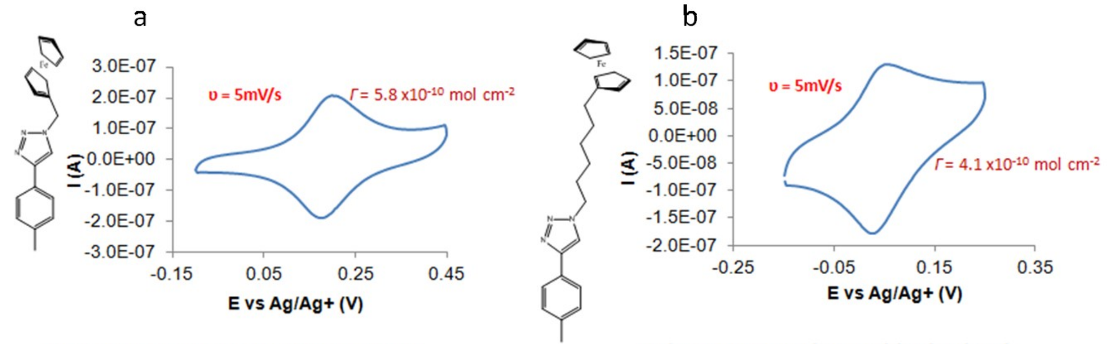

GC/De-TMS-MeFc CV in 0.1M LiClO4 in ethanol

GC/De-TMS-HexFc CV in 0.1M LiClO4 in ethanol

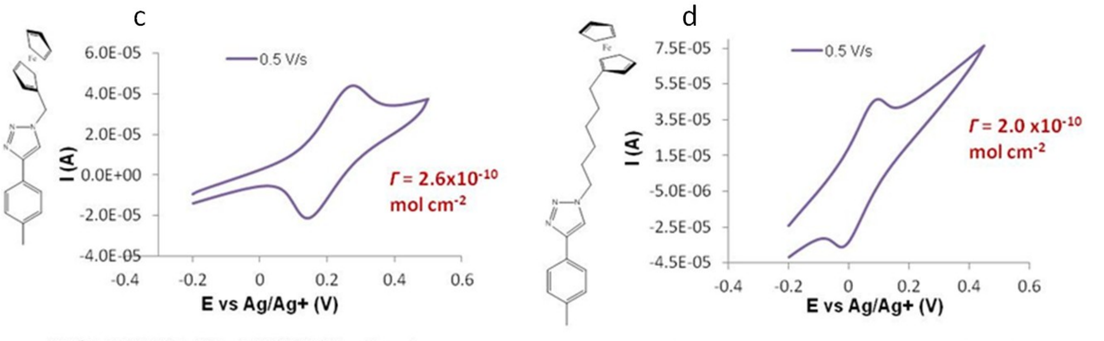

PPF/De-TMS-MeFc CV in 0.1M LiClO4 in ethanol

PPF/De-TMS-HexFc CV in 0.1M LiClO4 in ethanol

Figure 2.36: Cyclic voltammetry a,b. at 0.005 V/s of GC and c,d. at 0.5 V/s of PPF modified surfaces with a,c. EB-MeFc and b,d. EB-HexFc in ethanolic solution of 0.1 M $LiClO_4$ as supporting electrolyte.

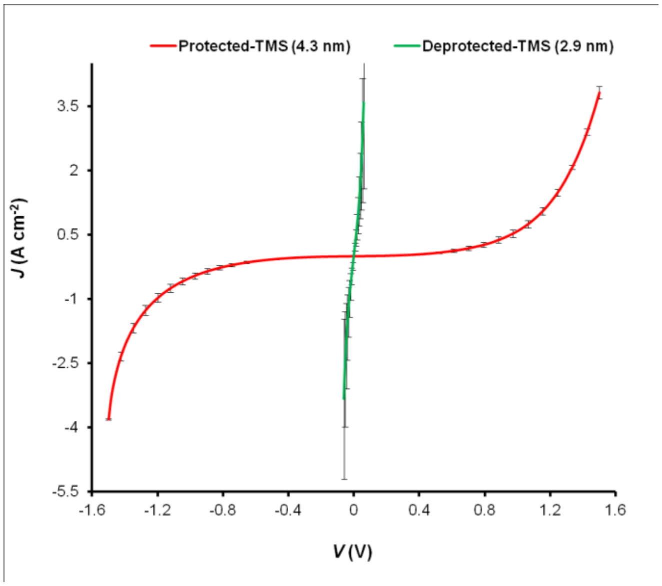

Figure 2.37: J-V curves of TMS junctions before and after deprotection.

J-V curves of the bilayers formed by click chemistry with the deprotected TMS layer are shown in Figure 2.38. The roughness of all layers was less than 0.6 nm.

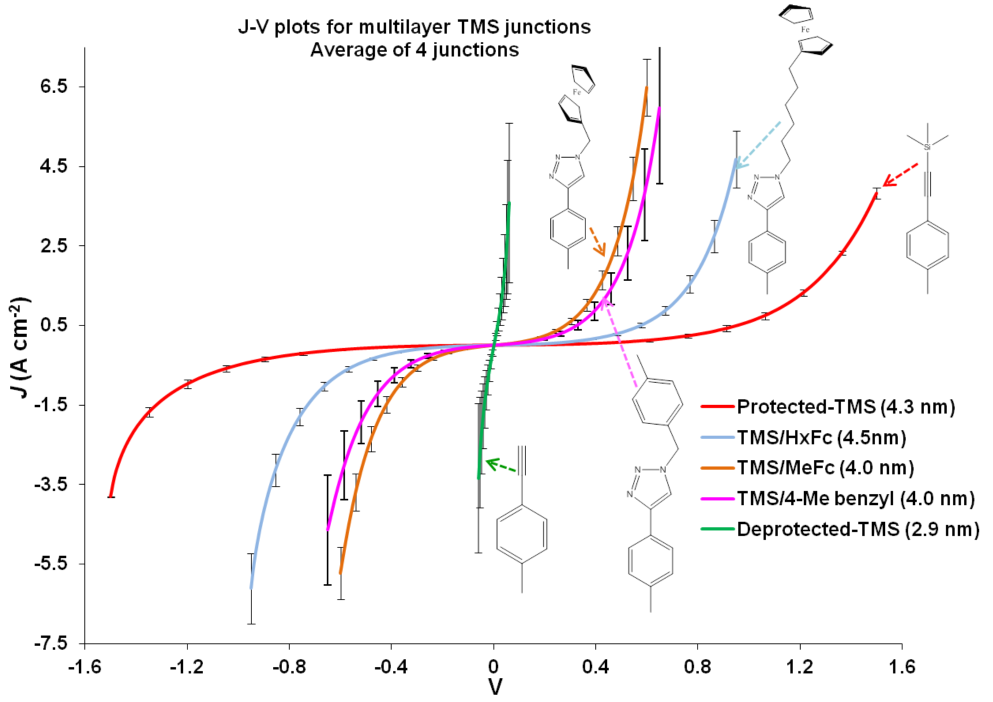

Figure 2.38: J-V curves of TMS based bilayer junctions. The standard deviation in thicknesses was less than ±0.6 nm in all cases.

Despite the near short circuit response for deprotected TMS, the click bilayers were all working junctions with 100% yield. This shows that the clicked layer has successfully covered the pinholes in deprotected TMS layer although the higher conductivity of TMS/HexFc than protected TMS suggests that the coverage of the original pinholes was only partial. The effect of the porosity of the primer layer is also evident in the comparison of the EB-click bilayers with TMS-click bilayers shown in Figure 2.39.

The J-V curves of EB based bilayers were very similar to TMS based bilayers but the EB based layers with the same conductivity were thinner. Because of the porosity of the deprotected TMS layer, a thicker layer of it, is needed to match the conductivity of a thinner compact EB layer.

The temperature dependence of TMS based layers was also similar to EB based layers. The J-V curves of deprotected TMS/HexFc at various temperatures along with its Arrhenius plot are shown in Figure 2.40.

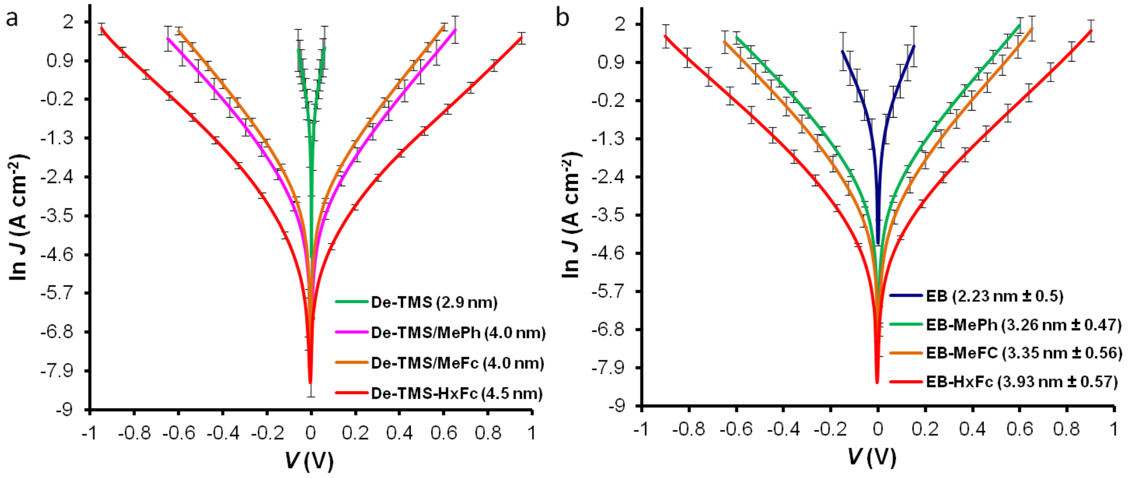

Figure 2.39: Comparison of the lnJ-V curves of a. TMS based and b. EB based bilayers.

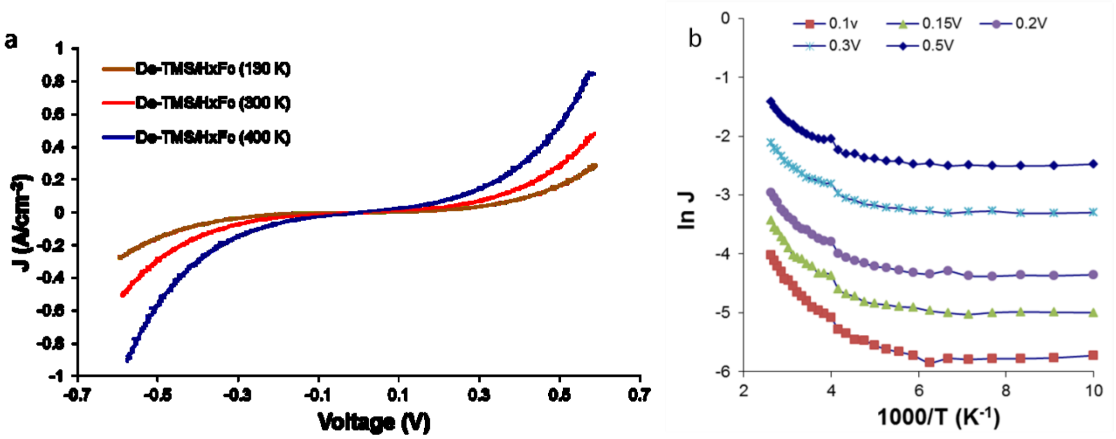

Figure 2.40: a. J-V curves of deprotected TMS/HexFc at various temperatures. b. Arrhenius plots for the same junction in a at different voltages.

Table 2.5: Activation energies for TMS based bilayers at different temperature ranges and bias voltages.

Ea, meV				
	Deprotected TMS-MeFc		Deprotected TMS-HexFc	
Bias, V	120-200 K	320-400 K	120-200 K	320-400 K
0.1	4.1	78	2.3	108
0.2	3.7	74	2.3	96
0.3	2.4	72	1.8	83
0.4	1.6	77	1.4	75
0.5	1.5	75	1.5	77

The activation energies at high and low temperatures and various voltages are listed in table 2.5 for TMS based bilayers. The activation energies are close to values observed for EB based bilayers which suggests these bilayers follow the same tunneling transport mechanism.

2.4 Conclusion

Compositionally asymmetric molecular junctions were fabricated via azide-alkyne click chemistry modification of the electrochemically deposited aromatic alkyne layer. The J-V behavior of the resultant thin (<5 nm) bilayers were symmetric despite the introduced asymmetry in the structure of the molecular junction. The structure of the second layer of the bilayer did not affect the β value of the bilayer and even bilayers with aliphatic second layer behaved the same as aromatic layers. In addition to similar β values, the current densities were also similar for all of the bilayers of a given thickness. This finding was attributed to majority aromatic structure of the bilayer and electronic coupling with the contact. The exponential dependence of the current on thickness and the weak temperature dependence of current are consistent with a tunneling mechanism of charge transport in these thin bilayers.

Chapter 3

Rectification in Bilayer Molecular Junctions, Beyond Tunneling

3.1 Introduction

This Chapter describes the charge transport properties of molecular bilayers made by reduction of aromatic diazonium salts. The term “bilayer” in this Chapter refers to the multilayer of one kind of molecule formed on top of the multilayer of a different kind of molecule (see Figure 3.10); although each multilayer can be considered a monolayer of a larger molecule by virtue of covalent bonding between the molecules. Unlike the click-bilayers discussed in Chapter 2, the thickness of the second layer is not limited to one layer as both layers form multilayers via diazonium reduction. The variation of the thickness of both layers allows us to investigate the relation between the structure and thickness of each layer and the current-voltage characteristics.

Despite limitations of the molecules amenable to diazonium chemistry, there is still a range of molecules with very different energy levels available for bilayer formation. In this Chapter, bilayers formed by various molecules with different HOMO and LUMO energy levels are described and the relation between energy levels and rectification is revealed. Controlling the thickness of both layers enables the study of the transport characteristics of junctions with thickness range between 5 and 25 nm, bridging the gap between monomolecular rectifiers and organic bilayer rectifiers with thicknesses more than 50 nm.

3.1.1 Overview of rectification in molecular junctions

The origin of molecular electronics is usually traced back to the 1974 paper[129] by Aviram and Ratner (AR) in which an organic analogue to inorganic p-n junction diodes is described. The original AR concept is illustrated schematically is Figure 3.1 in which a donor molecule is separated from an acceptor molecule with a non-conjugated covalent bridge. A donor molecule (D) is a molecule with an accessible HOMO level and an acceptor (A) is a molecule with an accessible LUMO level. In other words a donor molecule is easily oxidizable with small HOMO offset from the electrode Fermi level, and an acceptor molecule is easily reducible with small LUMO offset. This combination of D-σ-A forms a rectifier that allows more current flow at one bias direction than the opposite.

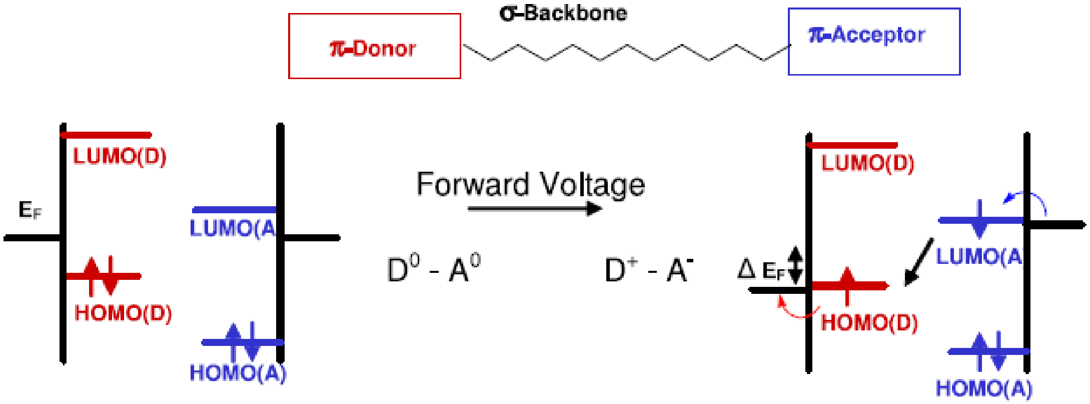

Figure 3.1: Schematic representation of Aviram–Ratner concept. At forward bias the Fermi level of the electrodes are aligned with the HOMO and LUMO levels of donor and acceptor respectively, giving rise to higher current. Figure adapted from ref[130].

In the forward direction when more current flows in AR proposal, the E_F of the electrode closer to donor molecule becomes aligned with the HOMO of donor and the E_F of the electrode closer to acceptor molecule becomes aligned with the LUMO of the acceptor molecule. This leads to formation of D^+ - A^- zwitterionic form as an electron moves from the HOMO of the donor to the Fermi level of the adjacent electrode to form D^+ and an electron moves from the Fermi level of the opposite electrode to the LUMO of the acceptor to form A^-. The energy levels of donor and acceptor are separated and localized by presence of the σ bridge, but a conjugated bridge with high torsion angle that breaks the conjugation between D and A also acts the same as σ bridge[131]. The formation of of D^+ - A^- zwitterionic form is followed by internal relaxation to D-A as an electron moves from the LUMO of A^- to the HOMO of D^+. Consequently the overall direction of electron flow in AR proposal is from acceptor to donor. In the opposite polarity when the electrodes closer to donor and acceptor are negatively and positively biased respectively, the alignment of Fermi levels with molecular levels is not easily achieved as the LUMO of D and HOMO of A are not accessible; therefore a smaller current flows in reverse voltage.

The donor is analogous to p type semiconductor because it is a better hole conductor and the acceptor is analogous to n type semiconductor that is a better electron conductor. The electron flows easily from n-type acceptor to p-type donor as it does in inorganic p-n junctions as well as organic p-n junctions.

Bilayer organic p-n junction rectifiers have been made as OLEDs[132], [133], organic photodiodes and photodetectors[134]–[136] and diodes[137] with or without a gate electrode. The main difference between organic p-n junction rectifiers and AR D-σ-A rectifiers is the difference in size of the active layers. AR rectifiers are only a few nanometers and tunneling plays an important role in AR rectification that is evident from rectification at 4K[138]. Organic rectifiers on the other hand are much thicker at around 100 nm and almost always have dissimilar electrodes. The contact adjacent to the n-type acceptor layer has a low work function (such as Al, Mg, Ag and Ca) and the contact adjacent to p-type donor layer has a high work function (such as ITO or Au). This work function difference between contacts facilitates electron injection into n-type acceptor and hole injection into p-type donor in OLEDs and diodes and also creates the necessary built-in filed (V_{bi}) in photodetectors to guide electrons towards cathode (the electrode with low work function such as Al) and holes towards anode (the electrode with high work function such as ITO) to give rise to a current.

Here it is necessary to distinguish between organic and inorganic p and n type materials. An inorganic n-type material has electrons in conduction band thus it has higher Fermi level and is electron rich. An organic n-type material however does not have electrons in LUMO level (equivalent to conduction band) and is electron poor. The inorganic p-type material is electron poor with lower Fermi level but an organic p-type material is electron rich and has a high Fermi level (considered halfway among HOMO and LUMO levels). These differences become quite important when discussing the Schottky barrier formation at the contact-material interface: An n-type inorganic semiconductor-metal Schottky barrier is conceptually similar to a p-type organic semiconductor-metal Schottky barrier. Charge transfer at the p-type organic semiconductor-metal interface results in formation of positively charged polarons with energy levels inside the neutral HOMO-LUMO gap (refer to Chapter 4, 4.1), at the same time due to inaccessibility of the LUMO of p-type organic semiconductor, it would be difficult to inject electrons into the p-type semiconductor from the Ohmic contact unless the device is so thin that tunneling can take over. Finally “the Fermi level pinning” at the organic-metal interface (refer to Chapter 1, section 1.3) “ties” the HOMO of p-type organic semiconductor to the Fermi level of the metal at the Schottky contact and makes it inaccessible for hole injection from the Schottky contact side. Consequently the directions of organic and inorganic Schottky diodes end up being similar in spite of their differences.

It is worth mentioning that some organic p-n junctions are made by doping and are truly equivalent to inorganic p-n junctions. An example is p-type pentacene-n-type pentacene p-n junction[139]. p-type pentacene is a pentacene layer doped with an electron accepting molecule to make some pentacene molecules positively charged that creates holes and brings the Fermi level down; the n-type pentacene is a layer of pentacene doped with a good electron donating molecules that makes some pentacene molecules negatively charged and bring the Fermi level up by creating excess electrons. Nevertheless even these organic p-n junctions have the same direction of rectification as AR rectifiers. There are however many reports of molecular rectification and organic p-n junctions[140] that are not consistent with AR proposal as reviewed by Metzger[141] (see Figure 3.2).

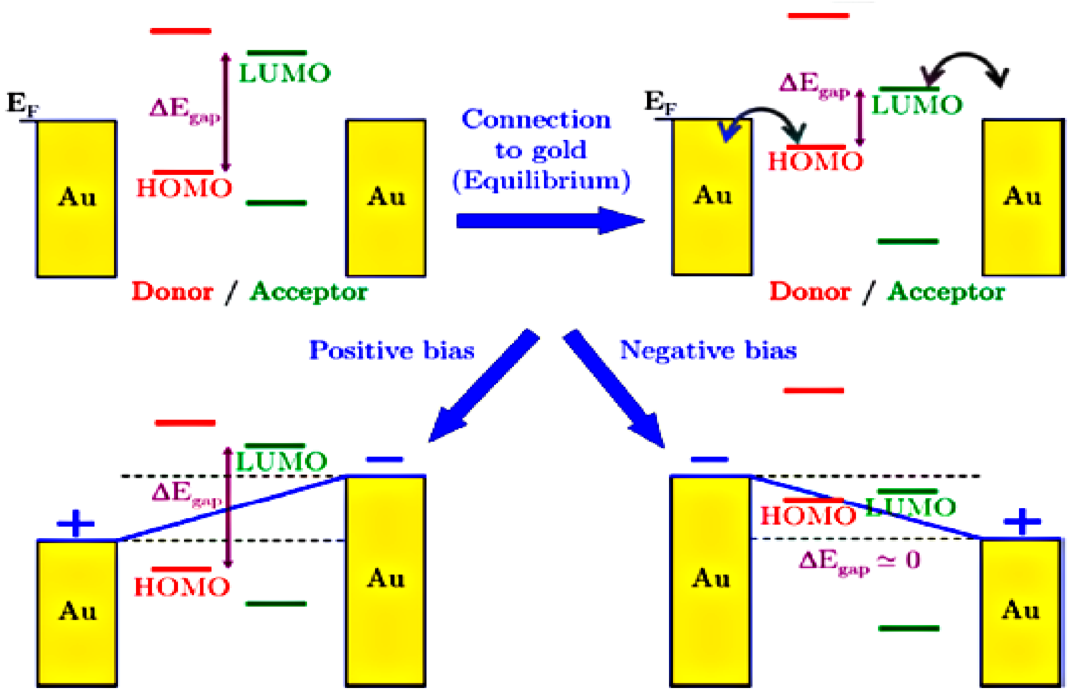

Figure 3.2: A D-σ-A structure is brought into contact with the electrodes. The HOMO of donor and the LUMO of acceptor can be pinned to the Fermi level of the electrodes in their vicinity using suitable anchoring groups. Now when positive voltage is applied to the donor side, the HOMO of donor does not become available as it is tied to electrode Fermi level and goes down with it and the same happens to acceptor's LUMO that goes up with electrode Fermi level. When the donor side is negatively biased the electron can move from the HOMO of donor to LUMO of acceptor and larger current flows. This is consistent with anti-AR mechanism. Figure used with permission from ref[142].

These rectifiers follow the anti-AR mechanism. The anti-AR rectifier has the same D-σ-A structure but the direction of electron flow is from donor to acceptor which is opposite of AR rectifier. Metzger suggests[143] that the Anti-AR rectifier is due to formation of D^+-A^- zwitterionic form under electric field followed by movement of electron from the LUMO of A^- to positive electrode next to it and movement of another electron from negative electrode next to D^+ to the HOMO of D^+. This leads to overall electron movement direction opposite to AR proposal. The anti-AR proposal is also consistent with the proposal of strong coupling of donor and acceptor to electrodes as shown in Figure 3.2.

The anti-AR mechanism also avoids the formation of D^+ close to positively charged electrode and A^- close to negatively charged electrode that would be quite unstable for very thin devices.

There are a variety of mechanisms discussed in different papers for rectification of organic molecular junctions[144] but the main remaining rectification mechanisms include Schottky barrier formation or rectification due to formation of dipoles[145], [146], dissimilar coupling strengths to electrodes[147] and asymmetric placement of a chromophore within molecular junction using a long alkane that leads to a significant field drop across the alkane[90], [148], [149]. This last mechanism of asymmetric placement has the same direction as a Schottky barrier diode formed between the chromophore and the contact and can get a boost from Fermi level pinning effect.

3.2 Experimental section

Fabrication of the PPF lines, preparation of the 3 electrode electrochemical setup and top contact deposition procedure were performed similar to the methods described in the experimental section of Chapter 2.

3.2.1 Material synthesis

Most of the diazonium salts used in this Chapter were already synthesized, characterized and used in device fabrication in our group[31], [150] A similar method to that described in the experimental section of Chapter 2 to prepare ethynyl benzene (EB) diazonium salt was used. Briefly, this method includes reaction of sodium nitrite with the corresponding amine compound in tetrafluoroboric acid, filtering the solid diazonium salt product and dissolving it in acetonitrile (ACN) followed by crystallization of the diazonium salt by adding ether to the acetonitrile solution. Nitroazobenzene (NAB) diazonium salt, 2-Anthraquinone (AQ) diazonium salt and fluorene (FL) diazonium salt were all synthesized by this method and characterized by LC-MS spectrometry. BTB diazonium salt was prepared in-situ (due to instability of BTB diazonium salt) in accordance with the method described in the experimental section of Chapter 4 by adding 60 µL of tert-butyl nitrite to 20 mL solution of BTAB in 0.1 M $TBABF_4$ in ACN.

N-(4-tert-butylphenyl)-N'-(4-aminophenyl)-1,4,5,8-naphthalenecarboxylic acid diimide (NDI-amine) was the starting material for synthesis of NDI diazonium salt. The slurry of NDI-amine in 12 mL dry ACN (dried over molecular sieves) was slowly added to a solution of $NOBF_4$ (nitrosonium tetrafluoroborate from ACROS) in 4 mL dry ACN at -40 ºC (in dry ice/ACN bath). The mixture was stirred at -40 ºC for 1 hour. 100 mL ACN was added to the reaction mixture to obtain a clear solution and NDI diazonium salt was crystallized by adding diethyl ether to this solution. The NDI diazonium salt precipitate was vacuum filtrated and washed with diethyl ether. The LC-MS spectrum of NDI diazonium salt is shown in appendix Figure A2.

The structures of all amine starting materials used for preparation of diazonium salts used in this Chapter are shown in Figure 3.3.

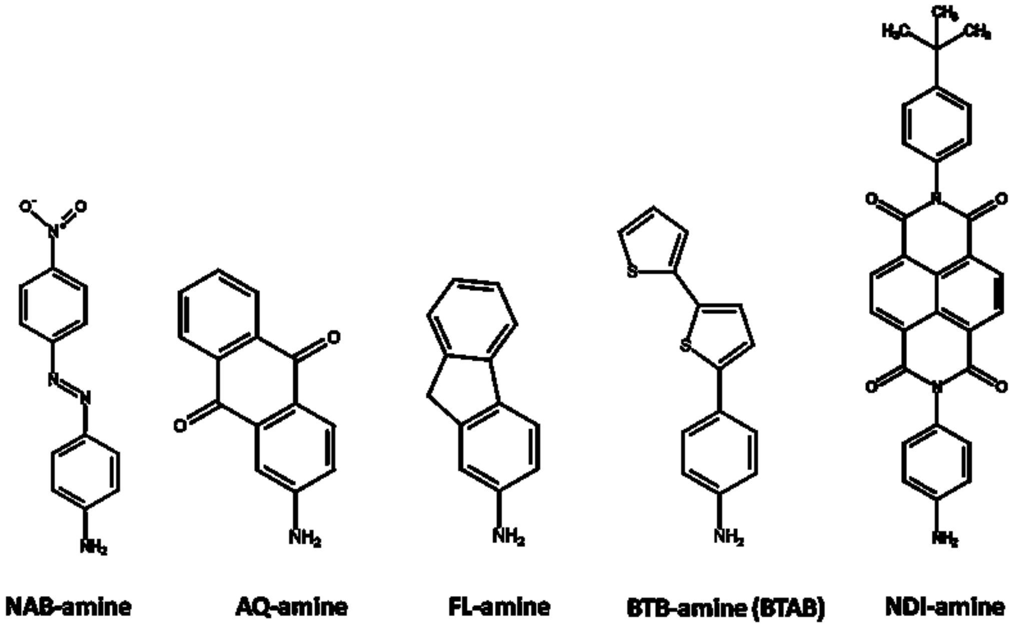

Figure 3.3: The structure of the amine starting materials used to make diazonium salts. Reagents were purchased from Aldrich and used as received, except for BTAB, which was provided by JC Lacroix of the University of Paris.

3.2.2 Junction fabrication

Bilayers were made by successive electroreduction of two different diazonium salts on PPF strips in a three-electrode cell with PPF as working electrode, platinum wire as counter electrode and Ag/Ag$^+$(described in Chapter 2) as reference electrode. In a typical procedure, a solution of 0.5 mM NDI diazonium salt in 0.1 M $TBABF_4$ in ACN was bubbled with argon gas through a Pasteur pipet for 10 min. The reference and counter electrodes were put in the solution and the Pasteur pipet was raised just enough to stop bubbling inside the solution but to continue to provide a cushion of argon on the solution. The SiO_x/Si chip with PPF lines was put in solution as working electrode. Cyclic voltammetry was performed by sweeping the voltage from 0.4 V to -0.6 V at 0.05 V/s for 10 cycles as shown in Figure 3.4. These conditions results in ~10.7 nm layer of NDI on PPF. As indicated in table 3.1, variations in scan range and number of cycles were used to deposit different thicknesses of various diazonium reagents, determined largely empirically.

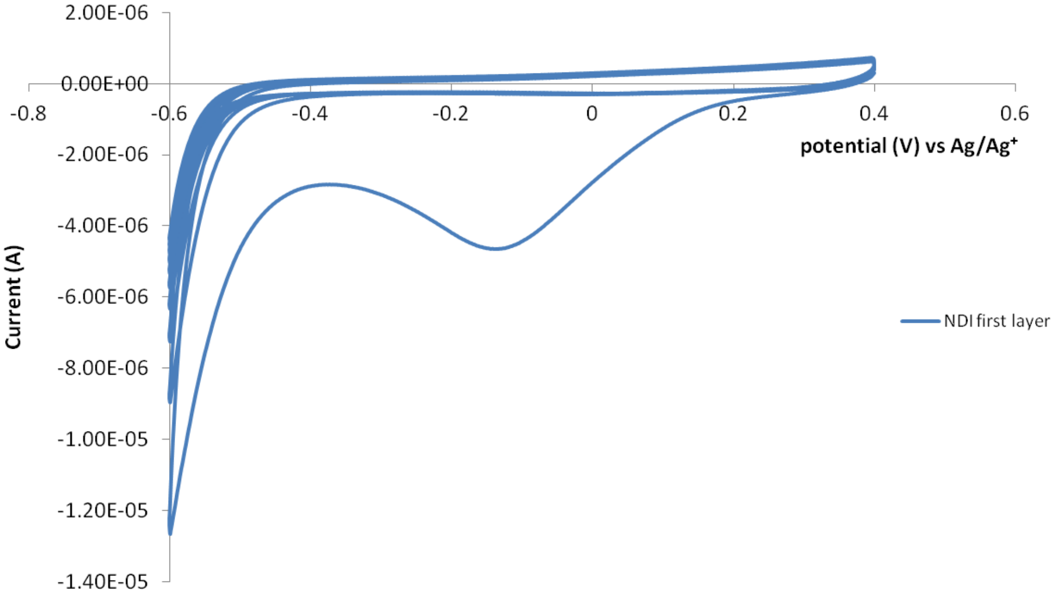

Figure 3.4: CV modification curve for NDI on PPF. This forms a 10.7 nm layer of NDI.

After Modification of PPF surface with NDI as first layer, the chip was rinsed with ACN and dried with a stream of nitrogen gas.

To form the second layer of the bilayer, a 0.5 mM BTAB solution in ACN /TBABF$_4$ was bubbled for 10 min with argon gas and after putting the reference and counter electrodes in BTAB solution, 60 µL of t-butyl nitrite was added to solution to form a bright red solution. Pasteur pipet was raised above the solution surface and the PPF chip already modified with NDI was put in the solution as working electrode. The voltage was swept from 0 to -1.2 V at 0.05 V/s for 10 cycles as shown in Figure 3.5. These conditions form a ~10.3 nm BTB layer on top of 10.7 nm NDI layer which makes the total thickness of NDI-BTB bilayer to be 21 nm.

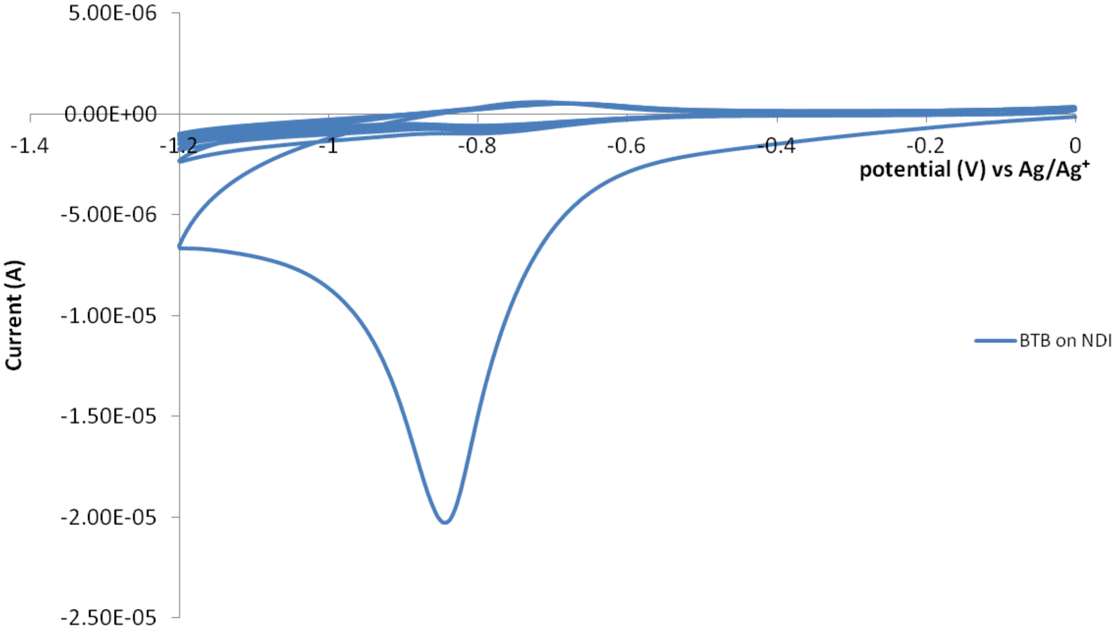

Figure 3.5: CV modification curve for BTB on NDI. This forms a 10.3 nm layer of BTB on top of NDI with NDI-BTB bilayer totaling 21 nm in thickness.

The chip was rinsed with ACN again after BTB modification, dried with nitrogen and 10 nm eC/ 30 nm Au top contact was evaporated on top through a shadow mask using e-beam PVD to form the complete device, as described in Chapter 2.

Table 3.1: Modification conditions and thicknesses from AFM for bilayers.

Layer	Solution in 0.1M $TBABF_4$ in ACN	CV conditions vs. Ag/Ag+	thickness(nm)
NDI	0.5 mM NDI DS	0.4 to -0.6 V at 0.05 V/s for 10 cyc	10.7 ± 0.7 nm
BTB on NDI	0.5 mM BTAB + 60μL t-butylnitrite	0 to -1.2 V at 0.05 V/s for 10 cyc	10.3 ± 1 nm
AQ on NDI	1mM AQ DS	0.4 to -0.8 V at 0.05 V/s for 10 cyc	11.9 ± 0.7 nm
NAB on NDI	1mM NAB DS	0.4 to -0.8 V at 0.05 V/s for 10 cyc	11.4 ± 0.7 nm
FL on NDI	1mM FL DS	0.4 to -1.8 V at 0.05 V/s for 20 cyc (bubbling argon)	13 ± 0.8 nm
AQ	1mM AQ DS	0.4 to -0.65 V at 0.05 V/s for 10 cyc	8.4 ± 0.6 nm
FL on AQ	1mM FL DS	0.4 to -1.8 V at 0.05 V/s for 10 cyc (bubbling argon)	12.3 ± 0.8 nm
BTB on AQ	0.5 mM BTAB + 60μL t-butylnitrite	0 to -1.8 V at 0.2 V/s for 20 cyc (bubbling argon)	11.6 ± 1 nm
FL	1mM FL DS	0.4 to -1.5 V at 0.05 V/s for 10 cyc	12 ± 1 nm
AQ on FL	1mM AQ DS	0.4 to -1.8 V at 0.05 V/s for 10 cyc (bubbling argon)	5.3 ± 0.9 nm
BTB	0.5 mM BTAB + 60μL t-butylnitrite	0 to -0.8 V at 0.05 V/s for 10 cyc	11 ± 1 nm
AQ on BTB	1mM AQ DS	0 to -1.8 V at 0.2 V/s for 20 cyc	13 ± 4 nm

The thickness of NDI layer can be varied from ~3 nm (0.4 to -0.5 V for 5 cycles) to ~24 nm (0.4 to -0.65 V for 10 cycles) by changing the potential window and number of cycles during modification. The thickness of BTB layer on top of a 10.7 nm NDI layer can also be varied from ~3 nm (0 to -0.7 V for 8 cycles) to ~10 nm (0 to -1.2 V for 10 cycles) by changing the potential window and number of scans.

The modification curves for BTB (appendix Figure A3), AQ (appendix Figure A4) and FL (appendix Figure A5) as first layer are shown in appendix and the conditions are summarized in table 3.1.

The modification curves for NAB on NDI (appendix Figure A6), AQ on NDI (appendix Figure A7), FL on NDI (appendix Figure A8), FL on AQ (appendix Figure A9), BTB on AQ (appendix Figure A10), AQ on BTB (appendix Figure A11) and AQ on FL (appendix Figure A12) are shown in appendix and the conditions and the resulting thicknesses are also summarized in table 3.1. In some cases when the applied voltage window was wide toward negative direction, argon gas was bubbling in solution during the modification process to prevent oxygen from getting reduced on the electrode instead of the diazonium reagents.

3.2.3 Characterization

AFM (DI 3100 atomic force microscope) was used as described in experimental part of Chapter 2 to obtain layer thicknesses by scratching method. The thickness of the second layer in bilayers was obtained by subtracting the thickness of the first layer from the thickness of the total bilayer.

XPS analysis was acquired with the AXIS 165 spectrometer equipped with a monochromatic Al K_α source (1486.6 eV). UPS spectra were obtained by a Kratos Ultra spectrometer with a He I source (21.21 eV).

UV-Vis spectroscopy was carried out using Perkin Elmer UV-Vis/NIR double beam spectrometer. The thin molecular layers for UV-Vis analyses were deposited on quartz/Cr(3nm)/Au(13nm)/eC(7nm) as substrate instead of Si/SiO_x/PPF, since Si/SiO_x/PPF is not transparent. The reference beam was going through air and the absorption of the molecular layer was obtained by manual subtraction of the absorption of substrate from the absorption of substrate + molecular layer. The quartz/Cr_3/Au_{13}/eC_7/molecular layer(s) samples were also used for electrochemical analysis as these samples are made as blankets and have larger surface area than PPF lines used for device fabrication.

Electrochemical impedance spectroscopy (EIS) was carried out with GAMRY Instruments Reference 600 to obtain capacitance values. The measurements were done by applying a 50 mV AC voltage in the frequency range of 100 to 10^6 Hz at several positive and negative DC voltages.

A KP Technology Ltd series 6 Kelvin probe was utilized to obtain the surface potential values under illumination with NCL 150 (VOLPI MFG. USA CO. INC) light source.

Temperature experiments were performed in a Janis ST-500-1 cryogenic probe station cooled with liquid nitrogen or helium. The chamber was pumped down to pressures less than 10^{-4} torr before lowering the temperature and obtaining the J-V data. Electrical measurements of bilayer molecular junctions were carried out using a custom made LabVIEW based system[151] in voltage scanning four-wire mode at 1000 V/s under vacuum. Only some measurements at the beginning of the Chapter were carried out using Keithley 2602A in four-wire configuration or in air. All the voltages are PPF voltage relative to eC/Au top contact.

3.3 Results and discussion

The molecular bilayers were made by successive diazonium reduction of two different diazonium reagents. Initial layers of NAB, AQ, FL and BTB were prepared as described previously[31]. Reduction of the diazonium reagent for NDI has not been described previously, so NDI film formation is described in the next section, followed by the investigation of bilayers.

3.3.1 Characterization results

The electrochemical reduction peaks of NDI layer in 0.1 M $LiClO_4$ in ethanol are presented in Figure 3.6.

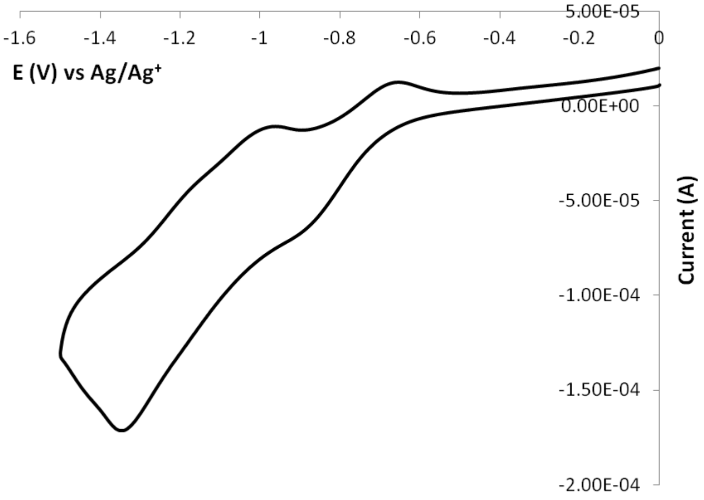

Figure 3.6: Cyclic voltammogram of NDI layer grafted on Cr(3nm)/Au(15nm)/eC(3nm) by diazonium reduction. CV carried out in 0.1 M solution of $LiClO_4$ in ethanol at 0.3 V/s.

NDI has two reduction peaks with the first reduction peak located at -0.9 V versus Ag/Ag^+ reference electrode and ~ -1 V versus Fc/Fc^+ redox couple. Therefore the LUMO level of NDI is located at -3.8 eV under the vacuum level assuming that the Ferrocene HOMO level is at -4.8 eV vs. vacuum. The second reduction peak is located at 3.35 eV, at -1.35 V versus Ag/Ag^+. The relevant transport orbital in the completed junction depends on the coupling of the transport orbitals together among molecules (delocalization) and coupling to both contacts. Based on the data extracted from photocurrent experiments done on thin NDI tunnel junctions[152], transport in NDI tunnel junctions are mediated by the LUMO level with barrier height of ~1.35 eV above PPF Fermi level (at ~ 4.8 eV).

Although characterization of 10-20 nm films on carbon surfaces is difficult with optical spectroscopy due to sensitivity constraints, absorption spectroscopy was carried out to characterize the bilayers. The simplest case is when the absorption peaks of two layers do not overlap which is the case in Figure 3.7 for AQ-BTB bilayer. The absorption spectra are shown after subtraction of the absorption of quartz/$Cr_3/Au_{15}/eC_3$ substrate[153].

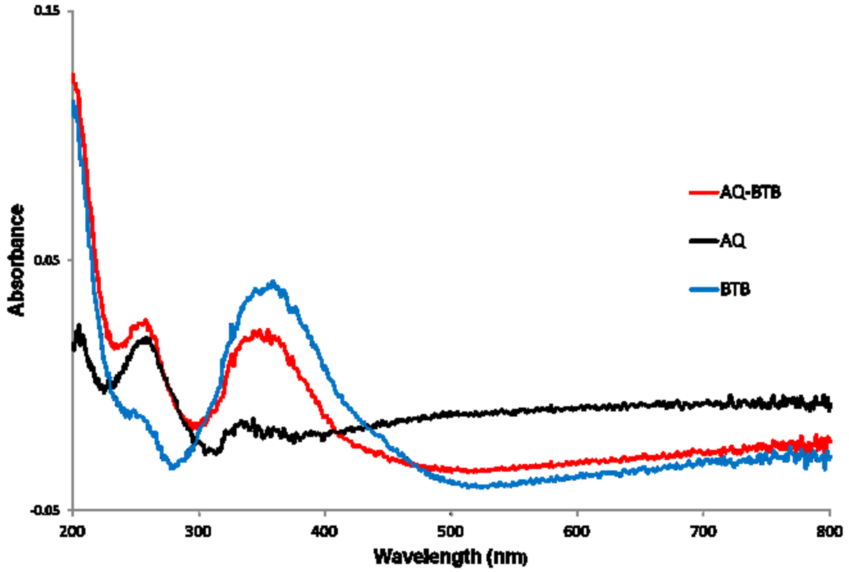

Figure 3.7: Absorption spectrum of AQ-BTB bilayer compared with AQ layer and BTB layer.

The main peak of AQ is at ~256 nm and the main peak of BTB is at ~355 nm. The bilayer has both peaks with almost the same absorbance as the component layers.

The absorption spectrum of NDI-BTB bilayer is harder to compare with its components due to the featureless NDI spectrum, as shown in Figure 3.8. The calculated NDI-BTB spectrum simply is the result of addition of NDI and BTB spectra together.

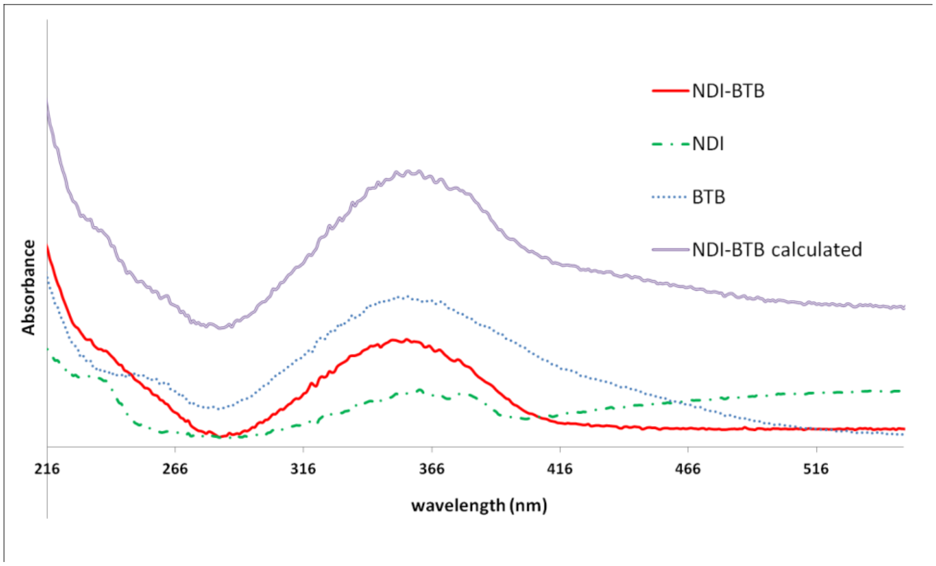

Figure 3.8: Absorption spectrum of NDI-BTB bilayer compared with NDI layer, BTB layer and NDI-BTB calculated or (NDI+BTB).

The NDI-BTB calculated spectrum and the measured NDI-BTB spectrum are parallel which means they have the same components consisting of NDI and BTB absorbing separately in this wavelength window. While the UV-Vis spectra show no indication that deposition of BTB layer on top of the NDI layer causes damage or desorption of the NDI layer, the evidence is not as strong as that for AQ and BTB in Figure 3.7

The presence of both layers in the final bilayer was also probed using XPS of both single and bilayers, as shown in Figure 3.9. The oxygen 1s signal for NDI and sulfur 2p doublet for BTB were observed in the NDI-BTB bilayer. The nitrogen signal was not used because the diazonium reduction process usually leaves behind some azo groups in the layers. The deposition of BTB on top of NDI decreases the oxygen 1s signal intensity (see part B of Figure 3.9) as expected to be the case for a buried layer using a mostly surface sensitive technique.

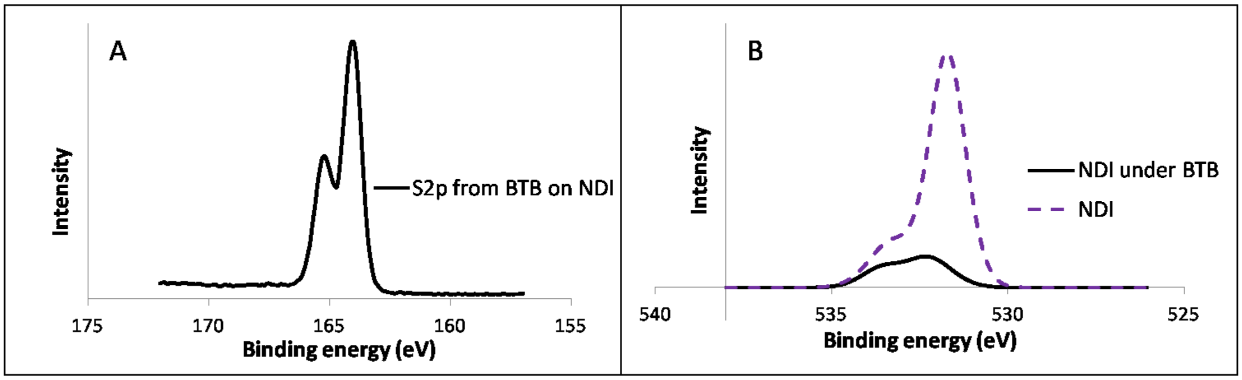

Figure 3.9: A- S2p signal from BTB in NDI-BTB bilayer. B- O1s signal from NDI layer compared with the signal from the NDI/BTB bilayer.

The peak at 532.5 eV is assigned as oxygen peaks in NDI[154] and the peak at 533.5 eV belongs to chemisorbed oxygen[155] or contamination from air[156], [157].

3.3.2 Electrical characteristics

Throughout this Chapter the A_x-B_y bilayer denotes a bilayer with A as the first or bottom layer which is immediately on top of PPF and B as second or top layer which is located on top of A and directly under the eC/Au top contact, as shown in Figure 3.10. The thicknesses in nm are shown as subscripts x and y. For all junctions, PPF was the bottom contact and eC(10nm)/Au(20 nm) was the top contact. All the voltages reported are PPF voltage relative to top contact.

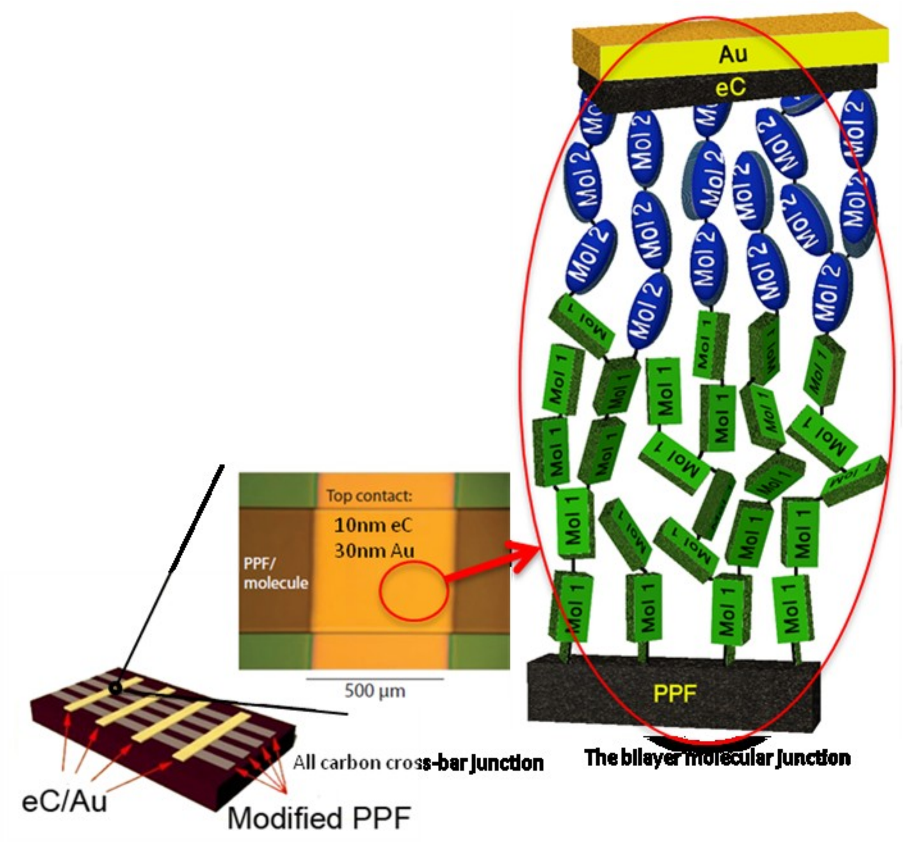

Figure 3.10: The structure of A-B bilayer molecular junction with units of molecule 1 (Mol 1) forming the layer A and units of molecule 2 (Mol 2) forming the layer B.

The electrical measurements were first carried out in air with various scan rates as shown in Figure 3.11 A. The junctions became more conducting during the reverse scan in air and the hysteresis was bigger at lower scan rates. The junctions were measured in the vacuum of less than 5×10^{-4} torr and the observed hysteresis went away (see Figure 3.11 part B). As discussed below, hysteresis is a sign of changes in the junction during scanning, and may indicate structural alterations due to the presence of water. To avoid this complication, all subsequent experiments were performed in vacuum. After junctions were completed by e-beam deposition, they were transferred into a vacuum probe station with minimal air exposure. The redox behavior of water at the interfaces and its ability to provide ions to reduce the injection barrier at the interface and stabilize the charges in the layer are possible reasons for the observation of the hysteresis and it is discussed later on in the Chapter.

All the measurements under vacuum were done initially at the scan rate of 1000V/s to avoid damaging the devices by applying high voltages for long time. The scan rate was then gradually decreased to get higher sensitivity in current and permit observation of low currents at lower voltages. The scan rate does not affect the device behavior under vacuum as shown in part B of Figure 3.11 but it does change the sensitivity of the measurements. The pronounced rectification apparent in 3.11 will be discussed in a later section, after considering the properties of a single component NDI film. All measurements were done at 1000V/s unless otherwise stated.

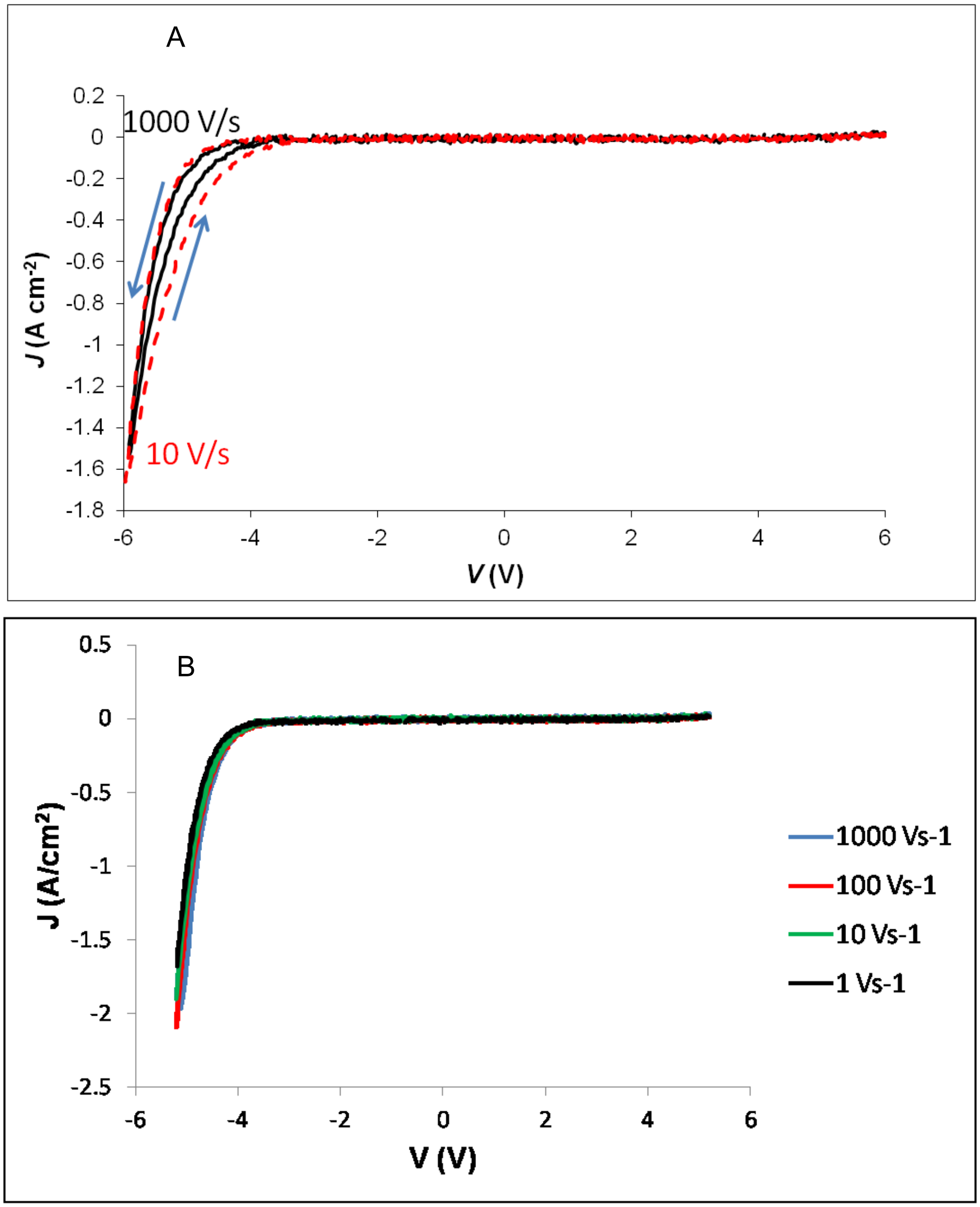

Figure 3.11: A- J-V curves for NDI-BTB bilayer junctions at different scan rates in air. B- J-V curves for NDI-BTB bilayer junctions at different scan rates in vacuum.

The J-V curves of NDI junctions with three NDI thicknesses are shown in Figure 3.12-A. Each NDI J-V curve is the average of 4 junctions with standard deviation in current shown with error bars. Figure 3.11B is an attenuation plot of lnJ vs. d at V=0.5 V compared to published results for BTB alone[47]. BTB and NDI junctions have similar behavior for thinner layers (d< 8 nm) consistent with the measured similar tunneling barrier heights of ~1.2 eV for BTB[31] and ~1.3 eV for NDI[152], but thick NDI junctions are less conducting than thick BTB junctions probably due to the bulky structure of the NDI molecule and weaker electronic coupling between the subunits compared with BTB.

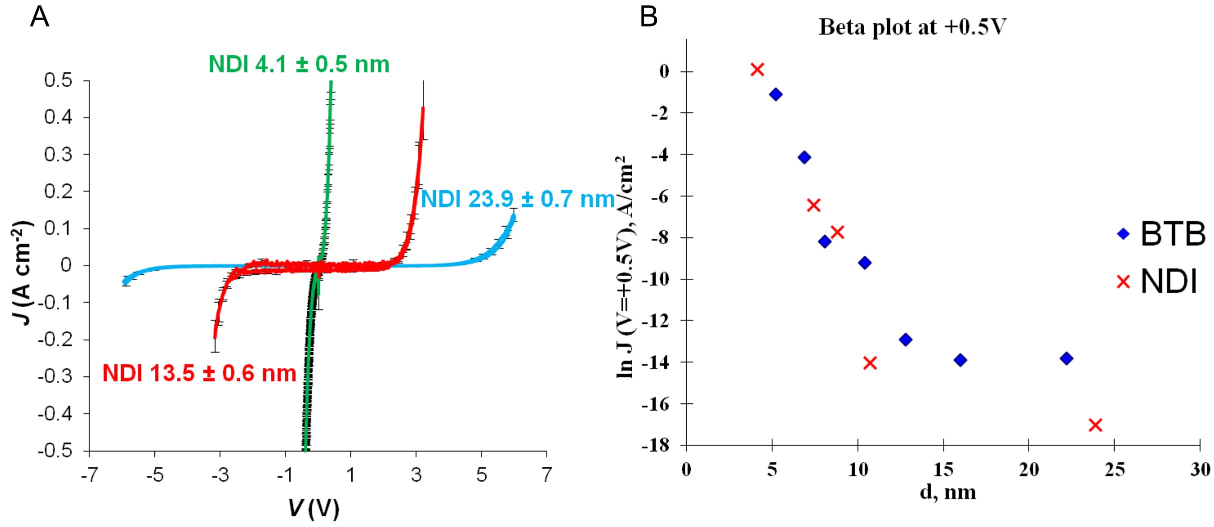

Figure 3.12: A- Average J-V curves for NDI only junctions with three different thicknesses. B- NDI beta plot at 0.5 V compared with BTB from ref([47]).

The similarity of the electrical behavior of thin NDI and BTB also results in symmetric J-V curves for thin bilayers as shown in Figure 3.13. This Figure shows the J-V curve for a 3.8 nm NDI layer and a bilayer made from the same thickness NDI layer with the total thickness of 10.3 nm. Both of these layers are symmetric and show no rectification.

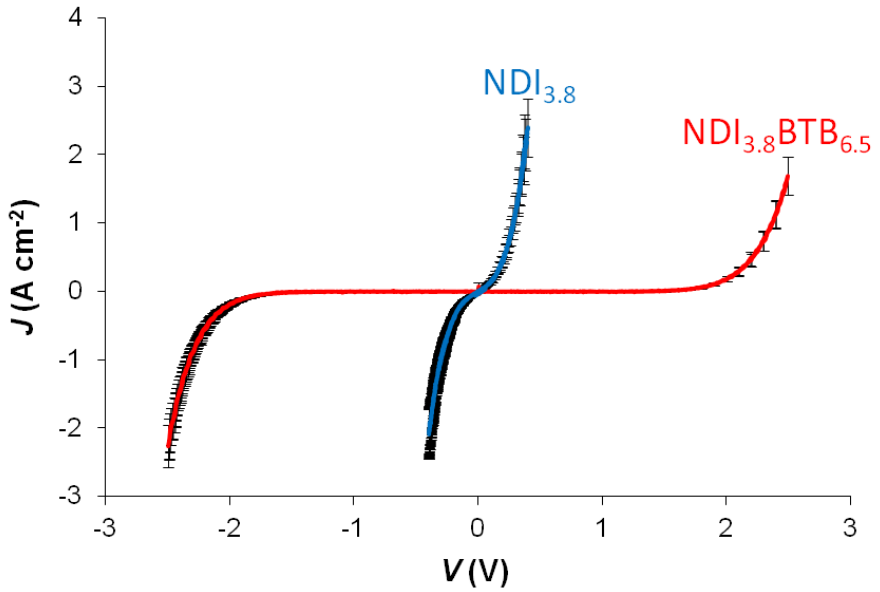

Figure 3.13: J-V curves for 3.8 nm NDI only junction and 10.3 nm NDI-BTB bilayer.

In fact all NDI only and BTB only junctions are symmetric across the bias range and the rectification ratio varies only between 0.5 and 2.

Rectification ratio (RR) is defined as $I_{at\ -V}/I_{at+V}$ or the ratio of the current at a certain negative voltage to the current at the same positive voltage. As discussed in Chapter 2 (for thin click bilayers), the rectifiers purely based on single step coherent tunneling from similar contacts are not expected to show big rectifications and the interactions with the contacts[31] also washes out the differences between different molecules. Therefore the thin bilayers dominated by single step tunneling and interaction with both contacts are not expected to show rectification. RR values for NDI, BTB and NDI-BTB bilayers with various thicknesses at the same negative current density (J=0.2 A/cm^2) are listed in table 3.2.

The effect of the increase in the thickness of BTB layer on top of a thin NDI layer with the thickness of 4.1 nm is shown in Figure 3.14-A.

The junctions with 4.1 nm of NDI and 6.6 nm of BTB are symmetric but the junctions with 9.2 nm of BTB are asymmetric. The rectification ratio at the highest voltage (3V) for NDI$_{4.1}$BTB$_{9.2}$ of Figure 3.14A is 7. The junctions on the same device (NDI$_{4.1}$BTB$_{9.2}$) are compared to another device with similar thickness of BTB of 9nm but thicker NDI layer of 13.5 nm on the right side of Figure 3.14. It is clear that increasing the thickness of NDI improves the rectification ratio. The RR value of these thicker junctions at 5V is 50.

Table 3.2: Rectification ratios for NDI, BTB and NDI-BTB molecular junctions (MJs).

	first layer thickness	second layer thickness	total thickness	*V* for |*J*|=0.2 A/cm^2	*J* (-*V*)	*J* (+*V*)	*RR* (±V)
	nm	nm	nm				
NDI	13.5	0	13.5	-3.2	-0.195	0.391	0.50
NDI	10.7	0	10.7	-2.96	-0.208	0.484	0.43
NDI	4.1	0	4.1	-0.27	-0.204	0.188	1.09
NDI	23.9	0	23.9	6	-0.064	0.182	0.35
BTB	10.4	0	10.4	-1.47	-0.202	0.157	1.29
BTB	22	0	22.2	-3.63	-0.210	0.483	0.43
NDI/BTB	13.5	2	15.7	-3.59	-0.212	0.264	0.80
NDI/BTB	13.5	6	19.7	-3.92	-0.203	0.008	25.0
NDI/BTB	3.8	6.5	10.3	-1.97	-0.212	0.199	1.06
NDI/BTB	4.1	9.2	13.3	-2.58	-0.199	0.061	3.27
NDI/BTB	13.5	9	22.5	-4.53	-0.208	0.006	34.8
NDI/BTB	10.7	10.3	21	-3.92	-0.207	0.003	80

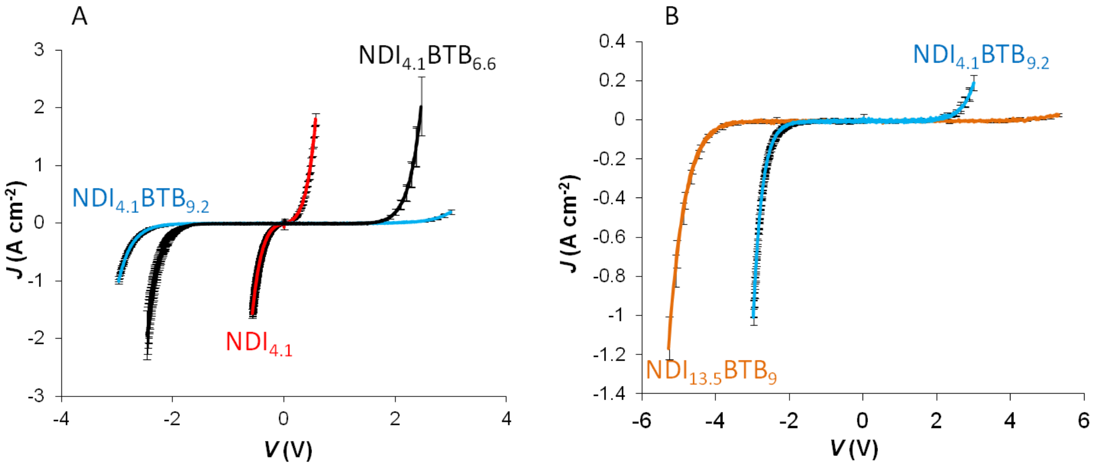

Figure 3.14: A- J-V curves for series of bilayers with increasing thickness of BTB, based on NDI 4.1 nm. B- J-V curves of junctions with similar thickness of BTB and different thicknesses of NDI. The $NDI_{4.1}BTB_{9.2}$ junctions are shown in both panels.

The J-V curves for a series of bilayers based on this 13.5 nm NDI and various thickness of BTB are shown in Figure 3.15-A. The junctions with only 2.2 nm BTB do not rectify but the junctions with 6.2 nm or 9 nm of BTB on $NDI_{13.5}$ are rectifiers. The inset of part B of Figure 3.15 shows the trend of RR with the thickness of BTB on $NDI_{13.5}$. The current at negative voltages starts to exceed the current at positive voltages when the thickness of BTB on $NDI_{13.5}$ exceeds 4 nm (see Figure 3.15-B).

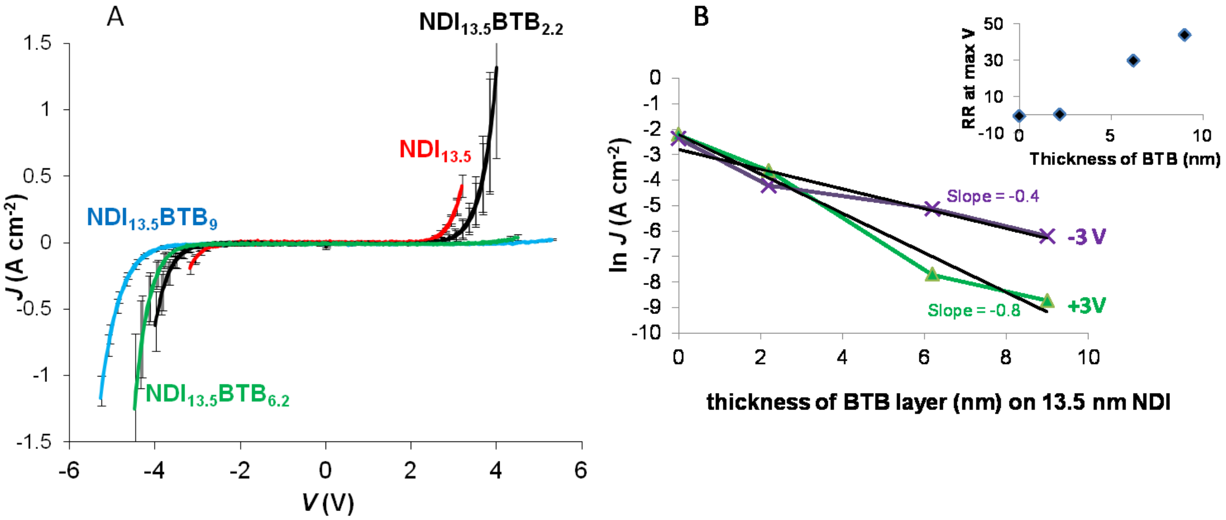

Figure 3.15: A- J-V curves for series of bilayers with increasing thickness of BTB, based on NDI 13.5 nm. B- Beta plot based on the thickness of BTB layer on top of 13.5 nm NDI at +3 and -3 volts. The inset is the plot of RR versus the thickness of BTB on $NDI_{13.5}$.

Based on Figure 3.15-B, the current at the negative voltage (forward direction) has lower attenuation than current at positive voltage (reverse direction). The negative voltage β value at room temperature is closer to hopping values (~0) while the positive voltage β value is closer to molecular ionization value (~1 nm^{-1})[47].

The general observation that the higher current flows when NDI side is negatively biased is consistent with AR rectifier and P-N junction theories. The electron donor property of BTB molecule compared with NDI is evident in UPS valence band studies in Figure 3.16.

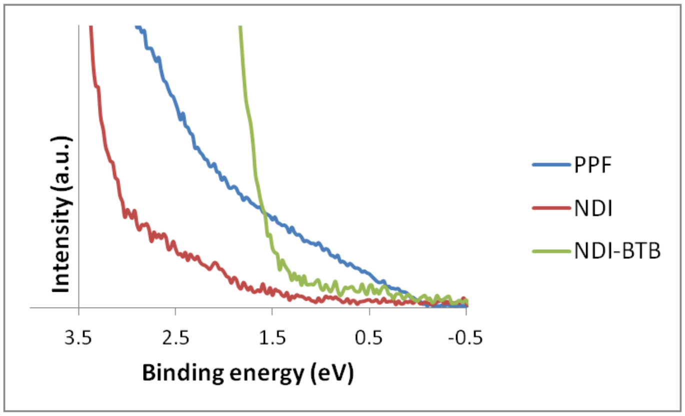

Figure 3.16: Valence band region in UPS spectra of PPF bottom contact compared with PPF/NDI and PPF/NDI-BTB. BTB HOMO onset is higher than NDI.

Based on the normalized UPS spectra shown in Figure 3.16, PPF electrode starts emitting electrons at the Fermi level (0 eV) and NDI layer does not emit electrons until ~ 2 eV under the Fermi level which is consistent with the onset of UV-Vis absorption of ~400 nm considering the LUMO energy level at 1 eV above the Fermi level from electrochemistry. The onset of BTB HOMO is more than 1 eV lower in energy even though BTB is deposited on top of the NDI layer.

To study whether both donor (BTB) and acceptor (NDI) layers are necessary for rectification, The NDI layers with various thicknesses were deposited on PPF by diazonium reduction and 1.5 nm aluminium was e-beam evaporated on top of the NDI layers at high PVD chamber pressure (>10^{-5} torr) to help oxidized the aluminum as it is deposited. After evaporation of Al layer, the chips were put in a vacuum oven over night at ambient pressure under the flow of oxygen gas. The eC/Au top contact was evaporated on the following day to obtain the NDI/AlO_x bilayers (see Figure 3.17).

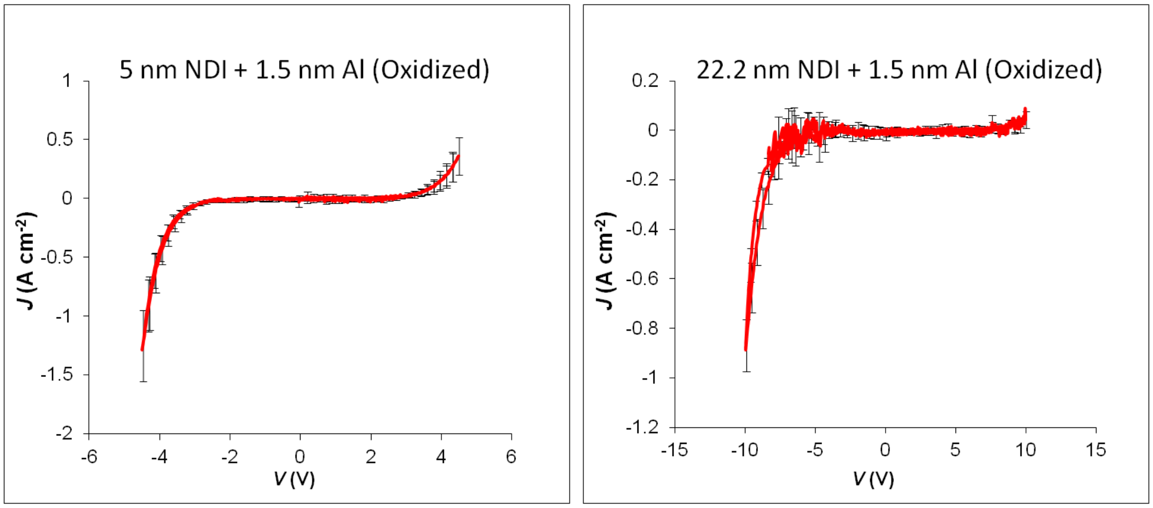

Figure 3.17: J-V behavior of NDI/AlO_x bilayers for different thicknesses of NDI.

The AlO_x layer formed by oxidation of aluminium is rough and adds to the standard deviation of the current but a general trend appears in the behavior of NDI/AlO_x bilayers. Based on the results shown in Figure 3.17, the rectification ratio increases by increasing the thickness of NDI layer using AlOx as neutral barrier(not donor or acceptor, just tunneling barrier). The highest RR for 13.3 and 22.2 nm of NDI is only ~10.

The result of the same experiment for 10.4 nm BTB layer is shown in Figure 3.18.

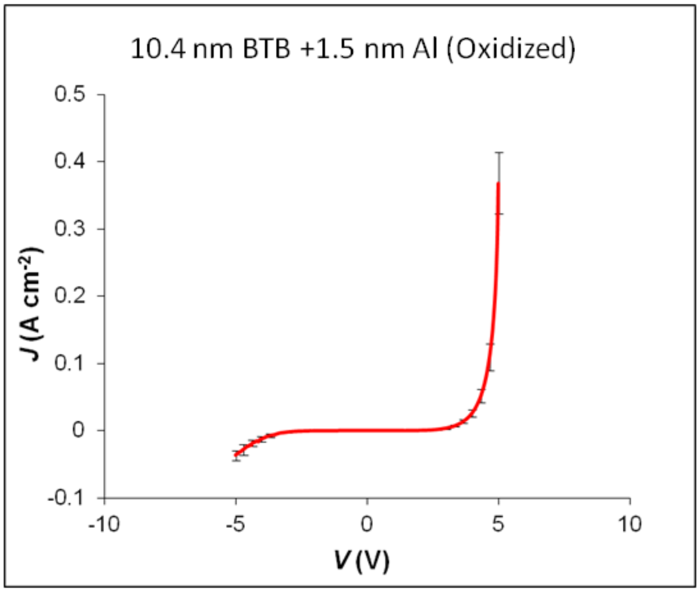

Figure 3.18: J-V behavior of PPF/$BTB_{10.4}$/AlO_x/eC/Au bilayer.

The $BTB_{10.4}$/AlO_x bilayers also exhibit RR value of only ~10. This signifies the importance of having both donor and acceptor molecules in the bilayer together to achieve high RR values. There are a number of reports in molecular electronics literature on molecular rectifiers based on asymmetric placement of a chromophore in molecular junctions[84], [87], [92], [148] but all these rectifiers use alkanes with low dielectric constant as spacer and not AlO_x (which acts mostly like a gate oxide). The significant drop of voltage across the alkane region is important to achieve rectification in alkane-chromophore bilayers. The direction of rectification of NDI-alkane bilayer would be the opposite direction of the observed direction for NDI-AlO_x bilayers.

Knowing the combination (n-type NDI- p type BTB) and thickness (NDI and BTB both ~ 10 nm thick) needed for high RR values from these experiments; 2 batches of a total of 28 NDI-BTB junctions on 4 chips were made on different days using the same conditions to investigate the reproducibility of the bilayer rectifiers electrical behavior. The yield of working (non short) junctions was 89% of 28 junctions. Figure 3.19 represents the overlay of average J-V curves of the 4 NDI-BTB chips made under the same conditions on different days.

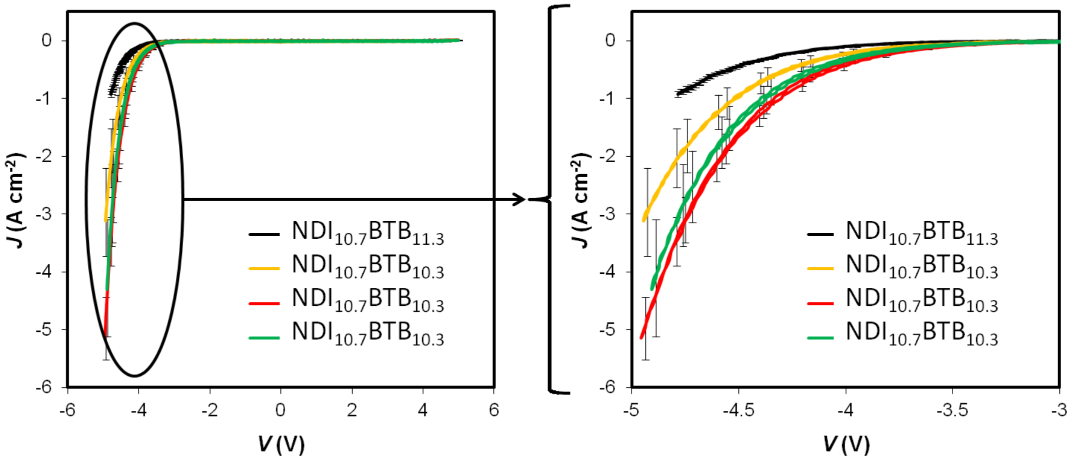

Figure 3.19: Overlay of average J-V curves of junctions on 4 NDI-BTB chips made using the same conditions in 2 batches. The Figure on the right is the expansion of -3 to -5 volts region of the left Figure.

The average J value of all working junctions shown in Figure 3.19 and listed in table 3.3 is -2.6 A/cm^2 at -4.8 V, and RSD of J is 36%. The average RR for all 25 working junctions at 4.8 V is 232 and RSD of RR is 37%.

Table 3.3: Rectification ratios for NDI-BTB junctions shown in Figure 3.19 at 4.8 V.

#	NDI (nm)	BTB (nm)	*J* (-*V*)	*J* (+*V*)	*RR* (±V)	#	NDI (nm)	BTB (nm)	*J* (-*V*)	*J* (+*V*)	*RR* (±V)
1	10.7	10.3	-1.67	0.008	205	14	10.7	10.3	-3.38	0.008	415
2	10.7	10.3	-2.59	0.013	196	15	10.7	10.3	-2.01	0.014	140
3	10.7	10.3	-2.57	0.011	233	16	10.7	10.3	-4.11	0.015	269
4	10.7	10.3	-2.05	0.016	126	17	10.7	10.3	-2.18	0.013	162
5	10.7	10.3	-1.62	0.018	88	18	10.7	10.3	-3.41	0.013	255
6	10.7	10.3	-2.63	0.015	175	19	10.7	10.3	-3.12	0.012	255
7	10.7	10.3	-2.47	0.012	203	20	10.7	10.3	-4.17	0.016	258
8	10.7	10.3	-3.03	0.008	372	21	10.7	10.3	-3.05	0.014	212
9	10.7	10.3	-1.90	0.013	150	22	10.7	10.3	-3.30	0.014	235
10	10.7	10.3	-3.43	0.013	263	23	10.7	11.3	-0.92	0.004	225
11	10.7	10.3	-3.45	0.010	331	24	10.7	11.3	-0.98	0.004	241
12	10.7	10.3	-3.26	0.012	282	25	10.7	11.3	-0.66	0.006	107
13	10.7	10.3	-3.19	0.008	392						

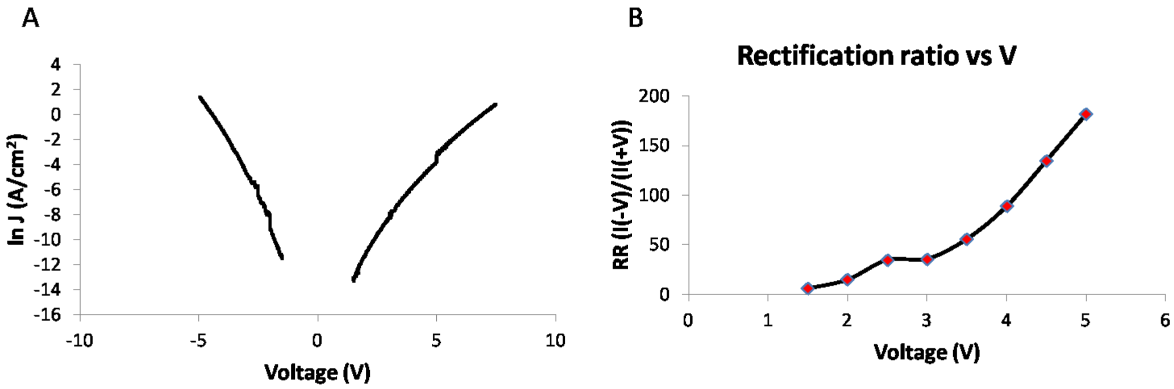

Figure 3.20: A- lnJ vs. V for a NDI$_{10.7}$BTB$_{10.3}$ junction and B- RR vs. V for the same junction shown in A.

Figure 3.20 above shows the lnJ versus voltage curve for a NDI-BTB junction along with the voltage dependence of the rectification ratio for these devices. lnJ is not linear with voltage and the rectification ratio is small at low voltages and becomes larger with voltage. In inorganic Schottky diodes, RR versus bias has a peak after which RR decreases.

To elucidate the mechanism of conduction in these bilayers, the temperature dependence of current and RR was studied, with the JV results shown in Figure 3.21.

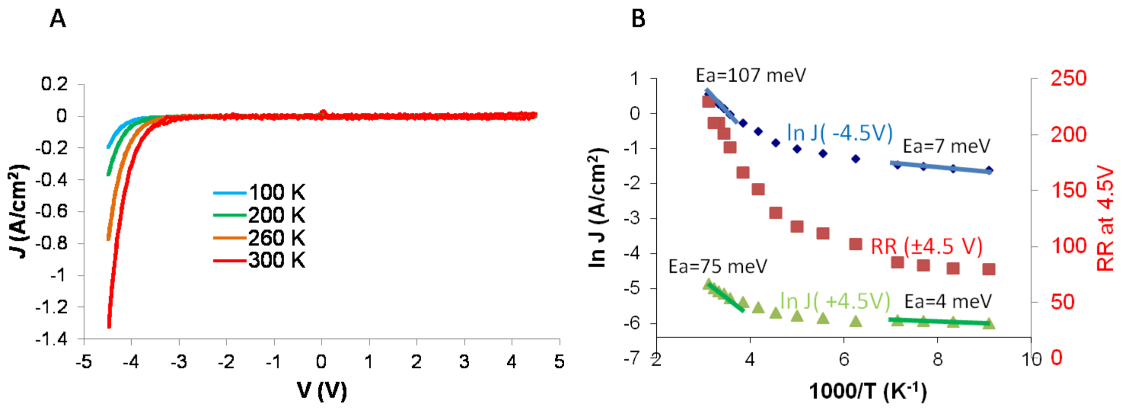

Figure 3.21: A- Temperature dependence of current density in NDI$_{10.7}$BTB$_{10.3}$ bilayer junction. B- Arrhenius plot at -4.5 V along with RR at 4.5 V vs. temperature for the same device in A.

For two NDI$_{10.7}$BTB$_{10.3}$ junctions tested from 320 K down to 100 K, the rectification ratio at 4.5 V went down from 230 to 80 for one junction and from 210 to 100 for the second junction. The Arrhenius plots at other voltages are shown in Figure 3.22.

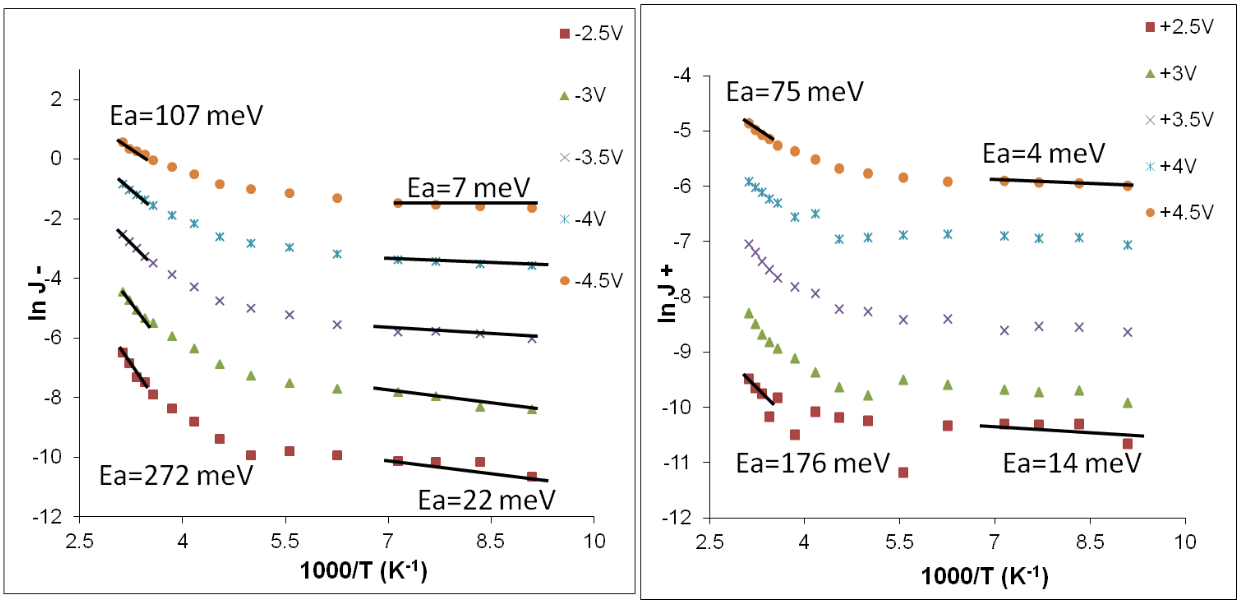

Figure 3.22: Arrhenius plots at negative (forward bias) and positive (reverse bias) voltages for NDI$_{10.7}$BTB$_{10.3}$ junction.

The activation energies from Arrhenius plots for different temperature ranges and various voltages for two NDI$_{10.7}$BTB$_{10.3}$ junctions and two NDI only junctions are summarized in table 3.4. The activation energies for NDI only junctions are all under 50 meV and are explainable by Fermi function broadening of the contacts.

The activation energies for NDI-BTB junctions decrease with temperature and reach small values at low temperatures and high voltages but do not become zero in the experimental range using liquid nitrogen.

Liquid helium was used to extend the range of temperatures to lower values and the result is shown in Figure 3.23.

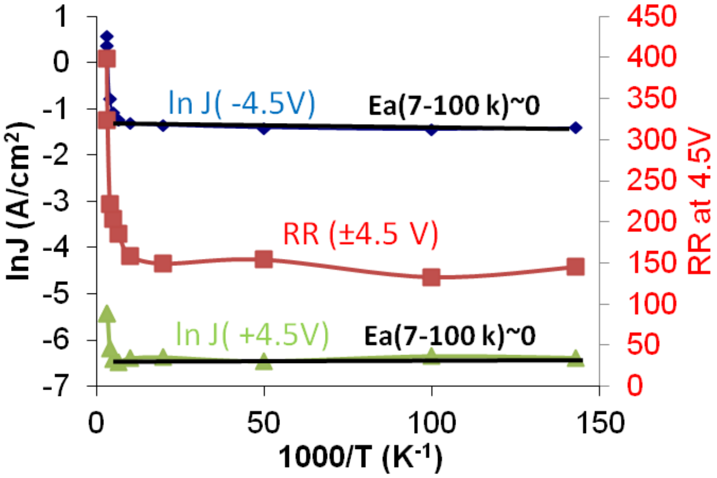

Figure 3.23: Arrhenius plot at -4.5 V for a NDI$_{10.7}$BTB$_{10.3}$ junction along with RR values using liquid hellium down to 7 K.

Table 3.4: Activation energies obtained from Arrhenius plots at different voltages and temperature ranges for two NDI$_{10.7}$BTB$_{10.3}$ and two NDI junctions.

NDI/BTB 21 ± 1 nm					
V (110-140K)	+2.5	+3	+3.5	+4	+4.5
Ea (meV)	14	9	1	6	4
V (110-140K)	-2.5	-3	-3.5	-4	-4.5
Ea (meV)	22	28	11	9	7
V (290-320K)	+2.5	+3	+3.5	+4	+4.5
Ea (meV)	176	141	123	79	75
V (290-320K)	-2.5	-3	-3.5	-4	-4.5
Ea (meV)	272	240	196	137	107
NDI/BTB 21 ± 1 nm					
V (110-140K)	+2.5	+3	+3.5	+4	+4.5
Ea (meV)	2	6	6	3	3
V (110-140K)	-2.5	-3	-3.5	-4	-4.5
Ea (meV)	11	16	20	11	8
V (290-320K)	+2.5	+3	+3.5	+4	+4.5
Ea (meV)	236	151	132	70	82
V (290-320K)	-2.5	-3	-3.5	-4	-4.5
Ea (meV)	253	221	169	143	103
NDI 8.8± 0.6 nm					
V (110-140K)	+1	+1.5	+2	+2.5	+3
Ea (meV)	3.5	1	0.1	0.3	
V (280-320K)	+1	+1.5	+2	+2.5	+3
Ea (meV)	10.2	5.4	38.3	19.5	
NDI 10.7± 0.7 nm					
V (110-140K)	+1	+1.5	+2	+2.5	+3
Ea (meV)			6.5	2	1.8
V (280-320K)	+1	+1.5	+2	+2.5	+3
Ea (meV)			44.3	56	41.6

The RR value at 4.5 V for the NDI$_{10.7}$BTB$_{10.3}$ junction studied using liquid helium cooling, went down from 398 at 320 K to 145 at 100 K and RR=145 was nearly constant down to 7 K. The activation energy at temperatures lower than 100 K became almost zero and RR and current are independent of temperature at temperatures lower than ~110 K. The values of activation energy for $NDI_{10.7}BTB_{10.3}$ junctions around room temperature are over 200 meV at low voltages which suggests an activated conduction process but the activation energy decreases at higher voltages to ~100 meV. The activation energies at low temperature range are also much smaller than room temperature. The activation energies at negative voltages (forward current) are higher than positive voltages (reverse current). The result of higher activation energy at forward current is that RR at room temperature is on average ~2 times higher than RR at 7-100 K. Activated rectification and higher activation energy at forward bias has been observed in donor-acceptor multilayer rectifiers[158] and have been attributed to hopping conduction in the forward bias but tunneling at the reverse bias, however their RR decreases from ~30 at room temperature for a 6nm bilayer at 1 V to 1 at 260 K. RR in $NDI_{10.7}BTB_{10.3}$ junctions is ~ 210 at 4 V for 21 nm junctions (almost the same electric field) at room temperature and does not go down to 1 even at 7 K.

The observation of temperature independent conduction within certain range of temperatures (7-110K) is usually taken as the evidence for trap assisted or multistep tunneling[159]. At higher temperatures thermally assisted ionization of the traps is also added to the multistep tunneling process. Figure 3.24 depicts the linearity of lnJ with $V^{1/2}$. This linearity has been observed in molecular p-n junction multilayers[160] and was attributed to bulk conduction in multilayers. However, in $NDI_{10.7}BTB_{10.3}$ junctions this linearity also holds true at low temperatures of ~100K, where hopping is unexpected (see appendix Figure A12) and is consistent with the multistep tunneling model discussed in Chapter 4[161] as the dominant mechanism along with increasing ionization of the molecular levels at higher temperatures[47]. The possible involvement of traps can also be deduced from Figure 3.25. The rectification ratio is almost constant for the first 10000 voltage cycles at room temperature but goes down to ~19 after 50000 voltage cycles. The RR value almost fully recovers and comes back from 19 to ~ 220 during 3 weeks.

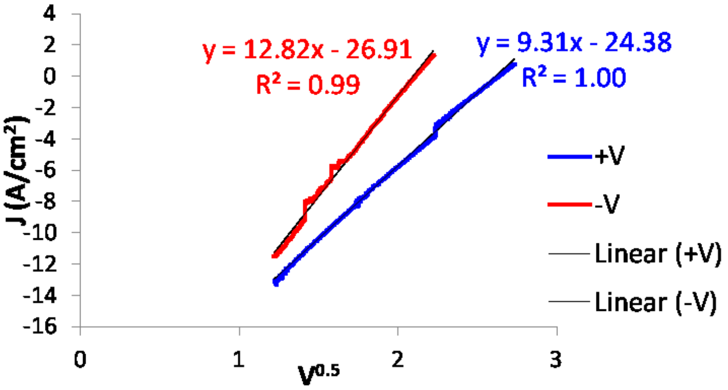

Figure 3.24: Linearity of lnJ with square root of voltage at positive and negative voltages for $NDI_{10.7}BTB_{10.3}$ junction at room temperature.

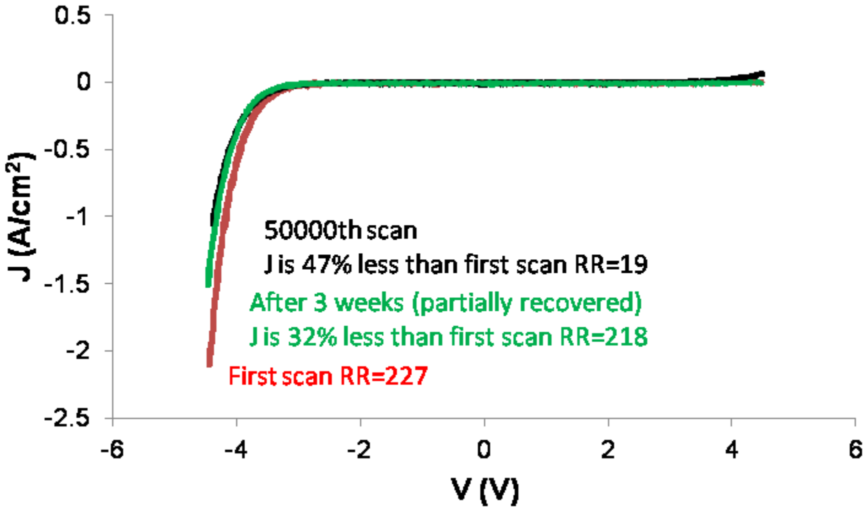

Figure 3.25: Stability of $NDI_{10.7}BTB_{10.3}$ junction during 50000 scans at 1000V/s in vacuum and recovery of the device.

The decrease in current at forwards bias and increase in current at reverse bias after many cycles is consistent with temperature dependence of rectification at room temperature and ionization of deep traps. After many cycles some of the traps may keep the charge and do not release it. This is especially true in ambient conditions in the presence of moisture or polar solvents. It was found for perylene diimide molecular junctions that the temperature dependence of conductance is more pronounced in polar medium[162] due to reorganization of the polar solvent. The moisture from air can also create ions at the electrodes that can stabilize ionized molecular orbitals inside the bilayer. It is for these reasons that all measurements for bilayers were performed under vacuum. However even under vacuum especially at low scan rates (giving enough time for activated ionization process), some of NDI molecules may become negatively charged and some of BTB molecules positively charged under forward bias. The accumulation of these space charges inside the bilayer can decrease the forward current by inhibiting injection and increase the reverse current by enhancing injection in the reverse voltage which leads to a decrease in rectification ratio. Given enough time, the space charges will recombine and the RR recovers.

Currently the rectification of these bilayer rectifiers at high scan rates is obscured by large charging current due to size of the junctions as is shown in Figure 3.26. These bilayer junctions have large area of 0.00125cm^2 that leads to significant capacitance at lower voltages and higher scan rates.

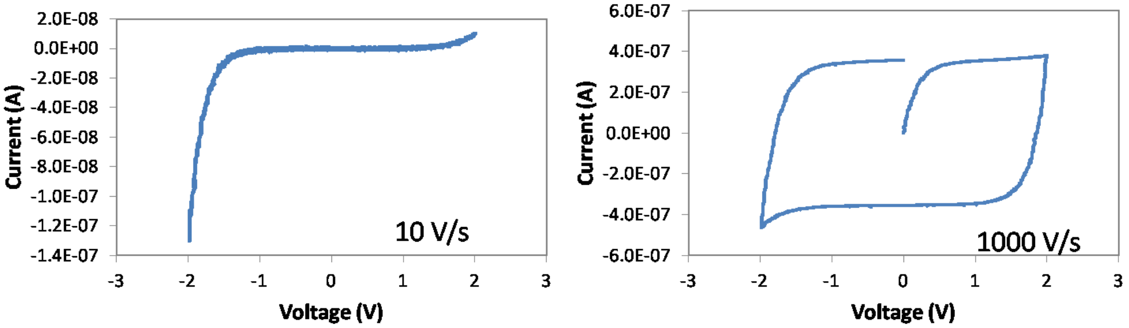

Figure 3.26: Limitation in observation of rectification at high scan rates in a $NDI_{10.7}BTB_{10.3}$ bilayer junction due to capacitive current.

The capacitance and dielectric constant of $NDI_{10.7}BTB_{10.3}$ junctions were measured by electrochemical impedance spectroscopy and the results are shown in Figure 3.27. The capacitance depends on frequency (f) according to $C(f) = \frac{-1}{2\pi f Z''(f)}$, in which Z"(f) is the frequency dependent imaginary part of the impedance[163]. Based on the value of capacitance (4×10^{-10} F) at high frequencies from 3.27-A, the dielectric constant of the $NDI_{10.7}BTB_{10.3}$ junction with 0.00125 cm^2 surface area is 7.5. This number is a good estimate for a conjugated organic layer[164] and attests the quality of the film. It also shows that NDI^--BTB^+ charged species are not likely to spontaneously form at the NDI-BTB interface upon formation of the NDI-BTB bilayer as these charged complexes are expected to show higher dielectric constants. The capacitance at -2 volts is almost constant across the frequency range based on the plot in 3.27-A. The phase plot in 3.27-B shows that at -2V the phase of the current vs. voltage is 90 degrees (perfect capacitor) at high frequencies and starts to decrease (become more resistor like) at lower frequencies.

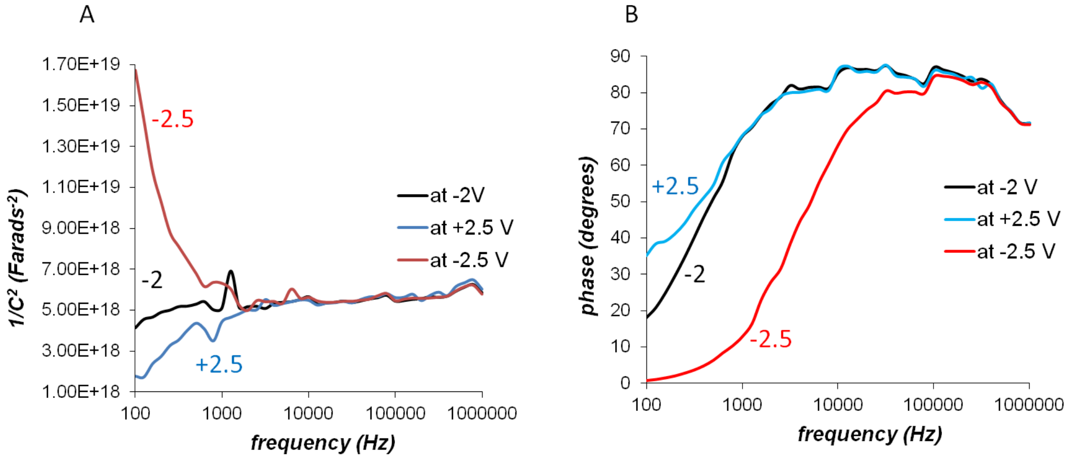

Figure 3.27: A-Plot of 1/square of capacitance vs. frequency for a NDI$_{10.7}$BTB$_{10.3}$ bilayer at various DC voltages at room temperature. B- Phase shift BODE plot for the same junction in A.

At lower frequencies, the capacitive current becomes small compared to resistive current even at -2 volts (low forward bias) and the phase value decreases (in Figure 3.27-B). The capacitance at +2.5 volts increases at low frequencies based on 3.27-A and has the least decrease in capacitive component at low frequencies based on 3.27-B. This is equivalent to a p-n junction diode under reverse bias. In inorganic p-n junctions, the depletion region becomes wider at reverse bias and capacitance decreases unlike NDI-BTB at positive voltage. This is because NDI-BTB bilayer does not have an already charged interface between NDI and BTB or a depletion region. In NDI-BTB bilayer, a partial electron transfer from BTB to NDI under reverse bias, probably increases the polarizability of the bilayer at reverse bias [131] and leads to higher capacitance values at reverse bias. The bilayer is a total resistor (phase=0) at low frequencies at -2.5 volts and have the smallest capacitance as it is expected for a rectifier in forward bias when current easily flows instead of storing the electric field and partial electron transfer from NDI to BTB is not possible.

3.3.3 Orbital control of electronic behavior

A series of bilayer junctions based on NDI as the first layer and various molecular layers as second layer were fabricated to study the effect of molecular energy levels on rectification ratio. The HOMO and LUMO energy levels of all these molecules from DFT calculations using B3LYP functionals and 6-31G(d) basis set are listed in table 3.3. These HOMO and LUMO energy levels are calculated for gas phase free molecules in the optimized structure. The energy level values for the molecules in the junctions are different due to interaction with contacts, interaction with other molecules and steric hindrance, but the values in table 3.5 can still serve as a guide.

Table 3.5: DFT calculated energy levels of molecules used in this work.

Molecule	HOMO (eV)	LUMO(eV)
AQ	-6.999	-2.765
NDI	-6.919	-3.352
NAB	-6.655	-3.032
BTB	-4.994	-1.925
FL	-5.754	-0.714

The overlay of J-V curves for $NDI_{10.7}AQ_{11.9}$, $NDI_{10.7}NAB_{11.4}$, $NDI_{10.7}BTB_{10.3}$ and $NDI_{10.7}FL_{13}$ is shown in Figure 3.28. Each J-V curve is the average of four junctions. The error bars are omitted for clarity but the RSD in current density does not exceed 40% in any bilayer. According to Figure 3.28, the bilayers with AQ or FL are less conducting than the bilayers with similar thickness of NAB or BTB. This is consistent with higher band gap (HOMO-LUMO gap from table 3.3) for FL and AQ molecules.

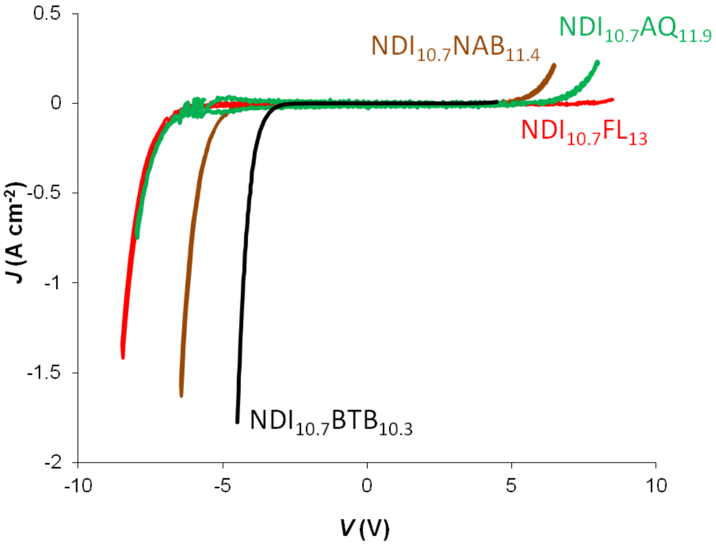

Figure 3.28: Overlay of J-V plots for a series of bilayers based on $NDI_{10.7}$ with similar total thicknesses.

From Figure 3.28 It is also clear that NDI-AQ bilayer is not a good rectifier compared to NDI-FL or NDI-BTB.

The simple model represented in Figure 3.29 is suggested to explain the observed trend in rectification. In this model the rectification ratio is dictated by energy barriers of the donor-acceptor bilayer depicted in Figure 3.29. A_{LUMO}-Fermi indicates the barrier between the LUMO of the electron acceptor (e.g. NDI or AQ) molecule and the Fermi level of the contact and D_{HOMO}-Fermi indicates the barrier between the HOMO of the electron donor molecule (e.g. BTB or FL) and the Fermi level of the contacts.

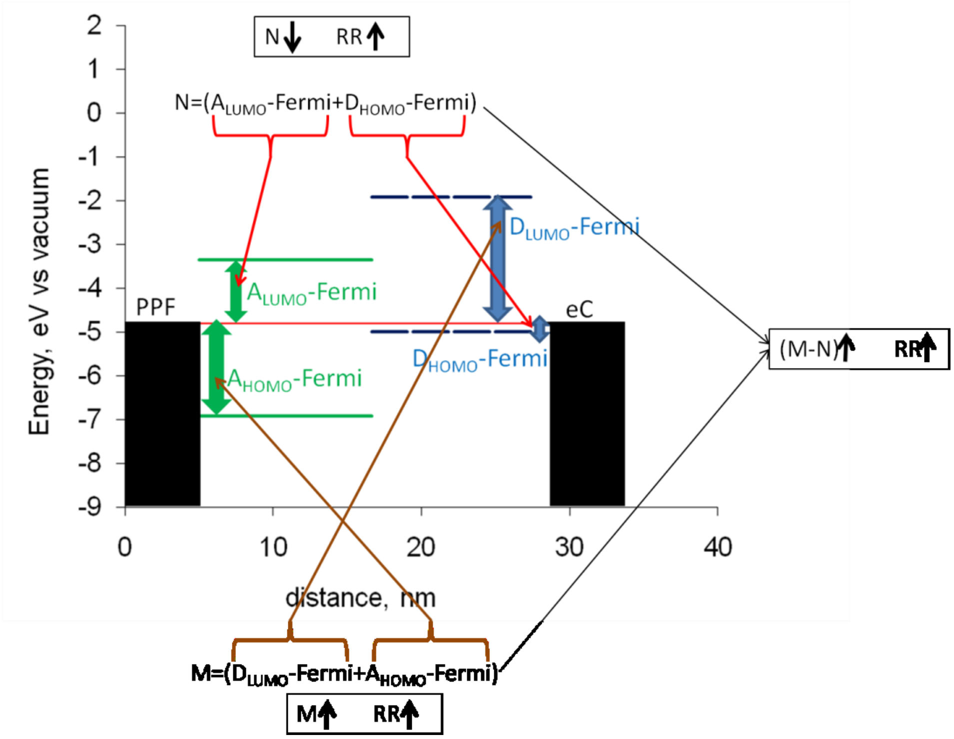

Figure 3.29: Important energy barriers in donor-acceptor bilayers to explain the trend in rectification. A stands for acceptor and D for donor.

When A_{LUMO}-Fermi and D_{HOMO}-Fermi are smaller, we expect the forward current to be bigger and RR to be bigger. When A_{LUMO}-Fermi is smaller, electron transport is favored when the PPF is biased negative, and larger current would occur for negative bias. Similarly, if D_{HOMO}-Fermi is small, electron transport from D_{HOMO} into eC is efficient, also resulting in higher current at negative bias on PPF. Therefore the sum of A_{LUMO}-Fermi and D_{HOMO}-Fermi is named as parameter N. RR would be bigger for smaller values of N.

A_{HOMO}-Fermi stands for the barrier height between acceptor HOMO and Fermi level. This is what inhibits hole injection into the acceptor layer in reverse bias therefore a bigger A_{HOMO}-Fermi value increases RR by inhibiting current flow in reverse bias. Similarly D_{LUMO}-Fermi stands for the barrier between Fermi level and the LUMO of the donor which inhibits electron injection into donor layer in the reverse bias. A larger D_{LUMO}-Fermi value also increases RR by inhibiting current under reverse bias. The sum of A_{HOMO}-Fermi and D_{LUMO}-Fermi is denoted by parameter M. RR increases for bigger M values. Because we expect RR to increase with the value of M and decrease with the value of N, there should be a correlation between RR and the value of (M-N). The values of rectification ratio at the same negative current density of J=-0.2 A/cm^2 along with the values of M, N and M-N for these bilayers are tabulated in table 3.6.

Table 3.6: RR values for series of bilayers with similar thicknesses based on $NDI_{10.7}$. The RR values are reported at the same negative current density of -0.2 A/cm^2.
M= (A_{HOMO}-Fermi + D_{LUMO}-Fermi) and N= (A_{LUMO}-Fermi + D_{HOMO}-Fermi)

Bilayer	Total thickness (nm)	RR at J=-0.2	M (eV)	N (eV)	M-N
NDI-AQ	22.6	2	4.16	3.65	0.51
NDI-NAB	22.1	5	3.89	3.31	0.58
NDI-BTB	21	80	5	1.64	3.36
NDI-FL	23.7	167	6.21	2.4	3.81

The rectification ratio is larger for bilayers with larger (M-N) values based on the data presented in table 3.6. The Fermi level is considered at 4.8 eV.

To evaluate this model, the bilayers based on $AQ_{8.4}$ were studied. Based on the energy levels of AQ molecule in table 3.5, the molecule is an electron acceptor compared with molecules like BTB or FL. AQ molecule also has better LUMO coupling to the contact based on previous calculations[165]. The overlay of $AQ_{8.4}FL_{12.3}$ and $AQ_{8.4}BTB_{11.6}$ average J-V curves is shown in Figure 3.30.

The RR values at J=-0.2 A/cm^2 and (M-N) values for these bilayers are presented in table 3.7. A similar trend again exists between RR and (M-N).

However the correlation of RR with (M-N) based on this simple model breaks down when comparing bilayers with no shared component (like AQ-FL and NDI-BTB) or bilayers with significant thickness difference ($AQ_{8.4}FL_{12.3}$ and $NDI_{10.7}FL_{13}$). There is however a correlation between [(A_{HOMO}-D_{HOMO}) + (D_{LUMO}-Fermi)] and RR among these pairs.

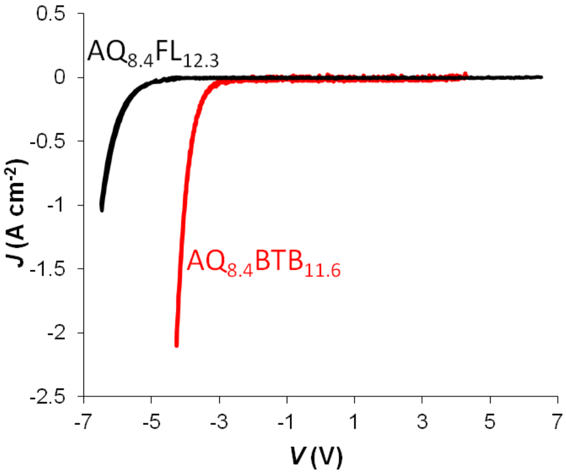

Figure 3.30: Overlay of J-V plots for bilayers based on $AQ_{8.4}$ with similar total thicknesses.

Table 3.7: RR values for series of bilayers with similar thicknesses based on $AQ_{8.4}$.

Bilayer	Total thickness (nm)	RR at J=-0.2	M (eV)	N (eV)	M-N
AQ-BTB	20	66	5.08	2.23	2.85
AQ-FL	20.7	437	6.29	2.99	3.3

To rule out the contact effects on the behavior of bilayer rectifiers, the $AQ_{8.4}$ based bilayers were fabricated along with the bilayers with reversed order. The J-V curves of these pairs are shown in Figure 3.31. The direction of rectification of PPF/AQ/FL/eC/Au and PPF/AQ/BTB/eC/Au which have the general PPF/acceptor/donor/eC/Au composition is the opposite of the direction of rectification of PPF/FL/AQ/eC/Au and PPF/BTB/AQ/eC/Au with the general composition of PPF/donor/acceptor/eC/Au.

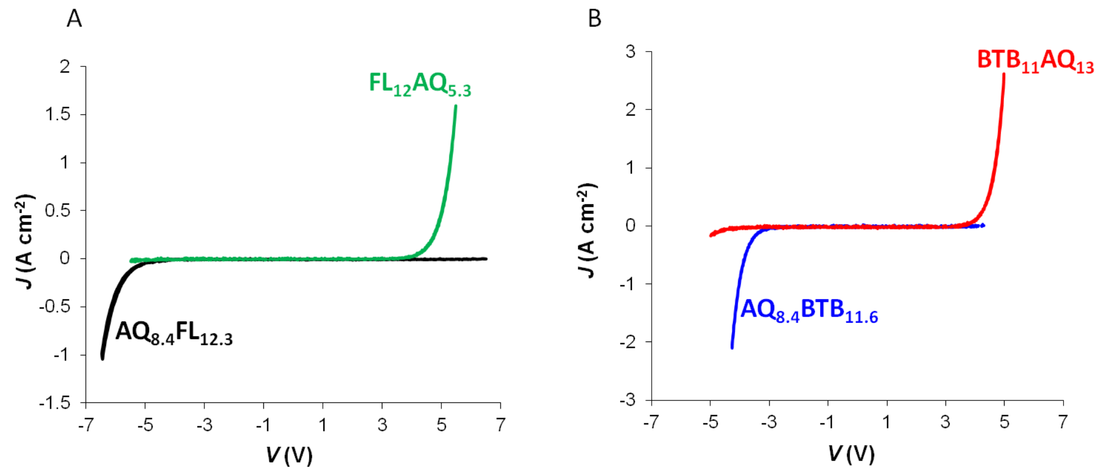

Figure 3.31: A- Overlay of AQ-FL and FL-AQ average J-V curves. B- Overlay of AQ-BTB and BTB-AQ average J-V curves.

The reversal of the direction of rectification with reversal of the order of layers, serves as a clear evidence for the effect of molecular layer (not the contact) on the rectification behavior, and that rectification consistently depends on the relative positions of donor and acceptor layers.

The rectification ratio of all bilayer combinations at the maximum voltage studied are summarized in table 3.8.

Table 3.8: Average current density and rectification ratio at designated voltages for all bilayer rectifiers studied along with the yield of working (non-short) junctions.

Contact 1	layer1	layer2	Contact2	Average RR	At V	RSD in RR (%)	Average J (A/cm^2)	At V	RSD in J (%)	Yield (%)
PPF	NDI	BTB	eC/Au	224	4.8	39.5	-2.6	-4.8	36.2	89
PPF	NDI	NAB	eC/Au	8	6.5	28	-1.6	-6.5	16	100
PPF	NDI	AQ	eC/Au	2.5	8	21	-0.8	-8	14	100
PPF	NDI	FL	eC/Au	124	8.5	103	-1.5	-8.5	9	100
PPF	AQ	FL	eC/Au	286	6.5	4.8	-1.5	-6.5	18	100
PPF	AQ	BTB	eC/Au	95	4.3	13	-2.2	-4.5	12.5	100
PPF	BTB	AQ	eC/Au	21	5	32	+2	+5	24	100
PPF	FL	AQ	eC/Au	73	5.5	38	+1.7	+5.5	49	75

The rectification ratio of PPF/donor-acceptor/eC/Au bilayers is not as large as PPF/acceptor-donor/eC/Au bilayers. This is presumably due to more extensive coupling between PPF and donor molecules owing to conjugated structure of donor molecules (FL and BTB) compared with cross-conjugated structure of acceptor molecules (AQ and NDI). This conjugation can lead to formation of hybrid states at the interface and change the dominant transport orbital[166] for some distance (<7 nm) from the surface. As a consequence of this coupling and washout of the molecular energy levels by PPF contact, the RR value of PPF/donor-acceptor/eC/Au bilayers are expected to be similar to thinner PPF/acceptor-donor/eC/Au bilayers.

The suggested general mechanism of current flow in donor-acceptor bilayer rectifiers is illustrated in Figure 3.32 using NDI-BTB as model bilayer. Similar to NDI-BTB bilayers, all other bilayers studied follow the linearity of lnJ with $V^{1/2}$ (see Figure A13 in appendix) so we can propose a similar mechanism for all bilayers. Part A of Figure 3.32 is a schematic representation of energy level alignment in the NDI-BTB bilayer device. Conduction when the PPF is biased negative happens by electron transport from contact to the acceptor, hole transport from contact to donor, hole transport from donor to acceptor and recombination of electrons in acceptor and holes in donor as depicted in 3.32-B. The conduction in reverse bias happens only through one channel which is electron transport from HOMO of donor to LUMO of acceptor followed by hole transport from HOMO of donor to contact as shown in 3.32-C. The LUMO of donor and HOMO of acceptor are energetically inaccessible for efficient transport in reverse bias.

At low temperatures the dominant transport mechanism is multistep tunneling but at higher temperatures the thermally assisted poole-frenkel like ionization also starts to happen and current becomes temperature dependent. Due to closeness of the LUMO of NDI to Fermi level compared to LUMO of BTB to Fermi level, the ionization of BTB HOMOs to NDI LUMOs at reverse bias (when PPF is biased positive) has a smaller barrier than ionization of BTB HOMOs to BTB LUMOs (or BTB conduction band) in forward bias. This is probably the reason that the forward current has higher temperature dependency than reverse bias current.

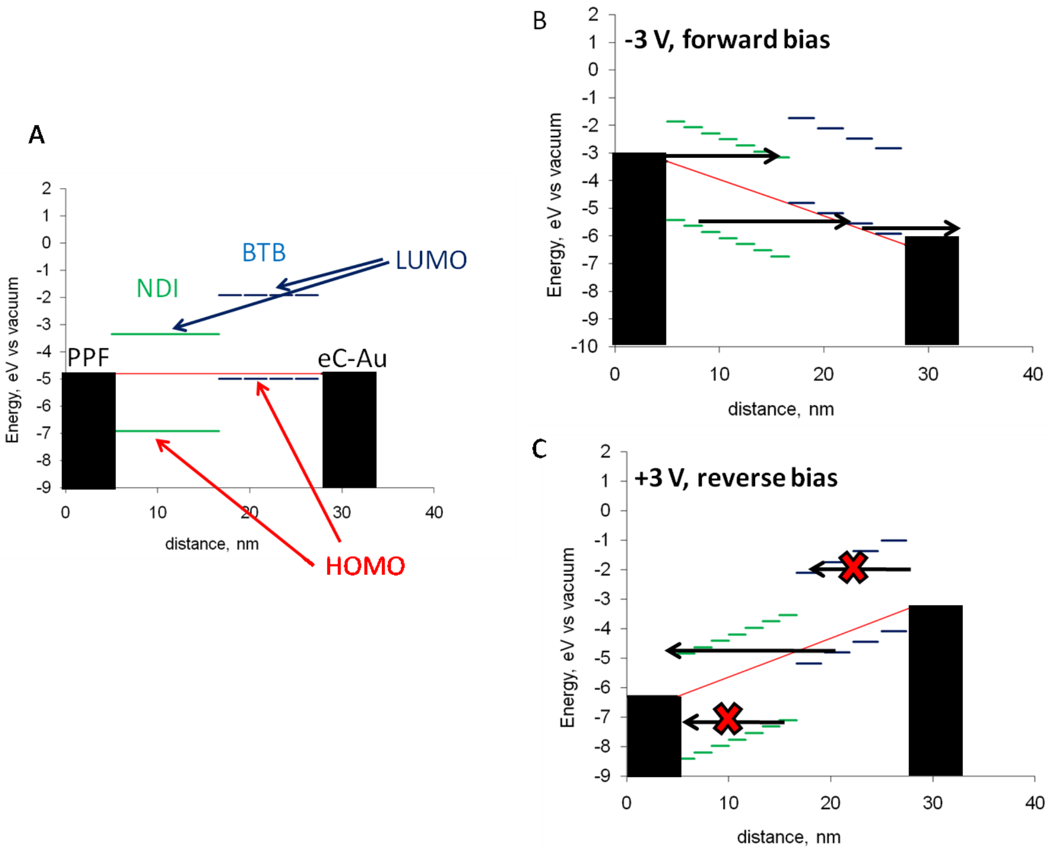

Figure 3.32: A- Energy levels in NDI-BTB bilayer. B- Conduction paths in forward bias. C- Conduction paths in reverse bias. The black arrows in B and C represent the direction of the movement of electrons.

3.3.3.1 p-n multilayer molecular junctions

The bilayers discussed in this Chapter can be considered molecular analogous to p-n junctions based on the discussion so far. But to clearly demonstrate that one layer is mainly electron conducting (n-type) and the other layer mainly hole conducting (p-type), the carriers should be probed in the layers. Photoeffects are possibility for studying organic/organic interfaces. One possible way is to study the spectral dependence of photocurrent in p-i-n molecular multilayers. The p-type and n-type molecules have non overlapping absorption regions and “I” is a non-absorbing layer that is thin enough to allow efficient tunneling of the photo-generated carriers. Depending on the energy levels of the layer i, electron or hole tunneling across it would be more efficient. Therefore the efficiency of the photocurrent generation when p-type molecule absorbs and electrons tunnel to n-type region through the layer i would be different than when n-type molecule absorbs and holes tunnel to p-type region through the layer i [167]. Another possible way is to measure the change in the surface potential of the bilayer due to creation and accumulation of photo-generated carriers at the surface under illumination[168].

To measure the surface potential under illumination, quartz/PPF/AQ, quartz/PPF/FL, quartz/PPF/AQ/FL and quartz/PPF/FL/AQ samples where made without the top contact, using the same conditions used for making the bilayer junctions.

Kelvin probe measurements on these samples were done in dark and under the illumination of NCL 150 light source with the intensity of ~12 mW at 200 nm and 7 mW at 248 nm at the sample location measured with Newport power meter model 1936-R.

The Kelvin probe tip oscillates close to the surface of the sample. The PPF substrate is electrically attached to the metallic substrate underneath the sample that is connected electrically to the Kelvin probe tip. Therefore a capacitor is formed between the surface of the sample and the Kelvin probe tip and the charges on the Kelvin probe tip depend on the opposite charges on the sample surface.

Figure 3.33 demonstrates the changes in the surface potential of the bilayers due to illumination. Y axis of Figure 3.33 is the difference between the work function of the Kelvin probe tip and the sample surface and the X axis is time.

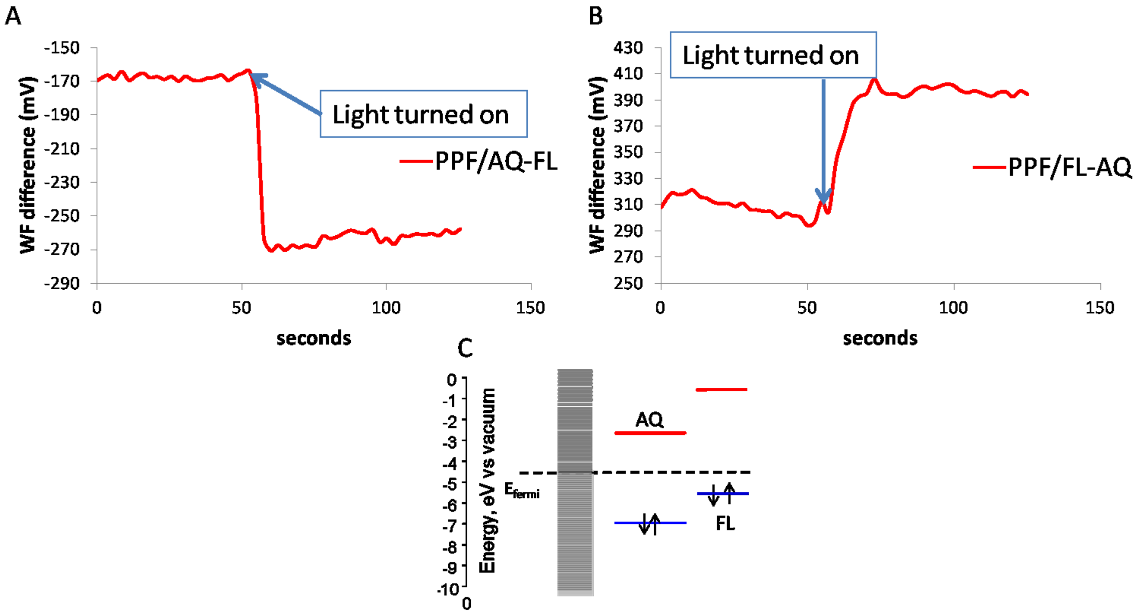

Figure 3.33: Changes in the Kelvin probe tip potential under illumination for A- AQ/FL and B- FL/AQ samples. C- Schematic of energy levels of AQ/FL bilayer.

Figure 3.33-A illustrates the situation when FL is at the surface of the sample. The photo-generated holes accumulate at the FL surface because FL is a donor molecule (p-type). The presence of positive charges on the sample surface induces a

negative charge on the Kelvin probe tip which is demonstrated by ~100 mV negative shift in the potential of the Kelvin probe tip at the moment that shutter is removed at around 50 seconds after the start of the measurements (see 3.33-A). The same amount of shift is observed when AQ is at the surface but at the opposite direction because AQ accumulates electrons and is n-type (see 3.33-B).

The changes observed for PPF/AQ and PPF/FL layers are smaller and only around 20 mV as is shown in Figure 3.34.

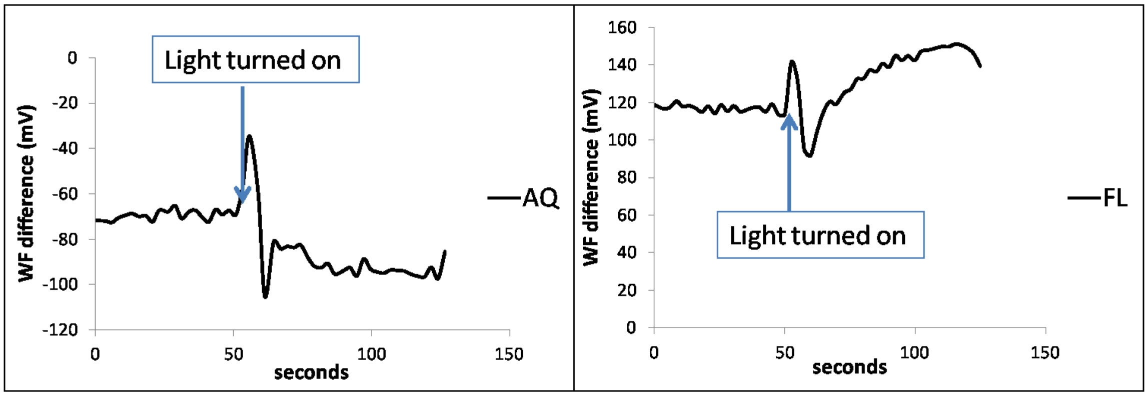

Figure 3.34: Changes in the Kelvin probe tip potential under illumination for PPF/AQ and PPF/FL samples.

The clear preferential accumulation of electrons in AQ and holes in FL is consistent with the model for rectification discussed in the previous section.

3.4 Conclusion

It was shown that under specific circumstances, the asymmetry in the composition of the thick molecular junctions leads to asymmetry in J-V behavior and observation of rectification. Thick molecular junctions (~20 nm) were made via reduction of diazonium salts using carbon as both contacts. These bilayers show rectification if one layer is donor and another layer acceptor. The rectification persists to liquid helium temperature pointing to multistep tunneling as conduction mechanism in these devices. The direction of rectification can be changed by changing the order of putting the layers on PPF surface. The p-n junction nature of the bilayers manifests itself in the change in surface potential under illumination. It is concluded from the study of charge transport in multilayer bilayers that by judicious choice of both the composition of the layers according to their molecular orbital energy levels and thicknesses, high rectification ratios can be achieved.

Chapter 4

Charge Transport in Oligo(phenylthiophene) Molecular Junctions, Beyond Tunneling

4.1 Introduction

The transport phenomena observed in previous Chapter for both EB only and (EB+Click) bilayers did not show any deviation from the tunneling behavior already reported for a wide range of other molecules within the same thickness range (<~6nm). The goal of this Chapter is to use a series of phenylthiophene derivative molecules that can be grown electrochemically up to thickness of around 10 nm and compare the charge transport behavior of the layers less than ~6nm to the thicker layers and also look for possible correlations between the energy levels of the constituent molecules and the transport properties of the resultant oligophenylthiophene layers. The single step tunneling process is expected to be increasingly inefficient for thicker layers and as the thickness of the organic layer increases, some general discussion on charge transport in organic materials is necessary to establish context.

The general form of the bulk limited current in organic electronics is $J=qn\mu E$. In this Equation, q is the unit charge, n is the concentration of carriers, E is the electric field and μ is mobility (in cm^2/Vs). The dependency of mobility on charge diffusion constant (D in cm^2/s) is described by Einstein-Smoluchowski Equation: $\mu=\frac{eD}{k_BT}$[54]. The main focus of the field of organic electronics is on studying mobility and its complicated dependence on variables such as temperature, electric field and the density of charge carriers under the influence of various factors such as crystallinity or disorder, doping or purity and interaction with interfaces. Some crystalline organic layers have been shown to demonstrate a decrease in mobility with increasing temperature (more scattering at higher temperatures similar to metals) and decrease in mobility with increasing electric field[54]. However the vast majority of organic semiconductors have various degrees of disorder and in general follow hopping transport mechanisms such as redox exchange and variable range hopping, as described below.

The mechanisms of charge transport in disordered organic semiconductors are briefly reviewed in the following section, followed by the experimental methods and results.

4.1.1 Charge transport in disordered organic materials

The basic understanding of hopping processes in organic semiconductors is possible by considering the Schrodinger Equation in a one dimensional chain of sites:

$$E\Psi_i=E_i\Psi_i+t_i\Psi_{i+1}+t_{i-1}\Psi_{i-1} \tag{4.1}$$

Each site (or trap) consists of one molecule or a conjugated segment of a polymer. The site energy level is E_i and t_i is the hopping matrix element or transfer integral between ith and (i+1)th sites (t or electronic coupling, see hopping in Chapter 1 for an estimation method). The Equation (4.1) is rewritten in matrix formalism as:

$$\begin{bmatrix} \Psi_{i+1} \\ \Psi_i \end{bmatrix} = M_i \begin{bmatrix} \Psi_i \\ \Psi_{i-1} \end{bmatrix} \tag{4.2}$$

Where

$$M_i = \begin{bmatrix} \frac{E-E_i}{t_i} & -\frac{t_i-1}{t_i} \\ 1 & 0 \end{bmatrix} \tag{4.3}$$

is the transfer matrix[169].

The various types of electronic disorder are named based on their effect on the transfer matrix. The diagonal disorder affects site energies and stems from distribution of conjugation lengths or dihedral angles and electrostatic effects that give rise to a distribution in HOMO and LUMO energies. Off diagonal disorder is due to variation in orientations of the molecules and distances between the sites that leads to fluctuation in the strength of interaction between the sites and variation of electronic coupling between the sites in the organic layer.

The description above only considers the electronic interactions between the sites and static disorders. The vibronic interactions should also be taken into account. These include the effect of molecular vibrations on the energy levels of the sites and the transfer integrals. These phonon (quantized vibration)-electron interactions make the transport parameters time-dependent and therefore introduce dynamic disorder[54]. The interactions between the sites in most organic materials are weak van der Waals interactions and the effect of polarization of the matrix by the charge on a given site can sometimes exceed the interaction energy between the neighboring sites. This can result in the deformation of the matrix and formation of a polaron (see Figure 4.1). The polaron therefore is a quasiparticle consisting of a positive or negative charge along with its surrounding polarization due to strong electron-phonon interactions. The polaronic segment of the polymer adopts a more planar structure to increase the delocalization of the charge and therefore has a narrower HOMO-LUMO gap. The polaron can then hop along the organic backbone[170]. The activation energy for this hopping process (called polaron binding energy) is estimated as half of Marcus's reorganization energy ($E_b=\lambda/2$). To account for the static disorder, an exponential or Gaussian shape is usually assumed for the density of states.

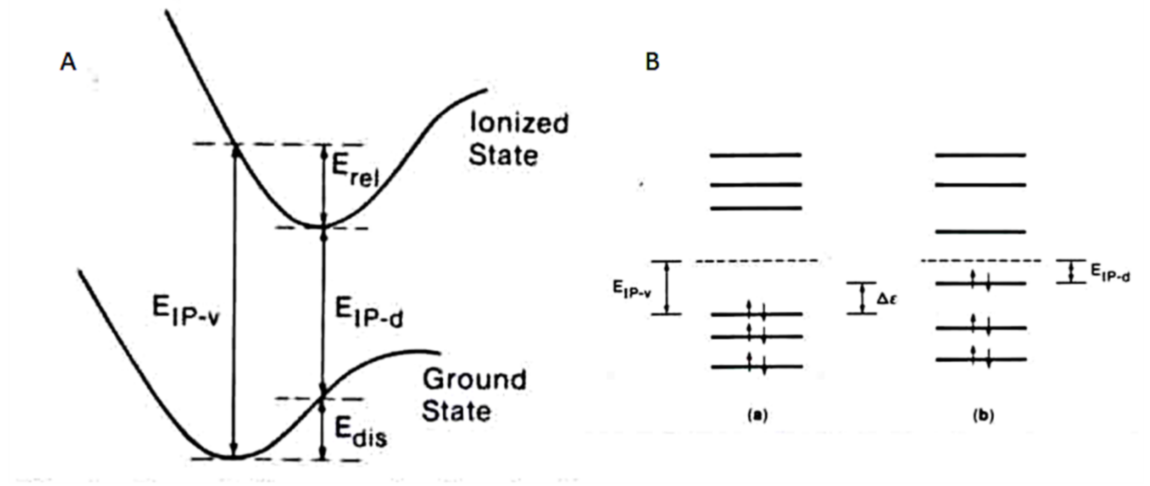

Figure 4.1: A- The illustration of the energies involved in Frank-Condon like, molecular ionization process. $E_{IP\text{-}v}$ is the vertical ionization energy from the ground state. E_{rel} is the relaxation energy gained in the ionized state. E_{dis} is the distortion energy needed for the ground state to adopt the equilibrium geometry of the ionized state. $E_{IP\text{-}d}$ is the vertical ionization energy of the distorted molecule. B- Energy levels of an organic molecule in its ground state electronic configuration (a) with equilibrium geometry of the ground state and (b) with the equilibrium geometry of the ionized state. $E_{IP\text{-}v}$ is the ionization energy to the Fermi level in the ground state geometry and $E_{IP\text{-}d}$ is the ionization energy to the Fermi level in the first ionized state geometry. $\Delta\epsilon = E_{IP\text{-}v} - E_{IP\text{-}d}$. Figure adapted with permission from [170].

The Gaussian DOS, g(ϵ) is given by:

$$g(\epsilon)=\frac{1}{\sqrt{2\Pi\sigma^2}}\exp\left(-\frac{\epsilon^2}{2\sigma^2}\right) \tag{4.4}$$

in which σ is the standard deviation of the distribution or the width of the diagonal disorder which is typically around 0.1 eV and ϵ is the energy level relative to the DOS center. The Gaussian density of states is an assumption based on the shape of the absorption bands in organic materials and there are some concerns about its validity for thinner layers where an electron experiences only a few energy levels along the short thickness of the layer and not the full Gaussian density of states of the whole width of the layer and the most conducting pathways are the most relevant in this case[50]. The zero electric field limit mobility based on numerical calculations (Gaussian DOS) is given by:

$$\mu(T)= \mu_o \exp\left[\left(-\frac{2\sigma}{3k_BT}\right)^2\right]= \mu_o \exp\left[\left(-\frac{T_o}{T}\right)^2\right] \tag{4.5}$$

This is while the general experimentally observed mobility[171] in disordered organic materials follows:

$$\mu= \mu_o \exp\left(\gamma\sqrt{E}\right) \tag{4.6}$$

Where E is electric field and γ is temperature dependent and usually has the form:

$$\gamma=\mathrm{B}\left[\frac{1}{\mathrm{k_B T}}-\frac{1}{\mathrm{k_B T_o}}\right] \tag{4.7}$$

in which B is a constant and T_o is a characteristic temperature usually well above room temperature. In some materials, T_o is below room temperature and γ becomes negative at temperatures above T_o. This means that by increasing the electric field, the mobility decreases for temperatures above T_o. At lower fields the carriers go through the least disordered current pathway and have higher mobility but by increasing the electric field, the carriers are forced to go through highly disordered pathways which decreases the mobility. This effect is only observed at higher temperatures when deep traps (highly disordered sites) become active and can exert their effect.

The mobility is occasionally found to be dependent on the density of the injected carriers from the contacts[172]. Organic materials usually have about the same hole and electron mobilities and whether an organic material is hole or electron conducting is controlled by the injection process. If the HOMO is closer to Fermi level of the contact the material is hole conducting because holes are primarily injected into the layer and if LUMO is closer to Fermi level of the contact, electrons are injected into the LUMO. In some disordered organic materials, an increase in mobility with increasing carrier density has been observed in SCLC regime. It is suggested that at low carrier densities, all carriers are affected by disorder and traps but at high carrier densities, some of the traps are filled by other carriers and the remaining carriers can move more freely[173].

To account for the empirical Poole-Frenkel form of the observed mobility, Monte Carlo simulations have been performed with the inclusion of time dependent off diagonal (position) disorder[174]. The restoring force for thermal fluctuations in the position of molecules is steric which leads to correlation between localized energy levels close to each other. A field dependence usually is observed in a system if the potential drop in eV=eEL across the length L of the system is larger than K_BT (if eV> K_BT). With uncorrelated energy levels, the corresponding length scale is the inter-site distance but correlation extends L to the correlation length. When L is bigger, the system can exhibit field dependence even for smaller E (field) values[175]. The result of simulations as a function of both electric field and temperature is:

$$\begin{cases} \mu=\mu_o \exp\left[\left(-\frac{2}{3}\tilde{\sigma}\right)^2\right]\exp\left[C(\tilde{\sigma}^2-\Sigma^2)E^{1/2}\right] \text{ for } \Sigma>1.5 \\ \mu=\mu_o \exp\left[\left(-\frac{2}{3}\tilde{\sigma}\right)^2\right]\exp\left[C(\tilde{\sigma}^2-2.25)E^{1/2}\right] \text{ for } \Sigma<1.5 \end{cases} \tag{4.8}$$

In which $\tilde{\sigma} = \sigma/kT$,C is a constant and Σ is the standard deviation of off-diagonal disorder. Further calculations have been performed considering correlated energy levels instead of randomly distributed ones for simulation of disorder. The correlations are the result of the interactions between the charge and permanent and induced dipoles in the neighboring sites. These simulations extended the Poole-Frenkel behavior to low fields[176]. In organic electronics, the notion of transport energy is used to refer to the energy level within DOS that is active in charge transport[177]. Most hops happen around transport energy and this energy level is assumed to be close to the Fermi level. However it should be noted that although hopping theories neglect the presence of a band and consider the current to be the result of charge hopping between localized states, the idea of band transport is still applicable to organic materials, even necessary. A band in inorganic semiconductors is the result of covalent bonds between the atoms. The same idea is still applicable in organic materials especially for the covalently bonded chains. The distinction with inorganic semiconductors is that the band itself can have an exponential or Gaussian shape instead of the sharply defined bands of crystalline inorganic materials. As the extent of disorder increases, the edge of the band moves further away from the Fermi level and if the Fermi level is located in the band, the material has metallic properties. The fact that current slowly dies out under constant DC voltage in organic semiconductors is hard to rationalize based on hopping theories. However according to band theory, the charge is injected into the delocalized band and slowly some charges become trapped in the localized states where they can’t easily move and so current decreases with time until the system reaches a thermal equilibrium between the mobile and trapped charges[57].

Multiple trapping and release model (MTR) and percolation theory based on variable range hopping (refer to Chapter 1) have also been employed for modeling the experimental results in organic electronics. The effect of the high applied electric fields has been included in percolation theory by carrier heating effect. The carrier heating refers to the widening of the charge distribution under the effect of an electric field which resembles a higher effective temperature[178]. This is not Joule heating and refers to the ability of charges to get further away from the Fermi level under applied electric field. Actual heating of the matrix happens in devices like LEDs that work based on recombination effects.

MTR model describes the organic semiconductor as ordered crystalline regions of the polymer connected together by a web of disordered and twisted chains of the polymer. The conduction inside the ordered regions follows band theory and can even be metallic[179] but the total conductivity depends on the weakest conducting connections which are the tangled chains of the polymer in between the ordered segments that act as traps. The total conductivity therefore is described as trapping of the charge in the disordered regions followed by their thermal release into the ordered region and trapping in another trap and so on. This model follows the Arrhenius temperature dependence except when the traps are only located at small regions like grain boundaries between the ordered segments which makes tunneling possible across the disordered region and results in temperature independent behavior[180]. There is a possibility for resonance tunneling between two ordered or metallic segments across the one disordered chain among many connecting them that have energy levels in resonance with the metallic grains. If the metallic segments are small and have quantized energy levels, the coulomb blockade effects are a possibility at low temperatures and low fields.

In general the total mobility of an organic material is modeled[181] as the sum of two contributions from tunneling and hopping ($\mu = \mu_{tun} + \mu_{hop}$). Tunneling is the main process at low temperatures while hopping is dominant at higher temperatures. For systems with strong electron-phonon coupling, the mobility is expected to be dominated by coherent tunneling at low temperatures and decrease with increasing temperature, but at higher temperatures hopping is the dominant mechanism and mobility increases with increasing temperature. For systems with weak electron-phonon coupling, the mobility is expected to be controlled by tunneling and decrease with increasing temperature in the entire temperature range. In this case the mobility is band like and the movement of the charge is coherent and in a wavelike manner but scattering (by phonons) of the carriers in the band from one momentum state to another changes the wavelike nature to a diffusive process[54].

The processes mentioned so far in this Chapter are bulk limited conduction processes however when the interface is more resistive than the bulk, the current becomes injection limited. The injection limited processes include thermionic emission and tunneling. The thermionic emission depends on the nature (work function) of the contact and is an activated process although there is a possibility of tunneling through a Schottky barrier that leads to temperature independent behavior at low temperatures[182]. Injection limited current by both Schottky emission[183] and tunneling[184] have been observed in organic materials. The Schottky injection limited current is insensitive to the thickness of the organic layer. $J_{\text{Thermionic}}$ (at constant E) is independent of d and the voltage needed to achieve a certain current is linearly proportional to thickness of the organic layer ($V \propto d$) in an injection limited device controlled by thermionic emission. Modeling thermionic emission in organic materials is difficult because the electric field at the interface is not known[185]. Electric field for an ideal insulator depends only on voltage and the thickness of the layer and is constant throughout the insulator. However space charge due to charge injection modifies the field and usually the electric field is larger at the interface (injected charge at the interface induces image charge in the contact which effectively forms an electric double layer[186]). The tunneling current usually decreases exponentially with thickness but if the injection process is the only step where tunneling is involved and the less resistive bulk conduction is due to hopping, then the total current at a constant field would be independent of the thickness of the organic layer and temperature independent. Another form of injection limited current is due to injection of the charge from the interface states to the bulk as shown in Figure 4.2.

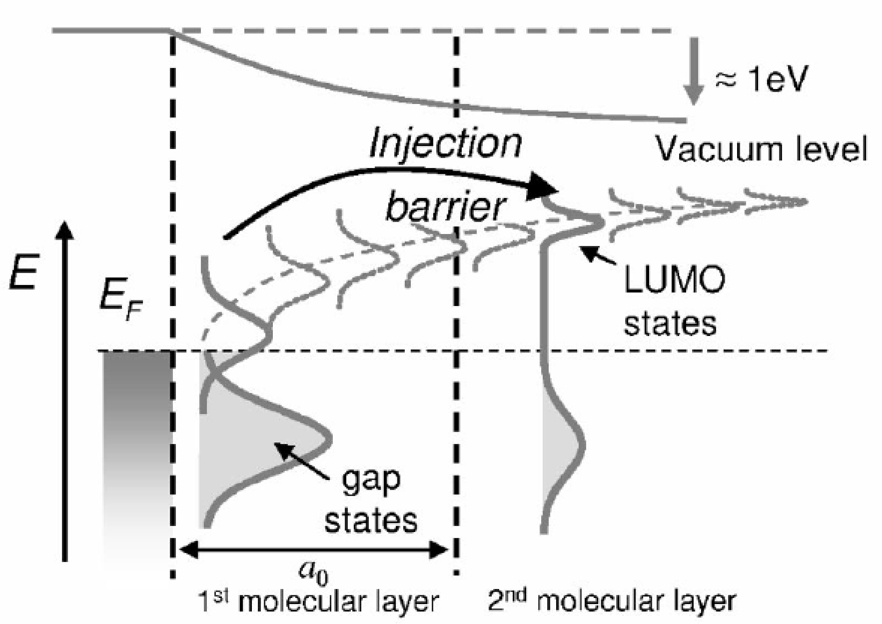

Figure 4.2: The model of the metal-organic interface for a reactive metal and disordered organic layer. The filled gap states are created due to the reaction of the metal with the organic material. The molecular levels (LUMO in this case) are broader and closer to the Fermi level at the interface. The most difficult step in charge transport is the injection from the interface states to the bulk. Figure adapted with permission from ref [187].

The injection limited mechanism of Figure 4.2 describes the low temperature conductivity of a series of molecules with a range of HOMOs and LUMOs of ~1eV and a variety of top contact materials. The molecular organic layers with thickness of ~100 nm were deposited via evaporation on top of an ITO layer covered with a hole blocking layer. The top contact was then evaporated on top of the organic layer. The conductivity was found to be independent of the nature of the organic layer or the contact metal[187]. The current was generally described with a power law Equation ($I=V^m$) which is similar to SCLC current. m decreased from ~20 at T<50K to ~5 at room temperature. Crucially to an injected limited current, the current at a constant field, was found to be independent of the thickness of the organic layer[188]. The independence of current from the choice of metal or molecules was attributed to the lowering of the interfacial energy level offsets due to image charge effects and broadening of the energy levels of the molecules at the interface due to the disorder induced by the interfacial dipoles which are large as a consequence of the easy polarizability of the metallic contact (see Chapter 1-4). Theoretical calculations suggested that for an angular distribution of interfacial dipoles of $\sigma_\Theta=1.5$ rad, the width of the induced broadening of the LUMO is σ~0.8 eV[188]. This distribution of the interfacial dipoles was present due to random orientation of the molecules and the roughness of the metal surface. The broadening of the molecular energy levels close to the contact results in the overlap between the Fermi level of the metal and the molecules irrespective of the nature of the metal or molecule. The electrons easily flow from the contact to the first molecular level via resonant tunneling and the main energy barrier for transport would be the energy barrier between the first broadened molecular level and the second narrower molecular level.

4.1.2 Charge transport in polythiophenes

Polythiophenes are generally utilized as p-type semiconductors with good mobilities (~0.1cm^2/V·s for well known regio-regular P3HT), although the fluorination of their back bone can render them n-type[54]. The films of poly(3,4-ethylenedioxythiphene) grown by electro-oxidation of the 3,4-ethylenedioxythiophene monomer were found to be doped by the anion of the electrolyte and contain unpaired electrons (localized spin). PEDOT layers doped with PF_6^- were found[189] to be more conductive and more temperature dependent than the layers doped with BF_4^-. These PEDOT samples were found to become metallic[190] and display an increase in current with the decrease in temperature at temperatures below 10K[191].

BTB junctions within the thickness range of ~4-22 nm using carbon as both contacts exhibited symmetric current-voltage behavior[47] while BTB junctions with the thickness of >6 nm using Au as bottom contact and Ti/Au as top contact were rectifiers[192]. BTB junctions made by diazonium reduction utilizing carbon contacts were found to have a β value of ~3 nm^{-1} for thicknesses below ~7 nm, and a β value of ~1 nm^{-1} for thicknesses above 7 and below 16 nm. The devices with thicknesses of below 7 nm were temperature independent while the devices with thicknesses between 7 and 16 nm were found to be only weakly temperature dependent and exhibit a Poole-Frenkel like behavior[47]. In addition, self assembled junctions of π-conjugated oligophenylene thiopheneimine on gold surface had a beta value of ~3.5 nm^{-1} for thicknesses below ~5 nm and for thicknesses between 5-8 nm the resistance was found to increase linearly with thickness and was fully temperature dependent (Ea~0.35 eV)[193]. This higher level of temperature dependence in self assembled layers compared with covalently attached layers via diazonium reduction might be due to more disorder in the latter layers which increases the chance of downwards temperature independent hops.

4.2 Experimental section

The procedures for fabrication of PPF bottom contact and deposition of top contact were the same as those described in Chapter 2.

4.2.1 Material synthesis

Diazonium reagents for surface modification were generated either by dissolution of an isolated diazonium fluoroborate salt (for TB case) described below or by in-situ generation of the diazonium reagent for four other cases.

4-(Thiophene-2-yl)aniline (TAB) from Aldrich was used as starting material without further purification for synthesis of TB diazonium salt. To synthesize the diazonium salt, the solution of 0.11 g TAB in 4 mL dry ACN was slowly added to a solution of 0.14 g $NOBF_4$ (nitrosonium tetrafluoroborate from Aldrich) in 4 mL dry ACN at -40 ºC (in dry ice/ACN bath). The mixture was stirred at -40 ºC for 1 hour. TB diazonium salt was precipitated by adding diethyl ether to this solution. The diazonium salt was then vacuum filtrated and washed with diethyl ether. The LC-MS spectrum of TB diazonium salt is shown in appendix, Figure A14.

4.2.2 Junction fabrication

The modification of PPF lines was accomplished via in-situ reduction of the corresponding diazonium ion in electrolyte solution. [194]. In this process, the synthesized diazonium salt was not separately crystallized. The diazonium ion was generated in the solution from the corresponding amine and was immediately used for electro-grafting without further separation. Four different amines provided by our collaborator Professor Jean-Christophe Lacroix at University of Paris, Diderot were used in this Chapter. These include 2-(4-aminophenyl)thiophene (TAB), 2-(4-aminophenyl)-3,4-ethylenedioxy thiophene (EAB), 2-(4-aminophenyl)-3,4-ethylenedioxy-5,2'-bithiophene (TEAB) and 2-(4-aminophenyl)-3',4'-ethylenedioxy-5,2'-bithiophene (ETAB). The structures of these amines are shown in Figure 4.3.

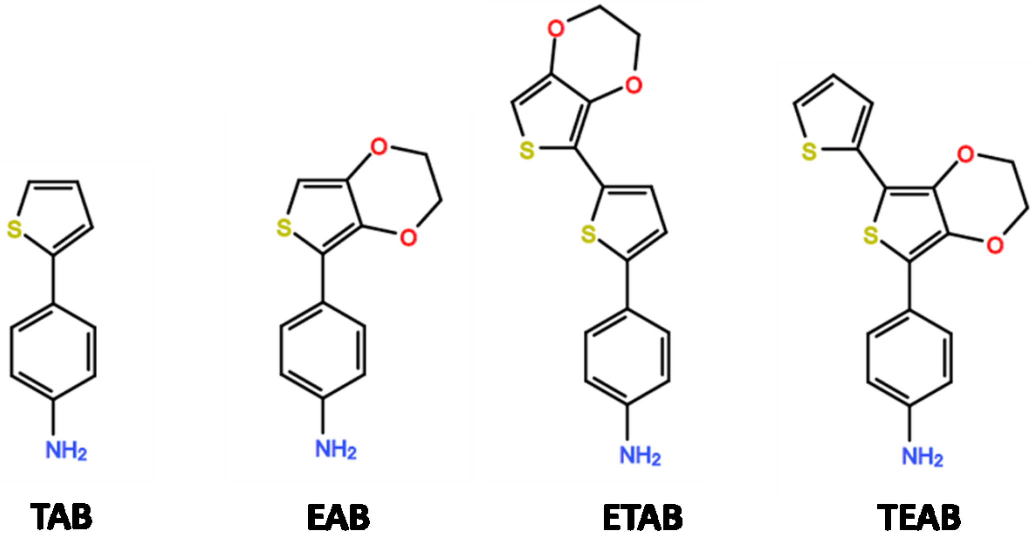

Figure 4.3: The structure of the phenylthiophene amines used in this chapter.

The diazotization of the amines was performed by addition of tert-butyl nitrite in acetonitrile. In a typical procedure, a solution of the aromatic amine in anhydrous ACN (Caledon) was slowly stirred with a small magnetic stir bar and bubbled with Argon gas through a Pasteur pipet for 10 min. The platinum coil as counter electrode along with Ag/Ag$^+$(described in Chapter 2) as reference electrode were put in the solution and then tert-butyl nitrite (Sigma-Aldrich 90%) was added to the solution with a micropipette. 30 seconds after adding t-butylnitrite, the stirrer was turned off and after another 30 seconds the Pasteur pipet was raised above the solution surface to stop the bubbling but still provide an atmosphere of Argon above the solution surface. Then the SiO$_x$/Si chip with PPF stripes was put in the solution as working electrode and cyclic voltammetry was performed to modify the surface of the PPF. The conditions for modification including the concentration of the amines, the amount of the added tert-butylnitrite and the CV sweeping conditions for 3 thicknesses of each layer (measured by AFM) are presented in table 4.1. The in-situ diazotization of the aromatic amine results in the conversion of the amine group to the diazonium cation which is reduced to a phenyl radical and nitrogen. Then phenyl radical reacts with the electrode or another molecule. Consequently the layers formed by in-situ diazonium reduction do not contain the amine groups shown in Figure 4.3 or the corresponding diazonium groups, similar to layers formed from separated diazonium salts as discussed in Chapter 1. Therefore the layers made from TAB are named TB after loss of the amine groups, the layers from TEAB are named TEB layers and the layers from ETAB are named ETB but the layers made from EAB are called EAB layers to distinguish them from EB (ethynylbenzene) layers in Chapter 2.

Table 4.1: Conditions for modification of PPF lines with phenylthiophene derivatives.

Layer	Solution (20 mL ACN)	t-butylnitrite	CV Conditions Vs. Ag/Ag+	Thickness (nm)
TB	0.5 mM TAB in 0.1 M $TBABF_4$	40 µL	0.4 to -0.6 V 5 cycles at 0.05 V/s	5.8
TB	0.5 mM TAB in 0.1 M $TBABF_4$	40 µL	0.4 to -1.5 V 25 cycles at 0.05 V/s	9.4
TB	0.5 mM TAB in 0.1 M $TBABF_4$	40 µL	0.1 to -1.7 V 25 cycles at 0.05 V/s	12
EAB	0.5 mM EAB in 0.1 M $TBABF_4$	80 µL	0.1 to -0.6 V 10 cycles at 0.05 V/s	3.2
EAB	0.5 mM EAB in 0.1 M $TBABF_4$	80 µL	0.1 to -1 V 10 cycles at 0.05 V/s	5.7
EAB	0.5 mM EAB in 0.1 M $TBABF_4$	80 µL	0.1 to -1.5 V 20 cycles at 0.05 V/s	7.8
ETB	0.5 mM ETAB in 0.1 M $TBABF_4$	50 µL	0 to -0.6 V 10 cycles at 0.05 V/s	4.9
ETB	0.5 mM ETAB in 0.1 M $TBABF_4$	50 µL	0 to -1.3 V 20 cycles at 0.05 V/s	9.2
ETB	0.5 mM ETAB in 0.1 M $TBABF_4$	50 µL	0 to -1.5 V 30 cycles at 0.05 V/s	14.7
TEB	0.2 mM TEAB in 0.1 M $TBABF_4$	100 µL	0.4 to -0.6 V 40 cycles at 0.2 V/s	3.9
TEB	0.2 mM TEAB in 0.1 M $TBABF_4$	100 µL	0.1 to -1.3 V 40 cycles at 0.2 V/s	7.4
TEB	0.2 mM TEAB in 0.1 M $TBABF_4$	100 µL	0.1 to -1.7 V 60 cycles at 0.05 V/s	16

TB layers were made by two methods. The first method was the reduction of in-situ made diazonium ions described above and in table 4.1. The second method was electroreduction of a 0.5 mM solution of the isolated TB diazonium salt in 0.1 M $TBABF_4$ in ACN, similar to the procedure described for the electroreduction of EB diazonium salt in Chapter 2. The thickness of the TB layer was varied by changing the number of cycles, potential window and the scan rate from 3.4 nm (0.4 to -0.6 V at 0.1 V/s for 10 cycles) to 11.2 nm (0.2 to -1.7 V at 0.05 V/s for 25 cycles).

After modification of PPF stripes with the desired molecule, 10 nm of eC was deposited as top contact by e-beam evaporation followed by 15 nm of gold to form large area cross bar junctions with the area of 0.00125 cm^2.

4.2.3 Measurements

AFM (DI 3100 atomic force microscope) was used as described in experimental part of Chapter 2 to obtain the thickness of the layers via scratching method.

UPS spectra were obtained by a Kratos Ultra spectrometer with a He I source (21.21 eV).

UV-Vis measurements were performed by a single beam Agilent 8453 spectrometer with quartz cuvettes (path length of 1 cm) using 0.1 M $TBABF_4$ in ACN as blank.

Raman spectrometry under bias was carried out using a custom made spectrometer equipped with an Argon ion laser (514.5 nm), a 50 mm f/1.8 Nikon camera collection lens, a 2000 groove/mm holographic reflection grating, and an Andor back-thinned CCD detector cooled to -80 °C[195]. The junctions for Raman measurements (only) were made on Cr(3nm)/Au(30nm)/eC(10nm) as bottom contact that shows enhancement of the Raman signal compared with PPF bottom contact. After modification of the bottom contact with the molecules, a 1.5 nm layer of aluminium was e-beam evaporated on top of the molecular layers at high PVD chamber pressure (>10^{-5} torr). The high chamber pressure helps to oxidize the aluminium as it is deposited. This AlO_x layer acts similar to gate oxide in FETs and permits the application of high fields on molecular layer to probe the possibility of polaron formation. The chips were then put in a vacuum oven over night at ambient pressure under the flow of oxygen gas. 3 nm of eC and 15 nm of gold were deposited as top contact on the following day to form the junctions. The laser power of 30 mW (at source) was used for measurements through the top contact with 100 seconds signal integration time.

Temperature experiments were performed in a Janis ST-500-1 cryogenic probe station cooled with liquid nitrogen. The chamber was pumped down to pressures less than 9×10^{-5} torr before lowering the temperature and acquisition of JV curves.

Electrical measurements of the molecular junctions were carried out using Keithley 2602A in four-wire configuration. All the voltages are PPF voltage relative to the eC/Au top contact.

4.3 Results and discussion

The conditions for optimal in-situ modification are discussed and the results of the in-situ method are compared to the isolated diazonium salt method. The J-V characteristics of various layers are presented, succeeded by discussion of the transport mechanism.

4.3.1 Conditions for insitu modification

In-situ generation of diazonium ions using tert-butyl nitrite has been reported to proceed slowly in dry acetonitrile and has been considered as a candidate method for diazonium generation in ionic liquids. The electroreduction of the insitu tert-butyl nitrite generated diazonium ion has been shown to produce the same layer composition and surface coverage as isolated diazonium salts for several cases, including nitrophenyl and anthraquinone[194]. The exact mechanism of diazonium formation by tert-butyl nitrite has not been reported, although kinetic studies on nitrosation reaction using alkyl nitrites have been shown to be consistent with nucleophilic attack of NH_2 group at the nitrogen center of the alkyl nitrite in an S_N2 type reaction[196].

Controlling the diazonium formation process from thiophene derivatives was found to be particularly challenging due to complications arising from polymerization reactions caused by diazonium electrophilic attack on another thiophene molecule in the solution[197].

UV-Vis measurements were performed on aminoazobenzene (AB NH_2) and azobenzene diazonium salt (AB DS) to confirm the formation of diazonium ion by this in-situ process and find out the optimum amount of tert-butyl nitrite needed to achieve the highest concentration of diazonium ions. Figure 4.4.A shows the absorption spectra of 4-amino azobenzene solution and azobenzene diazonium salt along with the absorption of 4-amino azobenzene solution after addition of different amounts of tert-butyl nitrite. The change in the absorbance spectrum is evidence that the t-butyl nitrite is converting AB amine to the corresponding diazonium ion, and that excess t-butylnitrite does not further alter the UV-Vis spectrum significantly.

To study the generation of diazonium ions from the thiophene derivatives, bisthienyl benzene (BTB) diazonium ion formation was investigated as a model molecule for thiophene derivatives as it is already shown to form diazonium ions using the t-butylnitrite method. It was observed that adding 24 μL of t-butyl nitrite to 20 mL of 0.5 mM BTB amine (BTAB) only gave thin layers by electroreduction while adding 100 μL of t-butyl nitrite resulted in precipitation of the BTB solution. UV-Vis spectroscopy showed the conversion of BTAB to BTB diazonium upon addition of t-butyl nitrite (see Figure 4.5 B). An excess of t-butyl nitrite is detectable by its absorption spectrum, shown for pure t-butylnitrite in Figure 4.4 B.

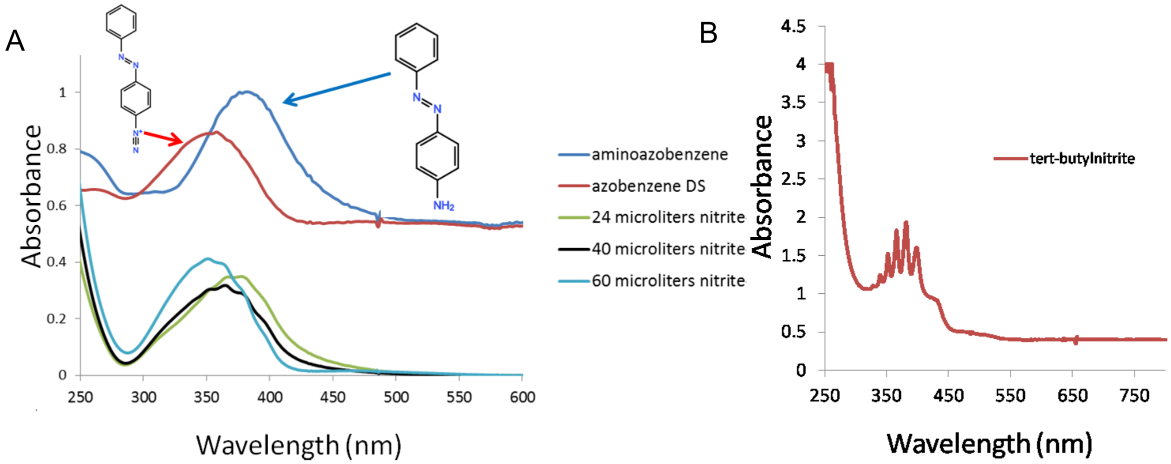

Figure 4.4: A. The absorption spectra of AB amine solution after adding 24, 40 and 60 microliters of tert-butyl nitrite. The spectrum becomes more and more similar to AB DS by addition of tert-butyl nitrite. The absorption spectra of AB amine and AB diazonium salt solutions are shown at an offset above the rest of the spectra. B. Absorption spectrum of tert-butyl nitrite.

The absorption of the excess t-butyl nitrite (Figure 4.4 B) can be easily recognized at 350- 400 nm in part B of Figure 4.5 and the BTB diazonium peak position in Figure 4.5 is consistent with previous study[197].

It should be mentioned that 24 μL of t-butyl nitrite is already 20 equivalents of the BTAB molecules present in the solution and still it obviously (based on 4.5 A) is not enough to convert all BTAB to BTB.

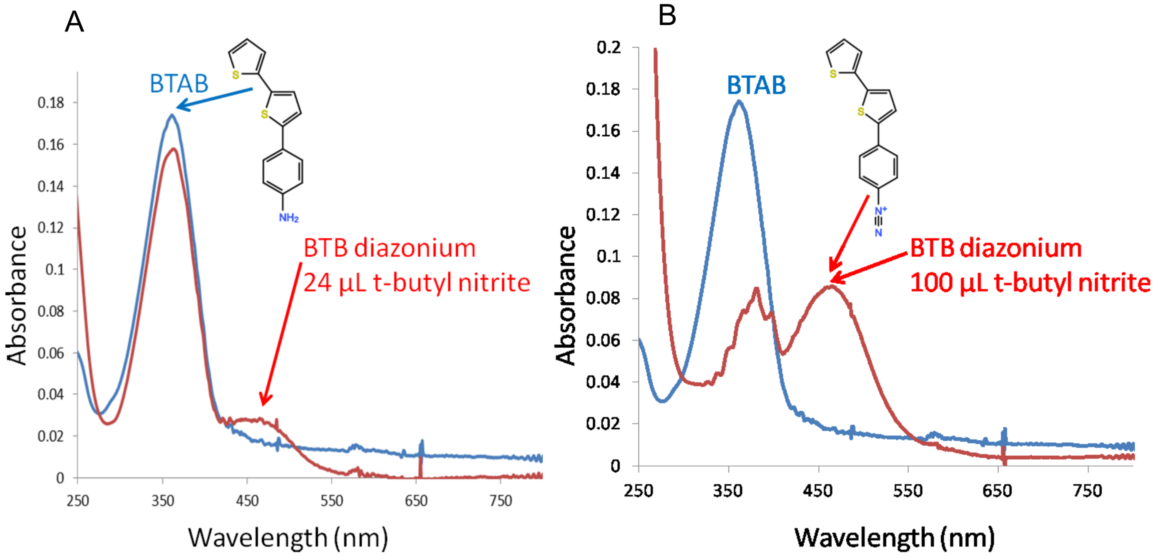

Figure 4.5: A. The absorption spectrum of BTAB solution compared with the same after adding 24 microliters of t-butyl nitrite. B. The absorption spectrum of BTAB solution compared with the same after adding 100 microliters of t-butyl nitrite.

A larger excess of t-butyl nitrite did convert all amines to diazonium ions but resulted in an unstable solution that precipitated in less than a minute after the addition of t-butyl nitrite. The precipitation is presumably the consequence of the polymerization of the diazonium ions due to their relatively high concentration in solution. The optimal amount of t-butyl nitrite was found to be 60 µL of t-butyl nitrite for diazonium formation from 20 mL of 0.5 mM BTAB in ACN. Addition of this amount of t-butyl nitrite to 20 mL of 0.5 mM BTAB gave a green solution at first which turned to a bright red stable solution after ~20 seconds that did not precipitate for 2 hours. The amount of t-butyl nitrite used was different from the volume reported by other researchers[47], [198]. These observations may be rationalized considering the hypothesized mechanism of diazonium formation using t-butyl nitrite (see Figure 4.6)

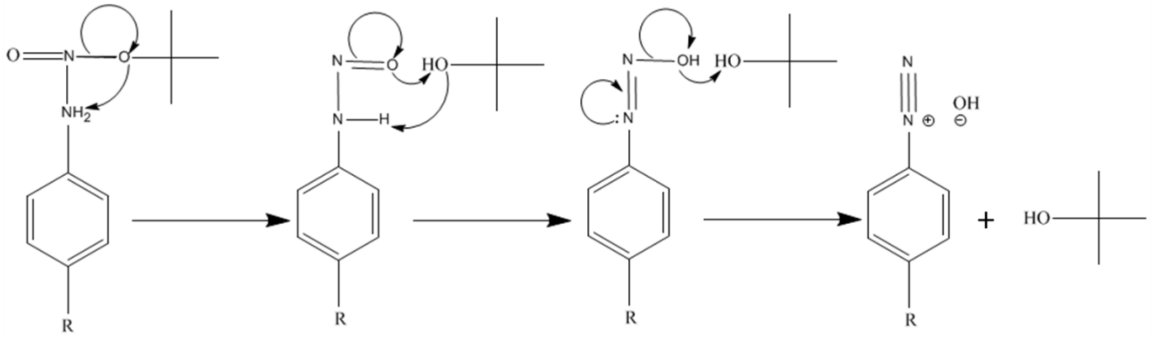

Figure 4.6: Possible mechanism for diazotization of the aromatic amines in dry solvent using t-butyl nitrite.

In this mechanism in dry media, the hydrolysis of the intermediates which normally occurs in acid or water is carried out by the alcohol produced from t-butyl nitrite which is a weak acid or by trace moisture. In principle one equivalent of t-butyl nitrite should be enough to convert one equivalent of the amine to diazonium ion. However the reaction between t-butyl nitrite and the amine in dry medium is expectedly slower than the reaction between NO^+ ion and amine in an aqueous medium due to the extra step shown in Figure 4.6 as the first step on the left and the week acidic property of the alcohol in the second and third steps of figure 4.6. Therefore a large excess of t-butyl nitrite is probably needed to encourage a large number of collisions from which some of them might proceed through all intermediates to diazonium formation. The green colour observed after addition of t-butyl nitrite is probably due to formation of the intermediates and the inconsistencies in the optimum quantity of tert-butyl nitrite used by different workers might be due to presence of various extents of moisture in t-butyl nitrite or ACN which can affect the amount of the t-butyl nitrite needed by completing the intermediate steps toward the diazonium product.

ETAB and EAB had a similar behavior to BTAB and precipitated by addition of too much t-butyl nitrite but formed a green solution at first and a bright red stable solution after few seconds by addition of suitable amounts of t-butyl nitrite. TAB was the only thiophene derivative with a stable enough diazonium ion that allowed the isolation of the diazonium fluoroborate salt. TEAB was found to form a green solution by addition of small quantity (less than 5 equivalents) of t-butyl nitrite and quickly formed precipitates by adding more t-butyl nitrite. Using a dilute solution of TEAB or putting the reaction container in an ice bath did not stop the precipitation process. The best results were obtained using 100 µL of t-butyl nitrite for 20 mL of 0.2 mM solution of TEAB which gave a bright red solution with some black agglomerates floating in it. Although the HOMO energy levels of the amines do not correspond to the HOMO levels of the molecules in the solid state film due to loss of the amine group during the modification, their trend can serve as a general guide for understanding the aforementioned observations. The HOMO energy level was estimated from the onset of the oxidation peak of the amine solution in 0.1 M $TBABF_4$ in ACN on Pt electrode (refer to appendix , Figure A15). The HOMO onset versus Ag/Ag^+ reference electrode was located at 0.3 V for TAB, 0.24 V for BTAB, 0.2 V for EAB, 0.18 V for ETAB and 0.15 V for TEAB. Assuming that Fc/Fc^+ redox couple located at 0.1 V vs. Ag/Ag^+ is 4.8 eV under the vacuum level, the position of the HOMO level for TAB is 5 eV, BTAB is 4.94 eV, EAB is 4.9 eV, ETAB is 4.88 eV and TEAB is 4.85 eV. TAB has the highest oxidation potential and this may be the reason that it is the most stable diazonium ion and can be separated and TEAB has the lowest oxidation potential and the best donor and consequently forms the most reactive and least stable diazonium ions exacerbated by small steric hindrance at the terminal thiophene compared to ETAB with bulky EDOT end group. It is possible that the HOMO levels of the diazonium ions show the same trend as the amines.

The layers made by in-situ diazonium reduction from TB, BTB, EAB, ETB and TEB have been shown electrochemically to become conductive beyond a certain positive potential[199], [200],[197]. This behavior can be seen in Figure 4.7 A. The layers were made on glassy carbon electrode (refer to Chapter 2 for polishing and cleaning) using the conditions listed in table 3.1 for ~ 8 nm layers. The redox activity of ferrocene (E=0.1 V vs. Ag/Ag$^+$) has been shown to become irreversible and shift to higher positive potentials on these layers. This switching behavior has been attributed to conductivity change for these layers at positive potentials that makes them more conductive and enables ferrocene oxidation while ferrocene reduction is blocked at more negative voltages when the layers are not yet conductive[200]. This mechanism was determined by Lacroix, et al. using a variety of redox probes and various oligomeric modification layers. The oxidation peaks observed in Figure 4.7 A are not the oxidation of the layers themselves but the oxidation of ferrocene. The oxidation peaks for the layers are shown in part B of Figure 4.7.

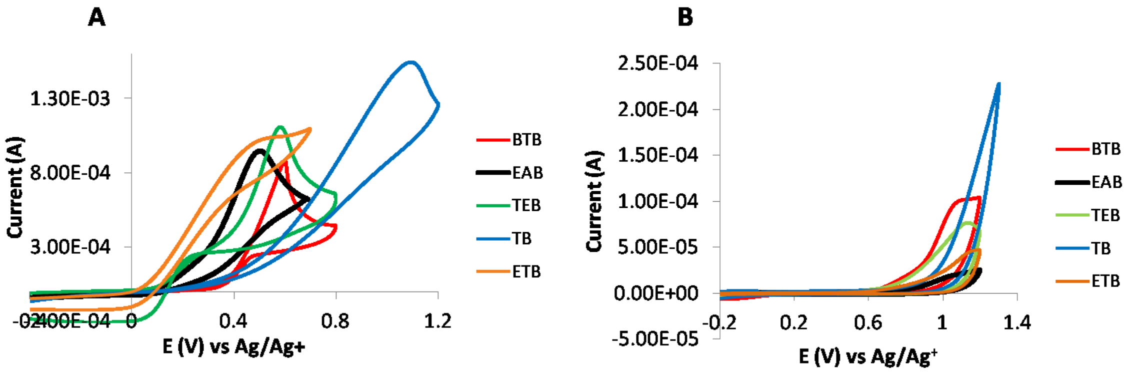

Figure 4.7: A. Redox behavior of 5 mM of Ferrocene in 0.1 M TBAPF$_6$ in ACN on various layers at scan rate of 0.1 V/s. BTB, TB and ETB layers were on PPF electrode while EAB and TEB were on GC electrode with ~10 times smaller surface area. Thus the current for EAB and TEB was multiplied by 10. The reversible oxidation peak of Ferrocene on bare electrode is positioned at ~0.1 V. B. Oxidation of various layers on GC electrode in 0.1 M solution of LiClO$_4$ in ethanol at 0.1 V/s scan rate.

Although the switching potentials were quite varied (Figure 4.7 A) from 1.1 V for TB layer to 0.51 V for EAB layer, the oxidation peaks of the layers were almost similar at around 1.15 V (see 4.7 B). This might indicate the importance of the diffusion of solvent and electrolyte in the layer for electrochemical switching. The layers containing the bulkier EDOT group probably allow more infusion of small ACN molecules in the solution that is highly polarizable which extends the reach of the electric field from the electrode and enables ferrocene oxidation by hole tunneling through accessible HOMO levels of oligo thiophenes without necessarily oxidizing the phenylthiophene layers.

4.3.2 In-situ diazonium modification compared with isolated salt method

PPF/TB/eC/Au molecular junctions were fabricated using both isolated and in-situ generated TB DS to compare the electrical characteristics of the junctions obtained by these two techniques. 48 multilayer TB junctions with 12 different thicknesses were made via the in-situ method with the yield of 98% non-shorted junctions (Figure 4.8 A & B) and 52 multilayer TB junctions with 13 different thicknesses were made using separated TB diazonium salt with the yield of 90% nonshort junctions (Figure 4.8 C & D). TB layers up to the thickness of 12 nm were made by these methods. Each curve in Figure 4.8 is the average J-V curves of 4 junctions on one chip with the standard deviations shown by error bars.

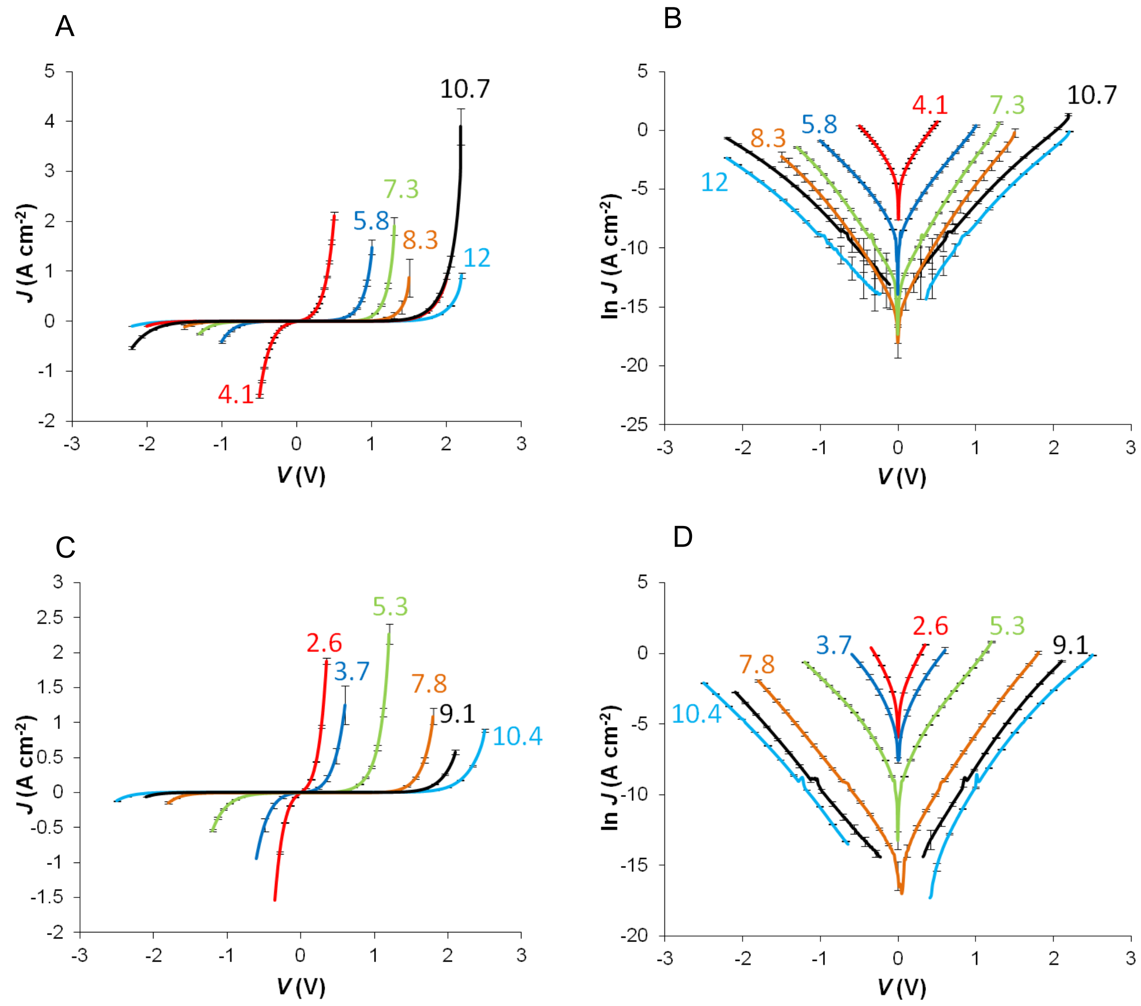

Figure 4.8: A. Representative J-V curves for various thicknesses of TB made by insitu method. B. lnJ vs. V for the same data in A. C. representative J-V curves for various thicknesses of TB made from isolated diazonium salt. D. lnJ vs. V for the same data in C.

The J-V curves of TB junctions with three different thicknesses made by both methods are compared in Figure 4.9. The current for in-situ made TB junctions is slightly higher than the current for isolated salt made TB junctions with the exact same thickness. The in-situ made junctions may be slightly more porous which means their effective thickness in the junction may be slightly less than the thickness measured by AFM. The β plots at 0.5 V and 1 V for both methods are shown in Figure 4.10. The standard deviations on current and thickness are shown by error bars. The β value at 0.5 V for layers made from isolated diazonium salt up to the thickness of 8.9 nm is 2.3±0.4 nm^{-1} while β value at 0.5 V for layers made by in-situ method up to the thickness of 8.3 nm is 2.4±0.08 nm^{-1}. This is while β value for multilayer BTB junctions at 0.5 V was 2.4 nm^{-1}[47].

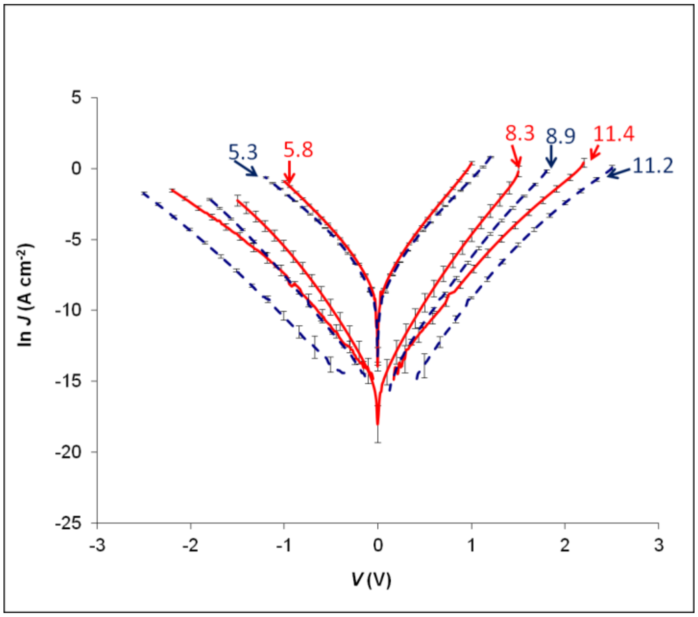

Figure 4.9: lnJ vs. V curves for TB junctions made using in-situ method (Red) compared with separated diazonium salt method (dashed blue).

The similarity in beta values between BTB and TB for thin layers is consistent with the results of the previous Chapter for thin layers.

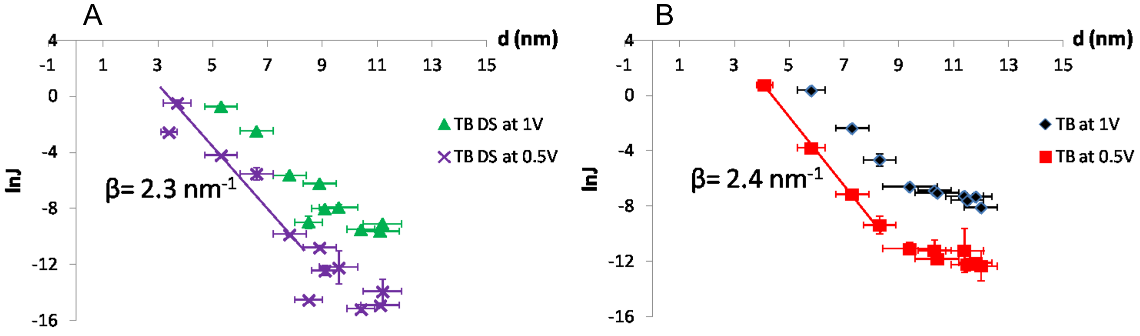

Figure 4.10: A. Beta plots at 0.5 V (purple Xs) and 1 V (green triangles) for PPF/TB/eC/Au devices made by isolated diazonium salt. B. Beta plots at 0.5 V (red squares) and 1 V (black diamonds) for PPF/TB/eC/Au devices made by insitu method.

The small currents for thicker layers at low voltage were close to the detection limit, yielding the larger error bars apparent in Figure 4.8 B. Therefore, the comparisons for d>8 nm were made at the bias voltage of 1 V. The β plots for isolated and in-situ methods are overlaid in Figure 4.11 A and the data are presented in table 4.2. The β value is 0.73 for in-situ layers thicker than 8.3 nm and 0.76 for isolated salt layers thicker than 8.9 nm. The two methods yield quite similar beta values for both thin and thicker layers. The in-situ method β plot is compared to the BTB β plot[47] in part B of Figure 4.11.

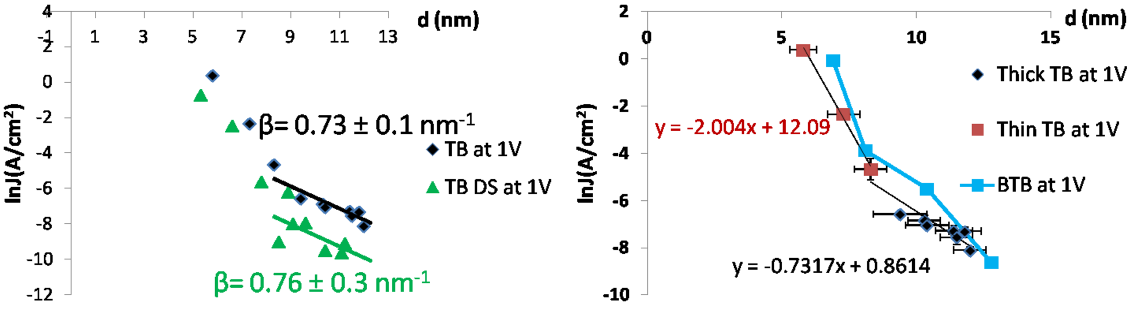

Figure 4.11: A. Overly of the beta plots for isolated salt (green triangles) and insitu (black diamonds) methods. B. Overlay of the beta plots for BTB[47] (Blue squares) and TB (black diamonds) from insitu method.

BTB data used in part B of Figure 4.11 were also reported using the in-situ method. Beta value for BTB layers with thicknesses between 8 and 16 nm at 1 V was 0.86 nm^{-1} in the previous study[47]. The β values for in-situ made BTB and TB with thicknesses higher than 8 nm are statistically indistinguishable according to one-tailed student's t test at 95% confidence limit with 10 degrees of freedom.

Table 4.2: lnJ and standard deviation of lnJ (stdev) at 1 volt for in-situ made TB samples and samples made by isolated TB diazonium salt. Thickness (d) and standard deviation in thickness for each sample from AFM and the number of working junctions (#) with each thickness are also listed.

In-situ made TB					Isolated TB DS				
Stdev (nm)	d (nm)	lnJ (at 1V)	Stdev lnJ (1V)	#	Stdev (nm)	d (nm)	lnJ (at 1V)	Stdev lnJ (1V)	#
0.5	5.8	0.388	0.100	4	0.6	5.3	-0.730	0.052	3
0.6	7.3	-2.34	0.07	4	0.6	6.6	-2.47	0.08	4
0.6	8.3	-4.66	0.45	4	0.6	7.8	-5.64	0.10	3
1	9.4	-6.58	0.06	4	0.5	8.5	-8.99	0.44	3
0.6	10.3	-6.85	0.24	4	0.6	8.9	-6.21	0.10	4
0.8	10.4	-7.05	0.04	4	0.5	9.1	-8.00	0.04	3
0.7	11.4	-7.27	0.20	4	0.7	9.6	-7.92	0.19	4
0.6	11.5	-7.56	0.29	4	0.5	10.4	-9.49	0.05	4
0.6	11.8	-7.30	0.17	4	0.7	11.1	-9.63	0.06	3
0.6	12	-8.1	0.1	3	0.7	11.2	-9.1	0.1	4

4.3.3 Electrical characteristics of oligo-phenylthiophene derivatives

PPF/oligophenylthiophene/eC/Au molecular junctions were made by insitu diazonium reduction for deposition of TB, EAB, TEB and ETB multilayers. The HOMO and LUMO energy levels of the phenylthiophene dimers in the gas phase as an estimate of the energy levels of the oligomers in solid state were calculated by DFT method at the B3LYP/6-31G(d) level of theory and are presented in table 4.3.

Charge transport in polythiophenes is usually governed by hole transport[54] and the HOMO levels of these phenylthiophenes differ by approximately 0.6 eV with each other according to table 4.3. This HOMO span of 0.6 eV is expected to affect the charge transport if the energy levels of the molecules in the solid state are not greatly disturbed and different from the gas phase predicted by DFT. Minor perturbations of the gas phase energies is characteristic of the Mott-Schottky limit, which occurs when the electronic coupling between the molecules and electrodes is weak. The difference in HOMO levels as well as the switching behavior presented in section 4.3.1[200] were the reasons for choosing these series of molecules for investigation.

Table 4.3: Energy levels of the phenylthiophene derivatives dimers from DFT calculations.

	HOMO, eV	LUMO, eV
	B3LYP	B3LYP
BTB dimer	-4.99	-1.93
TB (thiophene-benzene) dimer	-5.26	-1.57
EAB (EDOT-benzene) dimer	-4.83	-1.39
ETB (EDOT-thiophene-benzene) dimer	-4.65	-1.74
TEB (thiophene-EDOT-benzene) dimer	-4.63	-1.73

The similarity of J-V characteristics of TB and BTB layers described in section 4.3.2 suggests that the gas phase energy levels may not be a reliable indicator of the solid state energy levels even beyond tunneling distance where interactions with contacts is minimal. This might be due to the distribution of configurations and attachment points between the molecules in multilayers as a consequence of radical nature of diazonium reaction used for layer growth. The electronic coupling values calculated for TB and BTB dimers using the Equation: ($t = \frac{(HOMO)+(HOMO-1)}{2}$) are t=0.444eV for TB and t=0.261eV for BTB. The coupling for TB dimer is twice as large as in BTB which means TB can have more extended conjugation than BTB. This effect may reduce the HOMO-LUMO gap of TB in table 4.3 and bring its HOMO level close to BTB and reduce the HOMO span of the oligothophenes to ~0.3eV. The more extensive conjugation of TB to PPF contact probably also reduces the HOMO ionization barrier by reducing the HOMO-LUMO gap on the PPF side and causes the small asymmetry in current observed for thick TB layers (Figure 4.8).

To further study the effect of energy levels on transport, 20 multilayer EAB junctions with 100% non-short yield (Figure 4.12 A and B), 28 multilayer ETB junctions with 93% non-short yield (Figure 4.12 C and D) and 28 multilayer TEB junctions with 93% non-short yield (Figure 4.12 E and F) were made and tested. Although the growth of thick oligothiophene derivatives via reduction was difficult, 5 different EAB thicknesses, and 7 different ETB and TEB thicknesses were achieved. The thicknesses are shown in nm on J-V curves in Figure 4.12 and the standard deviations on these thicknesses are listed in the lnJ-V plots. Each curve in Figure 4.12 is an average of 4 junctions on one chip and the standard deviation in current is shown by error bars.

The comparison among similar thicknesses of various oligophenylthiophenes is presented in Figure 4.13. Part A of Figure 4.13 compares the lnJ-V curves for thicknesses around 13 nm of TB, BTB, TEB and ETB. Part B of Figure 4.13 is the comparison of around 15 nm BTB, TEB and ETB layers. It is clear that variations in molecular structures and energy levels are having small effects on electronic behavior, as discussed below.

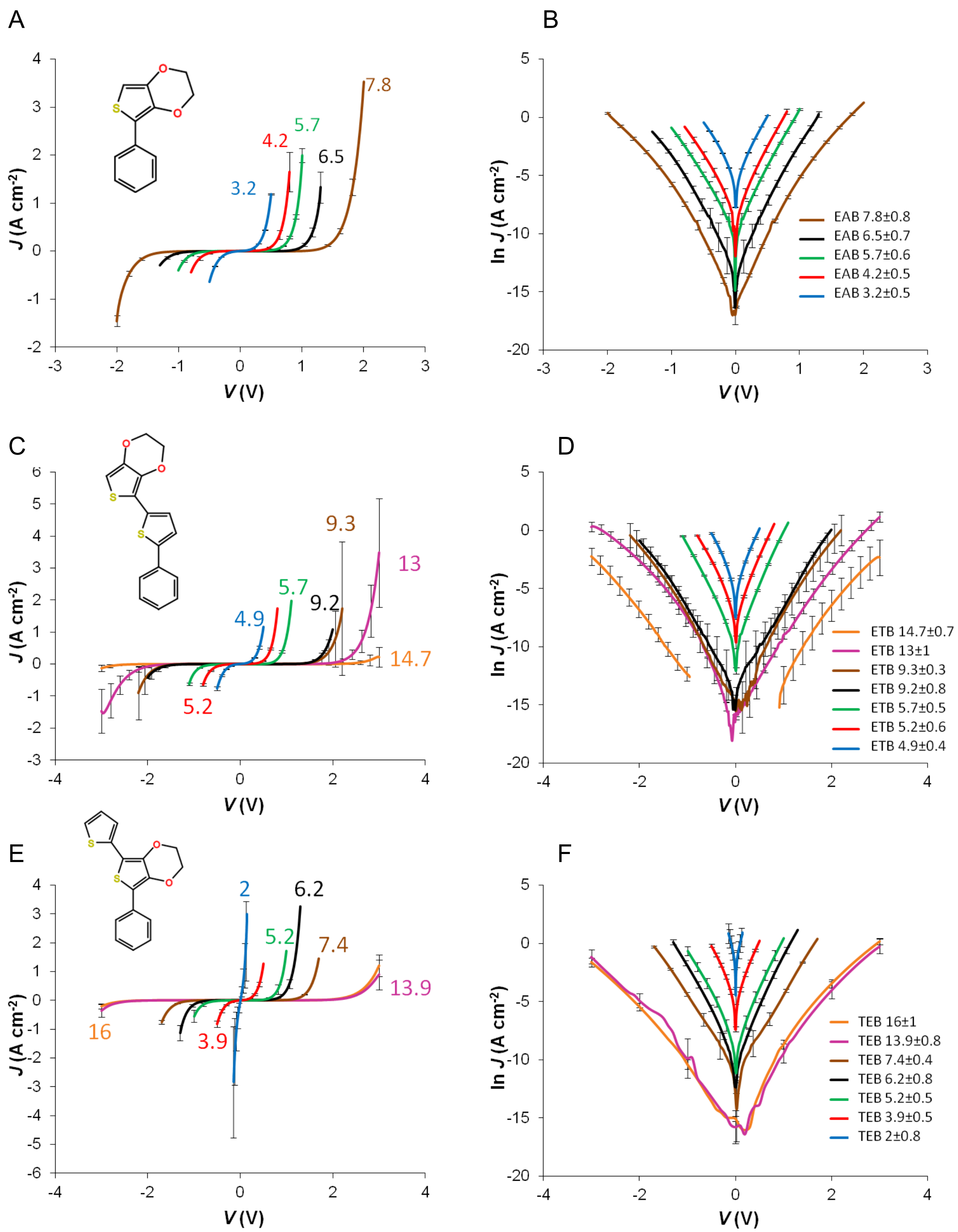

Figure 4.12: A. Overly of J-V curves for EAB molecular junctions. B. lnJ vs. V curves for EAB. C. Overly of J-V curves for ETB molecular junctions. D. lnJ vs. V curves for ETB. E. Overly of J-V curves for TEB molecular junctions. F. lnJ vs. V curves for TEB. Numbers next to each curve are the molecular layer thicknesses in nm for each set of molecular junctions.

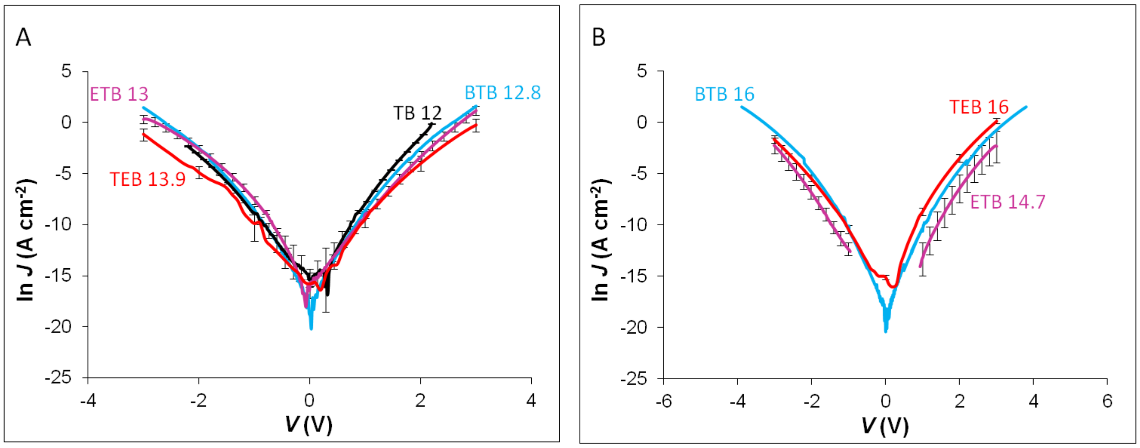

Figure 4.13: A. Overly of J-V curves for various oligophenylthiophenes with thicknesses around 13 nm. B. same comparison as A for thicknesses around 15 nm. The numbers on curves indicates the thickness of the layers in nm. The data for BTB are taken from ref[47].

This comparison reveals no appreciable difference between the electrical behaviour of different oligophenylthiophenes studied.

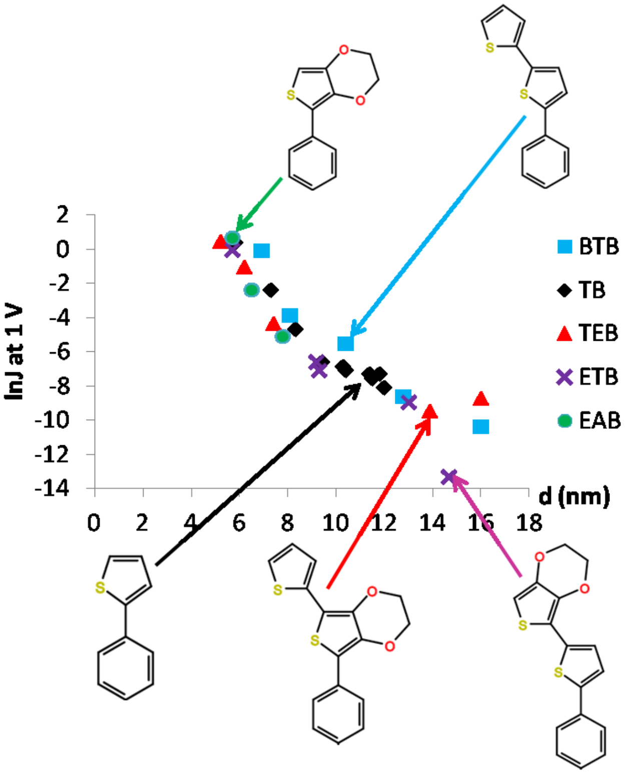

Figure 4.14: Beta plot for all oligophenylthiophenes studied. The data are plotted at 1 V. The data for BTB are from ref[47].

The similarity of electronic behavior of large area molecular junctions of various oligophenylthiophenes is also apparent in their β plots (see Figure 4.14). All thiophene derivatives follow the same trend in their β plots. The β value is 2.1±0.4 nm^{-1} for layers thinner than ~8 nm consistent with tunneling mechanism and 0.7±0.1 nm^{-1} for layers between 8 and 16 nm similar to BTB[47]. The only outlier is 14.7 nm ETB layer which is less conductive than the rest of the β plot junctions. This behavior can be rationalized by considering the structure of ETB molecule in Figure 4.14 or 4.12. The attachment to the thiophene with the EDOT group during the modification is less likely due to steric hindrance of the EDOT group as well as the angle of the molecule and the attachment to the thiophene without EDOT or the benzene ring causes branching (cross conjugation) and reduced electronic coupling and therefore localization. This reduced electronic coupling can be important beyond tunneling region and in thicker layers. This localization is also observed in UPS data shown in Figure 4.15.

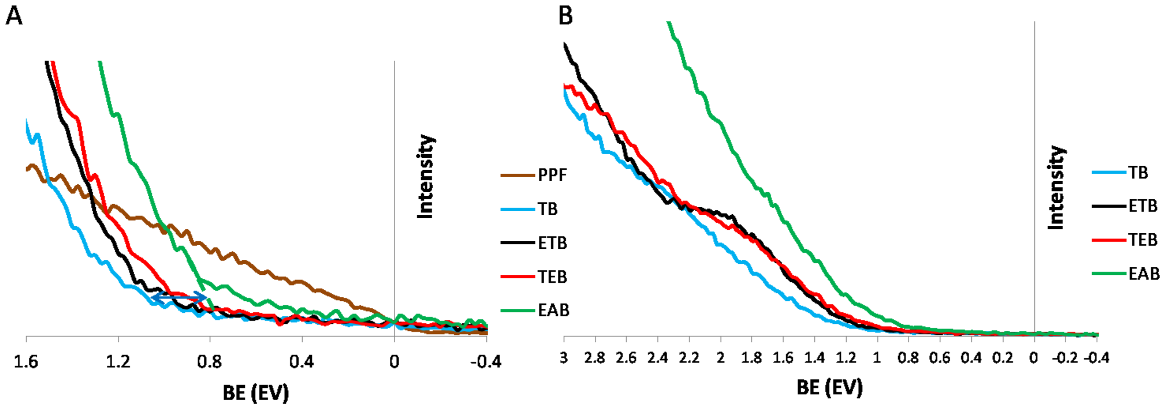

Figure 4.15: A. HOMO region in UPS spectra of the layers studied in this chapter. The onsets of HOMOs are different by 0.2 eV. B. HOMO region of the molecular layers studied in this chapter in the UPS spectra. ETB layer has a feature. The layers were made using the conditions for the thickest layers in table 4.1.

The HOMO onsets of the layers tested in this Chapter are quite similar as shown in Figure 4.15-A and the difference of 0.2 eV is close to the UPS error margin. The multilayers generally do not exhibit any HOMO feature close to the Fermi level. This is probably due to the wide distribution of the torsion angles and conjugation extents between molecules and the carbon contact and the molecules themselves that smears out the HOMO features. ETB is the only multilayer with a HOMO feature which might be due to localization as previously mentioned. The full width at half maximum of the Gaussian HOMO peak in UPS have been used to determine the extent (standard deviation=σ) of the disorder in the layer (FWHM=2.355σ)[74], [201]. The ETB feature broadening might have been induced by factors other than conjugation such as disorder and dipoles, because this is probably the broadening of a localized energy level. The disorder induced broadening is possibly the reason for similar HOMO onsets in 4.15-A.

4.3.4 Mechanism of charge transport in thick (>5nm) molecular junctions

The dependence of current on voltage, thickness of the layer and temperature were inspected to investigate the mechanism of charge transport in the oligothiophene layer junctions.

The dependence of current on thickness at a constant electric field of 1 MV/cm is represented in Figure 4.16 A for TB layers with various thicknesses.

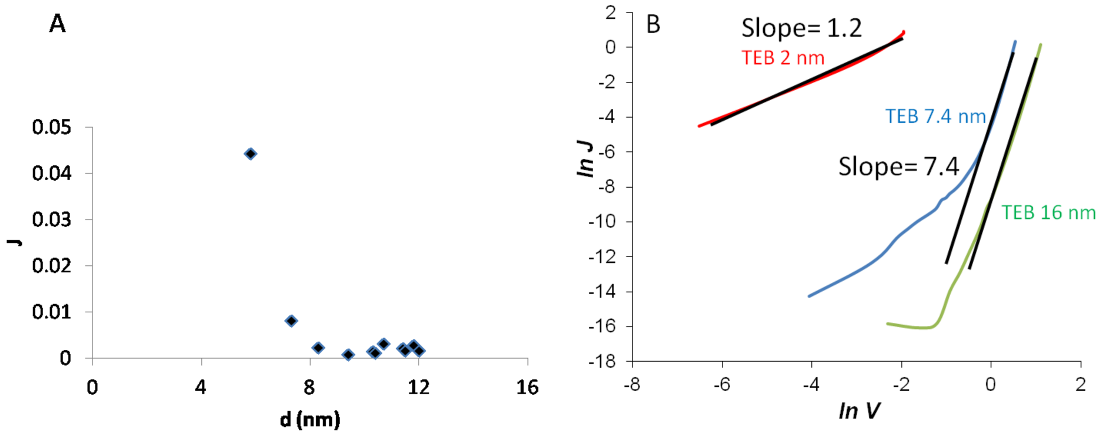

Figure 4.16: A. Dependence of current on thickness at constant electric field of E=1MV/cm for TB multilayers. B. lnJ versus lnV plots for TEB multilayers of various thicknesses.

Current at a constant field becomes independent of thickness for layers thicker than 8nm. The same trend was also observed for the rest of oligothiophenes. lnJ vs. lnV curves (see Figure 4.16 B) reveal that the current for thicker oligothiophene layers become exponentially dependent on voltage. This is true for all the oligothiophenes studied and TEB layers are shown in Figure 4.16 B as representatives. This $J=V^m$ behavior has been attributed to SCLC. These two observations are reminiscent of an injection limited mechanism for thicker organic layer which was discussed in the introduction[23] with m in $J=V^m$ strongly dependent on temperature. In this mechanism, the molecular layer close to the interface is broadened by the interactions with the interface and other molecules, therefore the charge injection barrier decreases significantly for the interfacial region. The charges easily tunnel into the broadened interfacial layer and create the space charge and the current is limited by the rate of the second step which is transport of the carrier out of the interfacial region. The mechanism of this rate limiting step is what is needed to determine the mechanism of charge transport in these oligothiophenes.

Figure 4.17 shows the linearity of lnJ with square root of the electric field for various oligothiophenes with different thicknesses.

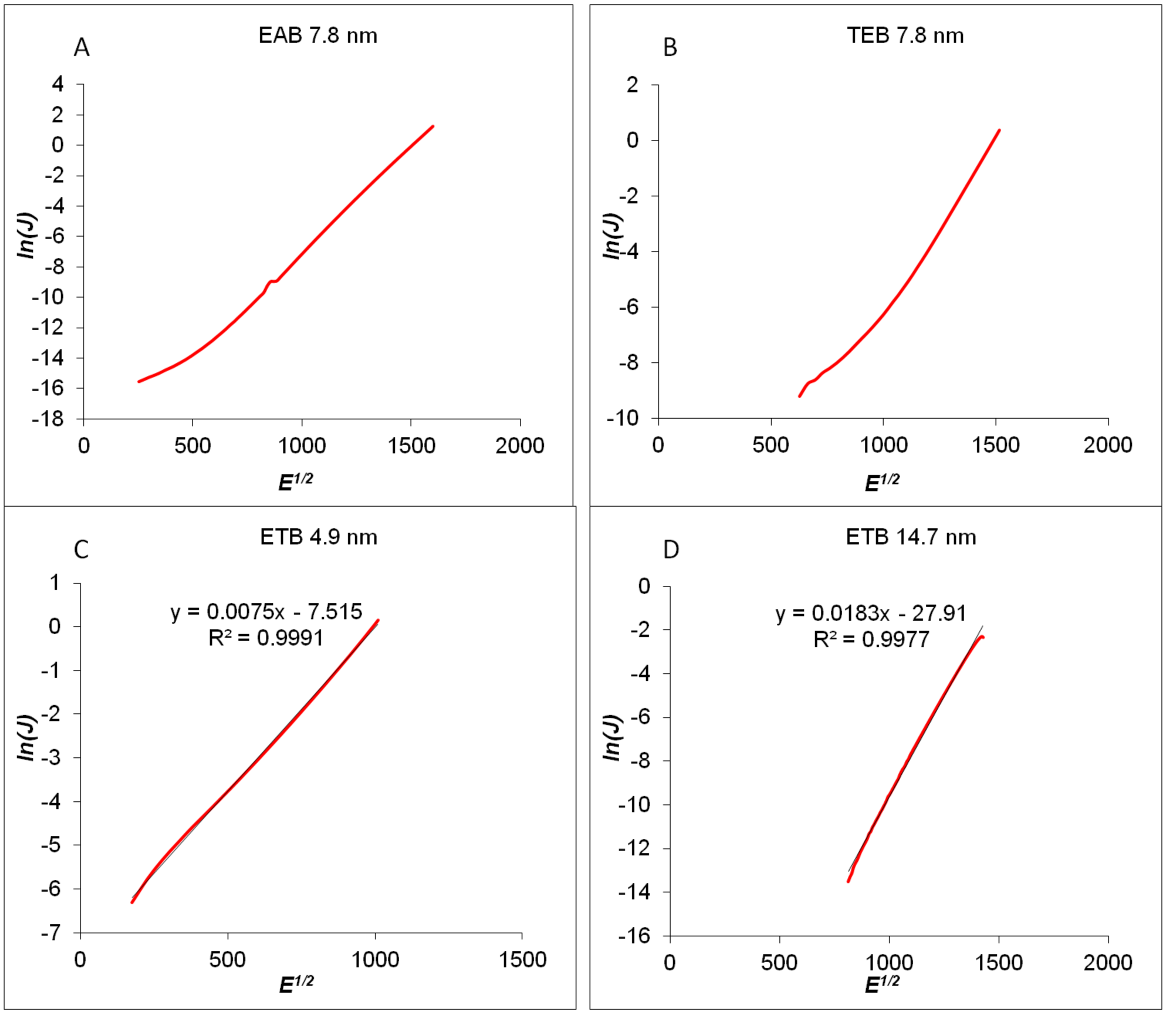

Figure 4.17: Dependence of lnJ on square root of the electric field (V/cm) for A. 7.8 nm EAB layer, B. 7.8 nm TEB layer, C. 4.9 nm ETB layer and D. 14.7 nm ETB layer.

The linearity of lnJ with square root of electric field is characteristic of Schottky emission, however Schottky emission from the contact is independent of the thickness of the layer. This is not consistent with the observation that the absolute value of both the slope and intercept of lnJ vs. $E^{1/2}$ lines increases with the thickness of the layer (Figure

4.17 part C and D). Pool-Frenkel emission could possibly have a thickness dependent slope and intercept. The complete Poole-Frenkel Equation is:

$$J = CEexp[-\left(\frac{q\varphi-\beta\sqrt{E}}{\xi kT}\right)] \tag{4.9}$$

In which C and β are constants and E is the electric filed. The parameter ξ in this Equation is related to the separation between Fermi level and the conductions band[59]. Usually when Fermi level is half way between the trap level and the conduction band the ξ value is 2, but when conduction band is further away from the trap levels, the ξ value decreases to 1. It is conceivable that by increasing the thickness of the molecular layer, the conduction band shifts further away from the Fermi level. Only HOMO-n and LUMO+n may be extended across the whole molecular layer and n increases with the thickness of the molecular layer. In this case the value of ξ slowly decreases for thicker layers which means the slope and intercept of lnJ vs. $E^{0.5}$ increase with the thickness. The problem is that lnJ/E vs. $E^{0.5}$ is the linear form for Poole-Frenkel mechanism instead of lnJ vs. $E^{0.5}$, however the same effect can in principle cause a thickness dependence for the Schottky mechanism.

To further investigate the possibility of some form of Schottky or Poole-Frenkel, the temperature dependence of a 12 nm TB molecular junction was explored (Figure 4.18).

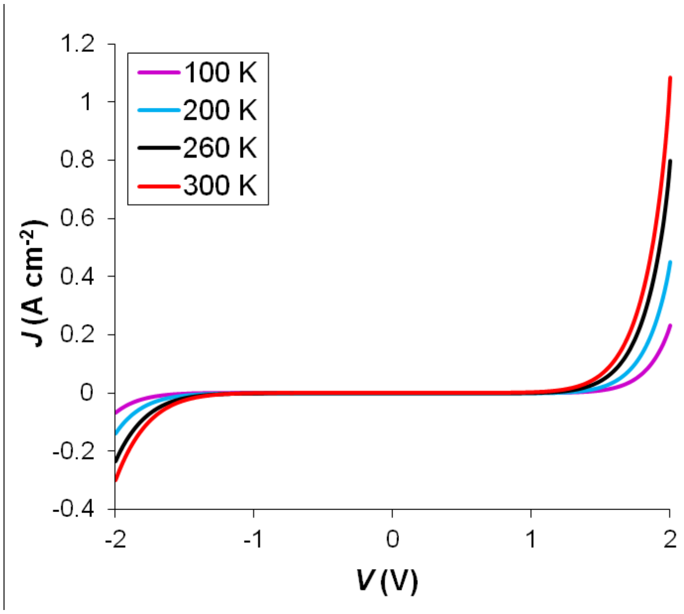

Figure 4.18: J-V curves of 12 nm TB multilayer at various temperatures.

The activation energies obtained from Arrhenius plots in Figure 4.9 are listed in table 4.4.

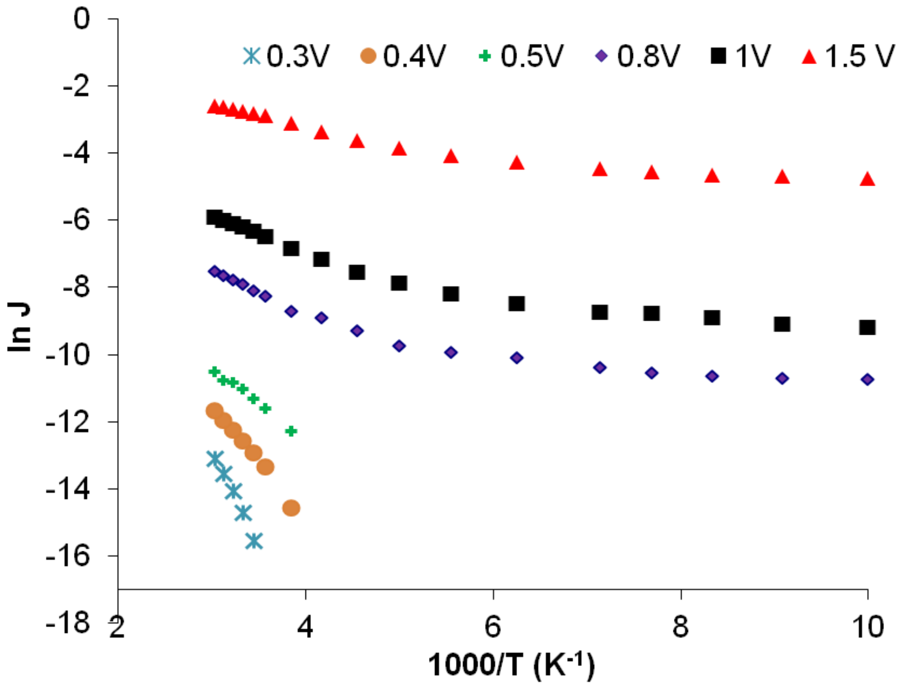

Figure 4.19: Arrhenius plots for 12 nm TB at various voltages. The data points at low temperatures and bias voltages less than 0.3 V were below the sensitivity limit (lnJ~ -15) of the measurement.

The temperature dependence at higher temperatures is significant (Ea=0.5 eV) but quickly decreases to close to zero at lower temperatures. The temperature independence of current at low temperatures is not consistent with the Schottky mechanism. It also is not consistent with hopping of the charge carriers out of the interfacial region.

Table 4.4: Activation energies at various voltages and temperatures for TB 12 nm and TB 5.3 nm layers.

TB 12 nm						
V	0.3	0.4	0.5	0.8	1	1.5
Ea(290-330K) meV	498	260	158	117	88	47
Ea(100-140K) meV				10	14	8
TB 5.3 nm						
V	0.1	0.2	0.3	0.4	0.5	
Ea(280-320K) meV	112	92	84	67	70	
Ea(120-150K) meV	0.1	0.06	0.06	0.2	0.2	

Figure 4.20 shows ln J vs. ln V and lnJ vs. V$^{1/2}$ plots for TB at two temperatures, in order to explore the possibility of a mechanism change at lower temperatures.

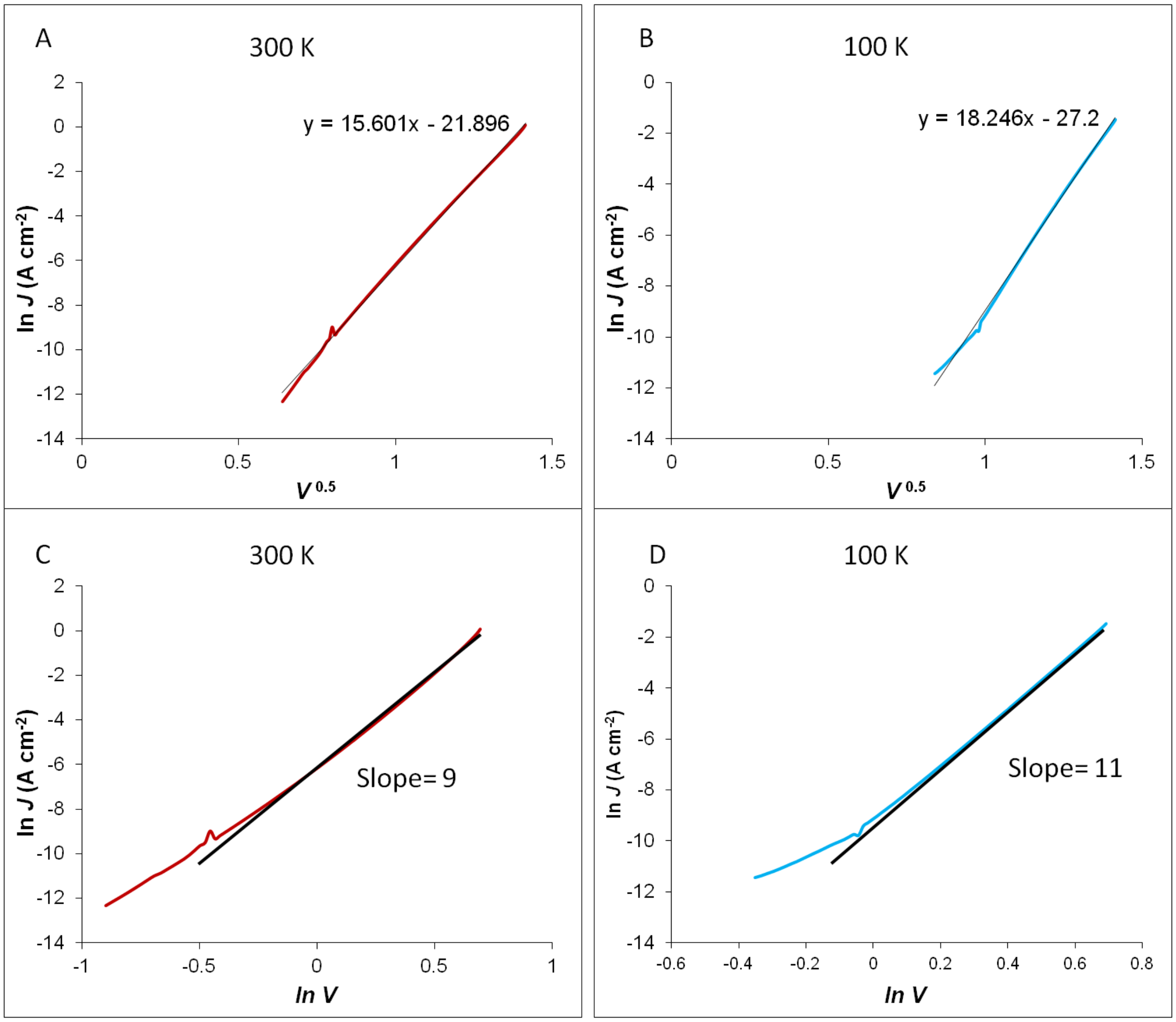

Figure 4.20: lnJ vs. V$^{0.5}$ lines for a 12 nm TB device at A. 300K and B. 100K. lnJ vs. lnV lines for a 12 nm TB device at C. 300K and D. 100K.

The linearity of lnJ with V$^{0.5}$ persists even at low temperatures (Figure 4.20 B), although it is unlikely for Schottky emission to be the charge transport mechanism down to 100K. lnJ versus lnV curves show that the current is still following I=V^{m} with slightly higher m at low temperatures (Figure 4.20 D). This is inconsistent with redox hopping as the mechanism of charge transport out of the interfacial space charge region as redox hopping is highly temperature dependent.

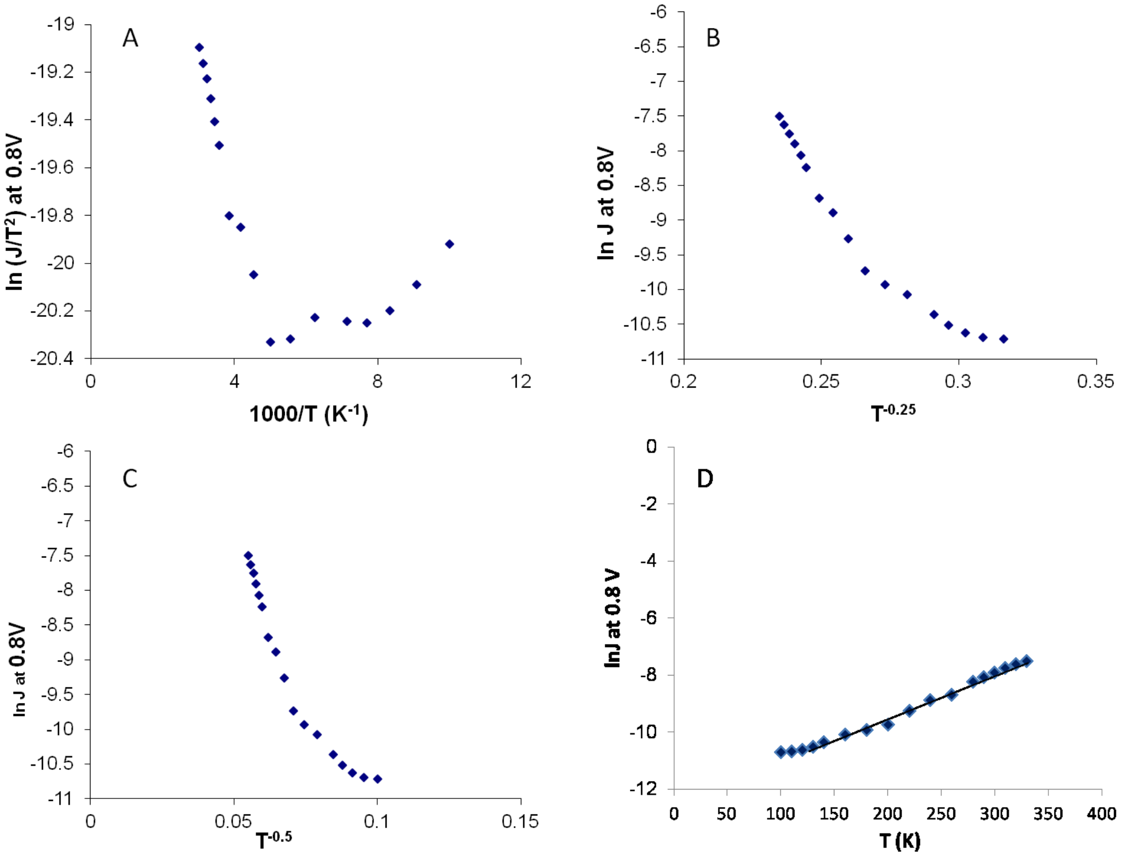

Figure 4.21: Temperature dependence of 12 nm TB at 0.8 V. A. Schottky emission model. B. variable range hopping model in three dimensions. C. variable range hopping model in one dimension. D. multistep tunneling with temperature dependent tunneling barrier.

The plot of ln(J/T^{2}) vs. 1/T should be linear for Schottky emission. This plot is shown in Figure 4.21 A for a 12 nm TB layer. The plot is not linear at lower temperatures while lnJ versus V$^{0.5}$ linearity was persistent to 100K (4.20 B). This confirms that the mechanism of charge transport is not Schottky emission and the linearity of lnJ with V$^{0.5}$ has another origin. The linearity of 4.21 A at higher temperatures might be due to increasing HOMO ionization (Poole-Frenkel like) at higher temperatures or some contribution from Schottky emission. It has been observed that the Poole-Frenkel emission from the interfacial region can have the same temperature dependence as Schottky emission[202]. Part B and C of Figure 4.21 show the plot of lnJ vs. 1/T$^{0.25}$ and lnJ vs. 1/T$^{0.5}$. These plots should be linear for 3D and 1D variable range hopping mechanisms respectively[47]. Nonlinearily of these plots rules out conventional hopping as the conduction mechanism. The plot of lnJ versus T shown in 4.21 D is expected to be linear for a multistep tunneling model with a temperature dependent tunneling barrier.

The linearity of this plot is pointing to multi-step tunneling as the conduction mechanism described further below. This plot is also linear above 160 K for thinner layers as shown in Figure 4.22 A for 5.3 nm TB layer.

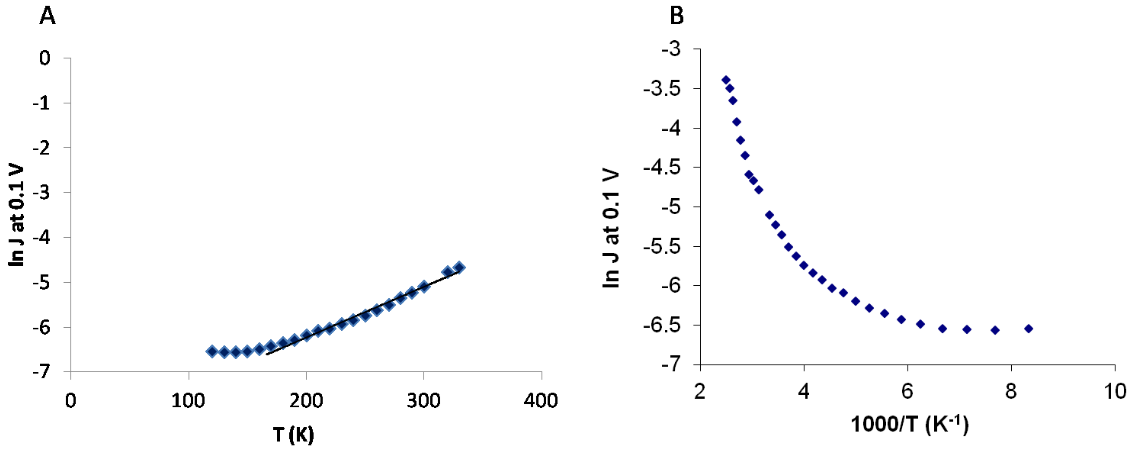

Figure 4.22: A. lnJ at 0.1 V vs. T for 5.3 nm TB layer. B. Arrhenius plot at 0.1V for the same layer in A.

The Arrhenius plots in 4.22 B and 4.19 are definitely nonlinear but the lnJ vs. T plots are linear down to low temperatures where current becomes essentially temperature independent.

The linearity of lnJ vs. T has been reported for multistep tunneling current in amorphous inorganic p-n junctions[161], [203], [204]. Multistep tunneling in these devices occurs in a staircase path. The current can empirically be described as:

$$J = C\exp(\beta V + \gamma T) \tag{4.10}$$

In which C, β and γ are constants. V is voltage and T is temperature. The temperature dependence of β and the voltage dependence of γ are also small. The linearity of lnJ with temperature has been attributed to a temperature dependent band gap. Smaller band gap at higher temperatures means a smaller tunneling barrier and higher current. The full form of this model can be written as[203]:

$$J = Cexp\left[\left(-\left(\alpha R_0^{-\frac{1}{2}} - bT\right)(V_b - V)\right) + \left(b(V_b - V) + \alpha R_0^{-\frac{1}{2}}h\right)T\right] \tag{4.11}$$

In this Equation b,C and h are constants and the small temperature dependence of β and the voltage dependence of γ in Equation 4.10 means that b is small. V_b is built in field in the p-n junction between the p and n sides. V_b is the barrier that the carriers should overcome during the multistep tunneling process. There is no built in field in the

PPF/oligothiophene/eC/Au junctions, therefore V_b should be replaced with φ. R_0 is the number of tunneling steps at zero K and the number of tunneling steps increases with temperature. The parameter α is:

$$\propto = \frac{8}{3\hbar}\left(\frac{m^*\epsilon}{N_d}\right)^{\frac{1}{2}} \tag{4.12}$$

In which ħ is the Planck constant, m^* is the reduced mass of the carrier, ϵ is the dielectric constant of the material and N_d is number of traps/d^3. The number of traps in unit volume is probably not relevant in a thin molecular junction in which charge transport happens only along one direction. Therefore we can define a new one dimensional N_d as the number of traps/d. The new α value for thin layers can then be written as:

$$\propto_{thin} = \frac{8}{3\hbar}\left(\frac{m^*\epsilon}{N_{d(1\ dimensional)}}\right)^{\frac{1}{2}} \tag{4.13}$$

Therefore $\alpha = \alpha_{thin}.d$. The α parameter can be replaced by α_{thin} multiplied by the thickness of the layer.

The voltage dependence of the Equation 4.11 is not what was experimentally observed for oligothiophenes. It has been reported that a combination of Fermi level tunneling (Tunneling through the whole trapezoidal barrier) and thermally assisted tunneling (Tunneling of the carriers inside the layer through a triangular portion of the whole barrier) can result in the same field dependence as Schottky emission. It was also reported that lnJ vs. T is linear for this kind of tunneling to low temperatures where current becomes temperature independent[205].

Given the SCLC in oligothiphenes, the multistep tunneling can be understood by the process illustrated in Figure 4.23. The broadening of the energy levels of the oligothiophenes close to the contacts brings the HOMO levels of some of the molecules so close to the Fermi level of the contact that electron tunneling from these HOMOs to the contact becomes possible by applying any voltage. The holes remaining in the layer give rise to the space charge and a potential profile similar to what is shown in Figure 4.23 by the red curve. Thus the traps are created by electron tunneling from broadened HOMOs to the contact based on the current hypothesis. Now the rest of the electrons in other HOMO levels and the contact should tunnel through this potential profile (energy barrier landscape). The barrier lowering in this case is similar to barrier lowering in Poole-Frenkel mechanism. Considering this argument and by inserting 4.13 into 4.11, the final empirical formula for multistep tunneling in thin layers can be written as:

$$J = Cexp\left[\left(-\left(d\alpha_{thin}R_0^{-\frac{1}{2}} - bT\right)\left(\varphi - \beta_{PF}\sqrt{E}\right)\right) + \left(b\left(\varphi - \beta_{PF}\sqrt{E}\right) + d \propto_{thin} R_0^{-\frac{1}{2}}h\right)T\right] \tag{4.14}$$

In which β_{PF} is Poole-Frenkel barrier lowering due to the presence of the holes that modify the barrier shape, even though the process does not involve Poole-Frenkel emission and E is the electric field.

Equation 4.14 is consistent with the linearity of lnJ with thickness and the change in the slope of beta plot is a sign of change in the number of tunneling steps. For oligothiophene layers thicker than 8 nm, $d.\alpha_{thin}$ should be replaced back by α to give a thickness independent current at constant electric field.

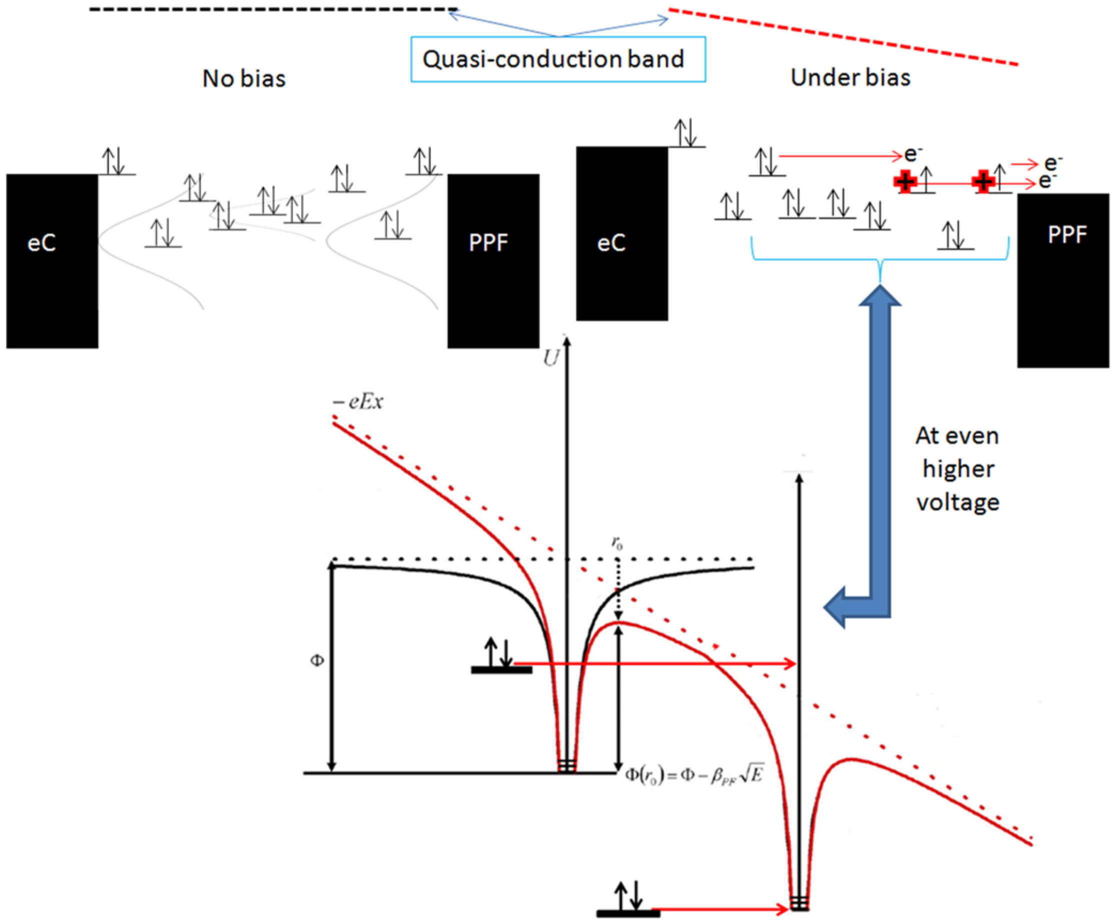

Figure 4.23: Illustration of the multistep tunneling process through a layer of positive space charge. The positively charged traps are created by hole tunneling from the contact to the broadened molecular levels. The rate limiting step is hole transfer from these traps to other molecular levels or in other words electron tunneling from other HOMO levels to these traps.

The multistep tunneling process described by Figure 4.23 can happen in elastic or inelastic steps[206]. The broadened energy levels close to the contacts bring some of the molecular energy levels close to resonance with the Fermi level of the contacts and make elastic multistep tunneling possible in thinner layers while for thicker layers, the narrower energy levels farther away from the contact can create deeper traps and give rise to inelastic trap assisted tunneling and both of these processes can be empirically described by Equation 4.14. The interfacial levels are located mostly close to the contacts and this is probably the reason that the charge transport in thin molecular layers can also be modeled by single step tunneling (1 step from interfacial layer close to one contact to another contact). The origin of the broadening of molecular energy levels close to the contact could be due to partial charge transfer or charge rearrangement at the interface[31], conjugation of the molecular layer to the PPF contact[166] and the interactions between the molecular dipoles with each other and with the image dipoles of other molecular dipoles that are induced in the contact[72] and the combination of these effects can extend the broadening to around 4 nm from each contact.

It is possible that the charge transport out of the interfacial region at high temperatures (close to room temperature) occur by Poole-Frenkel HOMO ionization in addition to tunneling. However such HOMO ionization process should be fast as no polaron was detected in BTB layers (Figure 4.24). The positively charged polarons in polyhtiophenes have been previously studied by Raman spectroscopy[207].

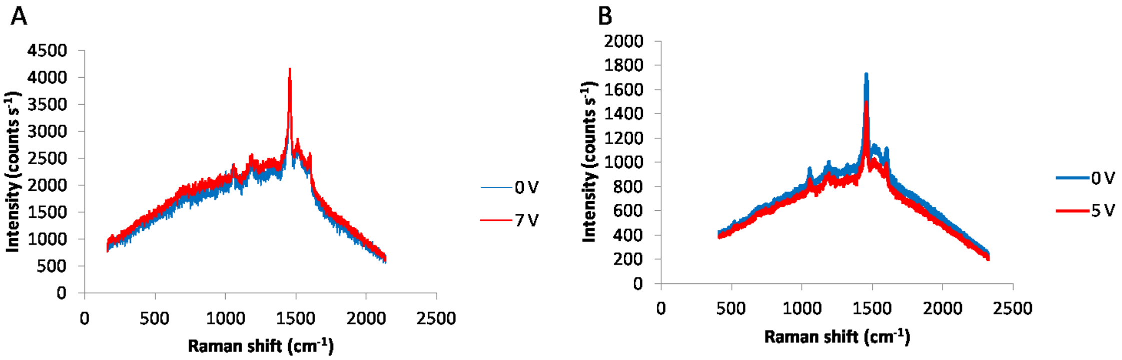

Figure 4.24: A. Raman spectra of Cr/Au/eC/BTB/eC/Au junction with and without applied bias. B. Raman spectra of Cr/Au/eC/BTB/AlOx(3nm)/Au with and without applied bias. No peak shift or new peaks were observed.

A slow Poole-Frenkel ionization process would mean that the positively charged trap remains positive for a long enough time that it can relax into a polaron. The Raman signal of a ~20 nm BTB layer was constant and unchanging under the applied bias as shown in Figure 4.24. Therefore no evidence of the formation of polarons in the device exists and this implies that charge transfer is fast enough to inhibit the formation of polarons.

The linearity of lnJ with $V^{0.5}$ and T was the main characteristic of the charge transport in oligothiophene junctions as shown in Figure 4.25 and is consistent with Equation 4.14.

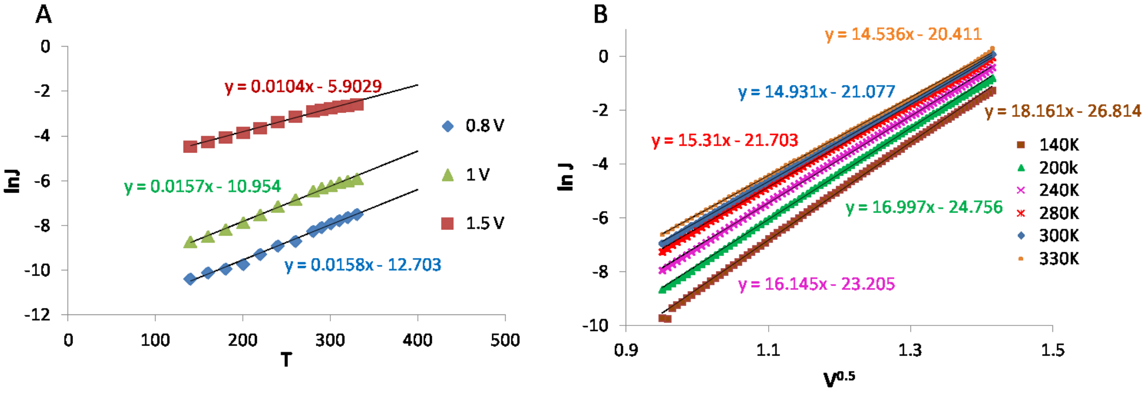

Figure 4.25: A. lnJ vs. T lines for 12 nm TB layer at various voltages. B. lnJ vs. $V^{0.5}$ lines for 12 nm TB layer for various temperatures.

Based on the Equation 4.14 and 4.10, the slope and intercept of the lnJ vs. $V^{0.5}$ plot should be linear with T. This is indeed the case as shown in Figure 4.26 although the dependence is small because the constant b is a small number as previously explained.

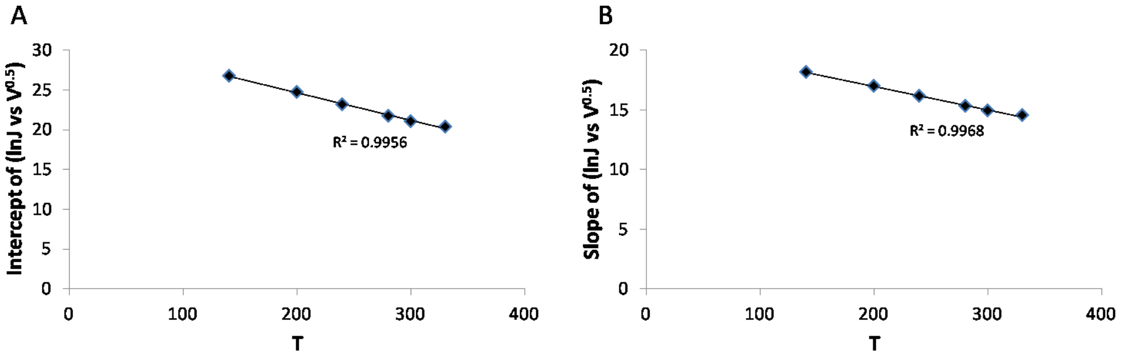

Figure 4.26: The linearity of A. the intercept and B. the slope of lnJ vs. $V^{0.5}$ lines for 12 nm TB layer.

The multistep tunneling model of Equation 4.14 was based on an empirically derived formula and was further modified to qualitatively describe the transport behavior of oligothiophene molecular junctions. Further studies on other thick molecular junctions can improve this Equation, clarify the arbitrary constants and obtain an exact quantitative solution.

4.4 Conclusion

Molecular junctions with thicknesses from 2 nm to 16 nm were successfully made from phenylthiophene derivatives by in-situ diazonium reduction in aprotic medium. The charge transport behavior of TB, BTB, EAB, ETB and TEB molecular junctions were similar despite their different gas phase energy levels. The similarity was attributed to various degrees of electronic coupling and disorder that changes the energy levels in solid state. The charge transport mechanism was found to be field dependent and weakly temperature dependent especially at lower temperatures. The weak temperature dependence ruled out Schottky and redox hopping transport mechanisms. The mechanism of charge transport was found to be consistent with multistep tunneling process as shown in Figure 4.23 through an empirical formula based on linearity of lnJ with T and $E^{0.5}$.

Chapter 5

Summary and outlook

5.1 Summary

The research presented in this document deals with charge transport in large area molecular junctions with carbon contacts. The aim of these kinds of studies is the rational design of molecular electronic devices with controllable electronic functions depending on the chosen molecules.

In Chapter 2, structurally asymmetric thin (<5 nm) bilayer molecular junctions were fabricated by electroreduction of a diazonium salt to form the first layer, and azide-alkyne click chemistry to form the second layer of the bilayer. The current was symmetric in bias voltage for all bilayers studied. The current density and tunneling attenuation constant were found to be independent of the structure of the second layer. This observation was attributed to the small thickness of second layer compared with the total thickness of the bilayer and strong interactions with the contact. Weak temperature dependence and strong exponential thickness dependence of current pointed to tunneling as mechanism responsible for charge transport in these bilayers.

In Chapter 3, thick (>5 nm) bilayer molecular junctions were fabricated by successive reduction of two diazonium ions to form two molecular layers. Current rectification was observed only when both layers were thicker than ~5nm and had different energy levels. A multilayer of acceptor molecule such as NDI and a multilayer of donor molecule such as BTB were needed for rectification and NDI/AQ combination with two acceptors was not rectifying. This is clearly an example of molecular signature in molecular junctions in which the function of the device depends on the choice of the molecules used in the junction. The persistence of rectification to lower temperatures was not consistent with thermally activated charge transport mechanisms and a multistep tunneling transport was suggested to be operative in these bilayers. This multistep mechanism along with the decrease in the electronic coupling to the contact and the concomitant decrease in the broadening of the molecular energy levels farther away from the contacts in the thicker bilayers were suggested to be responsible for the observed asymmetry in J-V response of these thick bilayers that was absent in thin bilayers.

Finally in Chapter 4, this multistep tunneling mechanism was studied in series of oligothiophene layers with thicknesses between 2 and 16 nanometers. The disorder caused by random orientations and attachment points due to radical diazonium reduction reaction, washed away ~0.5 eV difference between the energy levels of various oligothiophenes. The transport mechanism was described as multistep tunneling mechanism in which the first step is tunneling from contact to broadened molecular energy levels close to the contact. The rate determining step in thicker junctions was considered to be the second step which is tunneling out of the interfacial broadened energy levels to energy levels farther away from contact.

5.2 Outlook

Uncovering the charge transport rues in molecular junctions to enable the rational design of molecular electronic devices is the ultimate goal of the continuation of this work.

The success of azide-alkyne click chemistry reaction for junction fabrication in Chapter 2 is promising for incorporating molecular sensing motifs in molecular junctions. For instance a layer of clicked boronic acids as the second layer may sense the presence of saccharides using a sufficiently porous top contact. Despite interferences from the solvent, the presence of charges inside the layer formed from the reaction may be measurable by capacitance or photocurrent measurements as the presence of charges close to interface are expected to affect both capacitance and interfacial energy alignment under a small applied bias.

The rectifiers formed in Chapter 3, in principle can be used for fabrication of vertical all carbon amplifiers with structure PPF/rectifier/graphene/eC/molecule/eC/Au, in which the current through PPF-Au contacts can be controlled by the applied voltage to graphene/eC contact. The fabrication of light emitting diodes from the general donor-acceptor structure of the junctions in Chapter 3 is another likely future direction. Using a good emitter between the donor and acceptor layers such as $Ru(bipy)_3$ may result in LEDs capable of working at very low temperatures.

The oligothiophene layers formed by diazonium reduction in Chapter 4 were disordered. This disorder may be useful for charge separation at donor-acceptor interfaces of solar cells. Deposition of a disordered layer on top of the acceptor layer before adding the donor layer in bilayer solar cells may increase the charge separation efficiency at the interface by providing a range of energy levels in which charges can hop down in energy.

Structural characterization will continue to be important in future molecular electronics, given the difficulty of characterizing nanometer-scale organic layers on carbon. Of particular interest to transport is electronic interactions between molecules, and between molecules and contacts, which are amenable to characterization by optical spectroscopy.

Measuring resistance with varying the magnetic field direction as function of layer thickness might give information about the length scale at which the transport is one dimensional in these molecular junctions before it becomes diffusive in thicker layers. This study can lead to better understanding of the phenomena underlying charge transport in carbon based molecular junctions and uncover future possibilities.

Bibliography

[1] R. L. McCreery and A. J. Bergren, “Progress with Molecular Electronic Junctions: Meeting Experimental Challenges in Design and Fabrication,” *Adv. Mater.*, vol. 21, no. 43, pp. 4303–4322, Nov. 2009.

[2] R. L. Carroll and C. B. Gorman, “The genesis of molecular electronics,” *Angew. Chem. Int. Ed.*, vol. 41, no. 23, pp. 4378–4400, 2002.

[3] A. J. Bergren, L. Zeer-Wanklyn, M. Semple, N. Pekas, B. Szeto, and R. L. McCreery, “Musical molecules: the molecular junction as an active component in audio distortion circuits,” *J. Phys. Condens. Matter*, vol. 28, no. 9, p. 94011, Mar. 2016.

[4] N. J. Tao, “Electron transport in molecular junctions,” *Nat. Nanotechnol.*, vol. 1, no. 3, pp. 173–181, 2006.

[5] R. L. McCreery, H. Yan, and A. J. Bergren, “A critical perspective on molecular electronic junctions: there is plenty of room in the middle,” *Phys Chem Chem Phys*, vol. 15, no. 4, pp. 1065–1081, 2013.

[6] G. G. Roberts, “Molecular Electronics Using Langmuir—Blodgett Films,” in *Electronic and Photonic Applications of Polymers*, vol. 218, M. J. Bowden and S. R. Turner, Eds. Washington, DC: American Chemical Society, 1988, pp. 225–270.

[7] S. Seo, M. Min, J. Lee, T. Lee, S.-Y. Choi, and H. Lee, “Solution-Processed Reduced Graphene Oxide Films as Electronic Contacts for Molecular Monolayer Junctions,” *Angew. Chem. Int. Ed.*, vol. 51, no. 1, pp. 108–112, Jan. 2012.

[8] Z.-L. Cheng, R. Skouta, H. Vazquez, J. R. Widawsky, S. Schneebeli, W. Chen, M. S. Hybertsen, R. Breslow, and L. Venkataraman, “In situ formation of highly conducting covalent Au–C contacts for single-molecule junctions,” *Nat. Nanotechnol.*, vol. 6, no. 6, pp. 353–357, Jun. 2011.

[9] S. Seo, M. Min, S. M. Lee, and H. Lee, “Photo-switchable molecular monolayer anchored between highly transparent and flexible graphene electrodes,” *Nat. Commun.*, vol. 4, p. 1920, May 2013.

[10] T. Hines, I. Díez-Pérez, H. Nakamura, T. Shimazaki, Y. Asai, and N. Tao, “Controlling Formation of Single-Molecule Junctions by Electrochemical Reduction of Diazonium Terminal Groups,” *J. Am. Chem. Soc.*, vol. 135, no. 9, pp. 3319–3322, Mar. 2013.

[11] D. Xiang, H. Jeong, T. Lee, and D. Mayer, "Mechanically controllable break junctions for molecular electronics," *Adv. Mater.*, vol. 25, no. 35, pp. 4845–4867, 2013.

[12] L. Sun, Y. A. Diaz-Fernandez, T. A. Gschneidtner, F. Westerlund, S. Lara-Avila, and K. Moth-Poulsen, "Single-molecule electronics: from chemical design to functional devices," *Chem Soc Rev*, vol. 43, no. 21, pp. 7378–7411, Aug. 2014.

[13] D. Xiang, X. Wang, C. Jia, T. Lee, and X. Guo, "Molecular-Scale Electronics: From Concept to Function," *Chem. Rev.*, vol. 116, no. 7, pp. 4318–4440, Apr. 2016.

[14] S. K. Lee, R. Yamada, S. Tanaka, G. S. Chang, Y. Asai, and H. Tada, "Universal Temperature Crossover Behavior of Electrical Conductance in a Single Oligothiophene Molecular Wire," *ACS Nano*, vol. 6, no. 6, pp. 5078–5082, Jun. 2012.

[15] M. L. Perrin, R. Frisenda, M. Koole, J. S. Seldenthuis, J. A. C. Gil, H. Valkenier, J. C. Hummelen, N. Renaud, F. C. Grozema, J. M. Thijssen, D. Dulić, and H. S. J. van der Zant, "Large negative differential conductance in single-molecule break junctions," *Nat. Nanotechnol.*, vol. 9, no. 10, pp. 830–834, Aug. 2014.

[16] J. A. Malen, P. Doak, K. Baheti, T. D. Tilley, A. Majumdar, and R. A. Segalman, "The Nature of Transport Variations in Molecular Heterojunction Electronics," *Nano Lett.*, vol. 9, no. 10, pp. 3406–3412, Oct. 2009.

[17] J. P. Bergfield and M. A. Ratner, "Forty years of molecular electronics: Non-equilibrium heat and charge transport at the nanoscale: Forty years of molecular electronics," *Phys. Status Solidi B*, vol. 250, no. 11, pp. 2249–2266, Nov. 2013.

[18] L. Venkataraman, Y. S. Park, A. C. Whalley, C. Nuckolls, M. S. Hybertsen, and M. L. Steigerwald, "Electronics and Chemistry: Varying Single-Molecule Junction Conductance Using Chemical Substituents," *Nano Lett.*, vol. 7, no. 2, pp. 502–506, Feb. 2007.

[19] M. Min, S. Seo, S. M. Lee, and H. Lee, "Voltage-Controlled Nonvolatile Molecular Memory of an Azobenzene Monolayer through Solution-Processed Reduced Graphene Oxide Contacts," *Adv. Mater.*, vol. 25, no. 48, pp. 7045–7050, Dec. 2013.

[20] A. J. Bergren, K. D. Harris, F. Deng, and R. L. McCreery, "Molecular electronics using diazonium-derived adlayers on carbon with Cu top contacts: critical analysis of metal oxides and filaments," *J. Phys. Condens. Matter*, vol. 20, no. 37, p. 374117, Sep. 2008.

[21] M. L. Chabinyc, X. Chen, R. E. Holmlin, H. Jacobs, H. Skulason, C. D. Frisbie, V. Mujica, M. A. Ratner, M. A. Rampi, and G. M. Whitesides, “Molecular Rectification in a Metal−Insulator−Metal Junction Based on Self-Assembled Monolayers,” *J. Am. Chem. Soc.*, vol. 124, no. 39, pp. 11730–11736, Oct. 2002.

[22] K. T. Shimizu, J. D. Fabbri, J. J. Jelincic, and N. A. Melosh, “Soft Deposition of Large-Area Metal Contacts for Molecular Electronics,” *Adv. Mater.*, vol. 18, no. 12, pp. 1499–1504, Jun. 2006.

[23] J. G. Kushmerick, J. Naciri, J. C. Yang, and R. Shashidhar, “Conductance Scaling of Molecular Wires in Parallel,” *Nano Lett.*, vol. 3, no. 7, pp. 897–900, Jul. 2003.

[24] Y.-L. Loo, D. V. Lang, J. A. Rogers, and J. W. P. Hsu, “Electrical Contacts to Molecular Layers by Nanotransfer Printing,” *Nano Lett.*, vol. 3, no. 7, pp. 913–917, Jul. 2003.

[25] H. Haick and D. Cahen, “Contacting Organic Molecules by Soft Methods: Towards Molecule-Based Electronic Devices,” *Acc. Chem. Res.*, vol. 41, no. 3, pp. 359–366, Mar. 2008.

[26] F. Anariba and R. L. McCreery, “Electronic Conductance Behavior of Carbon-Based Molecular Junctions with Conjugated Structures,” *J. Phys. Chem. B*, vol. 106, no. 40, pp. 10355–10362, Oct. 2002.

[27] H. Yan and R. L. McCreery, “Anomalous Tunneling in Carbon/Alkane/TiO $_2$ /Gold Molecular Electronic Junctions: Energy Level Alignment at the Metal/Semiconductor Interface,” *ACS Appl. Mater. Interfaces*, vol. 1, no. 2, pp. 443–451, Feb. 2009.

[28] H. Yan, A. J. Bergren, and R. L. McCreery, “All-Carbon Molecular Tunnel Junctions,” *J. Am. Chem. Soc.*, vol. 133, no. 47, pp. 19168–19177, Nov. 2011.

[29] R. L. McCreery, A. Bergren, S. Nagy, H. Yan, A. Bayat, and M. Kondratenko, “Molecules in Circuits: A New Type of Microelectronics?,” *ECS Trans.*, vol. 61, no. 7, pp. 113–121, Mar. 2014.

[30] R. L. McCreery and A. J. Bergren, “Surface Functionalization in the Nanoscale Domain,” in *Nanofabrication*, M. Stepanova and S. Dew, Eds. Vienna: Springer Vienna, 2012, pp. 163–190.

[31] S. Y. Sayed, J. A. Fereiro, H. Yan, R. L. McCreery, and A. J. Bergren, “Charge transport in molecular electronic junctions: Compression of the molecular tunnel barrier in the strong coupling regime,” *Proc. Natl. Acad. Sci.*, vol. 109, no. 29, pp. 11498–11503, 2012.

[32] H. J. Yoon, N. D. Shapiro, K. M. Park, M. M. Thuo, S. Soh, and G. M. Whitesides, “The Rate of Charge Tunneling through Self-Assembled Monolayers Is Insensitive to Many Functional Group Substitutions,” *Angew. Chem. Int. Ed.*, vol. 51, no. 19, pp. 4658–4661, May 2012.

[33] N. Amdursky, D. Marchak, L. Sepunaru, I. Pecht, M. Sheves, and D. Cahen, “Electronic Transport via Proteins,” *Adv. Mater.*, vol. 26, no. 42, pp. 7142–7161, Nov. 2014.

[34] E. Tran, M. Duati, V. Ferri, K. Müllen, M. Zharnikov, G. M. Whitesides, and M. A. Rampi, “Experimental Approaches for Controlling Current Flowing through Metal–Molecule–Metal Junctions,” *Adv. Mater.*, vol. 18, no. 10, pp. 1323–1328, May 2006.

[35] R. Landauer and T. Martin, “Barrier interaction time in tunneling,” *Rev. Mod. Phys.*, vol. 66, no. 1, p. 217, 1994.

[36] M. Paulsson, F. Zahid, and S. Datta, “Resistance of a molecule,” *ArXiv Prepr. Cond-Mat0208183*, 2002.

[37] J. G. Simmons, “Generalized Formula for the Electric Tunnel Effect between Similar Electrodes Separated by a Thin Insulating Film,” *J. Appl. Phys.*, vol. 34, no. 6, p. 1793, 1963.

[38] G. Heimel and J.-L. Brédas, “Molecular electronics: Reflections on charge transport,” *Nat. Nanotechnol.*, vol. 8, no. 4, pp. 230–231, 2013.

[39] A. J. Bergren, R. L. McCreery, S. R. Stoyanov, S. Gusarov, and A. Kovalenko, “Electronic Characteristics and Charge Transport Mechanisms for Large Area Aromatic Molecular Junctions,” *J. Phys. Chem. C*, vol. 114, no. 37, pp. 15806–15815, Sep. 2010.

[40] R. L. Mccreery, “The merger of electrochemistry and molecular electronics,” *Chem. Rec.*, vol. 12, no. 1, pp. 149–163, Feb. 2012.

[41] D. K. Aswal, S. Lenfant, D. Guerin, J. V. Yakhmi, and D. Vuillaume, “Self assembled monolayers on silicon for molecular electronics,” *Anal. Chim. Acta*, vol. 568, no. 1–2, pp. 84–108, May 2006.

[42] I. Bâldea, “Important issues facing model-based approaches to tunneling transport in molecular junctions,” *Phys Chem Chem Phys*, vol. 17, no. 31, pp. 20217–20230, 2015.

[43] J. J. H. M. Schoonus, P. G. E. Lumens, W. Wagemans, J. T. Kohlhepp, P. A. Bobbert, H. J. M. Swagten, and B. Koopmans, “Magnetoresistance in Hybrid

Organic Spin Valves at the Onset of Multiple-Step Tunneling," *Phys. Rev. Lett.*, vol. 103, no. 14, Oct. 2009.

[44] K. A. Nasyrov and V. A. Gritsenko, "Charge transport in dielectrics via tunneling between traps," *J. Appl. Phys.*, vol. 109, no. 9, p. 93705, 2011.

[45] H. Song, M. A. Reed, and T. Lee, "Single molecule electronic devices," *Adv. Mater.*, vol. 23, no. 14, pp. 1583–1608, 2011.

[46] S. H. Choi, C. Risko, M. C. R. Delgado, B. Kim, J.-L. Brédas, and C. D. Frisbie, "Transition from Tunneling to Hopping Transport in Long, Conjugated Oligo-imine Wires Connected to Metals," *J. Am. Chem. Soc.*, vol. 132, no. 12, pp. 4358–4368, Mar. 2010.

[47] H. Yan, A. J. Bergren, R. McCreery, M. L. Della Rocca, P. Martin, P. Lafarge, and J. C. Lacroix, "Activationless charge transport across 4.5 to 22 nm in molecular electronic junctions," *Proc. Natl. Acad. Sci.*, vol. 110, no. 14, pp. 5326–5330, Apr. 2013.

[48] Y.-T. Long, E. Abu-Irhayem, and H.-B. Kraatz, "Peptide Electron Transfer: More Questions than Answers," *Chem. - Eur. J.*, vol. 11, no. 18, pp. 5186–5194, Sep. 2005.

[49] L. Luo, S. H. Choi, and C. D. Frisbie, "Probing Hopping Conduction in Conjugated Molecular Wires Connected to Metal Electrodes †," *Chem. Mater.*, vol. 23, no. 3, pp. 631–645, Feb. 2011.

[50] N. Tessler, Y. Preezant, N. Rappaport, and Y. Roichman, "Charge Transport in Disordered Organic Materials and Its Relevance to Thin-Film Devices: A Tutorial Review," *Adv. Mater.*, vol. 21, no. 27, pp. 2741–2761, Jul. 2009.

[51] P. W. Anderson, "Absence of diffusion in certain random lattices," *Phys. Rev.*, vol. 109, no. 5, p. 1492, 1958.

[52] A. Miller and E. Abrahams, "Impurity conduction at low concentrations," *Phys. Rev.*, vol. 120, no. 3, p. 745, 1960.

[53] R. A. Marcus, "On the Theory of Electron-Transfer Reactions. VI. Unified Treatment for Homogeneous and Electrode Reactions," *J. Chem. Phys.*, vol. 43, no. 2, p. 679, 1965.

[54] V. Coropceanu, J. Cornil, D. A. da Silva Filho, Y. Olivier, R. Silbey, and J.-L. Brédas, "Charge Transport in Organic Semiconductors," *Chem. Rev.*, vol. 107, no. 4, pp. 926–952, Apr. 2007.

[55] N. S. Hush, “An Overview of the First Half-Century of Molecular Electronics,” *Ann. N. Y. Acad. Sci.*, vol. 1006, no. 1, pp. 1–20, Dec. 2003.

[56] N. . Mott, “Conduction in non-crystalline materials,” *J. Non-Cryst. Solids*, vol. 8–10, pp. 1–18, 1972.

[57] P. Stallinga, “Electronic Transport in Organic Materials: Comparison of Band Theory with Percolation/(Variable Range) Hopping Theory,” *Adv. Mater.*, vol. 23, no. 30, pp. 3356–3362, Aug. 2011.

[58] J. Frenkel, “on Pre-Breakdown Phenomena in Insulators and Electronic Semi-Consuctors,” *Phys. Rev.*, pp. 647–648, Aug. 1938.

[59] W. R. Harrell and J. Frey, “Observation of Poole–Frenkel effect saturation in SiO 2 and other insulating films,” *Thin Solid Films*, vol. 352, no. 1, pp. 195–204, 1999.

[60] K. Berke, S. Tongay, M. A. McCarthy, A. G. Rinzler, B. R. Appleton, and A. F. Hebard, “Current transport across the pentacene/CVD-grown graphene interface for diode applications,” *J. Phys. Condens. Matter*, vol. 24, no. 25, p. 255802, Jun. 2012.

[61] A. Pillonnet and R. Ongaro, “Synthetic representations of the Poole Frenkel (PF) and Poole regimes,” *Rev. Phys. Appliquée*, vol. 25, no. 2, pp. 229–242, 1990.

[62] H. Bässler and A. Köhler, “Charge Transport in Organic Semiconductors,” in *Unimolecular and Supramolecular Electronics I*, vol. 312, R. M. Metzger, Ed. Berlin, Heidelberg: Springer Berlin Heidelberg, 2011, pp. 1–65.

[63] S. A. DiBenedetto, A. Facchetti, M. A. Ratner, and T. J. Marks, “Molecular Self-Assembled Monolayers and Multilayers for Organic and Unconventional Inorganic Thin-Film Transistor Applications,” *Adv. Mater.*, vol. 21, no. 14–15, pp. 1407–1433, Apr. 2009.

[64] G. Sharma, M. Roy, and M. Roy, “Charge conduction mechanism and photovoltaic properties of 1,2-diazoamino diphenyl ethane (DDE) based schottky device,” *Mater. Sci. Eng. B*, vol. 104, no. 1–2, pp. 15–25, Nov. 2003.

[65] X. Chen, Y.-M. Jeon, J.-W. Jang, L. Qin, F. Huo, W. Wei, and C. A. Mirkin, “On-Wire Lithography-Generated Molecule-Based Transport Junctions: A New Testbed for Molecular Electronics,” *J. Am. Chem. Soc.*, vol. 130, no. 26, pp. 8166–8168, Jul. 2008.

[66] J.-J. Andre, *Molecular semiconductors: photoelectrical properties and solar cells*. Springer, 1985.

[67] P. Stallinga, *Electrical characterization of organic electronic materials and devices*. WILEY-VCH, 2009.

[68] P. Murgatroyd, “Theory of space-charge-limited current enhanced by Frenkel effect,” *J Phys Appl Phys*, vol. 3, p. 151, 1970.

[69] J. Widmer, J. Fischer, W. Tress, K. Leo, and M. Riede, “Electric potential mapping by thickness variation: A new method for model-free mobility determination in organic semiconductor thin films,” *Org. Electron.*, vol. 14, no. 12, pp. 3460–3471, Dec. 2013.

[70] S. C. Jain, A. K. Kapoor, W. Geens, J. Poortmans, R. Mertens, and M. Willander, “Trap filled limit of conducting organic materials,” *J. Appl. Phys.*, vol. 92, no. 7, p. 3752, 2002.

[71] P. Anjaneyulu, C. S. Suchand Sangeeth, and R. Menon, “Carrier density-dependent transport in poly(3-methylthiophene): from injection-limited to space-charge-limited current,” *J. Phys. Appl. Phys.*, vol. 44, no. 31, p. 315101, Aug. 2011.

[72] O. L. A. Monti, “Understanding Interfacial Electronic Structure and Charge Transfer: An Electrostatic Perspective,” *J. Phys. Chem. Lett.*, vol. 3, no. 17, pp. 2342–2351, Sep. 2012.

[73] G. Heimel, S. Duhm, I. Salzmann, A. Gerlach, A. Strozecka, J. Niederhausen, C. Bürker, T. Hosokai, I. Fernandez-Torrente, G. Schulze, S. Winkler, A. Wilke, R. Schlesinger, J. Frisch, B. Bröker, A. Vollmer, B. Detlefs, J. Pflaum, S. Kera, K. J. Franke, N. Ueno, J. I. Pascual, F. Schreiber, and N. Koch, “Charged and metallic molecular monolayers through surface-induced aromatic stabilization,” *Nat. Chem.*, vol. 5, no. 3, pp. 187–194, Feb. 2013.

[74] J. Hwang, A. Wan, and A. Kahn, “Energetics of metal–organic interfaces: New experiments and assessment of the field,” *Mater. Sci. Eng. R Rep.*, vol. 64, no. 1–2, pp. 1–31, Mar. 2009.

[75] M. L. Cohen, “Schottky and Bardeen limits for Schottky barriers,” *J. Vac. Sci. Technol.*, vol. 16, no. 5, p. 1135, Sep. 1979.

[76] D. Cahen, A. Kahn, and E. Umbach, “Energetics of molecular interfaces,” *Mater. Today*, vol. 8, no. 7, pp. 32–41, 2005.

[77] M. G. Helander, Z. B. Wang, J. Qiu, and Z. H. Lu, “Band alignment at metal/organic and metal/oxide/organic interfaces,” *Appl. Phys. Lett.*, vol. 93, no. 19, p. 193310, 2008.

[78] S. J. Wang, J. C. Lin, W. R. Liou, Y. C. Luo, and C. Y. Cheng, “Observation of negative differential resistance phenomenon in a two-step barrier diode,” *Appl. Phys. Lett.*, vol. 68, no. 23, p. 3320, 1996.

[79] Y. Guo, B.-L. Gu, J.-Z. Yu, Z. Zeng, and Y. Kawazoe, “Resonant tunneling in step-barrier structures under an applied electric field,” *J. Appl. Phys.*, vol. 84, no. 2, p. 918, 1998.

[80] Y. N. Khanin, E. E. Vdovin, Y. V. Dubrovskii, K. S. Novoselov, and T. G. Andersson, “Tunneling resonances in structures with a two-step barrier,” *J. Exp. Theor. Phys. Lett.*, vol. 67, no. 10, pp. 863–868, 1998.

[81] P. A. Schulz and C. E. T. Gonçalves da Silva, “Two-step barrier diodes,” *Appl. Phys. Lett.*, vol. 52, no. 12, p. 960, 1988.

[82] M. G. Chapline and S. X. Wang, “Analytical formula for the tunneling current versus voltage for multilayer barrier structures,” *J. Appl. Phys.*, vol. 101, no. 8, p. 83706, 2007.

[83] P. E. Kornilovitch, A. M. Bratkovsky, and R. Stanley Williams, “Current rectification by molecules with asymmetric tunneling barriers,” *Phys. Rev. B*, vol. 66, no. 16, Oct. 2002.

[84] S. Lenfant, C. Krzeminski, C. Delerue, G. Allan, and D. Vuillaume, “Molecular Rectifying Diodes from Self-Assembly on Silicon,” *Nano Lett.*, vol. 3, no. 6, pp. 741–746, Jun. 2003.

[85] R. Liu, S.-H. Ke, W. Yang, and H. U. Baranger, “Organometallic molecular rectification,” *J. Chem. Phys.*, vol. 124, no. 2, p. 24718, 2006.

[86] C. A. Nijhuis, W. F. Reus, and G. M. Whitesides, “Molecular Rectification in Metal−SAM−Metal Oxide−Metal Junctions,” *J. Am. Chem. Soc.*, vol. 131, no. 49, pp. 17814–17827, Dec. 2009.

[87] C. A. Nijhuis, W. F. Reus, J. R. Barber, M. D. Dickey, and G. M. Whitesides, “Charge Transport and Rectification in Arrays of SAM-Based Tunneling Junctions,” *Nano Lett.*, vol. 10, no. 9, pp. 3611–3619, Sep. 2010.

[88] W. F. Reus, M. M. Thuo, N. D. Shapiro, C. A. Nijhuis, and G. M. Whitesides, “The SAM, Not the Electrodes, Dominates Charge Transport in Metal-Monolayer//Ga $_2$ O $_3$ /Gallium–Indium Eutectic Junctions,” *ACS Nano*, vol. 6, no. 6, pp. 4806–4822, Jun. 2012.

[89] H. J. Yoon, K.-C. Liao, M. R. Lockett, S. W. Kwok, M. Baghbanzadeh, and G. M. Whitesides, “Rectification in Tunneling Junctions: 2,2′-Bipyridyl-Terminated *n* -

Alkanethiolates," *J. Am. Chem. Soc.*, vol. 136, no. 49, pp. 17155–17162, Dec. 2014.

[90] L. Yuan, N. Nerngchamnong, L. Cao, H. Hamoudi, E. del Barco, M. Roemer, R. K. Sriramula, D. Thompson, and C. A. Nijhuis, "Controlling the direction of rectification in a molecular diode," *Nat. Commun.*, vol. 6, p. 6324, Mar. 2015.

[91] N. Nerngchamnong, L. Yuan, D.-C. Qi, J. Li, D. Thompson, and C. A. Nijhuis, "The role of van der Waals forces in the performance of molecular diodes," *Nat. Nanotechnol.*, vol. 8, no. 2, pp. 113–118, Jan. 2013.

[92] H. Jeong, D. Kim, G. Wang, S. Park, H. Lee, K. Cho, W.-T. Hwang, M.-H. Yoon, Y. H. Jang, H. Song, D. Xiang, and T. Lee, "Redox-Induced Asymmetric Electrical Characteristics of Ferrocene-Alkanethiolate Molecular Devices on Rigid and Flexible Substrates," *Adv. Funct. Mater.*, vol. 24, no. 17, pp. 2472–2480, May 2014.

[93] L. Müller-Meskamp, S. Karthäuser, H. J. W. Zandvliet, M. Homberger, U. Simon, and R. Waser, "Field-Emission Resonances at Tip/ *α* , *ω* -Mercaptoalkyl Ferrocene/Au Interfaces Studied by STM," *Small*, vol. 5, no. 4, pp. 496–502, Feb. 2009.

[94] H. Jeong, Y. Jang, D. Kim, W.-T. Hwang, J.-W. Kim, and T. Lee, "An In-Depth Study of Redox-Induced Conformational Changes in Charge Transport Characteristics of a Ferrocene-Alkanethiolate Molecular Electronic Junction: Temperature-Dependent Transition Voltage Spectroscopy Analysis," *J. Phys. Chem. C*, vol. 120, no. 6, pp. 3564–3572, Feb. 2016.

[95] H. Kolb, M. . Finn, and K. B. Sharpless, "Click Chemistry: Diverse Chemical Function from a Few Good Reactions," *Angew. Chem. Int. Ed.*, vol. 40, pp. 2004–2021, 2001.

[96] W. H. Binder and R. Sachsenhofer, "'Click' Chemistry in Polymer and Materials Science," *Macromol. Rapid Commun.*, vol. 28, no. 1, pp. 15–54, Jan. 2007.

[97] J. Escorihuela, A. T. M. Marcelis, and H. Zuilhof, "Metal-Free Click Chemistry Reactions on Surfaces," *Adv. Mater. Interfaces*, vol. 2, no. 13, p. n/a-n/a, Sep. 2015.

[98] P. Appukkuttan, W. Dehaen, V. V. Fokin, and E. Van der Eycken, "A Microwave-Assisted Click Chemistry Synthesis of 1,4-Disubstituted 1,2,3-Triazoles via a Copper(I)-Catalyzed Three-Component Reaction," *Org. Lett.*, vol. 6, no. 23, pp. 4223–4225, Nov. 2004.

[99] S. Gupta, B. Schade, S. Kumar, C. Böttcher, S. K. Sharma, and R. Haag, “Non-ionic Dendronized Multiamphiphilic Polymers as Nanocarriers for Biomedical Applications,” *Small*, vol. 9, no. 6, pp. 894–904, Mar. 2013.

[100] M. Firstenberg, K. N. Shivananda, I. Cohen, O. Solomeshch, V. Medvedev, N. Tessler, and Y. Eichen, “Harnessing ‘Click’-Type Chemistry for the Preparation of Novel Electronic Materials,” *Adv. Funct. Mater.*, vol. 21, no. 4, pp. 634–643, Feb. 2011.

[101] C. O. Kappe and E. Van der Eycken, “Click chemistry under non-classical reaction conditions,” *Chem Soc Rev*, vol. 39, no. 4, pp. 1280–1290, 2010.

[102] V. D. Bock, H. Hiemstra, and J. H. van Maarseveen, “CuI-Catalyzed Alkyne-Azide ‘Click’ Cycloadditions from a Mechanistic and Synthetic Perspective,” *Eur. J. Org. Chem.*, vol. 2006, no. 1, pp. 51–68, Jan. 2006.

[103] S. Bräse, C. Gil, K. Knepper, and V. Zimmermann, “Organic Azides: An Exploding Diversity of a Unique Class of Compounds,” *Angew. Chem. Int. Ed.*, vol. 44, no. 33, pp. 5188–5240, Aug. 2005.

[104] J. Nie, J.-P. Li, H. Deng, and H.-C. Pan, “Progress on Click Chemistry and Its Application in Chemical Sensors,” *Chin. J. Anal. Chem.*, vol. 43, no. 4, pp. 609–617, Apr. 2015.

[105] M. V. Gil, M. J. Arevalo, and O. Lopez, “Click chemistry-what’s in a name? Triazole synthesis and beyond,” *Synthesis*, vol. 2007, no. 11, pp. 1589–1620, 2007.

[106] C. W. Tornøe, C. Christensen, and M. Meldal, “Peptidotriazoles on Solid Phase: [1,2,3]-Triazoles by Regiospecific Copper(I)-Catalyzed 1,3-Dipolar Cycloadditions of Terminal Alkynes to Azides,” *J. Org. Chem.*, vol. 67, no. 9, pp. 3057–3064, May 2002.

[107] V. Castro, H. Rodríguez, and F. Albericio, “CuAAC: An Efficient Click Chemistry Reaction on Solid Phase,” *ACS Comb. Sci.*, vol. 18, no. 1, pp. 1–14, Jan. 2016.

[108] M. Natali, M. Ravaglia, F. Scandola, J. Boixel, Y. Pellegrin, E. Blart, and F. Odobel, “Long-Range Charge Separation in a Ferrocene–(Zinc Porphyrin)–Naphthalenediimide Triad. Asymmetric Role of 1,2,3-Triazole Linkers,” *J. Phys. Chem. C*, p. 130912075807001, Sep. 2013.

[109] Y. Li and C. Cai, “Click Chemistry-Based Functionalization on Non-Oxidized Silicon Substrates,” *Chem. - Asian J.*, vol. 6, no. 10, pp. 2592–2605, Oct. 2011.

[110] M. A. White, A. Maliakal, N. J. Turro, and J. Koberstein, “‘Click’ Dielectrics: Use of 1,3-Dipolar Cycloadditions to Generate Diverse Core-Shell Nanoparticle Structures

with Applications to Flexible Electronics," *Macromol. Rapid Commun.*, vol. 29, no. 18, pp. 1544–1548, Sep. 2008.

[111] D. I. Rozkiewicz, D. Jańczewski, W. Verboom, B. J. Ravoo, and D. N. Reinhoudt, "'Click' Chemistry by Microcontact Printing," *Angew. Chem. Int. Ed.*, vol. 45, no. 32, pp. 5292–5296, Aug. 2006.

[112] A. C. Cardiel, M. C. Benson, L. M. Bishop, K. M. Louis, J. C. Yeager, Y. Tan, and R. J. Hamers, "Chemically Directed Assembly of Photoactive Metal Oxide Nanoparticle Heterojunctions *via* the Copper-Catalyzed Azide–Alkyne Cycloaddition 'Click' Reaction," *ACS Nano*, vol. 6, no. 1, pp. 310–318, Jan. 2012.

[113] X. Chen, A. B. Braunschweig, M. J. Wiester, S. Yeganeh, M. A. Ratner, and C. A. Mirkin, "Spectroscopic Tracking of Molecular Transport Junctions Generated by Using Click Chemistry," *Angew. Chem. Int. Ed.*, vol. 48, no. 28, pp. 5178–5181, Jun. 2009.

[114] J. M. Casas-Solvas, A. Vargas-Berenguel, L. F. Capitán-Vallvey, and F. Santoyo-González, "Convenient Methods for the Synthesis of Ferrocene−Carbohydrate Conjugates," *Org. Lett.*, vol. 6, no. 21, pp. 3687–3690, Oct. 2004.

[115] Y. Lee, G. M. Morales, and L. Yu, "Self-Assembled Monolayers of Isocyanides on Nickel Electrodes," *Angew. Chem. Int. Ed.*, vol. 44, no. 27, pp. 4228–4231, Jul. 2005.

[116] S.-Y. Baek, Y.-W. Kim, S.-H. Yoo, K. Chung, N.-K. Kim, and J.-S. Kim, "Synthesis and Rust Preventing Properties of Dodecyl Succinate Derivatives Containing Triazole Groups," *Ind. Eng. Chem. Res.*, vol. 51, no. 28, pp. 9669–9678, Jul. 2012.

[117] D. Evrard, F. Lambert, C. Policar, V. Balland, and B. Limoges, "Electrochemical Functionalization of Carbon Surfaces by Aromatic Azide or Alkyne Molecules: A Versatile Platform for Click Chemistry," *Chem. - Eur. J.*, vol. 14, no. 30, pp. 9286–9291, Oct. 2008.

[118] Y. R. Leroux and P. Hapiot, "Nanostructured Monolayers on Carbon Substrates Prepared by Electrografting of Protected Aryldiazonium Salts," *Chem. Mater.*, vol. 25, no. 3, pp. 489–495, Feb. 2013.

[119] S. Ranganathan, R. Mccreery, S. M. Majji, and M. Madou, "Photoresist-derived carbon for microelectromechanical systems and electrochemical applications," *J. Electrochem. Soc.*, vol. 147, no. 1, pp. 277–282, 2000.

[120] Y. R. Leroux, H. Fei, J.-M. Noël, C. Roux, and P. Hapiot, "Efficient Covalent Modification of a Carbon Surface: Use of a Silyl Protecting Group To Form an

Active Monolayer," *J. Am. Chem. Soc.*, vol. 132, no. 40, pp. 14039–14041, Oct. 2010.

[121] S. Ranganathan, T.-C. Kuo, and R. L. McCreery, "Facile Preparation of Active Glassy Carbon Electrodes with Activated Carbon and Organic Solvents," *Anal. Chem.*, vol. 71, no. 16, pp. 3574–3580, Aug. 1999.

[122] A. L. Prince, "Homogeneous and Heterogeneous Approaches to 1, 2, 4-Triazine-Accelerated Copper-Catalyzed Azide-Alkyne Cycloadditions," 2011.

[123] J. J. Blackstock, A. A. Rostami, A. M. Nowak, R. L. McCreery, M. R. Freeman, and M. T. McDermott, "Ultraflat Carbon Film Electrodes Prepared by Electron Beam Evaporation," *Anal. Chem.*, vol. 76, no. 9, pp. 2544–2552, May 2004.

[124] F. Anariba, S. H. DuVall, and R. L. McCreery, "Mono- and Multilayer Formation by Diazonium Reduction on Carbon Surfaces Monitored with Atomic Force Microscopy 'Scratching,'" *Anal. Chem.*, vol. 75, no. 15, pp. 3837–3844, Aug. 2003.

[125] R. E. Ruther, Q. Cui, and R. J. Hamers, "Conformational Disorder Enhances Electron Transfer Through Alkyl Monolayers: Ferrocene on Conductive Diamond," *J. Am. Chem. Soc.*, vol. 135, no. 15, pp. 5751–5761, Apr. 2013.

[126] R. C. Chambers, C. E. Inman, and J. E. Hutchison, "Electrochemical Detection of Nanoscale Phase Separation in Binary Self-Assembled Monolayers," *Langmuir*, vol. 21, no. 10, pp. 4615–4621, May 2005.

[127] H. J. Yoon, C. M. Bowers, M. Baghbanzadeh, and G. M. Whitesides, "The Rate of Charge Tunneling Is Insensitive to Polar Terminal Groups in Self-Assembled Monolayers in $Ag^{TS}S(CH_2)_nM(CH_2)_mT//Ga_2O_3$/EGaIn Junctions," *J. Am. Chem. Soc.*, vol. 136, no. 1, pp. 16–19, Jan. 2014.

[128] W. J. Clark, J. D. Ramsey, R. L. McCreery, and G. S. Frankel, "A Galvanic Corrosion Approach to Investigating Chromate Effects on Aluminum Alloy 2024-T3," *J. Electrochem. Soc.*, vol. 149, no. 5, p. B179, 2002.

[129] A. Aviram and M. A. Ratner, "Molecular rectifiers," *Chem. Phys. Lett.*, vol. 29, no. 2, pp. 277–283, 1974.

[130] R. Stadler, V. Geskin, and J. Cornil, "A theoretical view of unimolecular rectification," *J. Phys. Condens. Matter*, vol. 20, no. 37, p. 374105, Sep. 2008.

[131] M. Elbing, R. Ochs, M. Koentopp, M. Fischer, C. von Hänisch, F. Weigend, F. Evers, H. B. Weber, and M. Mayor, "A single-molecule diode," *Proc. Natl. Acad. Sci. U. S. A.*, vol. 102, no. 25, pp. 8815–8820, 2005.

[132] T. Sengoku, T. Yamao, and S. Hotta, "Organic light-emitting diodes based on layered films of thiophene/phenylene co-oligomers," *J. Non-Cryst. Solids*, vol. 358, no. 17, pp. 2525–2529, Sep. 2012.

[133] D. Ammermann, A. Böhler, S. Dirr, H. H. Johannes, and W. Kowalsky, "Multilayer organic light emitting diodes for flat panel displays," *Int. J. Electron. Commun.*, vol. 50, pp. 327–333, 1996.

[134] E. Saracco, B. Bouthinon, J.-M. Verilhac, C. Celle, N. Chevalier, D. Mariolle, O. Dhez, and J.-P. Simonato, "Work Function Tuning for High-Performance Solution-Processed Organic Photodetectors with Inverted Structure," *Adv. Mater.*, vol. 25, no. 45, pp. 6534–6538, Dec. 2013.

[135] H. Kong, J. Sinha, D. Hoeft, S. B. Kirschner, D. H. Reich, and H. E. Katz, "Solution processable organic p–n junction bilayer vertical photodiodes," *Org. Electron.*, vol. 14, no. 3, pp. 703–710, Mar. 2013.

[136] X. Gong, M. Tong, Y. Xia, W. Cai, J. S. Moon, Y. Cao, G. Yu, C.-L. Shieh, B. Nilsson, and A. J. Heeger, "High-detectivity polymer photodetectors with spectral response from 300 nm to 1450 nm," *Science*, vol. 325, no. 5948, pp. 1665–1667, 2009.

[137] H. Kleemann, R. Gutierrez, S. Avdoshenko, G. Cuniberti, K. Leo, and B. Lüssem, "Reverse breakdown behavior in organic pin-diodes comprising C60 and pentacene: Experiment and theory," *Org. Electron.*, vol. 14, no. 1, pp. 193–199, Jan. 2013.

[138] C. M. Fischer, M. Burghard, S. Roth, and K. v Klitzing, "Organic quantum wells: molecular rectification and single-electron tunnelling," *EPL Europhys. Lett.*, vol. 28, no. 2, p. 129, 1994.

[139] H. Kleemann, S. Schumann, U. Jörges, F. Ellinger, K. Leo, and B. Lüssem, "Organic pin-diodes approaching ultra-high-frequencies," *Org. Electron.*, vol. 13, no. 6, pp. 1114–1120, Jun. 2012.

[140] H. Wang and D. Yan, "Organic heterostructures in organic field-effect transistors," *NPG Asia Mater.*, vol. 2, no. 2, pp. 69–78, Apr. 2010.

[141] R. M. Metzger, "Unimolecular rectifiers: Present status," *Chem. Phys.*, vol. 326, no. 1, pp. 176–187, Jul. 2006.

[142] C. Van Dyck and M. A. Ratner, "Molecular Rectifiers: A New Design Based on Asymmetric Anchoring Moieties," *Nano Lett.*, vol. 15, no. 3, pp. 1577–1584, Mar. 2015.

[143] R. M. Metzger, “Unimolecular Electronics,” *Chem. Rev.*, vol. 115, no. 11, pp. 5056–5115, Jun. 2015.

[144] A. Batra, J. S. Meisner, P. Darancet, Q. Chen, M. L. Steigerwald, C. Nuckolls, and L. Venkataraman, “Molecular diodes enabled by quantum interference,” *Faraday Discuss*, Jun. 2014.

[145] I. Díez-Pérez, J. Hihath, Y. Lee, L. Yu, L. Adamska, M. A. Kozhushner, I. I. Oleynik, and N. Tao, “Rectification and stability of a single molecular diode with controlled orientation,” *Nat. Chem.*, vol. 1, no. 8, pp. 635–641, Nov. 2009.

[146] J. Hihath, C. Bruot, H. Nakamura, Y. Asai, I. Díez-Pérez, Y. Lee, L. Yu, and N. Tao, “Inelastic Transport and Low-Bias Rectification in a Single-Molecule Diode,” *ACS Nano*, vol. 5, no. 10, pp. 8331–8339, Oct. 2011.

[147] A. Batra, P. Darancet, Q. Chen, J. S. Meisner, J. R. Widawsky, J. B. Neaton, C. Nuckolls, and L. Venkataraman, “Tuning Rectification in Single-Molecular Diodes,” *Nano Lett.*, vol. 13, no. 12, pp. 6233–6237, Dec. 2013.

[148] S. Lenfant, D. Guerin, F. Tran Van, C. Chevrot, S. Palacin, J. P. Bourgoin, O. Bouloussa, F. Rondelez, and D. Vuillaume, “Electron Transport through Rectifying Self-Assembled Monolayer Diodes on Silicon: Fermi-Level Pinning at the Molecule−Metal Interface,” *J. Phys. Chem. B*, vol. 110, no. 28, pp. 13947–13958, Jul. 2006.

[149] G. Zhang, M. A. Ratner, and M. G. Reuter, “Is Molecular Rectification Caused by Asymmetric Electrode Couplings or by a Molecular Bias Drop?,” *J. Phys. Chem. C*, vol. 119, no. 11, pp. 6254–6260, Mar. 2015.

[150] J. Wu, K. Mobley, and R. L. McCreery, “Electronic characteristics of fluorene/TiO[sub 2] molecular heterojunctions,” *J. Chem. Phys.*, vol. 126, no. 2, p. 24704, 2007.

[151] A. J. Bergren and R. L. McCreery, “Analytical Chemistry in Molecular Electronics,” *Annu. Rev. Anal. Chem.*, vol. 4, no. 1, pp. 173–195, Jul. 2011.

[152] J. A. Fereiro, M. Kondratenko, A. J. Bergren, and R. L. McCreery, “Internal Photoemission in Molecular Junctions: Parameters for Interfacial Barrier Determinations,” *J. Am. Chem. Soc.*, vol. 137, no. 3, pp. 1296–1304, Jan. 2015.

[153] A. Morteza Najarian, B. Szeto, U. M. Tefashe, and R. L. McCreery, “Robust All-Carbon Molecular Junctions on Flexible or Semi-Transparent Substrates Using ‘Process-Friendly’ Fabrication,” *ACS Nano*, Aug. 2016.

[154] S. Hillebrandt, T. Adermann, M. Alt, J. Schinke, T. Glaser, E. Mankel, G. Hernandez-Sosa, W. Jaegermann, U. Lemmer, A. Pucci, W. Kowalsky, K. Müllen, R. Lovrincic, and M. Hamburger, “Naphthalene Tetracarboxydiimide-Based n-Type Polymers with Removable Solubility via Thermally Cleavable Side Chains,” *ACS Appl. Mater. Interfaces*, vol. 8, no. 7, pp. 4940–4945, Feb. 2016.

[155] S. Biniak, G. Szymanski, J. Siedlewski, and A. Swiatkowski, “The characterization of activated carbons with oxygen and nitrogen surface groups,” vol. 35, pp. 1799–1810, 1997.

[156] C.-M. Chen, J.-Q. Huang, Q. Zhang, W.-Z. Gong, Q.-H. Yang, M.-Z. Wang, and Y.-G. Yang, “Annealing a graphene oxide film to produce a free standing high conductive graphene film,” *Carbon*, vol. 50, no. 2, pp. 659–667, Feb. 2012.

[157] J. Wang, C. R. Friedman, W. Cabrera, K. Tan, Y.-J. Lee, Y. J. Chabal, and J. W. P. Hsu, “Effect of metal/bulk-heterojunction interfacial properties on organic photovoltaic device performance,” *J. Mater. Chem. A*, vol. 2, no. 37, p. 15288, Aug. 2014.

[158] L. Luo, L. Balhorn, B. Vlaisavljevich, D. Ma, L. Gagliardi, and C. D. Frisbie, “Hopping Transport and Rectifying Behavior in Long Donor–Acceptor Molecular Wires,” *J. Phys. Chem. C*, vol. 118, no. 46, pp. 26485–26497, Nov. 2014.

[159] S. S. Simeonov, E. Kafedjiiska, A. Szekeres, C. Ristoscu, E. Gyorgy, and I. N. Mihailescu, “Trap-assisted tunneling at temperatures near 77 K in laser annealed Si n[sup +]-p junctions,” *J. Appl. Phys.*, vol. 90, no. 2, p. 860, 2001.

[160] K. Sakai, M. Saito, M. Sugi, and S. Iizima, “Molecular p-n junction photodiodes of langmuir multilayer semiconductors,” *Jpn J Appl Phys*, vol. 24, pp. 865–869, 1985.

[161] A. R. Riben and D. L. Feucht, “Electrical Transport in nGe-pGaAs Heterojunctions†,” *Int. J. Electron.*, vol. 20, no. 6, pp. 583–599, Jun. 1966.

[162] Li, J. Hihath, F. Chen, T. Masuda, L. Zang, and Tao, “Thermally Activated Electron Transport in Single Redox Molecules,” *J. Am. Chem. Soc.*, vol. 129, no. 37, pp. 11535–11542, Sep. 2007.

[163] M. Kim, H. Ju, and J. Kim, “Oxygen-doped porous silicon carbide spheres as electrode materials for supercapacitors,” *Phys Chem Chem Phys*, vol. 18, no. 4, pp. 3331–3338, 2016.

[164] Y. Lu, Z. Xiao, Y. Yuan, H. Wu, Z. An, Y. Hou, C. Gao, and J. Huang, “Fluorine substituted thiophene–quinoxalinecopolymer to reduce the HOMO level and

increase the dielectric constant for high open-circuit voltage organic solar cells," *J Mater Chem C*, vol. 1, no. 4, pp. 630–637, 2013.

[165] R. L. McCreery, "Effects of electronic coupling and electrostatic potential on charge transport in carbon-based molecular electronic junctions," *Beilstein J. Nanotechnol.*, vol. 7, pp. 32–46, Jan. 2016.

[166] M. Kondratenko, S. R. Stoyanov, S. Gusarov, A. Kovalenko, and R. L. McCreery, "Theoretical Modeling of Tunneling Barriers in Carbon-Based Molecular Electronic Junctions," *J. Phys. Chem. C*, vol. 119, no. 21, pp. 11286–11295, May 2015.

[167] M. Saito, M. Sugi, and S. Iizima, "Evidence for Ambipolar conduction in Dye-Sensitized p-n junctions of Langmuir-Blodgett Films.," *Jpn J Appl Phys*, vol. 24, p. 379, 1985.

[168] G. A. Rojas, Y. Wu, G. Haugstad, and C. D. Frisbie, "Measuring the Thickness and Potential Profiles of the Space-Charge Layer at Organic/Organic Interfaces under Illumination and in the Dark by Scanning Kelvin Probe Microscopy," *ACS Appl. Mater. Interfaces*, vol. 8, no. 9, pp. 5772–5776, Mar. 2016.

[169] H. klauk, *Organic Electronics II: More Materials and Applications*, 1st ed., vol. 2. WILEY-VCH, 2012.

[170] J. Bredas and G. Street, "Polarons, Bipolarons, and Solitons in Conducting Polymers," *Acc. Chem. Res.*, vol. 18, pp. 309–315, 1985.

[171] A. J. Mozer, P. Denk, M. C. Scharber, H. Neugebauer, N. S. Sariciftci, P. Wagner, L. Lutsen, and D. Vanderzande, "Novel Regiospecific MDMO−PPV Copolymer with Improved Charge Transport for Bulk Heterojunction Solar Cells," *J. Phys. Chem. B*, vol. 108, no. 17, pp. 5235–5242, Apr. 2004.

[172] R. Coehoorn, "Hopping mobility of charge carriers in disordered organic host-guest systems: Dependence on the charge-carrier concentration," *Phys. Rev. B*, vol. 75, no. 15, Apr. 2007.

[173] W. F. Pasveer, J. Cottaar, C. Tanase, R. Coehoorn, P. A. Bobbert, P. W. M. Blom, D. M. de Leeuw, and M. A. J. Michels, "Unified Description of Charge-Carrier Mobilities in Disordered Semiconducting Polymers," *Phys. Rev. Lett.*, vol. 94, no. 20, May 2005.

[174] H. Bässler, "Charge transport in disordered organic photoconductors a Monte Carlo simulation study," *Phys. Status Solidi B*, vol. 175, no. 1, pp. 15–56, 1993.

[175]Z. G. Yu, D. L. Smith, A. Saxena, R. L. Martin, and A. R. Bishop, “Molecular geometry fluctuation model for the mobility of conjugated polymers,” *Phys. Rev. Lett.*, vol. 84, no. 4, p. 721, 2000.

[176]D. H. Dunlap, P. E. Parris, and V. M. Kenkre, “Charge-dipole model for the universal field dependence of mobilities in molecularly doped polymers,” *Phys. Rev. Lett.*, vol. 77, no. 3, p. 542, 1996.

[177]D. Monroe, “Hopping in exponential band tails,” *Phys. Rev. Lett.*, vol. 54, no. 2, p. 146, 1985.

[178]B. N. Limketkai, P. Jadhav, and M. A. Baldo, “Electric-field-dependent percolation model of charge-carrier mobility in amorphous organic semiconductors,” *Phys. Rev. B*, vol. 75, no. 11, Mar. 2007.

[179]V. N. Prigodin and A. J. Epstein, “Nature of insulator–metal transition and novel mechanism of charge transport in the metallic state of highly doped electronic polymers,” *Synth. Met.*, vol. 125, no. 1, pp. 43–53, Nov. 2001.

[180]F. W. Schmidlin, “Theory of trap-controlled transient photoconduction,” *Phys. Rev. B*, vol. 16, no. 6, p. 2362, 1977.

[181]T. Holstein, “Studies of polaron motion: Part II. The ‘small’ polaron,” *Ann. Phys.*, vol. 8, no. 3, pp. 343–389, 1959.

[182]A. M. Gilbertson, J. M. S. Orr, P. D. Buckle, S. Clowes, M. Fearn, C. J. Storey, L. Buckle, L. F. Cohen, and T. Ashley, “Low-temperature Schottky barrier tunneling in In Sb ⁄ In x Al 1 − x Sb quantum well heterostructures,” *Phys. Rev. B*, vol. 76, no. 8, Aug. 2007.

[183]M. Michio, J. Yukitoshi, A. Tomonori, and K. Takashi, “Analysis of Current-Voltage Characteristics of Organic Electroluminescent Devices on the Basis of Schottky Emission Mechanism,” *Jpn J Appl Phys*, vol. 35, pp. 5735–5739, 1996.

[184]I. D. Parker, “Carrier tunneling and device characteristics in polymer light-emitting diodes,” *J. Appl. Phys.*, vol. 75, no. 3, p. 1656, 1994.

[185]G. Lengyel, “Schottky Emission and Conduction in Some Organic Insulating Materials,” *J. Appl. Phys.*, vol. 37, no. 2, p. 807, 1966.

[186]V. Mujica, A. E. Roitberg, and M. Ratner, “Molecular wire conductance: Electrostatic potential spatial profile,” *J. Chem. Phys.*, vol. 112, no. 15, p. 6834, 2000.

[187]B. N. Limketkai and M. A. Baldo, “Charge injection into cathode-doped amorphous organic semiconductors,” *Phys. Rev. B*, vol. 71, no. 8, Feb. 2005.

[188] M. A. Baldo and S. R. Forrest, “Interface-limited injection in amorphous organic semiconductors,” *Phys. Rev. B*, vol. 64, no. 8, Aug. 2001.

[189] R. Kiebooms, A. Aleshin, K. Hutchison, F. Wudl, and A. J. Heeger, “Doped Poly(3,4-ethylenedioxythiophene) Films: Thermal, Electromagnetical and Morphological Analysis,” *Synth. Met.*, vol. 101, pp. 436–437, 1999.

[190] A. Aleshin, R. Kiebooms, and A. J. Heeger, “Metallic conductivity of highly doped poly(3,4-ethylenedioxythiophene),” *Synth. Met.*, vol. 101, pp. 369–370, 1999.

[191] A. Aleshin, R. Kiebooms, R. Menon, F. Wudl, and A. J. Heeger, “Metallic conductivity at low temperatures in poly (3, 4-ethylenedioxythiophene) doped with PF 6,” *Phys. Rev. B*, vol. 56, no. 7, p. 3659, 1997.

[192] P. Martin, M. L. Della Rocca, A. Anthore, P. Lafarge, and J.-C. Lacroix, “Organic Electrodes Based on Grafted Oligothiophene Units in Ultrathin, Large-Area Molecular Junctions,” *J. Am. Chem. Soc.*, vol. 134, no. 1, pp. 154–157, Jan. 2012.

[193] C. E. Smith, S. O. Odoh, S. Ghosh, L. Gagliardi, C. J. Cramer, and C. D. Frisbie, “Length-Dependent Nanotransport and Charge Hopping Bottlenecks in Long Thiophene-Containing π-Conjugated Molecular Wires,” *J. Am. Chem. Soc.*, vol. 137, no. 50, pp. 15732–15741, Dec. 2015.

[194] S. Baranton and D. Bélanger, “In situ generation of diazonium cations in organic electrolyte for electrochemical modification of electrode surface,” *Electrochimica Acta*, vol. 53, no. 23, pp. 6961–6967, Oct. 2008.

[195] A. M. Mahmoud, A. J. Bergren, and R. L. McCreery, “Derivatization of Optically Transparent Materials with Diazonium Reagents for Spectroscopy of Buried Interfaces,” *Anal. Chem.*, vol. 81, no. 16, pp. 6972–6980, Aug. 2009.

[196] M. J. Crookes and D. L. H. Williams, “Nitrosation by alkyl nitrites. Part 5. Kinetics and mechanism of reactions in acetonitrile,” *J. Chem. Soc. Perkin Trans. 2*, no. 9, pp. 1319–1322, 1989.

[197] V. Stockhausen, “Modulation of material properties using Nanoelectrochemistry: from active plasmonic devices and photovoltaic systems to ultrathin electroactive layers,” These De Doctorat, Paris Diderot- Paris 7, France, 2011.

[198] T. Fluteau, C. Bessis, C. Barraud, M. L. Della Rocca, P. Martin, J.-C. Lacroix, and P. Lafarge, “Tuning the thickness of electrochemically grafted layers in large area molecular junctions,” *J. Appl. Phys.*, vol. 116, no. 11, p. 114509, Sep. 2014.

[199] V. Stockhausen, J. Ghilane, P. Martin, G. Trippé-Allard, H. Randriamahazaka, and J.-C. Lacroix, “Grafting Oligothiophenes on Surfaces by Diazonium

Electroreduction: A Step toward Ultrathin Junction with Well-Defined Metal/Oligomer Interface," *J. Am. Chem. Soc.*, vol. 131, no. 41, pp. 14920–14927, Oct. 2009.

[200] C. Fave, Y. Leroux, G. Trippé, H. Randriamahazaka, V. Noel, and J.-C. Lacroix, "Tunable Electrochemical Switches Based on Ultrathin Organic Films," *J. Am. Chem. Soc.*, vol. 129, no. 7, pp. 1890–1891, Feb. 2007.

[201] H. Fukagawa, H. Yamane, T. Kataoka, S. Kera, M. Nakamura, K. Kudo, and N. Ueno, "Origin of the highest occupied band position in pentacene films from ultraviolet photoelectron spectroscopy: Hole stabilization versus band dispersion," *Phys. Rev. B*, vol. 73, no. 24, Jun. 2006.

[202] D. S. Jeong and C. S. Hwang, "Tunneling-assisted Poole-Frenkel conduction mechanism in HfO[sub 2] thin films," *J. Appl. Phys.*, vol. 98, no. 11, p. 113701, 2005.

[203] S. Martinuzzi and O. Mallem, "Dark-current conduction processes in CdS–Cu2S thin-film photocells," *Phys. Status Solidi A*, vol. 16, no. 1, pp. 339–344, 1973.

[204] H. Sun, Y. Chen, L. Zhu, Q. Guo, D. Yang, J. Chen, and D. Ma, "Realization of Optimal Interconnector for Tandem Organic Light-Emitting Diodes with Record Efficiency," *Adv. Electron. Mater.*, vol. 1, no. 11, p. 1500176, Nov. 2015.

[205] G. G. Roberts and J. . Polanco, "Thermally assisted tunneling in dielectric films," *Phys Stat Sol A*, vol. 1, p. 409, 1970.

[206] O. Ivashenko, A. J. Bergren, and R. L. McCreery, "Light Emission as a Probe of Energy Losses in Molecular Junctions," *J. Am. Chem. Soc.*, vol. 138, no. 3, pp. 722–725, Jan. 2016.

[207] L. C. T. Shoute, Y. Wu, and R. L. McCreery, "Direct spectroscopic monitoring of conductance switching in polythiophene memory devices," *Electrochimica Acta*, vol. 110, pp. 437–445, Nov. 2013.

Appendix

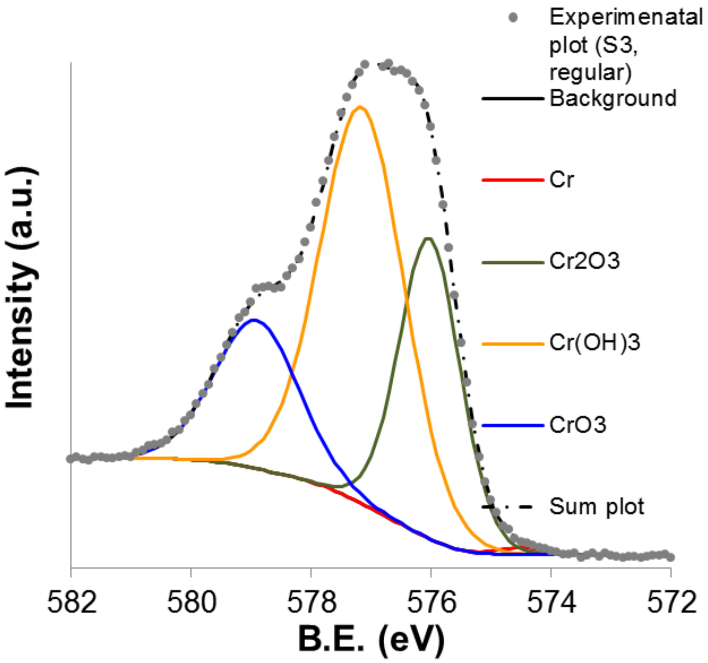

Figure A-1. XPS of chromium oxide layer.

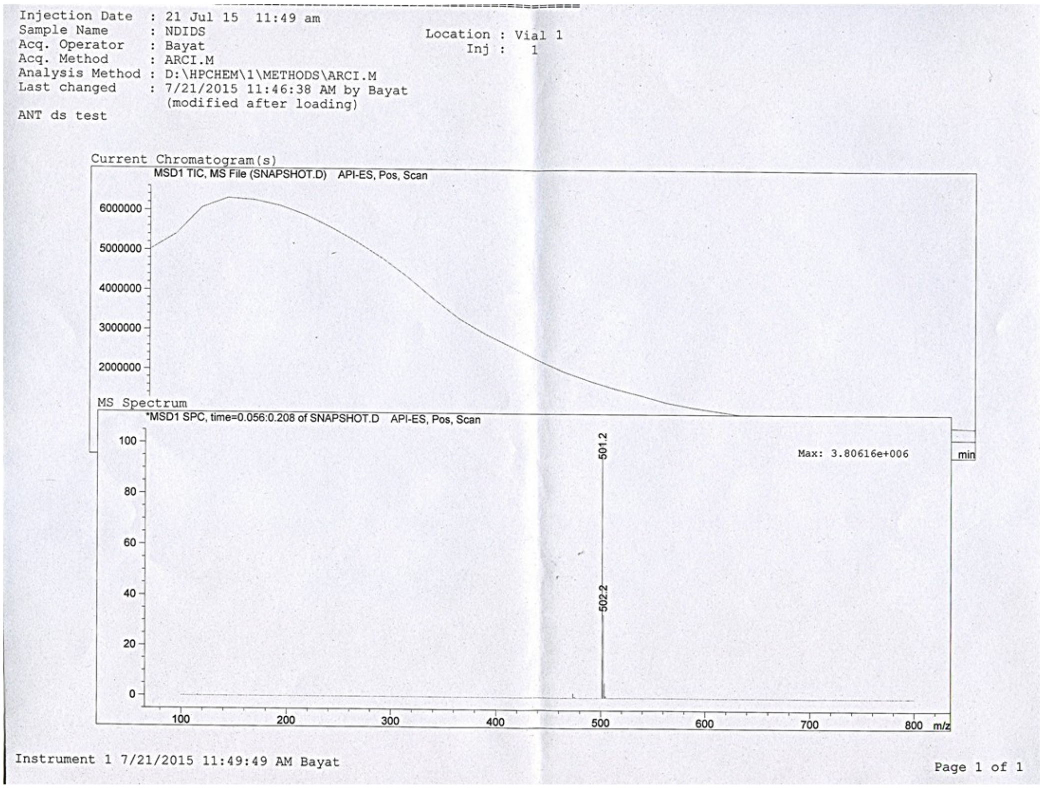

```
Injection Date  : 21 Jul 15   11:49 am
Sample Name     : NDIDS
Acq. Operator   : Bayat                        Location : Vial 1
Acq. Method     : ARCI.M                            Inj :   1
Analysis Method : D:\HPCHEM\1\METHODS\ARCI.M
Last changed    : 7/21/2015 11:46:38 AM by Bayat
                  (modified after loading)
ANT ds test
```

```
Instrument 1 7/21/2015 11:49:49 AM Bayat                    Page 1 of 1
```

Figure A-2. NDI DS LC-MS.

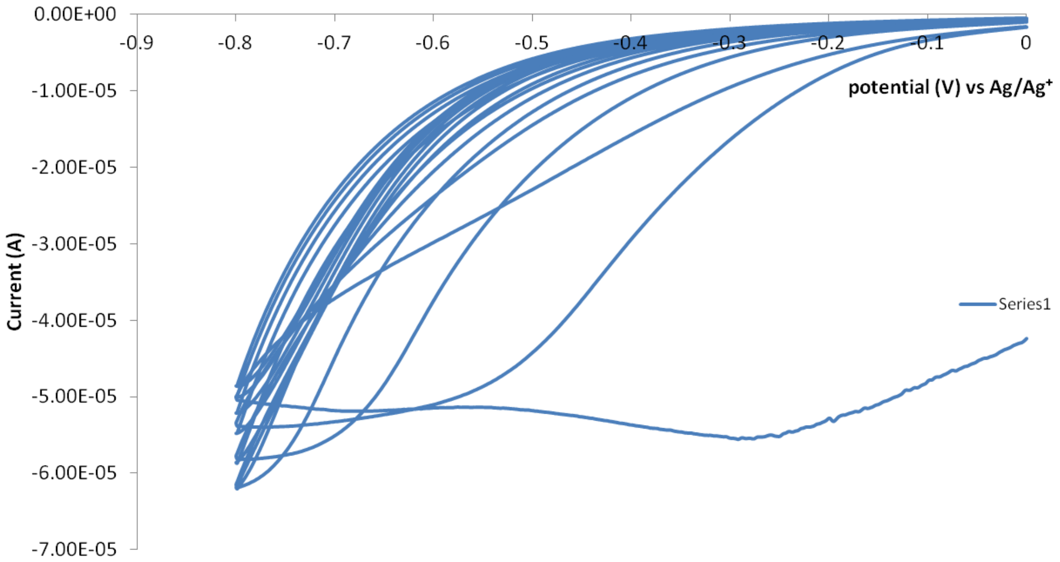

Figure A-3. Formation of BTB layer.

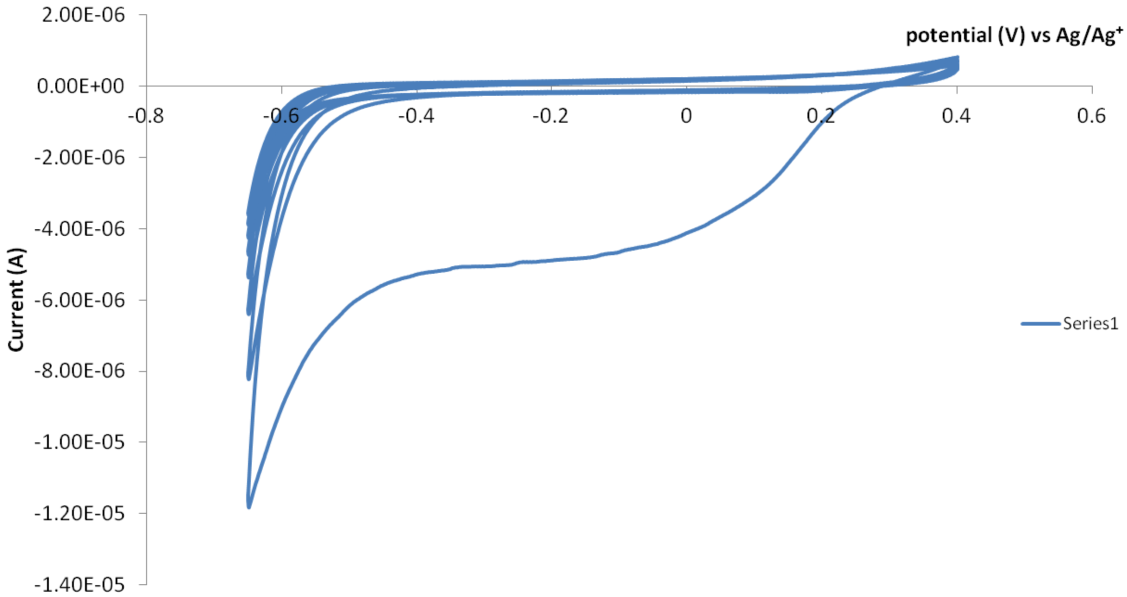

Figure A-4. Formation of AQ layer.

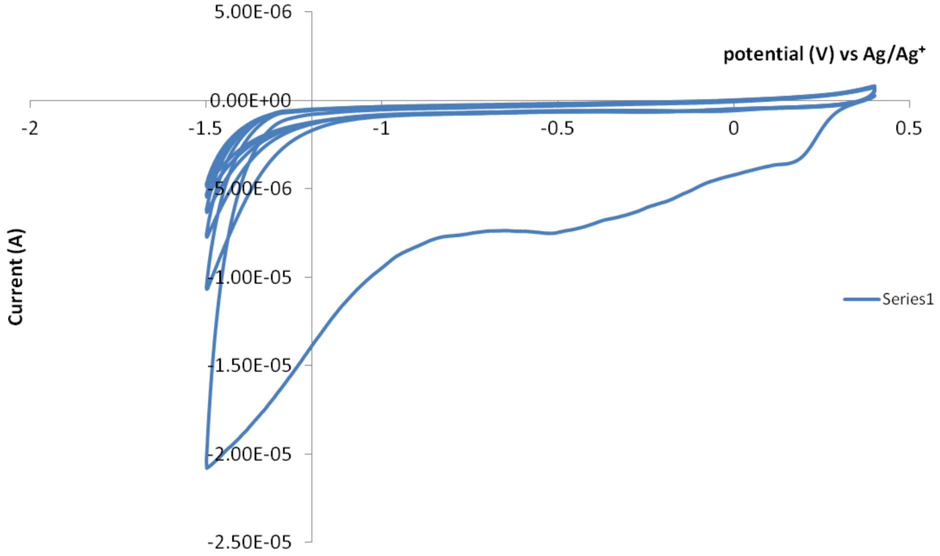

Figure A-5. Formation of FL layer.

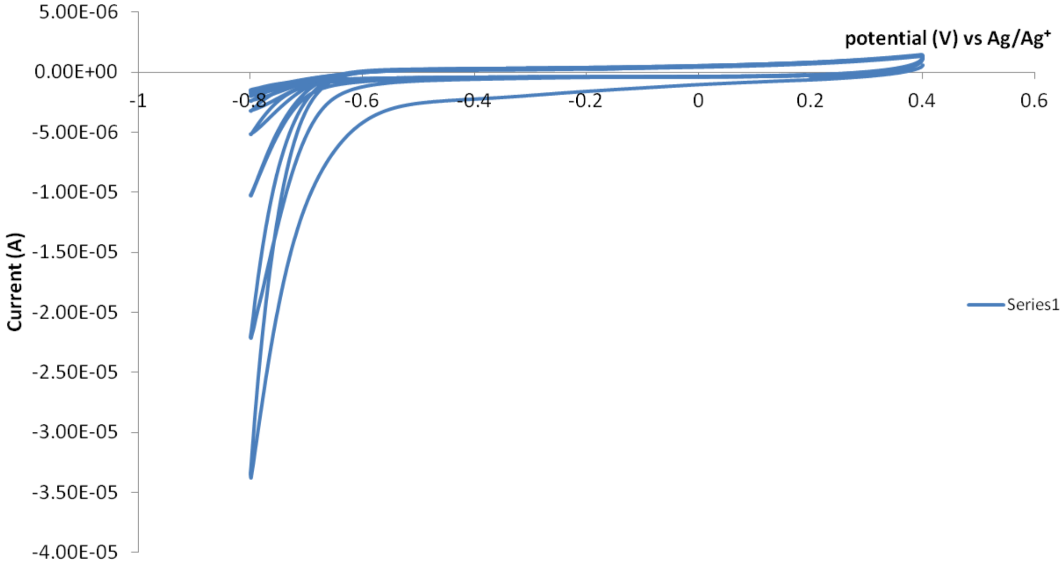

Figure A-6. Deposition of NAB on NDI.

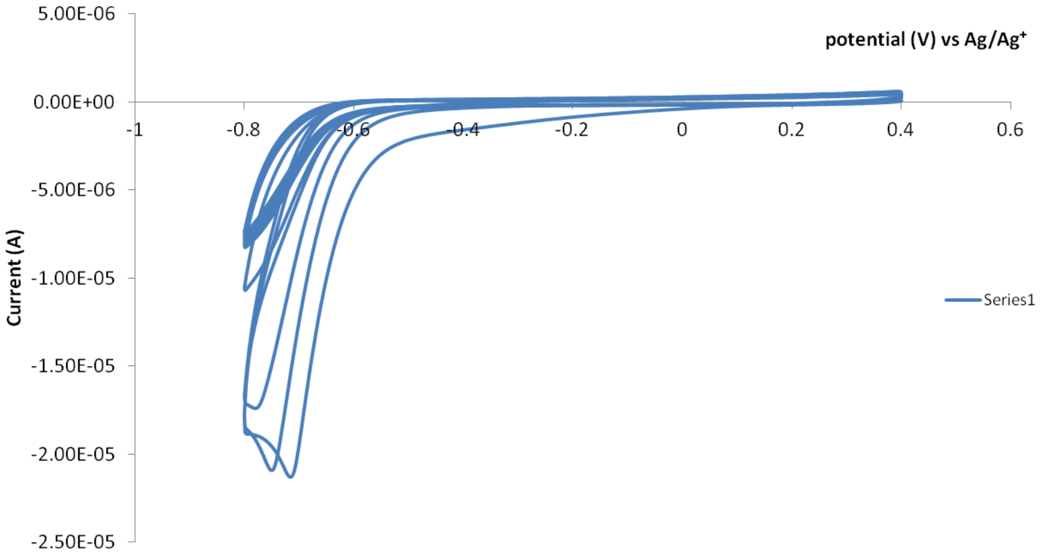

Figure A-7. Deposition of AQ on NDI.

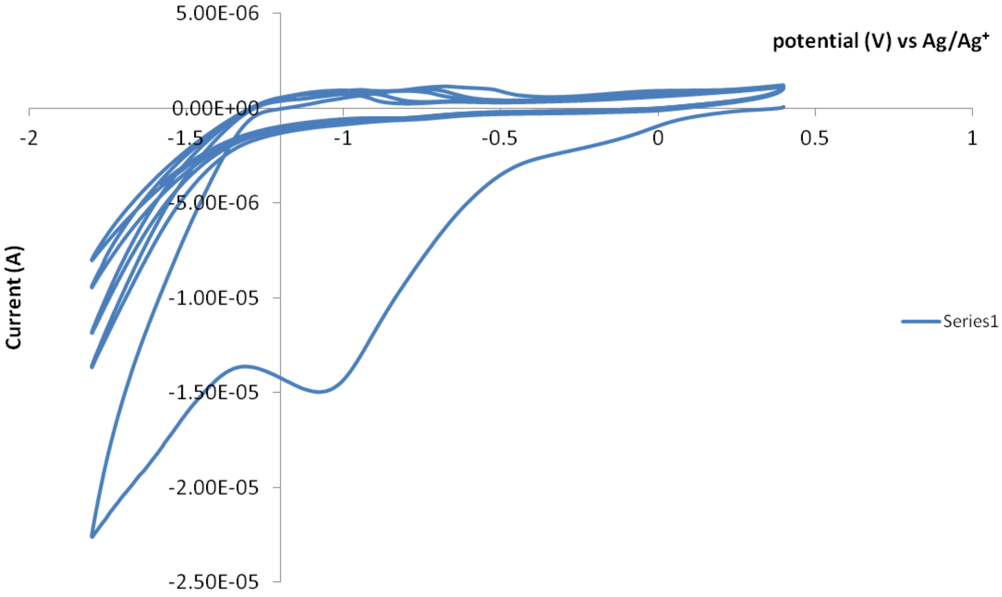

Figure A-8. Deposition of FL on NDI.

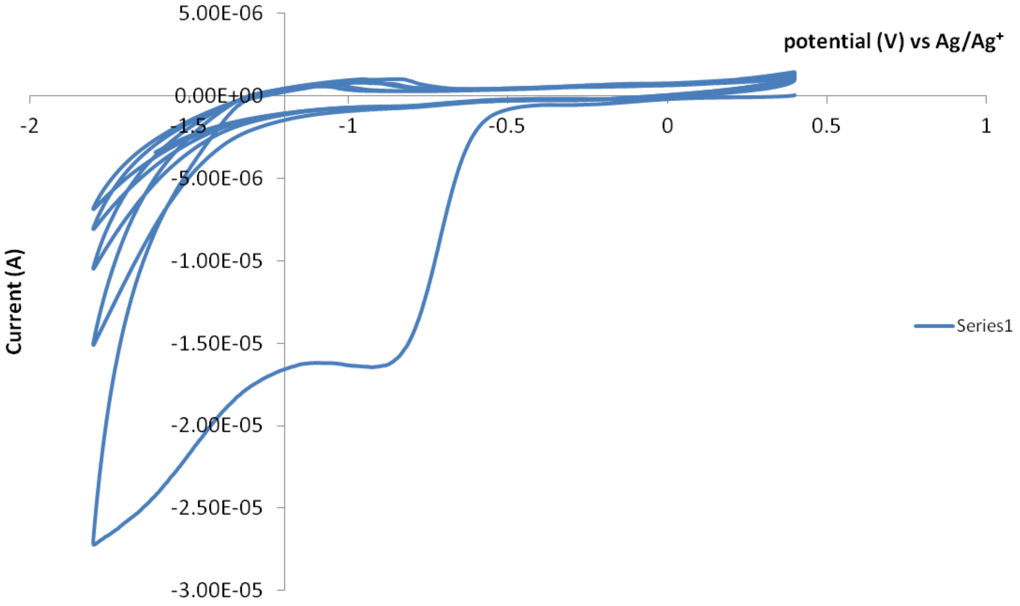

Figure A-9. Deposition of FL on AQ.

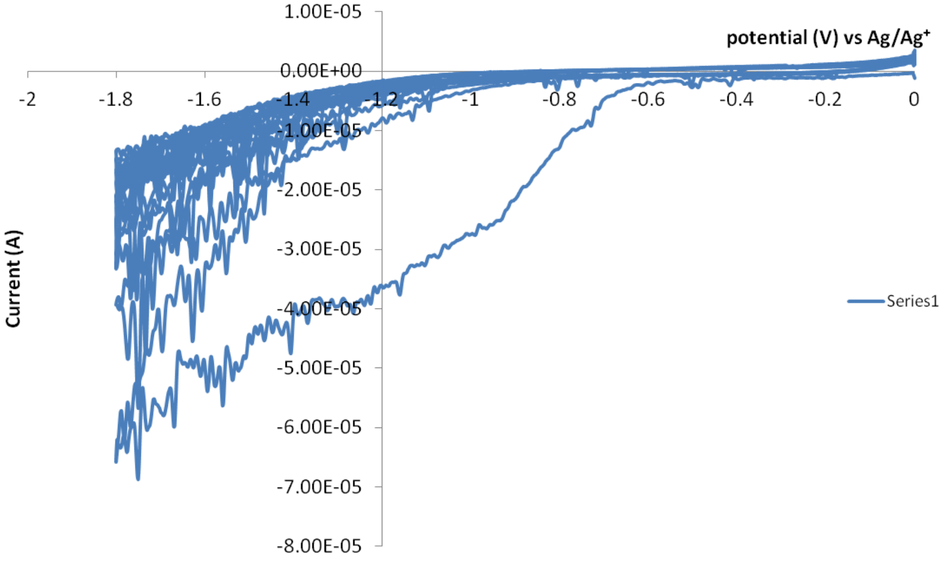

Figure A-10. Deposition of BTB on AQ.

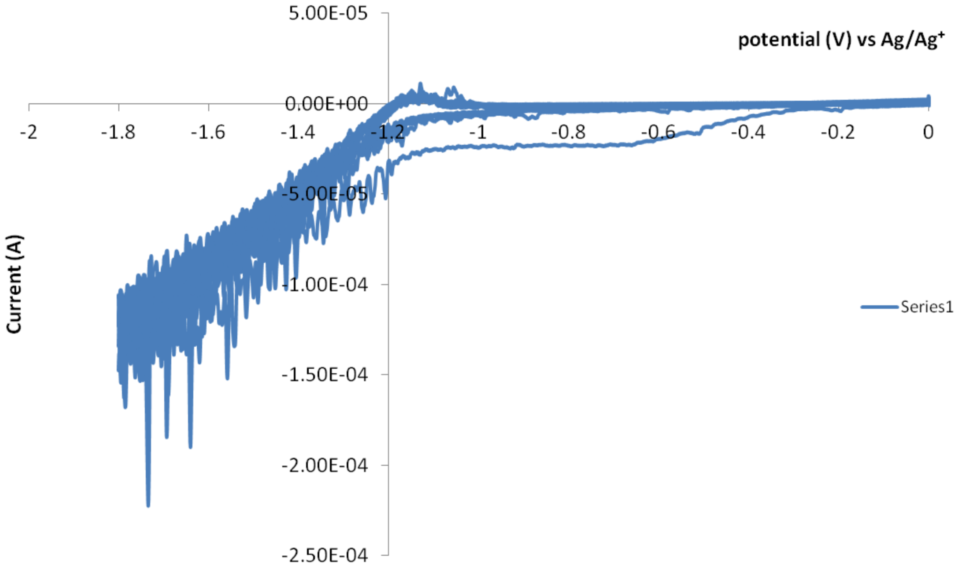

Figure A-11. Deposition of AQ on BTB.

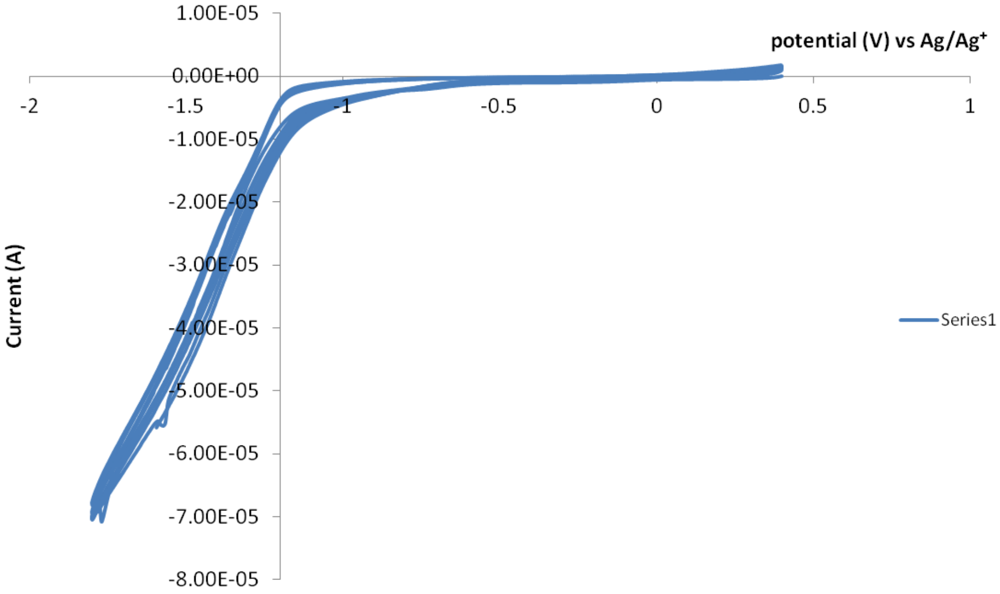

Figure A-11. Deposition of AQ on FL.

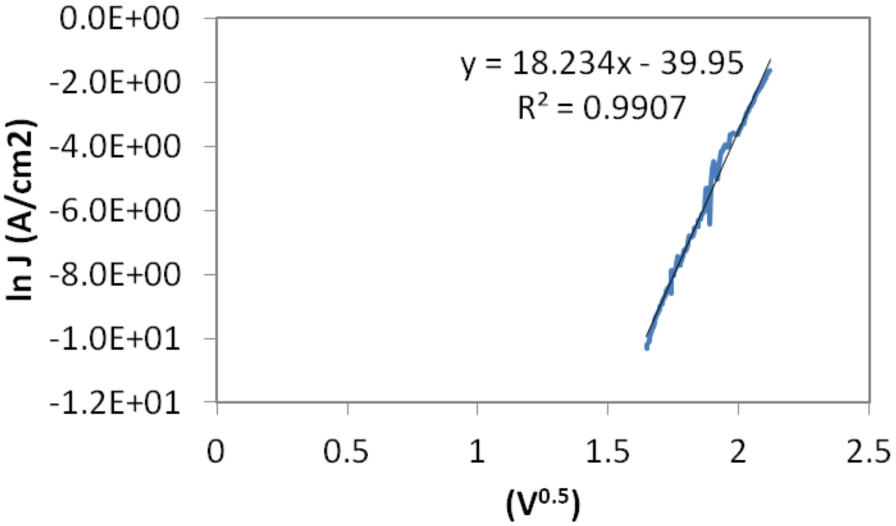

Figure A-12. lnJ versus $V^{0.5}$ for $NDI_{10.7}BTB_{10.3}$ device at 100K.

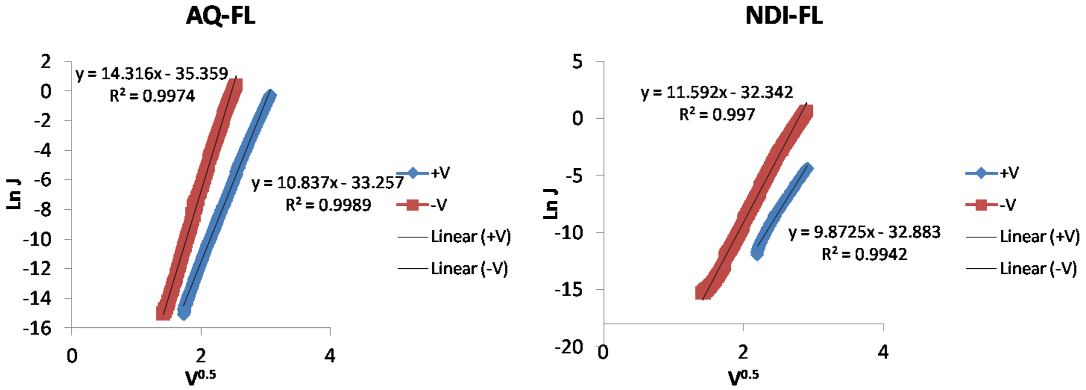

Figure A-13. lnJ versus $V^{0.5}$ for AQ-FL and NDI-FL bilayers.

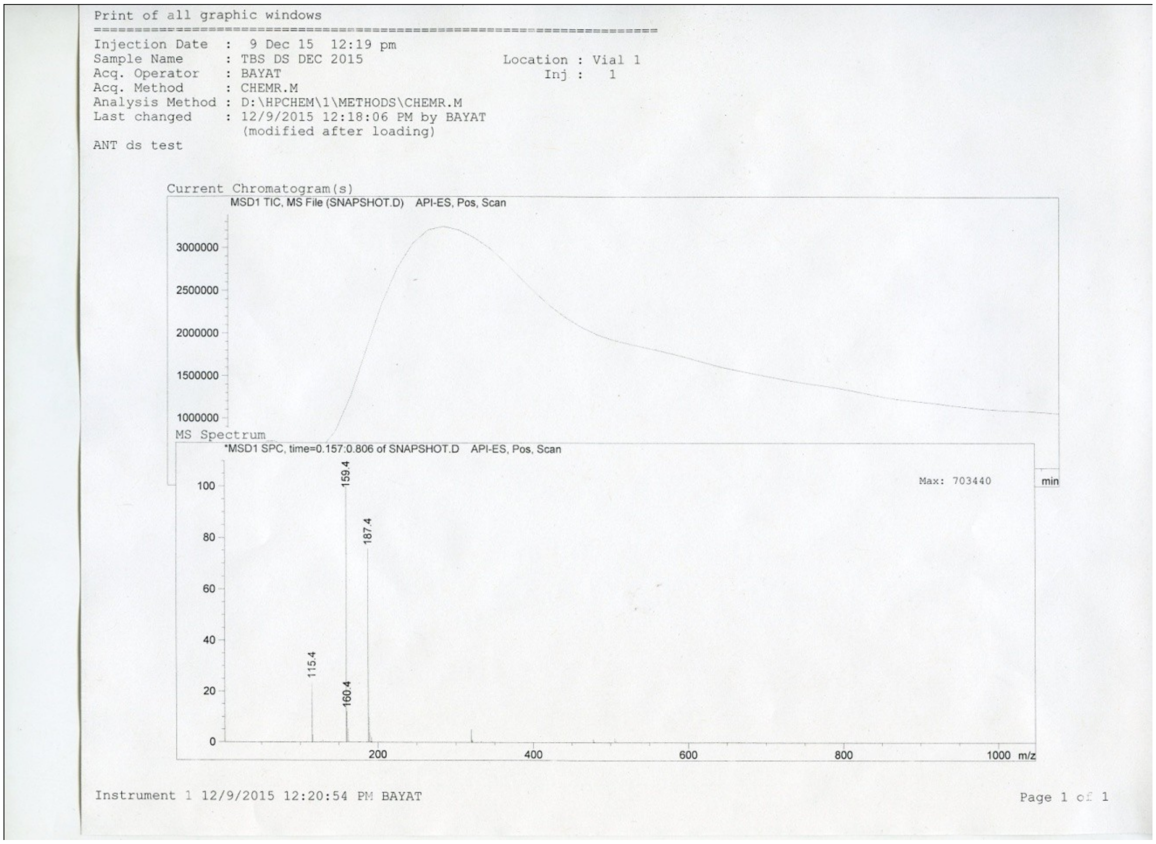

```
Print of all graphic windows
=====================================================================
Injection Date  :  9 Dec 15  12:19 pm
Sample Name     : TBS DS DEC 2015              Location : Vial 1
Acq. Operator   : BAYAT                             Inj :   1
Acq. Method     : CHEMR.M
Analysis Method : D:\HPCHEM\1\METHODS\CHEMR.M
Last changed    : 12/9/2015 12:18:06 PM by BAYAT
                  (modified after loading)
ANT ds test
```

```
Instrument 1 12/9/2015 12:20:54 PM BAYAT                          Page 1 of 1
```

Figure A-14. TB DS LC-MS.

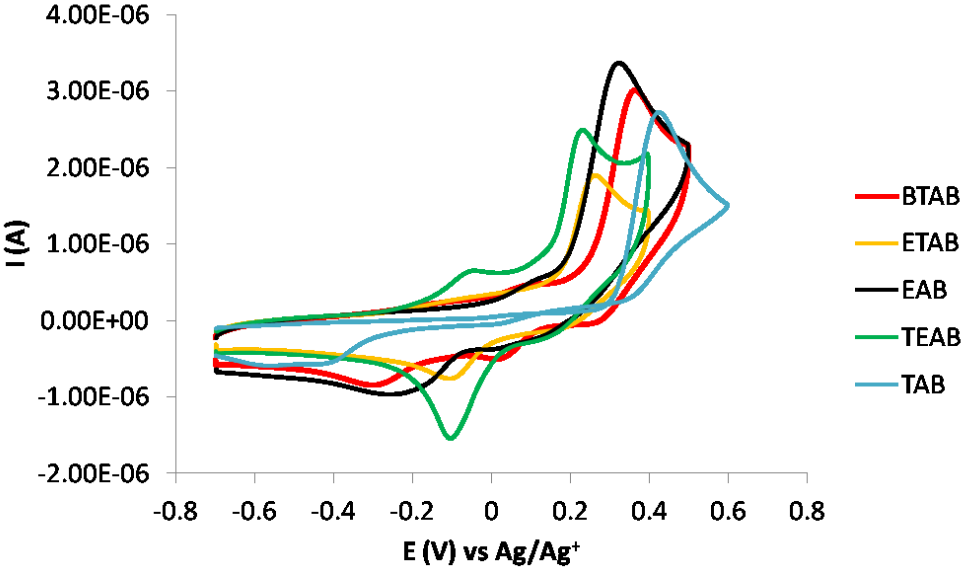

Figure A-15. Oxidation of amine starting materials of thiophene derivatives.